2014

Polymer Micro- and Nanofluidic Systems for In Vitro Diagnostics: Analyzing Single Cells and Molecules

Swathi Reddy Pullagurla
Louisiana State University and Agricultural and Mechanical College, spulla1@tigers.lsu.edu

POLYMER MICRO- AND NANOFLUIDIC SYSTEMS FOR IN VITRO DIAGNOSTICS: ANALYZING SINGLE CELLS AND MOLECULES

A Dissertation

Submitted to the Graduate Faculty of the
Louisiana State University and
Agricultural and Mechanical College
in partial fulfillment of the
requirements for the degree of
Doctor of Philosophy

in

The Department of Chemistry

by
Swathi Reddy Pullagurla
B.S., Nizam College, 2006
M.S., Osmania University, 2008
May 2014

This dissertation is dedicated to my loving mom Dhana Lakshmi Pullagurla whose unconditional love has been my greatest strength throughout my life. Without her sacrifices this arduous task would have been truly impossible.

ACKNOWLEDGMENTS

It is a pleasure to convey my gratitude to everyone who contributed in assorted ways to my doctoral studies. Firstly, I would like to express my gratitude to my advisor, Prof. Steven Soper for his thoughtful guidance, encouragement and for providing me an opportunity to work on some intriguing projects. His truly scientist intuition has made him an ocean of ideas which exceptionally inspired and enriched my growth as a student, a researcher and a scientist want to be. I am grateful for the comments and contributions of my dissertation committee members, Dr. Kevin Smith, Dr. Paul Russo, Dr. Jayne Garno and Dr. Mauld Walsh.

I am deeply indebted to Dr. Uma Vuruputuri who has been my role model. My journey to United States and my PhD career would not have begun without her constant guidance.

I am also extremely thankful to my uncle Venkatesh whose encouragement and support has been very pivotal to my journey to US and also successful completion of my work. He is definitely a person who is willing to do anything to see me happy.

Outside the lab, I would like to express my appreciation Dr.Manikanthan Bhavaraju, in particular, who has been a wonderful friend and witness to the challenges of my own doctoral process starting with graduate school applications and culminating with this dissertation. Gopi Payyavula for his constant motivation by showing me several reasons not to give up. He is a wonderful friend, whom I can always count upon. Also, Dr.Naveen Rondla & Dr. Raghavendra Rao Kurada for being with me during my rough and difficult phases of PhD career.

It has been my pleasure to work with talented “Super Soper group” members past and present including Dr. Chantiwas, Dr. Nesterova, Dr. Hong, Dr. Bala, Dr.Wonbae Lee, Sudha & Pratap as well as current group members Nyote, Mike, Joyce, Katrina, Brandon, Matt Jackson, Maria and Colleen.

My heartfelt and special thanks goes to Dr. Maggie Witek and Dr. Matt Hupert for their scientific advices, insightful discussions and friendly assistance with various scientific and non-scientific problems all the time. Franklin, Kumuditha, Dr. Udara Dharmasiri and Dr. Samuel Njoroge who were more than just labmates and who were always willing to help. I would cherish all the productive and fun moments in the lab with these wonderful people. I am deeply grateful to Tom Neish and all the members at UNC Cancer Blood Bank for providing the blood samples required for my research.

Lastly, none of this would have been possible without the love and support of my family my dad Vittal Reddy Pullagurla, sister Swetha, brother Srinivas and Raj Kanchipati. They believed in my capabilities and provided me with their unconditional love and support. I would also like to thank my and the members of my extended family. Finally, my greatest regards to the Almighty, Lord Hanuman for bestowing upon me the courage to face the complexities of life and complete this project successfully.

TABLE OF CONTENTS

LIST OF TABLES

LIST OF FIGURES

LIST OF SCHEMES

ABBREVIATIONS AND ACRONYMS

ACS	–	acute coronary syndrome
AFM	–	atomic force microscopy
ATP	–	Adenosine Triphosphate
BBB	–	blood brain barrier
BNP	–	brain natriuretic peptide
CD	–	cluster of differentiation
cDNA	–	complementary DNA
CE	–	capillary electrophoresis
CFD	–	computational fluid dynamics
CNS	–	central nervous system
COC	–	cyclic olefin copolymer
CRP	–	C-reactive protein
CSF	–	cerebro spinal fluid
CT	–	computed tomography
CTA	–	computed tomography angiography
DAPI	–	4',6-diamidino-2-phenylindole
DD	–	D dimer
DNA	–	deoxyribose nucleic acid
DWI	–	diffusion weighted imaging
EDA	–	ethylene diamine
EDC	–	1-Ethyl-3-(3-dimethylaminopropyl)carbodiimide
EDL	–	electrical double layer
ELISA	–	enzyme-linked immunosorbent assay
EOF	–	electroosmotic flow

EOLISA	–	elongated oligonucleotide-linked immunosorbent assay
FABP	–	fatty acid binding protein
FACS	–	fluorescence assisted cell sorting
FAST	–	face arm speech test
FDA	–	food and drug administration
FIB	–	focused ion beam
FITC	–	fluorescein isothiocyanate,
FLAIR	–	fluid attenuated inversion recovery
GFAP	–	glial fibrillary acid protein
HS	–	hemorrhagic stroke
IB	–	immobilization buffer
ICAM	–	intercellular cell adhesion molecule
ICH	–	intra cerebral hemorrhage
IL	–	interleukin
IRB	–	institutional review board
IS	–	ischemic stroke
LIF	–	laser induced fluorescence
LOC	–	lab on a chip
MALDI	–	matrix assisted laser desorption ionization
MBP	–	myelin basic protein
MEKC	–	micellar electrokinetic chromatography
MES	–	2-(*N*-morpholino)ethanesulfonic acid
miRNA	–	micro RNA
MMP	–	matrix metalloproteinase
MRA	–	magnetic resonance angiography

MRI	–	magnetic resonance imaging
MS	–	mass spectrometry
NA	–	nucleic acid
NCCT	–	non-contrast computed tomography
NDKA	–	nucleotide diphosphate kinase A
NHS	–	*N*-hydroxysuccinimide
NIHSS	–	national institutes of health stroke scale
NIL	–	nanoimprint lithography
NMDA	–	N-methyl-D-aspartate receptor
NSE	–	neuron specific enolase
PBMC	–	peripheral blood mononuclear cells
PC	–	polycarbonate
PCR	–	polymerase chain reaction
PCT	–	perfusion computed tomography
PEG	–	polyethylene glycol
PMMA	–	polymethyl methacrylate
POC	–	point of care
PPC	–	photoactivated polycarbonate
PWI	–	perfusion weighted imaging
qPCR	–	quantitative polymerase chain reaction
RMS	–	root mean square
RNA	–	ribo nucleic acid
RT	–	reverse transcription
SAH	–	subarachnoid hemorrhage
SELDI	–	surface-enhanced laser desorption

SM	–	stroke mimic
SPE	–	solid phase extraction
TIA	–	transient ischemic attack
TNF	–	tumor necrosis factor
TOF	–	time-of-flight
tPA	–	tissue plasminogen activator
VCAM	–	vascular cell adhesion molecule
VLP	–	visinin-like protein
vWF	–	von willebrand factor

ABSTRACT

Polymer micro- and nanofluidic systems, with their critical dimensions, offer a potential to outperform conventional analysis techniques and diagnostic methods by enhancing speed, accuracy, sensitivity and specificity. In this work, applications of microfluidics have been demonstrated to address the existing challenges in stroke diagnosis, by mRNA expression profiling from whole blood within <20 min. A brief overview of various biomarkers for stroke diagnosis is given in chapter 1 followed by design and testing of individual microfluidic modules (chapter 2 and 3) required for the development of POC diagnostic strategy for stroke. We have designed and evaluated the performance of polymer microfluidic devices for the isolation of leukocyte subsets, known for their differential gene expression in the event of stroke. Target cells (T-cells and neutrophils) were selected from with greater purities, from 50 µl whole human blood by using affinity based capture in COC devices within a 6.6 min processing time. In addition, we have also demonstrated the ability to isolate and purify total RNA by using UV activated polycarbonate solid phase extraction platform.

Polymer-based nanofluidic devices were used to study the effects of surface charge on the electrodynamic transport dynamics of target molecules. In this work, we report the fabrication of mixed-scale micro- and nanofluidic networks in poly(methylmethacrylate), PMMA, using thermal nanoimprint lithography using a resin stamp and surface modification of polymer nanoslits and nanochannels for the assessment of the associated electrokinetic parameters – surface charge density, zeta potential and electroosmotic flow. This study provided information on possible routes that can be adopted to engineer proper wall chemistry of polymer nanochannels for the enhancement or reduction of solute/wall interactions in a variety of relevant single-molecule studies.

CHAPTER 1.BIOMARKERS FOR POINT-OF-CARE DIAGNOSIS OF STROKE: A LITERATURE REVIEW

1.1 Stroke Introduction

Stroke is a major cause of neurological disability and mortality affecting more than 15 million people worldwide. It is the third leading cause of death in the United States after coronary heart disease and all cancers combined. In the United States alone, 795,000 cases are reported annually with approximately 75% being classified as incident cases.[1, 2] It is predicted that the mortality rate of stroke will almost double by 2020 simply because, the ageing population is more susceptible to stroke.[3] Mortality due to stroke and their higher incidence may be linked to a number of factors which are classified into modifiable and non-modifiable risk factors. Modifiable risk factors include high blood pressure, diabetes mellitus, cardiac diseases (such as atrial fibrillation, heart failure), high cholesterols, cigarette smoking, alcohol consumption, obesity, sedentary lifestyle, and unhealthy dietary habits which account for 60% of all strokes.[4] The other 40% of stroke cases are mediated by non-modifiable risk factors such as age, gender, ethnicity and genetics.

Strokes are classified as diseases of the brain vasculature that share a clinical syndrome, which exhibits the rapid onset of a focal cerebral disturbance. The World Health Organization defines clinical stroke syndrome as "rapidly developing clinical signs of focal (or global) disturbance of cerebral function lasting more than 24 hours or leading to death with no apparent cause other than that of vascular origin."[5] This definition includes stroke both due to infarction and hemorrhage. Stroke accounts for 16% of all cardiovascular diseases (see Figure 1.1) and 2-4% of the healthcare costs worldwide,[6] and has a devastating impact on public health. Hence, it

is imperative to identify early risk factors of stroke to predict the recurrence of the disease and for primary prevention.

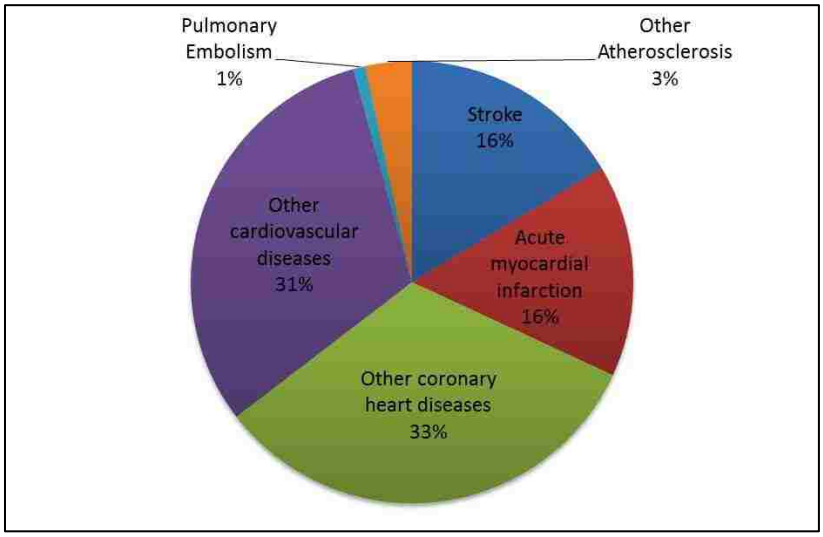

Figure 1.1 Deaths from cardiovascular diseases, U.S, 2010 (Adapted from National Heart, Lung and Blood Institute, Disease Statistics)

1.2 Subtypes of Stroke and Pathophysiology

Stroke can be broadly classified into two subtypes, ischemic and hemorrhagic (see Figure 1.2). Both forms of stroke are neurological deficits causing impairment of language, motor function, cognition, vision and affect and are caused by interruption of cerebral blood flow resulting in a temporary or permanent change in one or more regions of the brain. The functional changes associated with or resulting from (termed as pathophysiology) both subtypes are different and complex depending on the nature of the lesion (area of damaged brain tissue). Therefore, it is crucial to understand the biochemical mechanisms involved, to clearly delineate the type, diagnosis, and prognosis of stroke.

1.2.1 Ischemic Stroke (IS)

Ischemic stroke accounts for 84% of all strokes.[7] IS can be further categorized into i) intracranial thrombosis (large vessel and small vessel types, see table 1.1) primarily caused by

impairment of blood flow to the brain due to blockage of cerebral arteries and ii) extracranial embolisms caused due to blockage of blood vessels resulting from a clot (embolus).

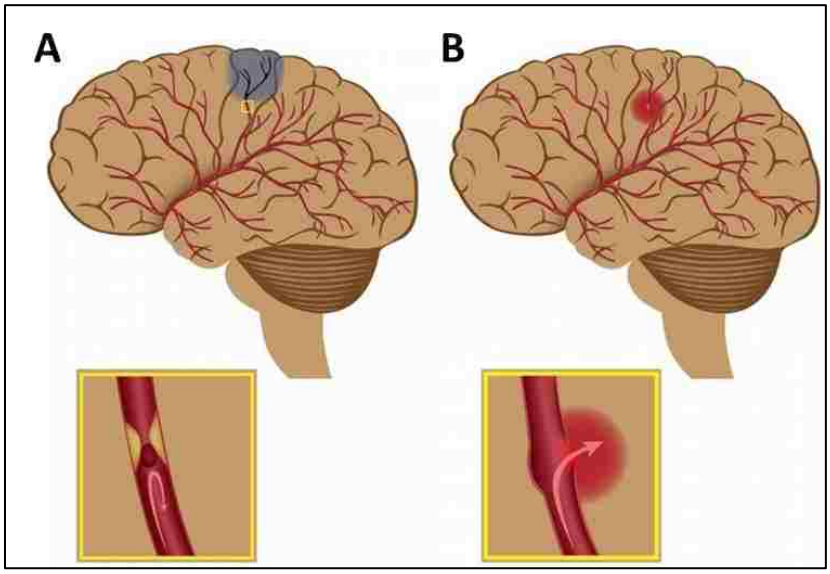

Figure 1.2 Subtypes of stroke. (A) Image of brain showing ischemic stroke. Blue area indicates deprivation of blood supply and the inset shows blockage of blood vessels due lack of blood flow to the affected area. (B) Hemorrhagic stroke showing an area of bleeding (in red). Inset shows the leakage of blood caused by rupture of blood vessels. Reproduced with permission from (www.alilamedicalmedia.com)

Table 1.1 Etiology of stroke

Stroke			
Ischemic (84%)		Hemorrhagic (16%)	
Embolic (31.5%)	Thrombotic (51.5%)	Subdural	Epidural
Large vessel (31.5%)	Small vessel (20%)	Intracerebral (10%)	Subarachnoid (6%)

The onset of ischemic stroke initiates a series of neurochemical events, which are referred to as an 'ischemic' cascade shown in Figure 1.3.

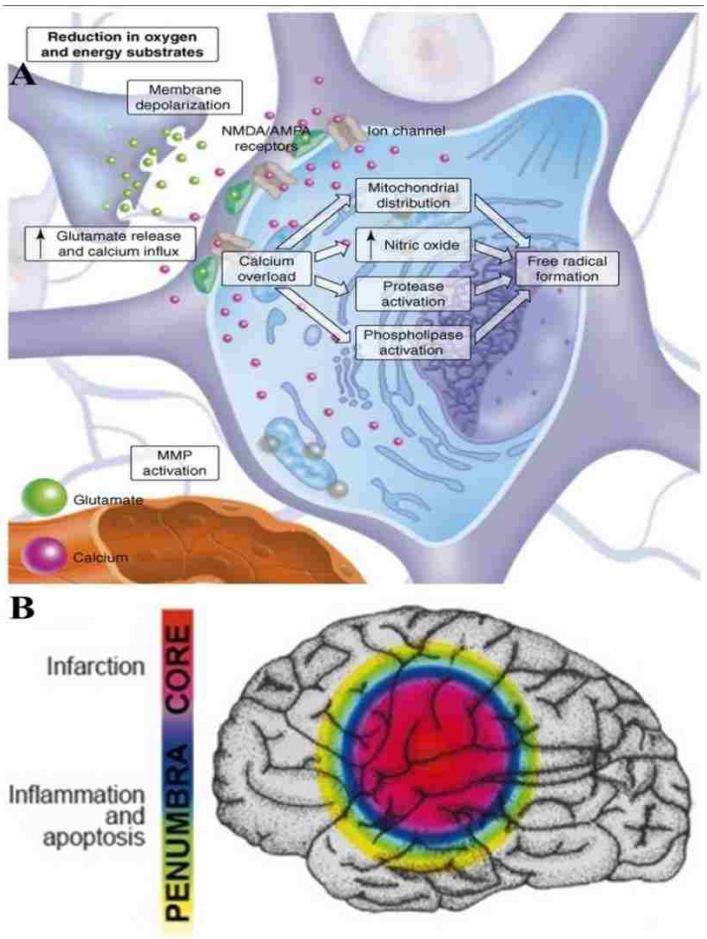

Figure 1.3 (A) Summary of neurochemical changes that trigger the initiation of ischemic cascade (B) Ischemic penumbra : a brain region of low perfusion in which cells have lost their membrane potential terminally (‘core’) is surrounded by an area in which intermediate perfusion prevails (‘penumbra’) and cells depolarize intermittently (‘peri-infarct depolarization’). Reproduced with permission from reference [8, 9].

During ischemia, brain damage or neuronal death is caused by the failure of energy producing compounds, like adenosine triphosphate (ATP), thereby causing a lack of glucose and oxygen to the brain; thus, cellular homeostasis is not supported. The inadequate energy production also affects the functioning of the ion gradient by the loss of potassium ions causing cytotoxic edema (neuronal swelling). Numerous other complex mechanisms are involved in the brain tissue causing ischemic stroke (see Figure 1.3A). They include the release of glutamate and aspartate neurotransmitters in the brain, calcium channel dysfunction, and production of reactive

oxygen species or oxygen radicals activating proteases and lipases that damage cellular and extracellular elements.[9, 10] All these processes result in either the immediate death of a part of the brain parenchyma (core) or partial injury (penumbra) with the potential of recovery with therapeutic intervention (see Figure 1.3B). The duration, severity, and location of ischemia are the main factors which determine the extent of brain damage.

1.2.2 Hemorrhagic Stroke (HS)

Hemorrhagic stroke, which is responsible for about 16% of stroke cases, occurs due to a ruptured aneurysm (abnormal bulging on the wall of arteries) in the brain causing blood leakage into the surrounding tissue.[11] Hemorrhage due to ruptured brain arteries is of two types, intracerebral hemorrhage (ICH) or subarachnoid hemorrhage (SAH).[12] ICH originates from the rupture of weakened cerebral vessels; most commonly, small arteries or arterioles causing a blood leakage within the parenchymal cerebral space. This forms a localized hematoma (cavity filled with blood) building up the pressure. The primary cause of ICH can be attributed to hypertension. SAH on the other hand, is triggered by bleeding of the ruptured arteries into the subarachnoid space further leaking into cerebral spinal fluid (CSF) blocking its circulation. This causes extensive damage to brain cells and therefore, SAH is the most deleterious type of stroke. The treatment for this type of stroke usually requires medications, which reverse the bleeding that has occurred and might even require surgical drainage in some cases. A report from Andersen *et al.* demonstrated the higher severity of stroke and mortality rates associated with HS (49.2%) when compared to IS (25.9%).[13]

Stroke mimics (SMs) are non-stroke conditions (false positives) that present symptoms similar to stroke and therefore, SMs are most often confused with stroke. SMs are defined as diseases caused by neurologic symptoms which resemble a stroke, and their frequency varies

from 1.2 to 25%[14, 15] depending on the clinical evaluation. They are reversible with no significant brain damage. The most common type of stroke mimics are migraine,[16] demyelinating disease, tumors,[17] meningitis,[14] glucose level abnormalities like hypoglycemia, non-cerebrovascular diseases such as epilepsy[18] (caused by focal dysfunction), dementia,[19] and transient global amnesia.[20] Misdiagnosis of stroke has serious ramifications and therefore SMs must be excluded for proper identification of stroke subtype and treatment management. A recent prospective study of more than 300 patients with suspected stroke found 31% had SMs at the time of final diagnosis.[21] Libman *et al.* were able to correctly identify and diagnose stroke in 81% cases, finding 19% to be SMs.[22] The possibility of a stroke in case of SMs are ruled out by neuroimaging methods, discussed in the next sections.

Transient ischemic attacks (TIAs), also known as mini-strokes, are defined as events caused by transient interruption of blood flow to a part of brain and can be typically resolved within a 24 h time window. Unlike an actual stroke event, there is no severe damage to the brain cells in TIAs. However, it is likely that the occurrence of stroke is preceded by a TIA, and studies show that 35% of TIA patients have a chance of stroke within five years.[23, 24] Also, the presence of TIA conditions leads to recurrent strokes. Therefore, confirming the probability of stroke or TIA versus SMs is extremely important.

1.3 Clinical Diagnosis of Stroke

The longer the treatment for stroke is delayed, the lesser the benefits from it. Hence, the phrase “time is brain.” One of the most critical elements in stroke diagnosis is the time of onset. In most cases, the arrival of the patient to the hospital is delayed due to the limited awareness of signs and symptoms of the disease. Rapid assessment of patients suspected with stroke is therefore highly crucial to accommodate the therapeutic treatment for any subtype of stroke by

excluding SMs within a fairly short time window. Incidents of acute myocardial infarction are also noticed in some of the stroke patients and as a part of the initial evaluation; electrocardiography should be performed in such cases. The major challenges associated with stroke diagnosis are the lack of imaging resources, lack of neurologic training in emergency clinicians, exclusion of SMs and misdiagnosis, and the limited time window for effective treatment.

1.3.1 Stroke Assessment Scales

Stroke scales are evaluation tools used to provide quick and quantitative assessments of the severity of neurologic deficits including motor, sensory, visual and cognitive impairment, functional outcome, global outcome due to stroke condition.[25] These scales also provide prognostic information and serve as a baseline to compare the progress or deterioration. Pre-hospital stroke scales are therefore critical for early recognition ultimately saving valuable time in triage (priority of the treatment based on severity) and treatment of the patient.

Initial attempts were made to develop a unified scale but due to the complex nature and heterogeneity of stroke, separate scales were developed.[26] Based on the type of information collected about the patient, they are divided into the following sub-categories. i) Global outcome scales such as the modified rankin scale, and the glasgow outcome scale, which provide a broad overview about the neurologic disability ii) Physical deficit scales, such as the National Institutes of Health Stroke Scale (NIHSS), which provides information about the deficit with the result scores attached to severity based on the neurologic examination iii) Activities of daily living scales, such as the barthel index , which measure the functional outcome and recovery useful in studies of rehabilitation.[27-30]

Stroke scale chosen must be simple, easily and expeditiously administered, and sensitive to a patient's condition.[31] Although currently, existing scales do not satisfy all the criteria, NIHSS is considered to be the best scale and is widely used in most stroke studies as it is a highly reproducible numeric scale that can be completed within 5-8 minutes. It can be used both by neurologists and non-neurologists. Higher scores in this 15-point assessment scale indicates greater deficit. Compared to other scales, this scale has proven intrarater and interrater reliability and has predictive validity for stroke outcome.[32-34]

It should be noted that these scales cannot be used in isolation in order to reach a decision about the treatment method. The important metrics for the use of these scales in diagnosis are validity and reliability. The diagnostic accuracy of most of these scales is about 80%, although their sensitivity and specificity differ to some extent. It is important to understand that clinical sensitivity and specificity differ from analytical sensitivity and specificity. Clinical sensitivity refers to the percentage of people with the disease, identified positive for the disease by a given assay whereas clinical specificity provides negative predictive value of the disease as determined by the assay.[35] Majority of these scales are used to measure severity and predict stroke outcome, but they are not capable of distinguishing stroke subtypes. They might provide better results when used in conjunction with brain imaging or blood biomarkers.

1.3.2 Neuroimaging Methods

Neuroimaging has become an invaluable tool for the initial and accurate diagnosis of stroke and its subtypes. The advent of various imaging techniques have enabled clinicians to understand the cause of the disease (etiology) and functional changes associated with the disease (pathophysiology) of stroke and guide future therapy and provide the utmost benefit to the patient by confirming the diagnosis. Stroke imaging serves two purposes: first to diagnose or

confirm the occurrence of stroke by ruling out SMs and, second, to assess the location and amount of potentially salvageable brain tissue and irreversibly infarcted tissue.

1.3.2.1 Computed Tomography (CT)

The most commonly used modality for imaging is CT because of its wide availability in most clinical settings and quick acquisition times compared to other imaging methods. CT is the "criterion standard" for stroke evaluation and the primary diagnostic test to detect ischemic lesions and rule out ICH. Types of CT include noncontrast head CT (NCCT), CT angiogram of the head and neck (CTA), and perfusion CT (PCT).[36] NCCT is usually performed to identify early signs of stroke and also exclude or confirm hemorrhages. It's wide availability and the speed of image acquisition makes it useful for initial evaluation of suspected stroke patients.[37] The limitation of an NCCT scan is that subtle signs due to the disease are missed in the first few hours of stroke, resulting in about 40% false negative rates.[38] The utility of CT for stroke has been enhanced by the advent of newer generation CT scanners such as for CTA and PCT.[39] CTA provides information about vessel occlusion such as the site and length of the occlusion, and gives a clear picture of cerebral blood vessels.[40] PCT requires a rapid injection of intravenous contrast and repeated imaging of sections of the brain. Based on the total amount and speed that blood flows to different vascular territories of the brain this technique can help in the assessment of potential areas of salvageable tissue in the ischemic penumbra.[41, 42] Ezzedine *et al.* demonstrated the improvement of diagnostic accuracy by combining these two neuroimaging modalities when compared to the use of NCCT alone.[39]

However, the limitations of CT are exposure to ionizing radiation, side effects associated with the use of intravenous contrast agents, inability of the scanners to image entire brain for perfusion imaging as current scanners are limited to 2-4 cm wide area of the brain.[41, 43]

1.3.2.2 Brain Magnetic Resonance Imaging (MRI)

MRI is another widely used neuroimaging method for the evaluation of stroke. This method is associated with high cost, limited availability, and lengthy image acquisition times, but, considered to be extremely sensitive in detecting ischemic lesions. MRI can also detect or exclude ICH with an accuracy comparable to CT.[44] It has also been shown that the sensitivity of MRI is 83% and that of CT is 26% for the diagnosis of any stroke subtype.[45] Diffusion weighted imaging (DWI), perfusion weighted MRI (PWI), magnetic resonance angiography, and fluid attenuated inversion recovery, are some of the imaging techniques under the MRI umbrella.[46]

Images from DWI give information about the onset of ischemia, which may not be sometimes seen using NCCT. Once a hemorrhagic stroke has been excluded by CT, DWI improves stroke detection from 50% to more than 95%.[47, 48] PWI helps in the identification of hypoperfused regions of the brain by using a contrast agent and like PCT, it can identify the ischemic penumbra. Perfusion imaging of the entire brain is one of the main advantages of PWI.[48] DWI/PWI mismatch values detect the tissue subjected to infarction by subtracting the volume of tissue restricted to diffusion from DWI and the volume of tissue that is poorly perfused from PWI. Information about penumbra from DWI/PWI mismatch helps to identify patients in need of tissue plasminogen activator **(**tPA), a clot buster drug or thrombolytic agent (also known IV rt-PA or alteplase, usually given through a catheter inserted into a vein in the arm).[49-51] Despite significant advances in MRI techniques, implementation of MRI becomes difficult due to longer scanning times, high costs, non-applicability in patients with claustrophobia, and also impracticality in an emergency setting.

1.4 Therapeutics for Stroke

Neurons in the low blood flow area of the penumbra are at a greater risk with elapsing time leading to neuronal cell death. This is linked to the short therapeutic time window which refers to time between the onset of symptoms and the treatment. For ischemic stroke, one therapeutic measure is the restoration of cerebral blood flow to the affected region (reperfusion) to limits the neurologic deficit. The most common therapy is thrombolytic therapy, which restores blood flow to the damaged ischemic tissue by dissolution of the clot and reduce the neuronal tissue damage.[52] Another approach is neuroprotection, which involves the use of drugs to protect the brain against neuronal dysfunction; their efficacy is limited due to the associated side effects, and additional trials are still ongoing.[8] However, the combination of thrombolysis and neuroprotectants may offer more advantages in the clinical management of stroke.[53]

1.4.1 Recombinant Tissue Plasminogen Activator (rt-PA)

Currently, the only FDA (Food and Drug Administration) approved drug for ischemic stroke is recombinant tissue plasminogen activator (rt-PA). It works by attaching to the fibrin in the blood clots, and then activates the production of plasmin, which causes the clots to disintegrate. This unblocks the blood vessel and restores the blood flow. The findings of a National Institutes of Neurological Disorders and Stroke trial have shown a complete neurologic recovery in about 31 – 50% of patients treated with rt-PA in three months.[54] However, rt-PA must be administered within a narrow time window of 3-4 h from the onset of stroke symptoms. As large number of patients arrive after the currently approved 3 h time window, administering a proper treatment remains difficult. Therefore, some studies have been conducted on the expansion of the effective therapeutic time window, but the results showed that increasing the time length between symptom onset and treatment from 4-6 h made the rt-PA treatment less beneficial compared to

treatment within 3 h.[55-57] Moreover, this thrombolytic therapy (rt-PA) is contraindicated in HS patients which might lead to threating outcomes. While the phenomenon about the increased risk of hemorrhage with rt-PA administration is yet to be clearly elucidated, a CT scan must be performed to check for the possibility of HS before administering rt-PA and patients with the risk of HS are excluded. Due to this delay, the treatment can only reach 3-5% of patients with IS in the United States.[58, 59] So far, there is no FDA approved treatment for hemorrhagic stroke. Other treatment methods for IS include perfusion enhancing approaches such as administration of aspirin and heparin,[60] use of anticoagulants (warfarin), antiplatelet agents, antihypertensive agents and telemedicine.[61]

1.5 Role of Blood Brain Barrier (BBB) in Brain Injury

Understanding the physiology of the BBB is very crucial in developing an effective diagnostic and therapy for several brain diseases, especially stroke. The BBB plays an essential role in brain homeostasis. The BBB is a dynamic barrier, which protects the central nervous system (CNS) from unwanted and neurotoxic substances circulating in blood and allows for the transport and permeability of required nutrients. Any disruption or leakage of this barrier causes brain dysfunction and stimulates natural immune or inflammatory responses.[62, 63] The BBB is comprised of endothelial cells forming the capillaries of the brain with tight junctions Fthat restrict the movement of molecules into the brain and maintain the cell polarity (which refers to diversification of cell shapes through asymmetric cell divisions of stem cells that are crucial proper functioning of differentiated cell types[64]). Other components of the BBB include pericytes, astrocytes, and microglia, which support the permeability of this barrier and are involved in the immune responses of the central nervous system (see Figure 1.4).[65] All these together form a complex neurovascular unit. The BBB plays a major role in the immune system

of the brain and any changes in the brain's microenvironment caused by diseases like stroke generates inflammatory responses due to activation of microglial cells and programmed cell death (apoptosis) occurs.[66, 67]

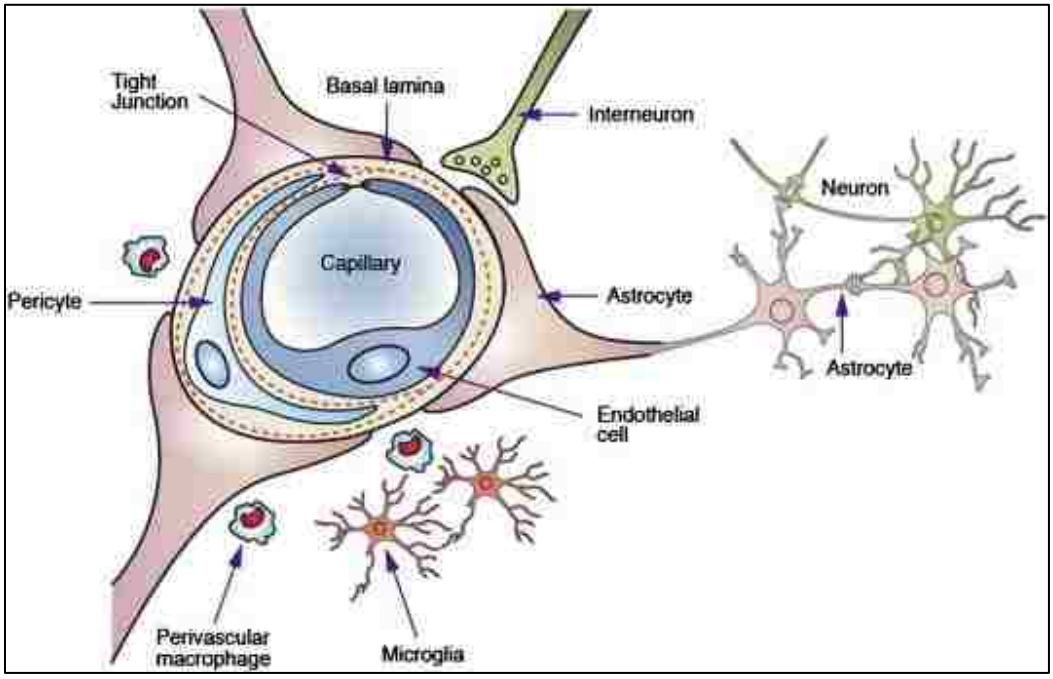

Figure 1.4 Cellular constituents of the blood–brain barrier. The barrier formed by capillary endothelial cells, surrounded by basal lamina and astrocytic perivascular endfeet. Astrocytes provide the cellular link to the neurons. The figure also shows pericytes and microglial cells which form the important components of a neurovascular unit. Reproduced with permission from reference [65].

Breakdown of the BBB and damage of endothelial cells following brain injury increases the permeability of the barrier and allows for the passage of biomarkers from the neurons and glial cells (neuron supporting cells) into peripheral blood.[68] There is also evidence of leukocyte infiltration into circulation in humans 48-72 h after stroke, and it has been hypothesized that the accumulation of these leukocytes is the primary cause of tissue damage and prevents blood flow after restoration.[69] Specifically, neutrophil penetration into brain tissue causes significant damage due to the release of oxygen free radicals and proteolytic enzymes.[70-73] Also, certain biomarkers like matrix metalloproteinase-9 (MMP-9) are shown to play a biphasic role in stroke by

disrupting the blood brain barrier during the initial phases of the stroke event and promote vascular growth during recovery phases.[74] Although the exact mechanisms and roles of different cells in stroke is still unclear, better investigation of the BBB would pave the way for novel therapeutic approaches.

1.6 Biomarkers for Stroke

Biomarkers are measurable indicators of any biological processes that may be used to diagnose a disease, monitor its activity, predict its course, or assess response to treatment.[75, 76] Cells, genes, hormones, enzymes, or changes in biological function can be considered as biomarkers.[77] Development of a proper diagnostic test for stroke through biomarker identification has remained a challenge for a variety of reasons, including the complexity of the ischemic cascade and presence of the blood-brain barrier; efforts are ongoing in this field of study. As discussed in the previous sections, neuroimaging techniques can be used as initial evaluation tools depending on their availability in the clinical setting to identify the type of stroke. Reaching a clinical decision may sometimes be limited by the experience of the medical staff. An adjunctive test along with the neurological assessment becomes important especially in cases where brain imaging appears normal. A rapid diagnostic test will, therefore, be extremely helpful for pre-hospital screening, and can guide the intervention of thrombolytic treatment.

Biomarkers have the potential to provide insight into the mechanisms of brain injury and, diagnostic information to improve patient management. They are also useful in the investigation of prognosis and response to a therapy. The major challenge associated with finding promising biomarkers for stroke diagnosis is due to their prolonged release following the event of stroke and their inability to perfuse through the BBB.[78] To date, no molecular diagnostic test exists for stroke and no marker has proven to be clinically sensitive and specific to diagnose either

ischemic or hemorrhagic stroke. One should note that analytical sensitivity and specificity are distinct from clinical sensitivity and specificity. High analytical sensitivity does not always guarantee high clinical sensitivity.[35]

Clinical sensitivity = $\frac{True\ positives}{[True\ positives+False\ Negatives]}$ and provides information on the positivity of the disease as determined by the assay. Clinical specificity = $\frac{True\ negatives}{True\ negatives+False\ positves}$ and provides information on the negativity of the disease as determined by the assay. Whereas, analytical sensitivity refers to the ability of the assay to detect the lowest possible concentration of an analyte in a given sample and analytical specificity is assay's ability to identify a target substance.[35]

There is no individual clinically useful biomarker for stroke, such as troponin or creatinine phosphokinase for the diagnosis of coronary syndrome, B-type/brain natriuretic peptide (BNP) for congestive heart failure, or D-dimer (DD) for pulmonary embolism, which have been used in point-of-care platforms.[79-81] Detection of ideal biomarkers in the case of neuronal injury is very complex compared to heart diseases, due to the physiological differences between the brain and the heart, such as cellular heterogeneity in the brain (multiple cell types and cells with differentially localized elements such as axons and cell bodies). Also, the BBB limits the access of markers in sufficient quantities to the vasculature, but there is direct vasculature access in heart. Furthermore, complex biochemical pathways occurring in the ischemic cascade makes biomarker isolation difficult. The validity of clinical judgment is also diminished by SMs . While a significant amount of research has yet to be conducted on the benefits of single marker vs. multi-marker panels, researchers postulate that multi-marker panel testing would increase clinical sensitivity for accurate diagnosis.[82]

Investigations done by the scientific community suggest that an ideal biomarker or a panel of biomarkers should be able to address the following diagnostic questions: (i) Does the patient have stroke; (ii) Is it IS or HS; (iii) Is there a need for initiation of thrombolytic treatment with the observed symptoms; and (iv) Is there a risk of recurrence? These questions can be addressed by finding an ideal biomarker that can be released into blood in a fair amount of time in detectable quantities, and the concentration levels should correlate with the volume of infarct. Some practical considerations in the choice of these biomarkers include cost, factors that affect the measurement, and the ease of obtaining the biomarkers. Ideal properties of biomarkers for clinical utility are summarized in the Table 1.2

Table 1.2 Ideal properties of biologic markers. Adapted from Biomarkers Definitions Working Group [Reference 76].

Uses and Properties	Ideal Properties
Physical properties	Stable, not susceptible to loss during storage or processing
Analytical properties	Extremely sensitive, specific and reproducible
Clinical and scientific validity properties	Biomarker levels should reflect different degrees of brain injury, different stages of clinical severity and correspond to patient's clinical status or prognosis
Practical properties	Minimal invasiveness or patient discomfort, low per-usage cost and wide availability at treatment centers
Uses	Drug development, prediction of response to treatment, understanding of molecular and cellular mechanisms

1.7 Types of Protein Biomarkers for Stroke

This section highlights the biomarkers relevant to ischemic stroke. Compared to ischemic biomarkers, very little research has been carried out on hemorrhagic biomarkers due to fewer

cases of HS. Biomarkers can be classified into several categories: (i) Imaging biomarkers that measure the changes in the nervous system through brain imaging; (ii) Molecular biomarkers; and (iii) Pharamacodynamic biomarkers, indicative of certain pharmacological responses useful in drug development.[83] Biomarkers based on drug development can be described as diagnostic (defining the population within a specific disease) and prognostic (correlated with outcome). The subsequent sections will focus mainly on molecular biomarkers in which measurements are made on biological fluids like blood, plasma, serum, or CSF. The onset of any brain disease triggers the release of several biomarkers into CSF and subsequently into the blood stream. Nevertheless, not all the biomarkers released may be specific to stroke.

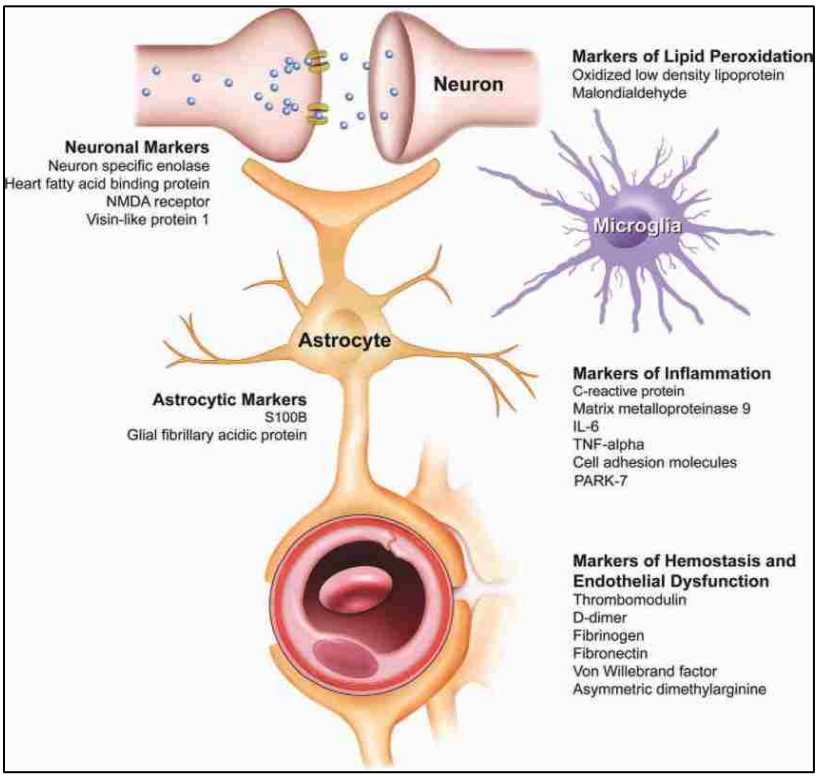

Figure 1.5 Categorization of potential biomarkers according to their role in ischemic cascade. Markers for neuronal injury, lipid peroxidation, inflammation and homeostasis are illustrated. Reproduced with permission from reference [84].

Advances in proteomics and genomics have helped in the identification the potential biomarker candidates. Among several current approaches, proteomics has attracted attention as proteins are readily available in most of the body fluids and, studies offer an insight into both the structure and function of proteins in relevance to stroke. Protein biomarkers are mostly studied due to the better understanding of their relation with pathophysiology of ischemic stroke. Some of the biomarkers involved in ischemic injury include those associated with glial activation, inflammation, oxidative stress; thrombus formation, neuronal injury, and endothelial dysfunction (see Figure 1.5).[85, 86]

1.7.1 Glial Biomarkers

During the initial events in the ischemic cascade, glial cells are activated, and inflammation is generated in response to ischemia. The most extensively studied markers specific to glial function are S100B, glial fibrillary acidic protein (GFAP), and myelin basic protein (MBP). S100B is an acidic calcium binding protein in astrocytes and glial cells; increased concentrations of S100B stimulate the cytokine production. In ischemic stroke, serum levels of S100B are elevated within 12 h from symptom onset with continuous increase even after three days.[87] Even in primary hemorrhagic stroke, higher S100B concentrations have been observed, predicting higher morbidity.[88, 89] It has also been shown that S100B correlates with the volume of infarction, neurologic outcome, and its elevated levels in serum are believed to be due to BBB dysfunction.[90, 91] S100B cannot be considered as a stroke-specific biomarker as its levels in serum and CSF are found to increase in other neurological disorders (trauma, Alzheimer's disease, and schizophrenia), extracranial malignancies (schwannoma, melanoma and neuroblastoma) and also due its delayed release.[92, 93]

GFAP is an immediate filament protein present in astrocytes and to a lesser extent in ependymal cells. It is a marker of glial cell lineage and has been reported to increase in stroke attacks with peak levels after 3 days.[94, 95] A study by Foerch *et al*. showed that GFAP is the strongest candidate for detecting hemorrhagic stroke due to its significantly increased levels observed in 81% of ICH patients compared to 5% of IS patients. Although increase in serum concentration of GFAP is found to be correlated with volume of infarcted brain as well as S100B concentration, its delayed release of 6 h after symptom onset limits its use in stroke diagnosis.[96, 97]

MBP is a hydrophilic protein that plays an important role in the structure of myelin sheaths.[98] Increased levels of this protein are found in CSF are found in cases of stroke and multiple sclerosis.[99] Detectable levels of CSF MBP in IS subjects are observed after one week and levels decreased after three weeks.[95] The increased concentrations of MBP correlated with higher NIHSS scores and large lesion volumes.[100] The limiting factor for the application of MBP as a diagnostic marker of stroke is its latency in response to a stroke event.

1.7.2 Neuronal Biomarkers

During stroke, certain neuronal markers are upregulated and released into the CSF and blood-stream as a result of CNS cellular responses. Increased levels of these neuronal isoenzymes signal damage to the brain parenchyma.[101] Several neurobiochemical markers that evaluate neuronal injury have been identified and some of them are listed below (see Table 1.3).

Neuron-specific enolase (NSE) is a glycolytic enzyme specific for neurons. NSE levels are detectable between 4-8 h of onset of stroke with peak levels after 24 h.[102] Some of the limitations in using this biomarker include latency in release and less sensitive serum levels to brain tissue damage, although the sensitivity is high in CSF.[103] There is no clear explanation in

the literature on the variation of CSF and serum NSE levels but serum NSE levels were significantly measured in case of greater injury.[104] Sensitivity may be the limiting factor for its clinical use.

N-methyl-D-aspartate (NMDA) receptor is an excitatory amino acid receptor and is a tetramer of two NR1 and two NR2 subunits.[105] A pilot study found increased serum levels of NMDA NR2 antibodies in patients with transient ischemic attack when compared to controls and even higher levels in IS subjects. These elevated levels correlated with NIHSS score and lesion volume.[106] Ongoing research is focusing on measuring NMDA receptor and its utility as a potential stroke biomarker.

Another neuronal biomarker, fatty acid–binding protein (FABP), is a cytosolic protein involved in transporting long chains of fatty acids. FABP is expressed in various tissues and rapidly released into circulation. In the central nervous system, heart-type FABP is present in glia and brain-type FABP is present in neurons at elevated levels within 2-3 h of stroke onset. Detection of this marker in a variety of other brain injury conditions does not make it stroke-specific.[107-109] FABP is also classified as a glial biomarker in some reports.

1.7.3 Inflammatory Biomarkers

One of the factors believed to cause neuronal death during the ischemic cascade is inflammation, which causes increased levels of inflammatory markers. These biomarkers are associated with increased infiltration of leukocytes. Biomarkers such as tumor necrosis factor-alpha (TNF-α),[110] MMPs,[111] vascular cell adhesion molecule 1 (VCAM-1), C-reactive protein (CRP),[112] intercellular adhesion molecule 1 (ICAM-1),[113] interleukin-6 (IL-6),[114] (Table 1.3) are some proteins involved in inflammation. All of these biomarkers have shown only moderate clinical utility, either due to low sensitivity or specificity.[115]

Table 1.3 Summary of all protein stroke biomarkers and their functions

	Protein	Description and Function	Ref.
Glial biomarkers	S100B	Astrocyte marker; a calcium-binding protein involved in cell cycle progression & differentiation	[88,96]
	GFAP	Astrocyte marker; an intermediate filament protein role in cell structure, blood brain barrier, communication	[96]
Inflammatory biomarkers	IL-6	Cytokine involved in acute-phase response	[116]
	CRP	An acute-phase reactant involved in atherothrombosis and ischemic injury	[117]
	MMP-9	Proteolytic enzymes that degrade collagen-disrupting endothelium and plaque matrix	[118, 119]
	VCAM-1	Immunoglobulin involved in leukocyte–endothelial cell interaction	[120, 121]
	TNF-α	Cytokine involved in inflammation and acute-phase response	[116]
	ICAM-1	Immunoglobulin involved in leukocyte–endothelial cell interaction	[120]
	ApoC-I ApoC-III	Lipid metabolism	[122]
Neuronal biomarkers	NSE	Neuronal marker; a neuronal glycolytic enzyme	[90, 123]
	FABP	Cytosolic protein involved in long chain fatty acid transportation	[107-109]
	NMDA	Glutamate excitotoxic response	[106]
Thrombosis biomarkers	vWF	A glycoprotein involved in coagulation, platelet adhesion, and factor VIII binding	[124]
	D-dimer	Marker of acute thrombosis; a breakdown product of fibrin blood clot	[125]
Other biomarkers	PARK7	An RNA-binding protein; elevated in neurodegenerative disease	[126]
	NDKA	Transfers phosphate between nucleosides	[126]
	BNGF	A growth factor involved in neuronal growth and differentiation	[82]

1.7.4 Evaluation of Protein Biomarkers for Clinical Utility in Stroke

Several studies have been conducted to evaluate the clinical utility of various stroke relevant protein biomarkers, which involves measuring biomarker performance and its statistical association with clinical state of interest to know more about the disease. As mentioned previously, due to the heterogeneity of stroke and no individually useful biomarker, researchers have evaluated multiple biomarker panels to obtain additional information useful for early management.

The potential utility of five blood-borne marker panel consisting of MMP-9, S100B, B-type neurotrophic growth factor (BNGF), von willebrand factor (vWF), and monocyte chemotactic protein (MCP) was demonstrated by Reynolds *et al*. Within 9 h of onset of cerebral ischemia, they distinguished IS from healthy controls with a sensitivity of 93% and a specificity of 93% based on 75 samples, indicating the use of this marker panel in conjunction with CT imaging.[82] A pilot study Lynch *et al.* used 26 blood-borne biomarkers including MMP-9, VCAM-1, S100B to differentiate IS from controls with a sensitivity and specificity was 90% within 24 h of symptom onset.[121] However, initial control subjects employed in this study were very less (65) Identification of high levels of S100B and low levels of soluble form of receptor for advanced glycation endproducts (sRAGE) blood biomarkers in ICH patients compared to IS patients, suggested the use of these two biomarkers to distinguish between IS and HS according to Montaner *et al.*[127] Within 6 h of symptom onset, the increased levels of plasmatic biomarkers, apoliprotein CI (ApoC-I) and apoliprotein CIII (ApoC-III) could distinguish between HS and IS. ApoC-I provided 94% sensitivity and 73% specificity and ApoC-III 94% sensitivity with 87% specificity. In this study, ApoC-III marker was also used to distinguish stroke (both IS and HS) from controls with a specificity and sensitivity of 97% and 58%, respectively.[122] A recent study

compared the performance of a biomarker panel (BNP, D-dimer, MMP-9, and S100B) to the cincinnati prehospital stroke scale administered by an emergency room triage nurse in diagnosing stroke.[128] The potential utility of this biomarker panel was supported by additional studies demonstrating the adaptability of this panel to point-of-care setting.[129, 130]

Although, some of the aforementioned studies showed good clinical sensitivity and specificity; reliability, validity and ease of obtaining results still remains an issue. Moreover, comparison between patient and healthy controls, typically results in overestimation of sensitivity and specificity of these protein biomarkers.[131]

1.8 Gene Expression Profiling of Peripheral Blood

Quantitative assessment of genes expressed in cells or blood samples is known as gene expression profiling. Gene expression profiling has been applied to various disease states like inflammatory disease,[132] toxic exposure,[133] multiple sclerosis,[134] and renal carcinoma.[135] These studies demonstrated a promising approach and formed the basis for gene expression profiles of white blood cells for finding diagnostic and prognostic biomarkers and providing mechanistic insights into stroke. A disease can be identified by grouping clusters of up-regulated and/or down-regulated genes and monitoring the changes in mRNA expression levels of the cells as a response to the injury.

Biomarkers based on mRNA levels, especially in blood, are an emerging and exciting area of research in medicine. mRNA biomarkers offers several advantages when compared to protein biomarkers. mRNA levels are chosen to be monitored as they can detect genes with a low expression level in protein.[136] Currently known coding RNAs have been well described and available on a single platform rather than identifying for best candidate biomarkers using proteomic approaches.[137] Moreover, mRNA is induced more quickly in response to injury when

compared to protein expression. Also, mRNA expression analysis offers high throughput as tens of thousands of genes can be analyzed at the same time.[138]

One of the challenges of biomarker use is obtaining samples from the appropriate tissue. Peripheral blood, therefore is a good source of mRNA for use in clinical trials, as plentitude of information can be obtained from expression profiling by studying thousands of genes simultaneously.[139] Blood, being a biological fluid circulating through every part of the body, has the potential to reflect any physiological changes during a disease state. It is also an easily accessible source of tissue to identify the biomarkers for any disease, especially in a clinical setting, as tissue biopsy is practically infeasible for neurological disorders.[139]

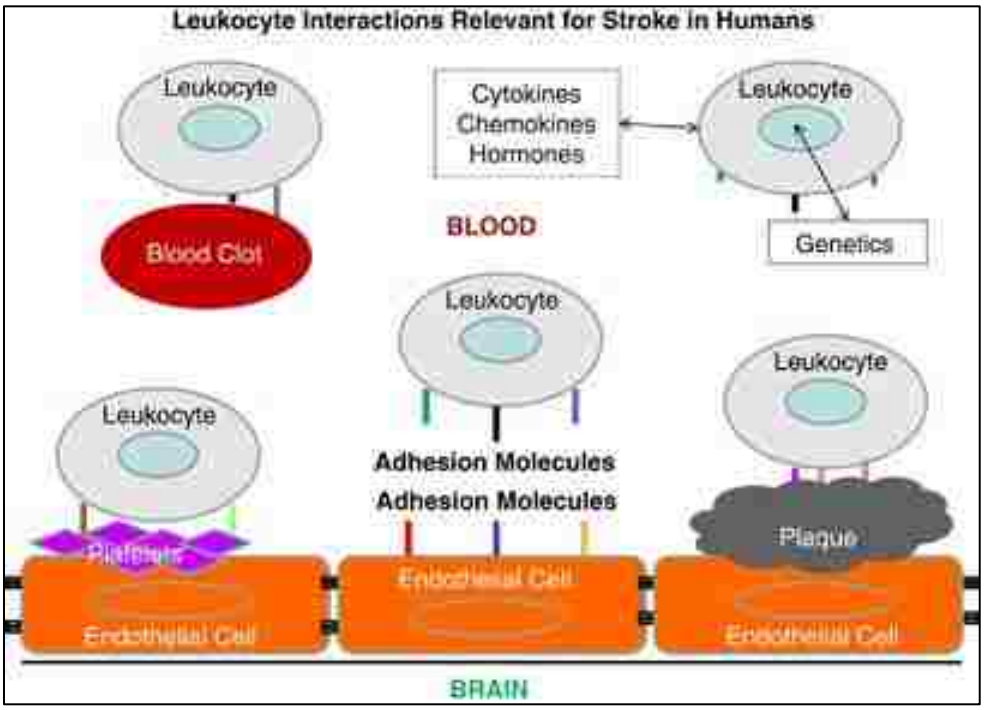

Figure 1.6 Leukocyte interactions with intravascular elements relevant for stroke in humans. Leukocytes (neutrophils, lymphocytes, and monocytes), platelets, red blood cells, and other cells interact with each other and with endothelial cells in normal vessels. Leukocyte interactions with endothelial cells, platelets, atherosclerotic plaque, blood clots, and intravascular molecules (cytokines, chemokines, hormones, others) account for some changes of gene expression following stroke. Leukocytes also signal to these other cell types, which also account for changes of gene expression. Reproduced with permission from reference [143].

Cell types involved with disease specific responses are mostly blood derived-mononuclear cells (lymphocytes and monocytes); hence, peripheral blood mononuclear cells (PBMCs) are highly significant in stroke.[140] As discussed previously, there is an infiltration of leukocytes during stroke that generates an inflammatory response. Each cell type has a unique gene expression profile, and the change in their expression as a result of any physiological or pathological change(s) can be studied from peripheral blood.[141] Although the exact role of leukocytes in brain injury is yet to be clearly understood, it is hypothesized that leukocytes interact with cells from every tissue, endothelial cells of the vasculature, foreign organisms or cells, injured cells and every element within blood (see Figure 1.6).[142] In addition, leukocytes have a complement of expressed RNAs that reflect a combination of the genetics of these cells as well as the interactions of those cells with their environment.

Two approaches that can be adopted for expression profiling are: (i) Extraction of RNA from isolated pure fractions of PBMCs; and (ii) Stabilization of whole blood and extraction of RNA from the whole blood cell lysate. Advancements in microarray technology utilizing porous glass and plastic membranes facilitated the study of thousands of genes obtained from a single RNA sample simultaneously.[144, 145] The verification of gene regulation is most commonly performed using real time/quantitative polymerase chain reaction (qPCR). Strict methods of RNA isolation are very critical specially when comparing ischemic and healthy subjects. PAXgene based tubes (for blood collection) are used for stabilization of whole blood, and the additive contained in them prevents any RNA degradation and further alteration in transcriptional profile. However, sensitivities less than 50% were reported using this approach.[146]

A pilot study of gene expression in humans using peripheral blood was first conducted by Moore *et al.* They identified a 22 gene-panel which distinguished ischemic stroke from controls

with 78% sensitivity and 80% specificity.[140] Further studies with whole blood using an 18 gene-panel showed a change in gene expression of monocytes and neutrophils.[147] Prior to this, studies by the same group suggested that differences in gene expression observed in white blood cells of rat subjected to various brain specific stimuli might serve as a genomic fingerprint for various diseases.[148] Barr *et al.* identified a panel of 9 genes from 64 samples using whole blood to distinguish stroke subjects from controls.[149] These studies demonstrated a proof-of-concept and open the possibility for gene expression studies to identify the genes as biomarkers for differentiating stroke subtypes.

1.8.1 MicroRNA Biomarkers

MicroRNAs (miRNAs) are a class of small, noncoding RNAs that target and regulate the expression of complementary mRNAs. miRNA-based diagnostic assays were developed for diseases such as lung cancer and pancreatic adenocarcinoma.[150, 151] Emerging studies on circulating micro RNAs (miRNAs) in several cardiovascular and other diseases demonstrate the potential of miRNAs as biomarkers. Some of the attractive features of miRNA include; i) detectable levels of miRNAs in plasma and serum; ii) ability to withstand freezing and thawing cycles; iii) stability at high pH and temperatures; and iv) reproducible detection in healthy individuals and expression levels are tissue specific.[152-154]

Initial studies in IS rat models have demonstrated the elevation of miR-124 in plasma with peak levels at 24 h. Furthermore, miR-210 decreased levels in IS were believed to be an indication of severity of brain damage, which were further confirmed in a rat model.[155] A recent study also revealed that elevated expression of circulatory miR-145 expression in peripheral blood of IS patients compared to controls, but the source of miR-145 could not be identified.[156] However, there remains a need for standardized quantification procedures and validation studies

for miRNA profiling, but it would be interesting to explore the role of circulating miRNAs in diagnosis and prognosis of stroke.[157]

1.9 Approaches for Stroke Biomarker Detection and Validation

Major components of successful biomarker development include discovery, qualification, verification, clinical validation and use in clinical trials (Figure 1.7). In the discovery phase of development, large sets of biomarker candidates are identified based on knowledge of the pathophysiology of the disease and differential expression between diseased and normal states.[75] In the verification phase, the potential for success of a marker is determined by its clinical specificity and sensitivity. Surviving biomarkers from the verification phase are then considered for validation in a clinical environment. Validation is a lengthy process requiring a large cohort of patients and robust clinical evidence obtained from several independent studies.[158] The major challenge during this phase is recruitment of properly matched controls (age, gender, demographics etc.) for comparison with the patient samples.[159]

Advancements in -omic approaches (proteomics, genomics, metabolomics) have made it possible to identify the expressional or functional changes of a protein, DNA or mRNA expression during a diseased state and screen for useful biomarkers.[160] Proteomic approaches have been used for the identification of potential biomarkers because the phenotypic diversity among common genes can be determined by bioenzymatic functions of proteins.[161] Whereas, genomic approaches like DNA or RNA microarray technology measures genome-wide mRNA expression changes or DNA sequence changes (*i.e.*, mutations), variations in biological/clinical samples during developmental stages, drug treatments, and disease states.[162]

Ideal biomarker detection strategies should be able to detect biomarkers present in limited quantities in complex biological/clinical samples. Multiplexed immunoassays and quantitative

mass spectrometry are two broader analytical platforms for the identification of biomarkers. These techniques have radically improved the speed and precision of biomarker identification and measurement in biological fluids and other samples**.** The type of analytical technique chosen depends on the question to be addressed and availability of biological fluid for study. After the discovery and verification, robust immunoassays must be developed and optimized to evaluate their potential clinical utility. Some of the most widely used, label-based and label-free approaches and their usefulness in identification and validation of stroke biomarkers will be discussed here.

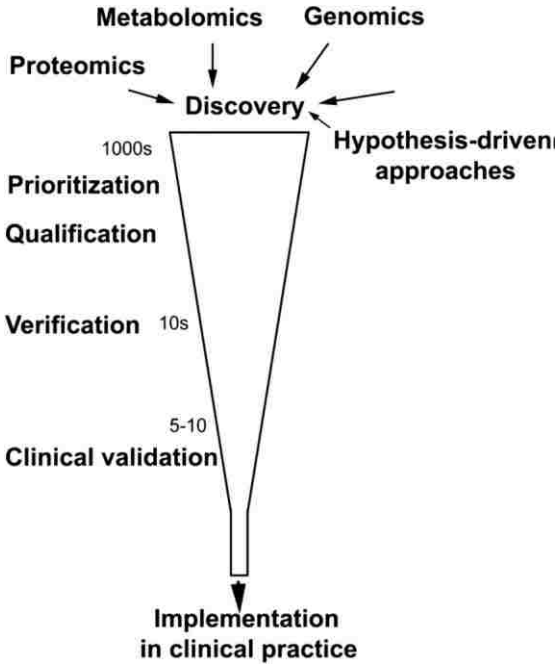

Figure 1.7 Representation of biomarker pipeline. Hypothesis-driven approaches and other high throughput technologies suggest thousands of candidate biomarkers from which a set of putative markers undergo systematic testing to establish the consistency of the association between marker and disease (qualification) and to study the sensitivity and specificity of the indicator in a larger number and a broader range of samples (verification). Few candidates after verification process undergo a lengthy and rigorous clinical validation. Reproduced with permission from reference [163].

1.9.1 Immunoassays

1.9.1.1 Enzyme-linked Immunosorbent Assay (ELISA)

ELISA is the most routinely employed technique for quantification and identification of proteins, peptides, antibodies and hormones. This plate-based immunoassay detects binding of the antigen and antibody is using an enzyme linked to a secondary antibody, which turns the colorless antigen-antibody complex into a colored product when enzyme substrate is added (see Figure 1.8).

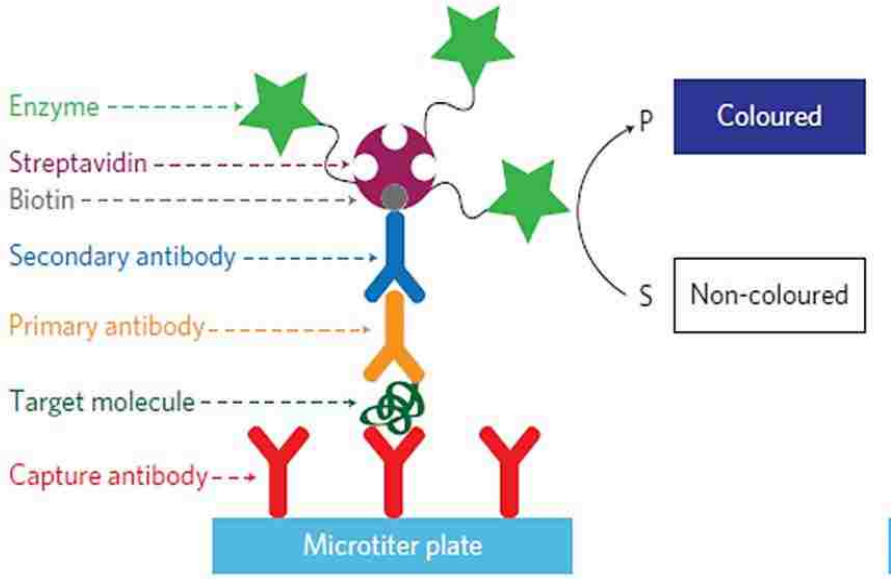

Figure 1.8 Schematic representation of the sandwich ELISA in which the target molecule is anchored to the substrate by capture antibodies and recognized by primary antibodies. The enzyme is linked to the immunocomplex through interactions between enzyme-decorated streptavidin and biotinylated secondary antibodies Enzymatic biocatalysis generates a coloured compound. P – product S – substrate. Reproduced with permission from reference [164].

In the direct ELISA, antigen is detected using an enzyme-conjugated primary antibody whereas; unlabeled primary and conjugated secondary antibodies are used in indirect detection. The most sensitive and robust format of ELISA is the sandwich assay. In this assay, the analyte to be measured is bound between the capture and detection antibodies. (see Figure 1.8). The most commonly used enzyme labels are horseradish peroxidase and alkaline phosphastase. These

enzymatic labels produce a detectable signal that is directly correlated to the binding of antibody to an antigen and the colorimetric output is usually measured by spectrophotometer. ELISA can be used for testing a few samples as well as high throughput screening with automated procedures.

A pilot study by Stejskal *et al.* used sandwich ELISA method to evaluate clinical utility of the visinin-like protein (VILIP-1), a CNS-abundant protein biomarker for brain injury and several neurogenerative diseases, released into the circulation as a consequence of neuronal destruction.[12] Serum and CSF levels of VILIP-1 were found to be elevated in IS patients within 3 h of stroke onset, compared to healthy subjects. This study was able to achieve 100% clinical sensitivity and specificity for stroke diagnosis. However, it cannot be completely assumed that this protein will serve as a single biomarker for stroke as it still needs a larger cohort of patient samples for further validation.[165] Another ELISA-based study using organ samples of mouse models enabled the measurement of VILIP-1 concentrations <100 ng/L and identified it as potential candidate for an acute blood-borne biomarker of IS.[161]

Further ELISA studies, in a large cohort of European and American populations, for stroke biomarker detection have shown increased concentrations of PARK7 (also called DJ-1) and nucleotide diphosphate kinase A (NDKA) in plasma samples after 3 h onset of a stroke event compared to a control population and remained increased up to 5 days after the initiation of the event. The authors hypothesized that the possible reason for overexpression of both PARK7 and VILIP-1 in plasma could be due to soluble protein produced by the injured neurons reaching the blood at the site of the lesion.[126] Zimmerman *et al.* used ELISA to detect heart-FABP in the serum of stroke patients and healthy controls. Clinical sensitivity and specificity were reported to be 68% and 100%, respectively.[166]

A new type of immunoassay, elongated oligonucleotide-linked immunosorbent assay (EOLISA), for protein biomarker detection has been reported by Han *et al.* This method utilized elongated DNA nucleotides (80-mer), a complementary RNA oligonucleotide and RNase H for signal amplification (see Figure 1.9). This assay was evaluated for detection of FABP spiked into healthy human serum samples. When compared to conventional ELISA, EOLISA showed 10-fold higher detection sensitivity (0–1 ng mL^{-1} range.).[167] Due to the improved sensitivity, this proposed immunoassay is expected to be potentially useful in clinical analysis of biomarkers.

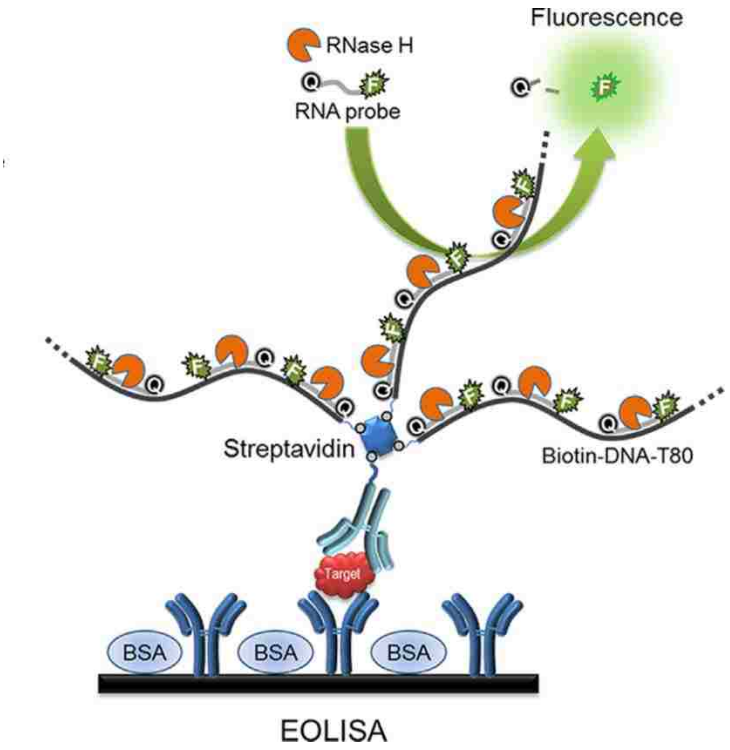

Figure 1.9 Illustration of EOLISA, a sandwich format which utilizes the biotinylated DNA strand and the fluorogenic RNA probes appended with a fluorophore and a quencher at each. At the signal amplification step, RNase H cleaves only the RNA part after forming RNA/DNA heteroduplexes, resulting in fluorescence recovery due to the release of fluorophore from the quencher. The iterative cycle of DNA/RNA duplexation and degradation of RNA by RNase H leads to the fluorescence signal amplification. Reproduced with permission from reference [167].

Newer ELISA-based technologies like Searchlight® and Fastquant® allow for operation with low final volumes, decreased analysis time and simultaneous analysis of multiple samples

unlike conventional ELISA-based methods.[168] Although ELISA is still considered as a gold standard method for biomarker detection, some challenges still exist. Diagnostic assay development using ELISA is limited due to the lower concentrations (lower than detection limit of ELISA) of biomarkers in biological samples at the early of the disease[169] and the availability of high-quality capture molecules, e.g., antibodies.

1.9.1.2 Microarray-based Assays

Microarray technologies have been extensively used to evaluate changes in gene expression associated with onset and progression of a disease.[170] They permit simultaneous screening of thousands of genes and allow i) in-depth understanding of genome-wide expression changes in health and disease ii) prediction of clinical outcome iii) identification of diagnostic or prognostic biomarkers.[144, 171]

In microarray studies, the term "probe" describes the nucleotide sequence attached to the microarray surface; typically employed probes are DNA, antibodies or aptamers. Target refers to what is hybridized to the probes.[172] Based on the length of the probe utilized, DNA microarrays are classified into i) cDNA microarrays (500-2500 bp double-strand cDNAs) and ii) oligonucleotide microarrays (20-90 single-strand nucleotide molecules). For these microarrays to be reliable tools, they must possess probe sequences that hybridize with high sensitivity and specificity, thereby allowing precise detection of their intended targets. Gene expression profiling using microarrays is performed according to the following steps described. mRNA samples extracted from biological samples and reverse transcribed.[173] Targets are then prepared by labeling mRNA samples with fluorescent dyes on the array. At the hybridization step, each labeled nucleotide molecule (mRNA, cRNA, or cDNA) in targets hybridizes with a probe complementary to its sequence on the array surface and forms a probe-target hybrid. An image is

then using laser-induced fluorescent imaging. The principle behind the quantification of expression levels is that the amount of fluorescence measured at each sequence specific location is directly proportional to the amount of mRNA with complementary sequence present in the sample analyzed. Signal intensities stored in image files can be transformed to numerical intensity values for every probe on the array by appropriate algorithms.

Using peripheral blood mononuclear cells, a panel of 22 genes were found to be 80% sensitive and specific for the diagnosis of stroke. The gene list was generated from a starting number of 22,283 gene probes, and reproducible gene expression was found within 24 h after IS and validated using qPCR.[140, 174] Barr *et al.* recruited 67 stroke patients and 25 control subjects and performed gene expression profiling of peripheral blood. They identified 9 genes based on the 2-fold expression differences between stroke and healthy subjects as determined by the statistical analysis. Significant changes on mRNA expression four genes were then validated using qPCR which revealed the up-regulation of arginase 1, lymphocyte antigen 96, MMP-9 and down-regulation of chemokine receptor 7.[149] However, the exact role of all these genes in ischemic stroke has not been specified.

Gene expression profiling of purified leukocyte populations (obtained from healthy donors) using DNA microarrays containing 18,000 genes enabled the identification of cell-type-specific gene patterns. Clustering analysis of these leukocytes revealed global expression levels of T-cells, B-cells and neutrophils from healthy donors and also variation of gene expression between cell types within an individual. This finding suggested that subtle variations of gene expression in peripheral blood cells can help in gaining an insight into any type of disease to develop diagnostic biomarkers.[175]

In order to circumvent the problems of translating a qualitative microarray approach into a clinical setting, Adamski *et al.* used a new approach, high-throughput reverse transcription qPCR which offers high throughput diagnosis, reduced background noise, this high sensitivity, allows simultaneous screening of 96 transcripts from nL sample volumes for detecting complementary DNA (cDNA) copies. Whereas, traditional qPCR is time consuming and offers low throughput. As specific leukocytes are involved in pathogen recognition, innate, adaptive, cellular, and humoral immune responses and tissue repair,[141, 147, 176] gene expression among leukocytes subsets were measured by extracting mRNA. Stroke related genes associated with white blood cell differentiation activation and differentiation,[139] *IL1R2, S100A9, F5, ETS2, C3AR1* were shown to up-regulate their expression in stroke patients relative to healthy controls. (see Figure 1.10).[177]

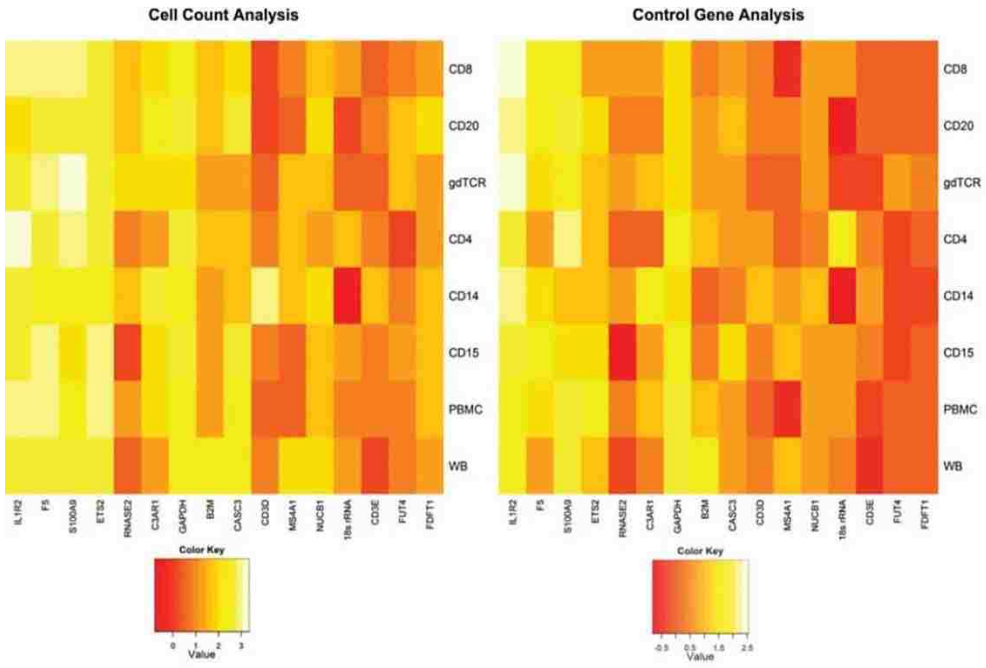

Figure 1.10 Comparison of cell count–based and control gene analytic methods by two independent approaches. The first was absolute, based on the cell count and normalized to the Cq value of the corresponding transcript for the commercial complementary DNA. The second was relative, measured relative to the average of the three selected control genes (*FDFT1*, *FUT4*, and *CD3E*). Reproduced with permission from reference [177].

Data analysis was performed based using cell counts and also control genes. Both the results were in agreement with each other but cell count method was chosen to overcome the expression alterations in control genes in different leukocyte subsets or in different disease states. Furthermore, expression level of each gene can be assessed independently using cell count method instead of relying upon standard control gene expression

1.9.2 Mass Spectrometry (MS) Techniques

MS is a label-free analytical technique used to measure the mass-to-charge ratio (m/z) of ions and serves as a means of generating semi-quantitative data for measuring abundant proteins. These technologies usually combine one or more means of high-resolution protein separation techniques. Regularly used techniques for the expression analysis of proteins are matrix assisted laser desorption ionization time-of-flight (MALDI-TOF) MS, Surface-enhanced laser desorption time-of-flight (SELDI-TOF) MS, and liquid chromatography combined with tandem MS (LC–MS–MS). Three basic analysis steps are involved in these approaches: (i) Sample preparation; (ii) sample separation and analysis; and (iii) data analysis, which include protein identification, quantification, and statistical analysis. Some studies for identification of stroke biomarkers are outlined below.

Capillary electrophoresis (CE) is used to separate molecular species by their mass to charge ratio in a small capillary filled with an electrolyte. This separation technique has high resolution and is used to fractionate and analyze samples before MS. Stroke-specific peptides were identified by performing CE-MS from 4,453 urinary proteins and peptides.[178] Dawson *et al*. developed a 35 biomarker model, consisting of proteins such as FXYD domain-containing ion transport regulator 4 (regulator of Na-K-ATPase), polymeric-immunoglobulin receptor (protein transport across BBB) and several other proteins related to stroke severity. This panel showed a

clinical sensitivity of 56% and specificity of 93%. Although their results show association of the biomarkers with stroke, the study can been improved further and by also comparing TIA and healthy controls instead of TIA and those having cardiovascular risk factors.[178]

MALDI-TOF-MS is a powerful tool for the analysis of proteins and peptides and a sensitive technique for the detection of compounds of interest below sub-femtomole ($<10^{-15}$ mol) levels.[179, 180] In MALDI, a matrix absorbs energy from a laser, often a 337 nm N_2 laser, and causes ionization of the matrix followed by proton transfer to the analyte.[181] TOF analyzers are commonly associated with MALDI due to their robustness, high data acquisition rate and sensitivity and a great mass range (1-300 kDa).[182] MALDI-TOF analysis was previously used to identify biomarkers for accurate diagnosis of myocardial infarction.[183]

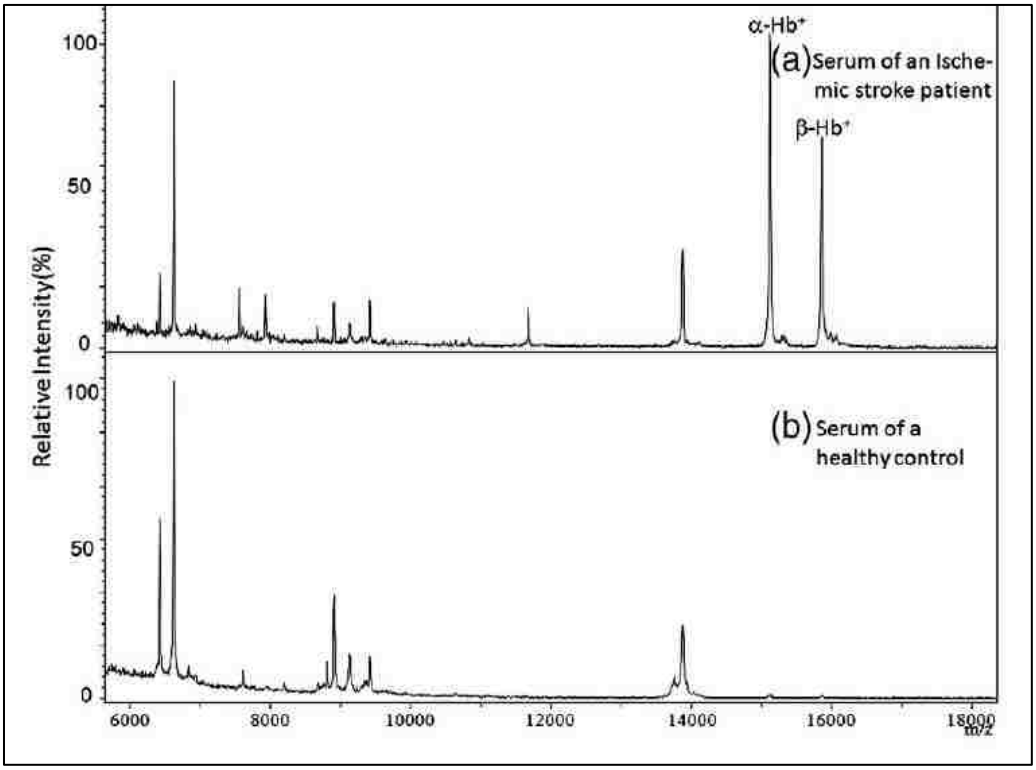

Figure 1.11 MALDI-TOF spectra of serum samples collected from ischemic stroke patients and healthy controls. Serum-free Hb peaks (α and β chains, 15.1 kDa and 15.8 kDa are labeled.[186]

A pilot study by Huang *et al.* suggested the use of serum free hemoglobin (Hb) as a novel biomarker for stroke due to the differential expression of Hb (α-chain and β-chain) in sera of IS patients compared to controls (see Figure 1.11). Serum free Hb is a marker of hemolysis associated with stroke and atherosclerosis.[184, 185] MALDI-TOF-MS analysis showed that the clinical sensitivity of diagnosing IS with this approach was 70.2% and specificity was 85.3%. However, clinical utility of this marker will be better understood by studying its correlation with outcome and severity.[186]

SELDI-TOF-MS is a variant of MALDI-TOF-MS and particularly used for analyzing low molecular weight proteins.[187] SELDI is an affinity-based MS method in which the sample is applied to a chromatographic surface so that it selectively binds to a subset of molecules from a crude preparation whereas in MALDI the sample has to be purified before application to the plate.[188] SELDI-TOF analysis was used to correlate overexpression of 6.63 kDa protein, ApoC III in plasma samples of stroke patients. ApoC III is a protein expressed in the liver and is known to inhibit lipoprotein lipase on the surface of vascular endothelial cells.[189, 190]. Summary and figures of merit for all biomarker studies using immunoassays and MS approaches is listed in Table 1.4.Some challenges associated with SELDI-TOF-MS and MALDI-TOF-MS concern reproducibility, which is critical for reliable differential diagnosis, their inability to detect high molecular weight proteins (>100 kDa).

Other approaches documented for the detection and validation of biomarkers for stroke included the use of a chemiluminiscence immunoassay and micellar electrokinetic chromatography coupled to laser induced fluorescence (MEKC-LIF). The presence of the most studied proteins in stroke, NSE and S100B, were detected using chemiluminiscence duplex immunoassay technique. It involved the detection of S100B, NSE with alkaline phosphatase and

horseradish peroxidase labels respectively; capture antibodies against markers coupled to magnetic beads. Detection limit for S100B was found to be 0.005 ng/mL, and NSE was 0.20 ng/mL achieved in a single experiment without any crosstalk.[191]

Table 1.4 Summary of biomarker studies of stroke using various immunoassays and mass spectrometric analysis

Technique	Biomarker	Sample Type	Sensitivity (%)	Specificity (%)	Ref.
Sandwich ELISA	PARK 7 NDKA	Plasma	84.9 72.6	96.7 96.7	[126]
Sandwich ELISA	VILIP-1	Serum	100	100	[1]
ELISA	H-FABP	Plasma	68	100	[166]
CE-MS	35 Biomarkers	Urine	56	93	[178]
MALDI-TOF-MS	Serum free hemoglobin	Serum	70.2	85.3	[186]

MEKC-LIF method based on the derivatization with 3-(2-furoyl)quinoline-2-carboxaldehyde was optimized to separate and detect primary amines from plasma. MEKC-LIF was used to simultaneously detect five amine biomarkers, homocysteine, excitatory amino acid neurotransmitters principally including glutamic acid, polyamines such as putrescine, spermine, and spermidine, from plasma samples of neuroimaged ischemic stroke patients with limits of detection 0.2–2.1 nM (at S/N=3), showing about 800 fold higher sensitivity compared with the usual concentration levels of these analyses in human plasma under normal or pathophysiological conditions.[192]

1.9.3 Nanotechnology and Lab-on-a-Chip (LOC) Approaches

An analytical platform integrating proteomics and nanotechniques is termed as “nanoproteomics”. The advent of several new nanomaterials has enabled the detection of novel

biomarkers for various diseases like cancer, cardio vascular diseases, infectious, and autoimmune diseases using nanoproteomic approaches.[193] Detection strategies such as gold nanoparticles,[194-196] silicon nanowires and nanoparticles,[197, 198] carbon nanotubes,[199, 200] nanomechanical resonators,[201] quantum dots[202, 203] have been extensively applied to cancer biomarker detection but none of these methods have been applied for stroke biomarker studies so far due to the lack of promising biomarkers specific only to stroke.

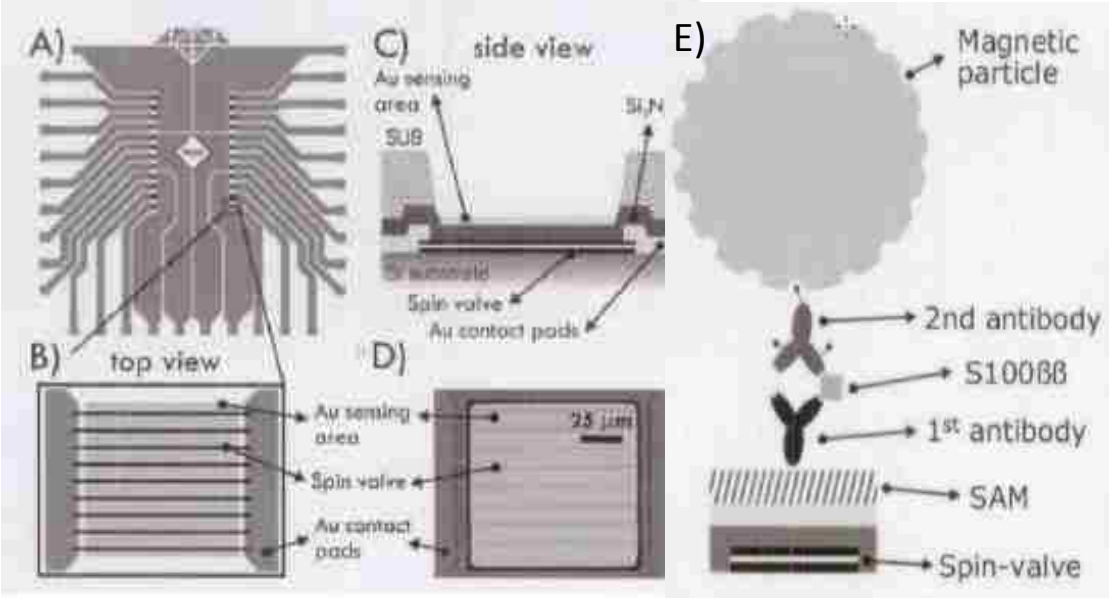

Figure 1.12 Design of the LOC detection area (left panel) consisting of magnetoresistive spinvalve sensors and each sensor is made up of multiple alternating magnetic and nonmagnetic metal layers of 1 to 10 nm each. The resistance of the spinvalve sensor changes in response to an external magnetic field which can be measured as output voltage change. (A) detection area consists of two rows of 12 sensors (B, D) each sensor is made of 9 spinvalves that are electrically connected in parallel (C) sensing area is covered with gold on which magneto-sandwich assay is build up (E) scheme of magneto-sandwich assay on the spin valve sensing area; coated with a self-assembling monolayer of alkane thiols, onto which the primary antibody is immobilized. Secondary antibody binds to the proteins added and forms a link with magnetic beads added in the final stage. [205]

The study for stroke diagnosis using LOC has been conducted by Belgian researchers. They built a magnetoresistive spin valve based detection platform (see Figure 1.12) for detecting low abundant stroke diagnostic marker like S100BB (a subtype of S100B and a ββ-homodimer).

S100BB is a glial protein which is released into CSF and blood between 48-72 h of stroke onset.[88] This protein predicts BBB disruption.[204] The concentration of S100BB is 1-100 pg/mL in blood and this LOC platform was able to achieve a detection of upto 27 pg/mL.[205] However, details about target analyte and sample processing have not been mentioned.

1.10 Point-of-Care Testing (POCT)

POCT refers to the diagnostic testing outside the central lab, without the need for trained personnel and lot of laboratory processing. The main objective of POCT is to provide immediate results and render better patient management by minimizing the time between testing to diagnosis and treatment.[206] The analytical targets for POC testing include proteins, nucleic acids, metabolites, drugs, human cells, and microbes from samples such as blood, saliva, urine, or other bodily fluids or (semi) solids.

Table 1.5 Desirable characteristics of point-of-care assay

1	Agreement of results with standard assays (validity)
2	Low intrareader and interreader variation of test results (reliability)
3	Rapid turnaround time
4	Ease of obtaining specimen
5	Simplicity of the assay without need for technical expertise or calibration
6	Efficient strategy of collection or transport
7	Disposable or low maintenance testing device
8	Low cost
9	Provides clinically useful results

For time sensitive medical conditions like stroke, developing a POC diagnostic device offers possibilities to accelerate stroke management by reducing times for transport, analyses, or transmission of results further reducing the healthcare costs. The need for easy-to-use medical technologies in low resource settings can be addressed by developing POC diagnostic tools. Two

types of POCT formats in use are benchtop analyzers and handheld portable devices. They require only basic instructions to use and provide easily interpretable results.[207] The desirable characteristics for such a device are outlined in Table 1.5 (Adapted from Cardiac markers: point of care testing [Reference 206]).

Triage stroke panel is a currently existing POC testing strategy based on a panel of biomarkers associated with IS to provide diagnostic information in patients with suspected stroke. It is a rapid, point-of-care fluorescence immunoassay used with the triage meters for the rapid, quantitative measurement of BNP, D-dimer, MMP-9, and S100B in whole blood or plasma specimens. The Triage meter plus (Biosite Incorporated, San Diego, CA) is a battery powered portable fluorometer that display digital results in a turn-around-time of 20 min, by conversion of fluorescence measurements into electrical signals.[208]

To eliminate the confusions in interpretation of clinical data due to multiple markers, Biosite® has developed an algorithm called MultiMarker Index™ (MMX). The MMX value, derived from individual analyte values, function like an analyte that is sensitive and specific to the disease. It has a receiver operating characteristic curve, and the MMX value cutoff can be chosen based on clinical needs. The clinical performance of this triage stroke panel assay has been assessed in few studies[128, 130, 209, 210] and it has been shown that utility and diagnostic of this marker panel when combined with other diagnostic methods. However, further validation studies are required before their use in clinics.

1.11 Conclusions

Advances in stroke research have clearly demonstrated that “time is brain” and immediate medical intervention is necessary due to the narrow time window (3 h). With the existing diagnostic methods, time required to perform neuro-imaging and the limited availability of

neuro-imaging instruments prompt the need for a rapid diagnostic test that is capable of providing results within a few hours of stroke onset.

Identification of clinically relevant markers is a challenge as not all biomarkers are legitimate therapeutic targets. A single biomarker however, cannot be ideal for use as a standalone diagnostic test due to the complexity in etiology of stroke. Substantial efforts are ongoing to identify different biomarkers associated with stroke. In order to improve clinical outcome, development of a multi-biomarker panel, which can indicate the brain damage by correlating to the volume of infarction and quick release into the blood/biological fluids upon stroke onset adds valuable and time-sensitive diagnostic information in the early evaluation of stroke.

Pilot studies conducted, identified protein biomarkers that distinguished stroke from controls and HS from IS suggesting their potential to provide rapid assessment and personalized patient care in acute stroke. It is very important to realize that a direct comparison cannot be made between clinical sensitivities and specificities obtained from different biomarker studies. This is because of large variance in factors such as the recruitment of control subjects, samples obtained within various time windows from symptom onset and total number of samples analyzed. Therefore, further validation studies in large cohort of patients are required for determining their clinical utility and cost effectiveness. Compared to the use of protein biomarkers, mRNA profiling of peripheral blood has the potential to improvement of accuracy of stroke diagnoses and to accommodate stroke therapy as the recent studies by Baird *et al,*[139] Tang *et al*[147] and Moore *et al*[140] provide an evidence on the reproducibility of peripheral blood gene expression signatures and also constant gene expression levels for atleast a week.

Also, the absence of a widely available and rapid diagnostic test for stroke remains a significant limitation in the evaluation and treatment of this disease. Therefore, stroke biomarker detection could benefit immeasurably from the application of microfluidic based technology for mRNA expression profiling and detection of stroke biomarkers to further create a portable and fully automated POC diagnostic tool for rapid blood-based diagnostic testing. This would reduce turn-around-time to assist physicians in making proper diagnostic decisions.

1.12 Outline of the Dissertation

This work consists of 5 chapters focusing on microfluidics and nanofluidics. A summary of the contents of each chapter is presented below.

The major focus of this work is to develop a portable, automated instrument which would serve as a near patient technology for the diagnosis of ischemic and/or hemorrhagic stroke using mRNA expression profiling directly from whole blood within a processing time <20 min to accommodate effective therapeutic treatment of this disease. This will be achieved by developing a fluidic bio-processor fabricated in polymers via micro-replication technology and integrating task specific modules on a fluidic motherboard. Chapters 2, 3, 5 provide an indepth elucidation of this project.

In chapter 2, cell isolation module is described in detail. This microfluidic cell isolation module enabled the isolation the multiple leukocyte subsets (T-cells and neutrophils) relevant for stroke diagnosis based on the differential expression of several genes in these cell types. Cell recoveries and purities of isolated cells were reported. Fluid dynamics and microfluidic design architectures were emphasized. Solid phase extraction (SPE) module for purification of RNA extracted from the isolated T-cells and neutrophils (as discussed in chapter 2) using photoactivated polycarbonate SPE bed remains the focus of chapter 3. RNA purification results in a single step

by serially connecting the cell isolation and SPE modules were also discussed. Finally in chapter 5 details on the proposed integration of aforementioned modules in addition to some other modules are discussed as the future work.

Chapter 4 describes the investigation of surface charge density, zeta potential and electroosmotic flow in surface modified nanofluidic systems (nanoslits and nanochannels). Surface modification of these nanofluidic devices via plasma modification and amination and relevant surface characterization studies were elucidated in this chapter.

1.13 References

1. Stejskal, D.; Sporova, L.; Svestak, M.; Karpisek, M. Determination of Serum Visinin Like Protein-1 and Its Potential for the Diagnosis of Brain Injury Due to the Stroke - a Pilot Study. *Biomed. Pap.* 2011, 155, 263-268.

2. Schwamm, L. H.; Pancioli, A.; Acker, J. E., 3rd; Goldstein, L. B.; Zorowitz, R. D.; Shephard, T. J.; Moyer, P.; Gorman, M.; Johnston, S. C.; Duncan, P. W.; Gorelick, P.; Frank, J.; Stranne, S. K.; Smith, R.; Federspiel, W.; Horton, K. B.; Magnis, E.; Adams, R. J. Recommendations for the Establishment of Stroke Systems of Care: Recommendations from the American Stroke Association's Task Force on the Development of Stroke Systems. *Stroke* 2005, 36, 690-703.

3. Di, C. A.; Baldereschi, M.; Gandolfo, C.; Candelise, L.; Ghetti, A.; Maggi, S.; Scafato, E.; Carbonin, P.; Amaducci, L.; Inzitari, D. Stroke in an Elderly Population: Incidence and Impact on Survival and Daily Function. The Italian Longitudinal Study on Aging. *Cerebrovasc Dis* 2003, 16, 141-50.

4. Gorelick, P. B.; Sacco, R. L.; Smith, D. B.; Alberts, M.; Mustone-Alexander, L.; Rader, D.; Ross, J. L.; Raps, E.; Ozer, M. N.; Brass, L. M.; Malone, M. E.; Goldberg, S.; Booss, J.; Hanley, D. F.; Toole, J. F.; Greengold, N. L.; Rhew, D. C. Prevention of a First Stroke: A Review of Guidelines and a Multidisciplinary Consensus Statement from the National Stroke Association. *JAMA* 1999, 281, 1112-20.

5. Hatano, S. Experience from a Multicentre Stroke Register: A Preliminary Report. *Bull World Health Organ* 1976, 54, 541-53.

6. Evers, S. M. A. A.; Struijs, J. N.; Ament, A. J. H. A.; van, G. M. L. L.; Jager, J. H. C.; van, d. B. G. A. M. International Comparison of Stroke Cost Studies. *Stroke* 2004, 35, 1209-15.

7. Writing Group, M.; Lloyd-Jones, D.; Adams, R.; Carnethon, M.; De Simone, G.; Ferguson, T. B.; Flegal, K.; Ford, E.; Furie, K.; Go, A.; Greenlund, K.; Haase, N.; Hailpern, S.; Ho, M.; Howard, V.; Kissela, B.; Kittner, S.; Lackland, D.; Lisabeth, L.; Marelli, A.; McDermott, M.; Meigs, J.; Mozaffarian, D.; Nichol, G.; O'Donnell, C.; Roger, V.; Rosamond, W.; Sacco, R.; Sorlie, P.; Stafford, R.; Steinberger, J.; Thom, T.; Wasserthiel-Smoller, S.; Wong, N.; Wylie-Rosett, J.; Hong, Y.; for the American Heart Association Statistics, C.; Stroke Statistics, S. Heart Disease and Stroke Statistics—2009 Update: A Report from the American Heart Association Statistics Committee and Stroke Statistics Subcommittee. *Circulation* 2009, 119, e21-e181.

8. Green, A. R.; Shuaib, A. Therapeutic Strategies for the Treatment of Stroke. *Drug Discovery Today* 2006, 11, 681-693.

9. Dirnagl, U.; Iadecola, C.; Moskowitz, M. A. Pathobiology of Ischaemic Stroke: An Integrated View. *Trends Neurosci* 1999, 22, 391-7.

10. Fisher, M.; Garcia, J. H. Evolving Stroke and the Ischemic Penumbra. *Neurology* 1996, 47, 884-8.

11. Litchfield, W. R.; Anderson, B. F.; Weiss, R. J.; Lifton, R. P.; Dluhy, R. G. Intracranial Aneurysm and Hemorrhagic Stroke in Glucocorticoid-Remediable Aldosteronism. *Hypertension* 1998, 31, 445-50.

12. Saenger, A. K.; Christenson, R. H. Stroke Biomarkers: Progress and Challenges for Diagnosis, Prognosis, Differentiation, and Treatment. *Clin. Chem. (Washington, DC, U. S.)* 2010, 56, 21-33.

13. Andersen, K. K.; Olsen, T. S.; Dehlendorff, C.; Kammersgaard, L. P. Hemorrhagic and Ischemic Strokes Compared: Stroke Severity, Mortality, and Risk Factors. *Stroke* 2009, 40, 2068-72.

14. Artto, V.; Putaala, J.; Strbian, D.; Meretoja, A.; Piironen, K.; Liebkind, R.; Silvennoinen, H.; Atula, S.; Happola, O. Stroke Mimics and Intravenous Thrombolysis. *Ann Emerg Med* 2012, 59, 27-32.

15. Hemmen, T. M.; Meyer, B. C.; McClean, T. L.; Lyden, P. D. Identification of Nonischemic Stroke Mimics among 411 Code Strokes at the University of California, San Diego, Stroke Center. *Journal of Stroke and Cerebrovascular Diseases* 2008, 17, 23-25.

16. Brunser, A. M.; Illanes, S.; Lavados, P. M.; Munoz, P.; Carcamo, D.; Hoppe, A.; Olavarria, V. V.; Delgado, I.; Diaz, V. Exclusion Criteria for Intravenous Thrombolysis in Stroke Mimics: An Observational Study. *J Stroke Cerebrovasc Dis* 2012.

17. Guillan, M.; Alonso-Canovas, A.; Gonzalez-Valcarcel, J.; Garcia, B. N.; Garcia, C. J.; Hernandez-Medrano, I.; Defelipe-Mimbrera, A.; Sanchez-Gonzalez, V.; Terecoasa, E.; Alonso, d. L. M.; Masjuan, J. Stroke Mimics Treated with Thrombolysis: Further Evidence on Safety and Distinctive Clinical Features. *Cerebrovasc Dis* 2012, 34, 115-20.

18. Norris, J. W.; Hachinski, V. C. Misdiagnosis of Stroke. *Lancet* 1982, 1, 328-31.

19. McKeith, I. G. Consensus Guidelines for the Clinical and Pathologic Diagnosis of Dementia with Lewy Bodies (Dlb): Report of the Consortium on Dlb International Workshop. *J Alzheimers Dis* 2006, 9, 417-23.

20. Fisher, C. M.; Adams, R. D. Transient Global Amnesia. *Acta Neurol Scand Suppl* 1964, 40, SUPPL 9:1-83.

21. Hand, P. J.; Kwan, J.; Lindley, R. I.; Dennis, M. S.; Wardlaw, J. M. Distinguishing between Stroke and Mimic at the Bedside: The Brain Attack Study. *Stroke* 2006, 37, 769-75.

22. Libman, R. B.; Wirkowski, E.; Alvir, J.; Rao, T. H. Conditions That Mimic Stroke in the Emergency Department. Implications for Acute Stroke Trials. *Arch Neurol* 1995, 52, 1119-22.

23. Johnston, S. C.; Gress, D. R.; Browner, W. S.; Sidney, S. Short-Term Prognosis after Emergency Department Diagnosis of Tia. *JAMA* 2000, 284, 2901-6.

24. Donnan, G. A.; O'Malley, H. M.; Quang, L.; Hurley, S.; Bladin, P. F. The Capsular Warning Syndrome: Pathogenesis and Clinical Features. *Neurology* 1993, 43, 957-62.

25. Lyden, P. D.; Hantson, L. Assessment Scales for the Evaluation of Stroke Patients. *Journal of Stroke and Cerebrovascular Diseases* 1998, 7, 113-127.

26. Spence, J. D.; Donner, A. Problems in Design of Stroke Treatment Trials. *Stroke* 1982, 13, 94-9.

27. Lyden, P.; Claesson, L.; Havstad, S.; Ashwood, T.; Lu, M. Factor Analysis of the National Institutes of Health Stroke Scale in Patients with Large Strokes. *Arch Neurol* 2004, 61, 1677-80.

28. Lyden, P. D.; Lu, M.; Levine, S. R.; Brott, T. G.; Broderick, J. A Modified National Institutes of Health Stroke Scale for Use in Stroke Clinical Trials: Preliminary Reliability and Validity. *Stroke* 2001, 32, 1310-7.

29. Kasner, S. E. Clinical Interpretation and Use of Stroke Scales. *Lancet Neurol* 2006, 5, 603-12.

30. Cavanagh, S. J.; Gordon, V. L. Grading Scales Used in the Management of Aneurysmal Subarachnoid Hemorrhage: A Critical Review. *J Neurosci Nurs* 2002, 34, 288-95.

31. Wright, J. G.; Feinstein, A. R. A Comparative Contrast of Clinimetric and Psychometric Methods for Constructing Indexes and Rating Scales. *J Clin Epidemiol* 1992, 45, 1201-18.

32. Lyden, P.; Brott, T.; Tilley, B.; Welch, K. M.; Mascha, E. J.; Levine, S.; Haley, E. C.; Grotta, J.; Marler, J. Improved Reliability of the Nih Stroke Scale Using Video Training. Ninds Tpa Stroke Study Group. *Stroke* 1994, 25, 2220-6.

33. Muir, K. W.; Weir, C. J.; Murray, G. D.; Povey, C.; Lees, K. R. Comparison of Neurological Scales and Scoring Systems for Acute Stroke Prognosis. *Stroke* 1996, 27, 1817-20.

34. Goldstein, L. B.; Bertels, C.; Davis, J. N. Interrater Reliability of the Nih Stroke Scale. *Archives of Neurology* 1989, 46, 660-662.

35. Saah, A. J.; Hoover, D. R. "Sensitivity" and "Specificity" Reconsidered: The Meaning of These Terms in Analytical and Diagnostic Settings. *Ann Intern Med* 1997, 126, 91-4.

36. Nour, M.; Liebeskind, D. S. Brain Imaging in Stroke: Insight Beyond Diagnosis. *Neurotherapeutics* 2011, 8, 330-9.

37. Adams, H. P., Jr.; Adams, R. J.; Brott, T.; del, Z. G. J.; Furlan, A.; Goldstein, L. B.; Grubb, R. L.; Higashida, R.; Kidwell, C.; Kwiatkowski, T. G.; Marler, J. R.; Hademenos, G. J. Guidelines for the Early Management of Patients with Ischemic Stroke: A Scientific Statement from the Stroke Council of the American Stroke Association. *Stroke* 2003, 34, 1056-83.

38. von, K. R.; Bourquain, H.; Bastianello, S.; Bozzao, L.; Manelfe, C.; Meier, D.; Hacke, W. Early Prediction of Irreversible Brain Damage after Ischemic Stroke at Ct. *Radiology* 2001, 219, 95-100.

39. Ezzeddine, M. A.; Lev, M. H.; McDonald, C. T.; Rordorf, G.; Oliveira-Filho, J.; Aksoy, F. G.; Farkas, J.; Segal, A. Z.; Schwamm, L. H.; Gonzalez, R. G.; Koroshetz, W. J. Ct Angiography with Whole Brain Perfused Blood Volume Imaging: Added Clinical Value in the Assessment of Acute Stroke. *Stroke* 2002, 33, 959-66.

40. Lev, M. H.; Farkas, J.; Rodriguez, V. R.; Schwamm, L. H.; Hunter, G. J.; Putman, C. M.; Rordorf, G. A.; Buonanno, F. S.; Budzik, R.; Koroshetz, W. J.; Gonzalez, R. G. Ct Angiography in the Rapid Triage of Patients with Hyperacute Stroke to Intraarterial Thrombolysis: Accuracy in the Detection of Large Vessel Thrombus. *J Comput Assist Tomogr* 2001, 25, 520-8.

41. Srinivasan, A.; Goyal, M.; Al, A. F.; Lum, C. State-of-the-Art Imaging of Acute Stroke. *Radiographics* 2006, 26 Suppl 1, S75-95.

42. Lev, M. H.; Segal, A. Z.; Farkas, J.; Hossain, S. T.; Putman, C.; Hunter, G. J.; Budzik, R.; Harris, G. J.; Buonanno, F. S.; Ezzeddine, M. A.; Chang, Y.; Koroshetz, W. J.; Gonzalez, R. G.; Schwamm, L. H. Utility of Perfusion-Weighted Ct Imaging in Acute Middle Cerebral Artery Stroke Treated with Intra-Arterial Thrombolysis: Prediction of Final Infarct Volume and Clinical Outcome. *Stroke* 2001, 32, 2021-8.

43. Mullins, M. E.; Schaefer, P. W.; Sorensen, A. G.; Halpern, E. F.; Ay, H.; He, J.; Koroshetz, W. J.; Gonzalez, R. G. Ct and Conventional and Diffusion-Weighted Mr

Imaging in Acute Stroke: Study in 691 Patients at Presentation to the Emergency Department. *Radiology* 2002, 224, 353-60.

44. Baird, A. E.; Warach, S. Magnetic Resonance Imaging of Acute Stroke. *J Cereb Blood Flow Metab* 1998, 18, 583-609.

45. Chalela, J. A.; Kidwell, C. S.; Nentwich, L. M.; Luby, M.; Butman, J. A.; Demchuk, A. M.; Hill, M. D.; Patronas, N.; Latour, L.; Warach, S. Magnetic Resonance Imaging and Computed Tomography in Emergency Assessment of Patients with Suspected Acute Stroke: A Prospective Comparison. *Lancet* 2007, 369, 293-8.

46. Schellinger, P. D.; Jansen, O.; Fiebach, J. B.; Hacke, W.; Sartor, K. A Standardized Mri Stroke Protocol: Comparison with Ct in Hyperacute Intracerebral Hemorrhage. *Stroke* 1999, 30, 765-768.

47. Kunz, A.; Hahn, G.; Mucha, D.; Muller, A.; Barrett, K. M.; von, K. R.; Gahn, G. Echo-Enhanced Transcranial Color-Coded Duplex Sonography in the Diagnosis of Cerebrovascular Events: A Validation Study. *AJNR Am J Neuroradiol* 2006, 27, 2122-7.

48. Schwartz, D.; David, T. S. McGraw-Hill Professional: 2008.

49. Fiehler, J.; Fiebach, J. B.; Gass, A.; Hoehn, M.; Kucinski, T.; Neumann-Haefelin, T.; Schellinger, P. D.; Siebler, M.; Villringer, A.; Rother, J. Diffusion-Weighted Imaging in Acute Stroke--a Tool of Uncertain Value? *Cerebrovasc Dis* 2002, 14, 187-96.

50. Wintermark, M.; Meuli, R.; Browaeys, P.; Reichhart, M.; Bogousslavsky, J.; Schnyder, P.; Michel, P. Comparison of Ct Perfusion and Angiography and Mri in Selecting Stroke Patients for Acute Treatment. *Neurology* 2007, 68, 694-7.

51. Schramm, P.; Schellinger, P. D.; Klotz, E.; Kallenberg, K.; Fiebach, J. B.; Kulkens, S.; Heiland, S.; Knauth, M.; Sartor, K. Comparison of Perfusion Computed Tomography and Computed Tomography Angiography Source Images with Perfusion-Weighted Imaging and Diffusion-Weighted Imaging in Patients with Acute Stroke of Less Than 6 Hours' Duration. *Stroke* 2004, 35, 1652-8.

52. Medcalf, R. L. Plasminogen Activation-Based Thrombolysis for Ischaemic Stroke: The Diversity of Targets May Demand New Approaches. *Curr. Drug Targets* 2011, 12, 1772-1781.

53. Turner, R. C.; Lucke-Wold, B.; Lucke-Wold, N.; Elliott, A. S.; Logsdon, A. F.; Rosen, C. L.; Huber, J. D. Neuroprotection for Ischemic Stroke: Moving Past Shortcomings and Identifying Promising Directions. *Int. J. Mol. Sci.* 2013, 14, 1890-1917.

54. Hacke, W.; Kaste, M.; Bluhmki, E.; Brozman, M.; Dvalos, A.; Guidetti, D.; Larrue, V.; Lees, K. R.; Medeghri, Z.; Machnig, T.; Schneider, D.; von, K. R.; Wahlgren, N.; Toni, D. Thrombolysis with Alteplase 3 to 4.5 Hours after Acute Ischemic Stroke. *N. Engl. J. Med.* 2008, 359, 1317-1329.

55. Hacke, W.; Kaste, M.; Fieschi, C.; Toni, D.; Lesaffre, E.; Von, K. R.; Boysen, G.; Bluhmki, E.; Hoexter, G.; et, a. Intravenous Thrombolysis with Recombinant Tissue Plasminogen Activator for Acute Hemispheric Stroke the European Cooperative Acute Stroke Study (Ecass). *JAMA, J. Am. Med. Assoc.* 1995, 274, 1017-25.

56. Hacke, W.; Kaste, M.; Fieschi, C.; Von, K. R.; Davalos, A.; Meier, D.; Larrue, V.; Bluhmki, E.; Davis, S.; Donnan, G.; Schneider, D.; Diez-Tejedor, E.; Trouillas, P. Randomised Double-Blind Placebo-Controlled Trial of Thrombolytic Therapy with Intravenous Alteplase in Acute Ischemic Stroke (Ecass Ii). *Lancet* 1998, 352, 1245-1251.

57. Clark, W. M.; Wissman, S.; Albers, G. W.; Jhamandas, J. H.; Madden, K. P.; Hamilton, S. Recombinant Tissue-Type Plasminogen Activator (Alteplase) for Ischemic Stroke 3 to 5 Hours after Symptom Onset. The Atlantis Study: A Randomized Controlled Trial. *JAMA, J. Am. Med. Assoc.* 1999, 282, 2019-2026.

58. Katzan, I. L.; Hammer, M. D.; Hixson, E. D.; Furlan, A. J.; Abou-Chebl, A.; Nadzam, D. M. Utilization of Intravenous Tissue Plasminogen Activator for Acute Ischemic Stroke. *Arch Neurol* 2004, 61, 346-50.

59. Gropen, T. I.; Gagliano, P. J.; Blake, C. A.; Sacco, R. L.; Kwiatkowski, T.; Richmond, N. J.; Leifer, D.; Libman, R.; Azhar, S.; Daley, M. B. Quality Improvement in Acute Stroke: The New York State Stroke Center Designation Project. *Neurology* 2006, 67, 88-93.

60. Pereira, A. C.; Brown, M. M. Aspirin or Heparin in Acute Stroke. *Br. Med. Bull.* 2000, 56, 413-421.

61. Shafi, N.; Levine, J. M. Emergency Management of Acute Ischemic Stroke. *Curr Atheroscler Rep* 2010, 12, 230-5.

62. Blanchette, M.; Fortin, D. Blood-Brain Barrier Disruption in the Treatment of Brain Tumors. *Methods Mol. Biol. (N. Y., NY, U. S.)* 2011, 686, 447-463.

63. Chen, Y.; Liu, L. Modern Methods for Delivery of Drugs across the Blood–Brain Barrier. *Advanced Drug Delivery Reviews* 2012, 64, 640-665.

64. Rolls, M. M.; Albertson, R.; Shih, H.-p.; Lee, C.-y.; Doe, C. Q. Drosophila Apkc Regulates Cell Polarity and Cell Proliferation in Neuroblasts and Epithelia. *J. Cell Biol.* 2003, 163, 1089-1098.

65. Abbott, N. J.; Lars, R.; Elisabeth, H. Astrocyte–Endothelial Interactions at the Blood–Brain Barrier. *Nature Reviews Neuroscience* 2006, 7, 41-53.

66. Ransohoff, R. M.; Perry, V. H. Microglial Physiology: Unique Stimuli, Specialized Responses. *Annu. Rev. Immunol.* 2009, 27, 119-145.

67. Nag, S.; Kapadia, A.; Stewart, D. J. Review: Molecular Pathogenesis of Blood-Brain Barrier Breakdown in Acute Brain Injury. *Neuropathol. Appl. Neurobiol.* 2011, 37, 3-23.

68. Papadopoulos, M. C.; Saadoun, S.; Davies, D. C.; Bell, B. A. Emerging Molecular Mechanisms of Brain Tumour Oedema. *Br J Neurosurg* 2001, 15, 101-8.

69. Tsao, N.; Hsu, H. P.; Wu, C. M.; Liu, C. C.; Le, H. Y. Tumour Necrosis Factor-A Causes an Increase in Blood-Brain Barrier Permeability During Sepsis. *J. Med. Microbiol.* 2001, 50, 812-821.

70. Hallenbeck, J. M.; Dutka, A. J.; Tanishima, T.; Kochanek, P. M.; Kumaroo, K. K.; Thompson, C. B.; Obrenovitch, T. P.; Contreras, T. J. Polymorphonuclear Leukocyte Accumulation in Brain Regions with Low Blood Flow During the Early Postischemic Period. *Stroke* 1986, 17, 246-53.

71. Chou, W.-H.; Choi, D.-S.; Zhang, H.; Mu, D.; McMahon, T.; Kharazia, V. N.; Lowell, C. A.; Ferriero, D. M.; Messing, R. O. Neutrophil Protein Kinase Cδ as a Mediator of Stroke-Reperfusion Injury. *J. Clin. Invest.* 2004, 114, 49-56.

72. Lawrence, M. B.; Springer, T. A. Leukocytes Roll on a Selectin at Physiologic Flow Rates: Distinction from and Prerequisite for Adhesion through Integrins. *Cell (Cambridge, Mass.)* 1991, 65, 859-73.

73. Justicia, C.; Panes, J.; Sole, S.; Cervera, A.; Deulofeu, R.; Chamorro, A.; Planas, A. M. Neutrophil Infiltration Increases Matrix Metalloproteinase-9 in the Ischemic Brain after Occlusion/Reperfusion of the Middle Cerebral Artery in Rats. *J. Cereb. Blood Flow Metab.* 2003, 23, 1430-1440.

74. Seo, J. H.; Guo, S.; Lok, J.; Navaratna, D.; Whalen, M. J.; Kim, K.-W.; Lo, E. H. Neurovascular Matrix Metalloproteinases and the Blood-Brain Barrier. *Curr Pharm Des* 2012, 18, 3645-8.

75. Rifai, N.; Gillette, M. A.; Carr, S. A. Protein Biomarker Discovery and Validation: The Long and Uncertain Path to Clinical Utility. *Nat. Biotechnol.* 2006, 24, 971-983.

76. Biomarkers and Surrogate Endpoints: Preferred Definitions and Conceptual Framework. *Clin. Pharmacol. Ther. (St. Louis, MO, U. S.)* 2001, 69, 89-95.

77. Naylor, S. Biomarkers: Current Perspectives and Future Prospects. *Expert Rev Mol Diagn* 2003, 3, 525-9.

78. Ge, S.; Song, L.; Pachter, J. S. Where Is the Blood-Brain Barrier ... Really? *J. Neurosci. Res.* 2005, 79, 421-427.

79. Penttila, K.; Koukkunen, H.; Halinen, M.; Rantanen, T.; Pyorala, K.; Punnonen, K.; Penttila, I. Myoglobin, Creatine Kinase Mb Isoforms and Creatine Kinase Mb Mass in Early Diagnosis of Myocardial Infarction in Patients with Acute Chest Pain. *Clin. Biochem.* 2002, 35, 647-653.

80. Gibler, W. B.; Blomkalns, A. L.; Collins, S. P. Evaluation of Chest Pain and Heart Failure in the Emergency Department: Impact of Multimarker Strategies and B-Type Natriuretic Peptide. *Rev Cardiovasc Med* 2003, 4 Suppl 4, S47-55.

81. Stein, P. D.; Hull, R. D.; Patel, K. C.; Olson, R. E.; Ghali, W. A.; Brant, R.; Biel, R. K.; Bharadia, V.; Kalra, N. K. D-Dimer for the Exclusion of Acute Venous Thrombosis and Pulmonary Embolism: A Systematic Review. *Ann Intern Med* 2004, 140, 589-602.

82. Reynolds, M. A.; Kirchick, H. J.; Dahlen, J. R.; Anderberg, J. M.; McPherson, P. H.; Nakamura, K. K.; Laskowitz, D. T.; Valkirs, G. E.; Buechler, K. F. Early Biomarkers of Stroke. *Clin. Chem. (Washington, DC, U. S.)* 2003, 49, 1733-1739.

83. Craig-Schapiro, R.; Fagan, A. M.; Holtzman, D. M. Biomarkers of Alzheimer's Disease. *Neurobiol. Dis.* 2009, 35, 128-140.

84. Kernagis, D. N.; Laskowitz, D. T. Evolving Role of Biomarkers in Acute Cerebrovascular Disease. *Ann. Neurol.* 2012, 71, 289-303.

85. Yoon, C. W.; Kim, S. J.; Bang, O. Y.; Chung, C. S.; Lee, K. H.; Kim, G. M. Premorbid Warfarin Use and Lower D-Dimer Levels Are Associated with a Spontaneous Early Improvement in an Atrial Fibrillation-Related Stroke. *J. Thromb. Haemostasis* 2012, 10, 2394-2396.

86. Motoki, H.; Tomita, T.; Aizawa, K.; Kasai, H.; Izawa, A.; Kumazaki, S.; Tsutsui, H.; Koyama, J.; Ikeda, U. Coagulation Activity Is Increased in the Left Atria of Patients with Paroxysmal Atrial Fibrillation During the Non-Paroxysmal Period. Comparison with Chronic Atrial Fibrillation. *Circ J* 2009, 73, 1403-7.

87. Rothermundt, M.; Peters, M.; Prehn, J. H. M.; Arolt, V. S100b in Brain Damage and Neurodegeneration. *Microsc. Res. Tech.* 2003, 60, 614-632.

88. Foerch, C.; Wunderlich, M. T.; Dvorak, F.; Humpich, M.; Kahles, T.; Goertler, M.; Alvarez-Sabin, J.; Wallesch, C. W.; Molina, C. A.; Steinmetz, H.; Sitzer, M.; Montaner, J. Elevated Serum S100b Levels Indicate a Higher Risk of Hemorrhagic Transformation after Thrombolytic Therapy in Acute Stroke. *Stroke* 2007, 38, 2491-2495.

89. Delgado, P.; Alvarez Sabin, J.; Santamarina, E.; Molina, C. A.; Quintana, M.; Rosell, A.; Montaner, J. Plasma S100b Level after Acute Spontaneous Intracerebral Hemorrhage. *Stroke* 2006, 37, 2837-2839.

90. Missler, U.; Wiesmann, M.; Friedrich, C.; Kaps, M. S-100 Protein and Neuron-Specific Enolase Concentrations in Blood as Indicators of Infarction Volume and Prognosis in Acute Ischemic Stroke. *Stroke* 1997, 28, 1956-60.

91. Marchi, N.; Cavaglia, M.; Fazio, V.; Bhudia, S.; Hallene, K.; Janigro, D. Peripheral Markers of Blood-Brain Barrier Damage. *Clin. Chim. Acta* 2004, 342, 1-12.

92. Martens, P.; Raabe, A.; Johnsson, P. Serum S-100 and Neuron-Specific Enolase for Prediction of Regaining Consciousness after Global Cerebral Ischemia. *Stroke* 1998, 29, 2363-6.

93. Dassan, P.; Keir, G.; Brown, M. M. Criteria for a Clinically Informative Serum Biomarker in Acute Ischaemic Stroke: A Review of S100b. *Cerebrovasc. Dis. (Basel, Switz.)* 2009, 27, 295-302.

94. Pelinka, L. E.; Kroepfl, A.; Schmidhammer, R.; Krenn, M.; Buchinger, W.; Redl, H.; Raabe, A. Glial Fibrillary Acidic Protein in Serum after Traumatic Brain Injury and Multiple Trauma. *J. Trauma: Inj., Infect., Crit. Care* 2004, 57, 1006-1012.

95. Aurell, A.; Rosengren, L. E.; Karlsson, B.; Olsson, J. E.; Zbornikova, V.; Haglid, K. G. Determination of S-100 and Glial Fibrillary Acidic Protein Concentrations in Cerebrospinal Fluid after Brain Infarction. *Stroke (Dallas)* 1991, 22, 1254-8.

96. Foerch, C.; Curdt, I.; Yan, B.; Dvorak, F.; Hermans, M.; Berkefeld, J.; Raabe, A.; Neumann-Haefelin, T.; Steinmetz, H.; Sitzer, M. Serum Glial Fibrillary Acidic Protein as a Biomarker for Intracerebral Haemorrhage in Patients with Acute Stroke. *J Neurol Neurosurg Psychiatry* 2006, 77, 181-4.

97. Dvorak, F.; Haberer, I.; Sitzer, M.; Foerch, C. Characterisation of the Diagnostic Window of Serum Glial Fibrillary Acidic Protein for the Differentiation of Intracerebral Haemorrhage and Ischaemic Stroke. *Cerebrovasc. Dis. (Basel, Switz.)* 2009, 27, 37-41.

98. Cohen, S. R.; Brooks, B. R.; Herndon, R. M.; McKhann, G. M. A Diagnostic Index of Active Demyelination: Myelin Basic Protein in Cerebrospinal Fluid. *Ann. Neurol.* 1980, 8, 25-31.

99. Matias-Guiu, J.; Martinez-Vazquez, J.; Ruibal, A.; Colomer, R.; Boada, M.; Codina, A. Myelin Basic Protein and Creatine Kinase Bb Isoenzyme as Csf Markers of Intracranial Tumors and Stroke. *Acta Neurol Scand* 1986, 73, 461-5.

100. Jauch, E. C.; Lindsell, C.; Broderick, J.; Fagan, S. C.; Tilley, B. C.; Levine, S. R. Association of Serial Biochemical Markers with Acute Ischemic Stroke. The National Institute of Neurological Disorders and Stroke Recombinant Tissue Plasminogen Activator Stroke Study. *Stroke* 2006, 37, 2508-2513.

101. Bharosay, A.; Bharosay, V. V.; Varma, M.; Saxena, K.; Sodani, A.; Saxena, R. Correlation of Brain Biomarker Neuron Specific Enolase (Nse) with Degree of Disability and Neurological Worsening in Cerebrovascular Stroke. *Indian J Clin Biochem* 2012, 27, 186-90.

102. Persson, L.; Hardemark, H. G.; Gustafsson, J.; Rundstrom, G.; Mendel-Hartvig, I.; Esscher, T.; Pahlman, S. S-100 Protein and Neuron-Specific Enolase in Cerebrospinal Fluid and Serum: Markers of Cell Damage in Human Central Nervous System. *Stroke* 1987, 18, 911-8.

103. Anand, N.; Stead, L. G. Neuron-Specific Enolase as a Marker for Acute Ischemic Stroke: A Systematic Review. *Cerebrovasc. Dis. (Basel, Switz.)* 2005, 20, 213-219.

104. Casmiro, M.; Maitan, S.; De, P. F.; Cova, V.; Scarpa, E.; Vignatelli, L. Cerebrospinal Fluid and Serum Neuron-Specific Enolase Concentrations in a Normal Population. *Eur J Neurol* 2005, 12, 369-74.

105. Dingledine, R.; Borges, K.; Bowie, D.; Traynelis, S. F. The Glutamate Receptor Ion Channels. *Pharmacol. Rev.* 1999, 51, 7-61.

106. Dambinova, S. A.; Khounteev, G. A.; Izykenova, G. A.; Zavolokov, I. G.; Ilyukhina, A. Y.; Skoromets, A. A. Blood Test Detecting Autoantibodies to N-Methyl-D-Aspartate Neuroreceptors for Evaluation of Patients with Transient Ischemic Attack and Stroke. *Clin. Chem. (Washington, DC, U. S.)* 2003, 49, 1752-1762.

107. Veerkamp, J. H.; Zimmerman, A. W. Fatty Acid-Binding Proteins of Nervous Tissue. *J. Mol. Neurosci.* 2001, 16, 133-142.

108. Pelsers, M. M. A. L.; Hanhoff, T.; van, d. V. D.; Arts, B.; Peters, M.; Ponds, R.; Honig, A.; Rudzinski, W.; Spener, F.; de, K. J. R.; Twijnstra, A.; Hermens, W. T.; Menheere, P. P. C. A.; Glatz, J. F. C. Brain- and Heart-Type Fatty Acid-Binding Proteins in the Brain: Tissue Distribution and Clinical Utility. *Clin. Chem. (Washington, DC, U. S.)* 2004, 50, 1568-1575.

109. Wunderlich, M. T.; Hanhoff, T.; Goertler, M.; Spener, F.; Glatz, J. F. C.; Wallesch, C.-W.; Pelsers, M. M. A. L. Release of Brain-Type and Heart-Type Fatty Acid-Binding Proteins in Serum after Acute Ischaemic Stroke. *J. Neurol.* 2005, 252, 718-724.

110. Licata, G.; Tuttolomondo, A.; Di, R. D.; Corrao, S.; Di, S. R.; Pinto, A. Immuno-Inflammatory Activation in Acute Cardio-Embolic Strokes in Comparison with Other Subtypes of Ischaemic Stroke. *Thromb. Haemostasis* 2009, 101, 929-937.

111. Mun-Bryce, S.; Rosenberg, G. A. Matrix Metalloproteinases in Cerebrovascular Disease. *J. Cereb. Blood Flow Metab.* 1998, 18, 1163-1172.

112. Di, N. M.; Schwaninger, M.; Cappelli, R.; Ceccarelli, E.; Di, G. G.; Donati, C.; Emsley, H. C. A.; Forconi, S.; Hopkins, S. J.; Masotti, L.; Muir, K. W.; Paciucci, A.; Papa, F.; Roncacci, S.; Sander, D.; Sander, K.; Smith, C. J.; Stefanini, A.; Weber, D. Evaluation of C-Reactive Protein Measurement for Assessing the Risk and Prognosis in Ischemic Stroke: A Statement for Health Care Professionals from the Crp Pooling Project Members. *Stroke* 2005, 36, 1316-1329.

113. Mocco, J.; Choudhri, T. F.; Mack, W. J.; Laufer, I.; Lee, J.; Kiss, S.; Poisik, A.; Quest, D. O.; Solomon, R. A.; Connolly, E. S. Elevation of Soluble Intercellular Adhesion Molecule-1 Levels in Symptomatic and Asymptomatic Carotid Atherosclerosis. *Neurosurgery* 2001, 48, 718-21; discussion 721-2.

114. Hoshi, T.; Kitagawa, K.; Yamagami, H.; Furukado, S.; Hougaku, H.; Hori, M. Relation between Interleukin-6 Level and Subclinical Intracranial Large-Artery Atherosclerosis. *Atherosclerosis (Amsterdam, Neth.)* 2008, 197, 326-332.

115. Chamorro, A.; Hallenbeck, J. The Harms and Benefits of Inflammatory and Immune Responses in Vascular Disease. *Stroke* 2006, 37, 291-3.

116. Tuttolomondo, A.; Di Sciacca, R.; Di Raimondo, D.; Serio, A.; D'Aguanno, G.; La Placa, S.; Pecoraro, R.; Arnao, V.; Marino, L.; Monaco, S.; Natale, E.; Licata, G.; Pinto, A.

Plasma Levels of Inflammatory and Thrombotic/Fibrinolytic Markers in Acute Ischemic Strokes: Relationship with Toast Subtype, Outcome and Infarct Site. *J. Neuroimmunol.* 2009, 215, 84-89.

117. Winbeck, K.; Poppert, H.; Etgen, T.; Conrad, B.; Sander, D. Prognostic Relevance of Early Serial C-Reactive Protein Measurements after First Ischemic Stroke. *Stroke* 2002, 33, 2459-2464.

118. Castellanos, M.; Leira, R.; Serena, J.; Pumar, J. M.; Lizasoain, I.; Castillo, J.; Davalos, A.; Hamann, G. F. Plasma Metalloproteinase-9 Concentration Predicts Hemorrhagic Transformation in Acute Ischemic Stroke. *Stroke* 2003, 34, 40-46.

119. Montaner, J.; Molina, C. A.; Monasterio, J.; Abilleira, S.; Arenillas, J. F.; Ribo, M.; Quintana, M.; Alvarez-Sabin, J. Matrix Metalloproteinase-9 Pretreatment Level Predicts Intracranial Hemorrhagic Complications after Thrombolysis in Human Stroke. *Circulation* 2003, 107, 598-603.

120. Sotgiu, S.; Zanda, B.; Marchetti, B.; Fois, M. L.; Arru, G.; Pes, G. M.; Salaris, F. S.; Arru, A.; Pirisi, A.; Rosati, G. Inflammatory Biomarkers in Blood of Patients with Acute Brain Ischemia. *Eur J Neurol* 2006, 13, 505-13.

121. Lynch, J. R.; Blessing, R.; White, W. D.; Grocott, H. P.; Newman, M. F.; Laskowitz, D. T. Novel Diagnostic Test for Acute Stroke. *Stroke* 2004, 35, 57-63.

122. Allard, L.; Lescuyer, P.; Burgess, J.; Leung, K.-Y.; Ward, M.; Walter, N.; Burkhard, P. R.; Corthals, G.; Hochstrasser, D. F.; Sanchez, J.-C. Apoc-I and Apoc-Iii as Potential Plasmatic Markers to Distinguish between Ischemic and Hemorrhagic Stroke. *Proteomics* 2004, 4, 2242-2251.

123. Wunderlich, M. T.; Lins, H.; Skalej, M.; Wallesch, C.-W.; Goertler, M. Neuron-Specific Enolase and Tau Protein as Neurobiochemical Markers of Neuronal Damage Are Related to Early Clinical Course and Long-Term Outcome in Acute Ischemic Stroke. *Clin Neurol Neurosurg* 2006, 108, 558-63.

124. Sato, M.; Suzuki, A.; Nagata, K.; Uchiyama, S. Increased Von Willebrand Factor in Acute Stroke Patients with Atrial Fibrillation. *J Stroke Cerebrovasc Dis* 2006, 15, 1-7.

125. Barber, M.; Langhorne, P.; Rumley, A.; Lowe, G. D. O.; Stott, D. J. D-Dimer Predicts Early Clinical Progression in Ischemic Stroke: Confirmation Using Routine Clinical Assays. *Stroke* 2006, 37, 1113-5.

126. Allard, L.; Burkhard, P. R.; Lescuyer, P.; Burgess, J. A.; Walter, N.; Hochstrasser, D. F.; Sanchez, J.-C. Park7 and Nucleoside Diphosphate Kinase a as Plasma Markers for the Early Diagnosis of Stroke. *Clin. Chem. (Washington, DC, U. S.)* 2005, 51, 2043-2051.

127. Montaner, J.; Mendioroz, M.; Delgado, P.; Garcia-Berrocoso, T.; Giralt, D.; Merino, C.; Ribo, M.; Rosell, A.; Penalba, A.; Fernandez-Cadenas, I.; Romero, F.; Molina, C.; Alvarez-Sabin, J.; Hernandez-Guillamon, M. Differentiating Ischemic from Hemorrhagic Stroke Using Plasma Biomarkers: The S100b/Rage Pathway. *J. Proteomics* 2012, 75, 4758-4765.

128. Vanni, S.; Polidori, G.; Pepe, G.; Chiarlone, M.; Albani, A.; Pagnanelli, A.; Grifoni, S. Use of Biomarkers in Triage of Patients with Suspected Stroke. *J Emerg Med* 2011, 40, 499-505.

129. Laskowitz, D. T.; Blessing, R.; Floyd, J.; White, W. D.; Lynch, J. R. Panel of Biomarkers Predicts Stroke. *Ann N Y Acad Sci* 2005, 1053, 30.

130. Sibon, I.; Rouanet, F.; Meissner, W.; Orgogozo, J. M. Use of the Triage Stroke Panel in a Neurologic Emergency Service. *Am J Emerg Med* 2009, 27, 558-62.

131. Tektonidou, M. G.; Ward, M. M. Validation of New Biomarkers in Systemic Autoimmune Diseases. *Nat. Rev. Rheumatol.* 2011, 7, 708-717.

132. Heller, R. A.; Schena, M.; Chai, A.; Shalon, D.; Bedilion, T.; Gilmore, J.; Woolley, D. E.; Davis, R. W. Discovery and Analysis of Inflammatory Disease-Related Genes Using Cdna Microarrays. *Proc. Natl. Acad. Sci. U. S. A.* 1997, 94, 2150-2155.

133. Pennie, W. D. Use of Cdna Microarrays to Probe and Understand the Toxicological Consequences of Altered Gene Expression. *Toxicol. Lett.* 2000, 112-113, 473-477.

134. Whitney, L. W.; Becker, K. G.; Tresser, N. J.; Caballero-Ramos, C. I.; Munson, P. J.; Prabhu, V. V.; Trent, J. M.; McFarland, H. F.; Biddison, W. E. Analysis of Gene

Expression in Mutiple Sclerosis Lesions Using Cdna Microarrays. *Ann Neurol* 1999, 46, 425-8.

135. Twine, N. C.; Stover, J. A.; Marshall, B.; Dukart, G.; Hidalgo, M.; Stadler, W.; Logan, T.; Dutcher, J.; Hudes, G.; Dorner, A. J.; Slonim, D. K.; Trepicchio, W. L.; Burczynski, M. E. Disease-Associated Expression Profiles in Peripheral Blood Mononuclear Cells from Patients with Advanced Renal Cell Carcinoma. *Cancer Res.* 2003, 63, 6069-6075.

136. Miura, N.; Hasegawa, J.; Shiota, G. Serum Messenger Rna as a Biomarker and Its Clinical Usefulness in Malignancies. *Clin. Med.: Oncol.* 2008, 2, 511-527.

137. Alizadeh, A. A.; Eisen, M. B.; Davis, R. E.; Ma, C.; Lossos, I. S.; Rosenwald, A.; Boldrick, J. C.; Sabet, H.; Tran, T.; Yu, X.; Powell, J. I.; Yang, L.; Marti, G. E.; Moore, T.; Hudson, J., Jr.; Luo, L.; Lewis, D. B.; Tibshirani, T. R.; Sherlock, G.; Chan, W. C.; Greiner, T. C.; Weisenburger, D. D.; Armitage, J. O.; Wamke, R.; Levy, R.; Wilson, W.; Grever, M. R.; Byrd, J. C.; Botstein, D.; Brown, P. O.; Staudt, L. M. Distinct Types of Diffuse Large B-Cell Lymphoma Identified by Gene Expression Profiling. *Nature (London)* 2000, 403, 503-511.

138. Pajer, K.; Andrus, B. M.; Gardner, W.; Lourie, A.; Strange, B.; Campo, J.; Bridge, J.; Blizinsky, K.; Dennis, K.; Vedell, P.; Churchill, G. A.; Redei, E. E. Discovery of Blood Transcriptomic Markers for Depression in Animal Models and Pilot Validation in Subjects with Early-Onset Major Depression. *Transl. Psychiatry* 2012, 2, e101/1-e101/10.

139. Baird, A. E. Blood Genomics in Human Stroke. *Stroke* 2007, 38, 694-698.

140. Moore, D. F.; Li, H.; Jeffries, N.; Wright, V.; Cooper, R. A.; Elkahloun, A.; Gelderman, M. P.; Zudaire, E.; Blevins, G.; Yu, H.; Goldin, E.; Baird, A. E. Using Peripheral Blood Mononuclear Cells to Determine a Gene Expression Profile of Acute Ischemic Stroke. *Circulation* 2005, 111, 212-221.

141. Du, X.; Tang, Y.; Xu, H.; Lit, L.; Walker, W.; Ashwood, P.; Gregg, J. P.; Sharp, F. R. Genomic Profiles for Human Peripheral Blood T Cells, B Cells, Natural Killer Cells, Monocytes, and Polymorphonuclear Cells: Comparisons to Ischemic Stroke, Migraine, and Tourette Syndrome. *Genomics* 2006, 87, 693-703.

142. Franks, Z. G.; Campbell, R. A.; Weyrich, A. S.; Rondina, M. T. Platelet-Leukocyte Interactions Link Inflammatory and Thromboembolic Events in Ischemic Stroke. *Ann. N. Y. Acad. Sci.* 2010, 1207, 11-17.

143. Sharp, F. R.; Jickling, G. C.; Stamova, B.; Tian, Y.; Zhan, X.; Liu, D. Z.; Kuczynski, B.; Cox, C. D.; Ander, B. P. Molecular Markers and Mechanisms of Stroke: Rna Studies of Blood in Animals and Humans. *J. Cereb. Blood Flow Metab.* 2011, 31, 1513-1531.

144. Schena, M.; Shalon, D.; Davis, R. W.; Brown, P. O. Quantitative Monitoring of Gene Expression Patterns with a Complementary DNA Microarray. *Science (Washington, D. C.)* 1995, 270, 467-70.

145. Lockhart, D. J.; Dong, H.; Byrne, M. C.; Follettie, M. T.; Gallo, M. V.; Chee, M. S.; Mittmann, M.; Wang, C.; Kobayashi, M.; Horton, H.; Brown, E. L. Expression Monitoring by Hybridization to High-Density Oligonucleotide Arrays. *Nat. Biotechnol.* 1996, 14, 1675-1680.

146. Rainen, L.; Oelmueller, U.; Jurgensen, S.; Wyrich, R.; Ballas, C.; Schram, J.; Herdman, C.; Bankaitis-Davis, D.; Nicholls, N.; Trollinger, D.; Tryon, V. Stabilization of Mrna Expression in Whole Blood Samples. *Clin. Chem. (Washington, DC, U. S.)* 2002, 48, 1883-1890.

147. Tang, Y.; Xu, H.; Du, X.; Lit, L.; Walker, W.; Lu, A.; Ran, R.; Gregg, J. P.; Reilly, M.; Pancioli, A.; Khoury, J. C.; Sauerbeck, L. R.; Carrozzella, J. A.; Spilker, J.; Clark, J.; Wagner, K. R.; Jauch, E. C.; Chang, D. J.; Verro, P.; Broderick, J. P.; Sharp, F. R. Gene Expression in Blood Changes Rapidly in Neutrophils and Monocytes after Ischemic Stroke in Humans: A Microarray Study. *J. Cereb. Blood Flow Metab.* 2006, 26, 1089-1102.

148. Tang, Y.; Lu, A.; Aronow, B. J.; Sharp, F. R. Blood Genomic Responses Differ after Stroke, Seizures, Hypoglycemia, and Hypoxia: Blood Genomic Fingerprints of Disease. *Ann. Neurol.* 2001, 50, 699-707.

149. Barr, T. L.; Conley, Y.; Ding, J.; Dillman, A.; Warach, S.; Singleton, A.; Matarin, M. Genomic Biomarkers and Cellular Pathways of Ischemic Stroke by Rna Gene Expression Profiling. *Neurology* 2010, 75, 1009-14.

150. Lebanony, D.; Benjamin, H.; Gilad, S.; Ezagouri, M.; Dov, A.; Ashkenazi, K.; Gefen, N.; Izraeli, S.; Rechavi, G.; Pass, H.; Nonaka, D.; Li, J.; Spector, Y.; Rosenfeld, N.; Chajut, A.; Cohen, D.; Aharonov, R.; Mansukhani, M. Diagnostic Assay Based on Hsa-Mir-205 Expression Distinguishes Squamous from Nonsquamous Non-Small-Cell Lung Carcinoma. *J. Clin. Oncol.* 2009, 27, 2030-2037.

151. Szafranska-Schwarzbach, A. E.; Adai, A. T.; Lee, L. S.; Conwell, D. L.; Andruss, B. F. Development of a Mirna-Based Diagnostic Assay for Pancreatic Ductal Adenocarcinoma. *Expert Rev. Mol. Diagn.* 2011, 11, 249-257.

152. Wang, K.; Zhang, S.; Marzolf, B.; Troisch, P.; Brightman, A.; Hu, Z.; Hood, L. E.; Galas, D. J. Circulating Micrornas, Potential Biomarkers for Drug-Induced Liver Injury. *Proc. Natl. Acad. Sci. U. S. A.* 2009, 106, 4402-4407.

153. Alevizos, I.; Illei, G. G. Micrornas as Biomarkers in Rheumatic Diseases. *Nat. Rev. Rheumatol.* 2010, 6, 391-398.

154. van Empel, V. P. M.; De Windt, L. J.; da Costa Martins, P. A. Circulating Mirnas: Reflecting or Affecting Cardiovascular Disease? *Curr. Hypertens. Rep.* 2012, 14, 498-509.

155. Zeng, L.; Liu, J.; Wang, Y.; Wang, L.; Weng, S.; Tang, Y.; Zheng, C.; Cheng, Q.; Chen, S.; Yang, G.-Y. Microrna-210 as a Novel Blood Biomarker in Acute Cerebral Ischemia. *Front. Biosci., Elite Ed.* 2011, E3, 1265-1272.

156. Gan, C. S.; Wang, C. W.; Tan, K. S. Circulatory Microrna-145 Expression Is Increased in Cerebral Ischemia. *GMR, Genet. Mol. Res.* 2012, 11, 147-152.

157. Laterza, O. F.; Lim, L.; Garrett-Engele, P. W.; Vlasakova, K.; Muniappa, N.; Tanaka, W. K.; Johnson, J. M.; Sina, J. F.; Fare, T. L.; Sistare, F. D.; Glaab, W. E. Plasma Micrornas as Sensitive and Specific Biomarkers of Tissue Injury. *Clin. Chem. (Washington, DC, U. S.)* 2009, 55, 1977-1983.

158. Fiore, L. D.; D'Avolio, L. W. Detours on the Road to Personalized Medicine: Barriers to Biomarker Validation and Implementation. *JAMA, J. Am. Med. Assoc.* 2011, 306, 1914-1915.

159. Ye, X.; Blonder, J.; Veenstra, T. D. Targeted Proteomics for Validation of Biomarkers in Clinical Samples. *Briefings Funct. Genomics Proteomics* 2009, 8, 126-135.

160. Ransohoff, D. F. Cancer: Developing Molecular Biomarkers for Cancer. *Science (Washington, DC, U. S.)* 2003, 299, 1679-1680.

161. Laterza, O. F.; Modur, V. R.; Crimmins, D. L.; Olander, J. V.; Landt, Y.; Lee, J.-M.; Ladenson, J. H. Identification of Novel Brain Biomarkers. *Clin. Chem. (Washington, DC, U. S.)* 2006, 52, 1713-1721.

162. He, Y. D. Genomic Approach to Biomarker Identification and Its Recent Applications. *Cancer Biomark* 2006, 2, 103-33.

163. Frangogiannis, N. G. Biomarkers: Hopes and Challenges in the Path from Discovery to Clinical Practice. *Transl Res* 2012, 159, 197-204.

164. de la Rica, R.; Stevens, M. M. Plasmonic Elisa for the Ultrasensitive Detection of Disease Biomarkers with the Naked Eye. *Nat. Nanotechnol.* 2012, 7, 821-824.

165. Stejskal, D.; Sporova, L.; Svestak, M.; Karpisek, M. Determination of Serum Visinin Like Protein-1 and Its Potential for the Diagnosis of Brain Injury Due to the Stroke - a Pilot Study. *Biomed. Pap.* 2011, 155, 263-268.

166. Zimmermann-Ivol, C. G.; Burkhard, P. R.; Floch-Rohr, J. L.; Allard, L.; Hochstrasser, D. F.; Sanchez, J.-C. Fatty Acid Binding Protein as a Serum Marker for the Early Diagnosis of Stroke. *Mol. Cell. Proteomics* 2004, 3, 66-72.

167. Han, K.-C.; Yang, E. G.; Ahn, D.-R. Elongated Oligonucleotide-Linked Immunosorbent Assay for Sensitive Detection of a Biomarker in a Microwell Plate-Based Platform. *Biosensors and Bioelectronics* 2013, 50, 421-424.

168. Collings, F. B.; Vaidya, V. S. Novel Technologies for the Discovery and Quantitation of Biomarkers of Toxicity. *Toxicology* 2008, 245, 167-174.

169. Wang, G.; Huang, H.; Zhang, G.; Zhang, X.; Fang, B.; Wang, L. Dual Amplification Strategy for Fabrication of Highly Sensitive Interleukin-6 Amperometric Immunosensor Based on Poly-Dopamine. *Langmuir* 2011, 27, 1224-1231.

170. MacGregor, P. F.; Squire, J. A. Application of Microarrays to the Analysis of Gene Expression in Cancer. *Clin. Chem. (Washington, DC, U. S.)* 2002, 48, 1170-1177.

171. Tarca, A. L.; Romero, R.; Draghici, S. Analysis of Microarray Experiments of Gene Expression Profiling. *Am. J. Obstet. Gynecol.* 2006, 195, 373-388.

172. Wingren, C.; Steinhauer, C.; Ingvarsson, J.; Persson, E.; Larsson, K.; Borrebaeck, C. A. K. Microarrays Based on Affinity-Tagged Single-Chain Fv Antibodies: Sensitive Detection of Analyte in Complex Proteomes. *Proteomics* 2005, 5, 1281-1291.

173. Smith, C. L.; Smith, C. Analysing Gene Expression: A Handbook of Methods, Possibilities and Pitfalls 2003s. Lorkowski, P. Cullen (Eds.) , Wiley-Vch Verlag, Gmbh & Co., Kga, Weinheim, Germany, Vols. 1?2, 950 Pp. *Biomolecular engineering* 2004, 21, 123.

174. Xu, H.; Tang, Y.; Liu, D.-Z.; Ran, R.; Ander, B. P.; Apperson, M.; Liu, X. S.; Khoury, J. C.; Gregg, J. P.; Pancioli, A.; Jauch, E. C.; Wagner, K. R.; Verro, P.; Broderick, J. P.; Sharp, F. R. Gene Expression in Peripheral Blood Differs after Cardioembolic Compared with Large-Vessel Atherosclerotic Stroke: Biomarkers for the Etiology of Ischemic Stroke. *J. Cereb. Blood Flow Metab.* 2008, 28, 1320-1328.

175. Palmer, C.; Diehn, M.; Alizadeh, A. A.; Brown, P. O. Cell-Type Specific Gene Expression Profiles of Leukocytes in Human Peripheral Blood. *BMC Genomics* 2006, 7, No pp. given.

176. Greene, J. M.; Wiseman, R. W.; Lank, S. M.; Bimber, B. N.; Karl, J. A.; Burwitz, B. J.; Lhost, J. J.; Hawkins, O. E.; Kunstman, K. J.; Broman, K. W.; Wolinsky, S. M.; Hildebrand, W. H.; O'Connor, D. H. Differential Mhc Class I Expression in Distinct Leukocyte Subsets. *BMC Immunol.* 2011, 12, 39.

177. Adamski, M. G.; Li, Y.; Wagner, E.; Yu, H.; Seales-Bailey, C.; Soper, S. A.; Murphy, M.; Baird, A. E. Next-Generation Qpcr for the High-Throughput Measurement of Gene Expression in Multiple Leukocyte Subsets. *J Biomol Screen* 2013.

178. Dawson, J.; Walters, M.; Delles, C.; Mischak, H.; Mullen, W. Urinary Proteomics to Support Diagnosis of Stroke. *PLoS One* 2012, 7, e35879.

179. Hillenkamp, F.; Karas, M. Mass Spectrometry of Peptides and Proteins by Matrix-Assisted Ultraviolet Laser Desorption/Ionization. *Methods Enzymol.* 1990, 193, 280-95.

180. Cramer, R.; Gobom, J.; Nordhoff, E. High-Throughput Proteomics Using Matrix-Assisted Laser Desorption/Ionization Mass Spectrometry. *Expert Rev. Proteomics* 2005, 2, 407-420.

181. Matthiesen, R.; Mutenda, K. E. Introduction to Proteomics. *Methods Mol. Biol. (Totowa, NJ, U. S.)* 2007, 367, 1-35.

182. Aebersold, R.; Goodlett, D. R. Mass Spectrometry in Proteomics. *Chem. Rev. (Washington, D. C.)* 2001, 101, 269-295.

183. Marshall, J.; Kupchak, P.; Zhu, W.; Yantha, J.; Vrees, T.; Furesz, S.; Jacks, K.; Smith, C.; Kireeva, I.; Zhang, R.; Takahashi, M.; Stanton, E.; Jackowski, G. Processing of Serum Proteins Underlies the Mass Spectral Fingerprinting of Myocardial Infarction. *J. Proteome Res.* 2003, 2, 361-372.

184. Na, N.; Ouyang, J.; Taes, Y. E. C.; Delanghe, J. R. Serum Free Hemoglobin Concentrations in Healthy Individuals Are Related to Haptoglobin Type. *Clin Chem* 2005, 51, 1754-5.

185. Watanabe, J.; Chou, K. J.; Liao, J. C.; Miao, Y.; Meng, H.-H.; Ge, H.; Grijalva, V.; Hama, S.; Kozak, K.; Buga, G.; Whitelegge, J. P.; Lee, T. D.; Farias-Eisner, R.; Navab, M.; Fogelman, A. M.; Reddy, S. T. Differential Association of Hemoglobin with Proinflammatory High Density Lipoproteins in Atherogenic/Hyperlipidemic Mice: A Novel Biomarker of Atherosclerosis. *J. Biol. Chem.* 2007, 282, 23698-23707.

186. Huang, P.; Lo, L.-H.; Chen, Y.-C.; Lin, R.-T.; Shiea, J.; Liu, C.-K. Serum Free Hemoglobin as a Novel Potential Biomarker for Acute Ischemic Stroke. *J. Neurol.* 2009, 256, 625-631.

187. Hortin, G. L. The Maldi-Tof Mass Spectrometric View of the Plasma Proteome and Peptidome. *Clin. Chem. (Washington, DC, U. S.)* 2006, 52, 1223-1237.

188. Meuleman, W.; Engwegen, J. Y. M. N.; Gast, M.-C. W.; Beijnen, J. H.; Reinders, M. J. T.; Wessels, L. F. A. Comparison of Normalisation Methods for Surface-Enhanced Laser Desorption and Ionisation (Seldi) Time-of-Flight Mass Spectrometry Data. *BMC Bioinf.* 2008, 9, No pp. given.

189. Hoffer, M. J.; Sijbrands, E. J.; De, M. F. H.; Havekes, L. M.; Smelt, A. H.; Frants, R. R. Increased Risk for Endogenous Hypertriglyceridaemia Is Associated with an Apolipoprotein C3 Haplotype Specified by the Ssti Polymorphism. *Eur J Clin Invest* 1998, 28, 807-12.

190. Surguchov, A. P.; Page, G. P.; Smith, L.; Patsch, W.; Boerwinkle, E. Polymorphic Markers in Apolipoprotein C-Iii Gene Flanking Regions and Hypertriglyceridemia. *Arterioscler Thromb Vasc Biol* 1996, 16, 941-7.

191. Zhang, Y.; Xu, Q.; Peng, Q.; Cao, Z.; Wang, X.; Lu, J. Magnetic Beads-Based Chemiluminescence Substrate-Resolved Duplex Immunoassay for Sequential Detection of Two Ischemic Stroke Markers with Two Orders of Concentration Difference. *Anal. Sci.* 2011, 27, 739-743.

192. Peng, L.; Wang, N.; Si, H.; Wu, C.; Zhang, X.; Yang, Q. Rapid and Sensitive Determination of Five Amine Biomarkers in Plasma Samples from Stroke Patients by Mekc with Precolumn Derivatization. *Chromatographia* 2012, 75, 1217-1221.

193. Ray, S.; Reddy, P. J.; Choudhary, S.; Raghu, D.; Srivastava, S. Emerging Nanoproteomics Approaches for Disease Biomarker Detection: A Current Perspective. *J. Proteomics* 2011, 74, 2660-2681.

194. Kang, J.-H.; Asami, Y.; Murata, M.; Kitazaki, H.; Sadanaga, N.; Tokunaga, E.; Shiotani, S.; Okada, S.; Maehara, Y.; Niidome, T.; Hashizume, M.; Mori, T.; Katayama, Y. Gold Nanoparticle-Based Colorimetric Assay for Cancer Diagnosis. *Biosens. Bioelectron.* 2010, 25, 1869-1874.

195. Crow, M. J.; Grant, G.; Provenzale, J. M.; Wax, A. Molecular Imaging and Quantitative Measurement of Epidermal Growth Factor Receptor Expression in Live Cancer Cells Using Immunolabeled Gold Nanoparticles. *AJR Am J Roentgenol* 2009, 192, 1021-8.

196. Lu, W.; Arumugam, S. R.; Senapati, D.; Singh, A. K.; Arbneshi, T.; Khan, S. A.; Yu, H.; Ray, P. C. Multifunctional Oval-Shaped Gold-Nanoparticle-Based Selective Detection of

Breast Cancer Cells Using Simple Colorimetric and Highly Sensitive Two-Photon Scattering Assay. *ACS Nano* 2010, 4, 1739-1749.

197. Lee, M.-H.; Lee, K.-N.; Jung, S.-W.; Kim, W.-H.; Shin, K.-S.; Seong, W.-K. Quantitative Measurements of C-Reactive Protein Using Silicon Nanowire Arrays. *Int. J. Nanomed.* 2008, 3, 117-124.

198. Lee, H.-S.; Kim, K. S.; Kim, C.-J.; Hahn, S. K.; Jo, M.-H. Electrical Detection of Vegfs for Cancer Diagnoses Using Anti-Vascular Endothelial Growth Factor Aptamer-Modified Si Nanowire Fets. *Biosens. Bioelectron.* 2009, 24, 1801-1805.

199. Rusling, J. F.; Yu, X.; Jensen, G.; Gong, J.; Bhirde, A.; Munge, B. S.; Patel, V.; Papadimitrakopoulos, F.; Kim, S.-N.; Gutkind, S. In *Carbon Nanotube Amplification Strategies for Highly Sensitive Immunodetection of Cancer Biomarkers*, American Chemical Society: 2006; pp ANYL-215.

200. Chikkaveeraih, B. V.; Bhirde, A.; Malhotra, R.; Patel, V.; Gutkind, J. S.; Rusling, J. F. Single-Wall Carbon Nanotube Forest Arrays for Immunoelectrochemical Measurement of Four Protein Biomarkers for Prostate Cancer. *Anal. Chem. (Washington, DC, U. S.)* 2009, 81, 9129-9134.

201. Waggoner, P. S.; Varshney, M.; Craighead, H. G. Detection of Prostate Specific Antigen with Nanomechanical Resonators. *Lab Chip* 2009, 9, 3095-3099.

202. Ko, M. H.; Kim, S.; Kang, W. J.; Lee, J. H.; Kang, H.; Moon, S. H.; Hwang, D. W.; Ko, H. Y.; Lee, D. S. In Vitro Derby Imaging of Cancer Biomarkers Using Quantum Dots. *Small* 2009, 5, 1207-1212.

203. Jokerst, J. V.; Raamanathan, A.; Christodoulides, N.; Floriano, P. N.; Pollard, A. A.; Simmons, G. W.; Wong, J.; Gage, C.; Furmaga, W. B.; Redding, S. W.; McDevitt, J. T. Nano-Bio-Chips for High Performance Multiplexed Protein Detection: Determinations of Cancer Biomarkers in Serum and Saliva Using Quantum Dot Bioconjugate Labels. *Biosens. Bioelectron.* 2009, 24, 3622-3629.

204. Hu, J.; Ferreira, A.; Van Eldik, L. J. S100β Induces Neuronal Cell Death through Nitric Oxide Release from Astrocytes. *J. Neurochem.* 1997, 69, 2294-2301.

205. Parton, E.; Lagae, L.; Borghs, G. Stroke Diagnosis with Lab-on-a-Chip. *Med Device Technol* 2009, 20, 15-7.

206. Hudson, M. P.; Christenson, R. H.; Newby, L. K.; Kaplan, A. L.; Ohman, E. M. Cardiac Markers: Point of Care Testing. *Clin. Chim. Acta* 1999, 284, 223-237.

207. Chin, C. D.; Linder, V.; Sia, S. K. Commercialization of Microfluidic Point-of-Care Diagnostic Devices. *Lab Chip* 2012, 12, 2118-2134.

208. Cima, M. J. Microsystem Technologies for Medical Applications. *Annu Rev Chem Biomol Eng* 2011, 2, 355-78.

209. Knauer, C.; Knauer, K.; Muller, S.; Ludolph, A. C.; Bengel, D.; Muller, H. P.; Huber, R. A Biochemical Marker Panel in Mri-Proven Hyperacute Ischemic Stroke-a Prospective Study. *BMC Neurol* 2012, 12, 14.

210. Laskowitz, D. T.; Kasner, S. E.; Saver, J.; Remmel, K. S.; Jauch, E. C. Clinical Usefulness of a Biomarker-Based Diagnostic Test for Acute Stroke: The Biomarker Rapid Assessment in Ischemic Injury (Brain) Study. *Stroke* 2009, 40, 77-85.

CHAPTER 2. PARALLEL AFFINITY-BASED ISOLATION OF LEUKOCYTE SUBSETS USING MICROFLUIDICS: APPLICATION FOR STROKE DIAGNOSIS*

2.1 Introduction

Isolation of pure leukocyte subsets and their molecular analysis from whole blood is challenged by the presence of numerous interfering cells.[1] The use of conventional isolation methods such as density gradient centrifugation, sedimentation, and fluorescence assisted cell sorting (FACS) are typically time consuming, require large volumes of blood and employ sophisticated equipment. Microfluidics, however, are extremely attractive for blood analysis because of the potentially short assay turnaround times and the ability to scale devices for point-of-care applications.[2, 3]

The use of microfluidics to isolate a certain type of leukocyte has attracted wide interest. For example, Cheng *et al.* reported a two-stage microfluidic for the isolation of CD4+ T-cells; a purity of ~90% was achieved.[4-6] Lee and coworkers constructed a functionalized silicon and quartz nanowire array to separate CD4+ T-cells from mouse splenocytes.[7, 8] Thorslund *et al.* fabricated a glass/PDMS/anti-CD4 microfluidic chip containing different architectural features for CD4+ T-cell isolation.[9] Warner *et al.* reported a microfluidic neutrophil-capture device followed by gene expression analysis to observe changes after trauma injury.[10] They obtained purities of 95% by processing 150 µL of whole blood through the chip that isolated ~25,000 cells and yielded 69 ng of RNA. Common to these elegant examples was that only a single cell type was isolated from the sample.

Stroke is the third leading cause of disability and death in the United States.[11] There are two

*Reproduced with permission from *Analytical Chemistry*

types of stroke: (i) Ischemic stroke caused by vessel occlusion and occurs at a frequency of 80-85%; and (ii) hemorrhagic stroke resulting from vessel rupture and is identified in 15-20% of all stroke-related cases. Unfortunately, these two conditions cannot be differentiated using existing clinical tests, which typically employ CT or MRI. Additionally, a third of all patients presenting stroke-like symptoms actually suffer from non-vascular disease.[12] It is imperative that stroke diagnosis be made quickly and accurately because treatments for ischemic and hemorrhagic stroke differ and there is a short time window (~3 h) for effective treatment.[13-17]

Because head-related trauma or stroke tissue is not easily acquired, researchers have looked for markers in the peripheral blood due to its accessibility,[18-20] and there have been ongoing efforts to find reliable blood-based stroke biomarkers that afford high clinical sensitivity and specificity.[21] Several potential biomarker candidates that can be measured in serum or plasma have been identified with their role in the underlying pathophysiology investigated.[22]

Reports have shown that T-lymphocyte mediated anti-inflammatory responses in ischemic brain injury[23-26] and the expression of nearly 5,700 genes related to T-cell function change in cases of head trauma.[27] mRNA can be harvested from specific types of blood cells and used as biomarkers that reflect the systemic changes in stroke.[28] Transcripts of promise for detecting and differentiating between ischemic and hemorrhagic stroke include *S100A9* and *IL1R2*.[29-32] Gene expression studies conducted by Adamski *et al.* identified differential expression across different leukocyte subsets, such as CD4 T-cells and neutrophils.[33] These cells are known to express genes found in stroke-related expression profiles.[34] Therefore, the ability to rapidly isolate these leukocyte subsets and secure their mRNA expression profile without interference from other leukocyte subsets could provide a viable test for diagnosing various types of stroke.[35-38] Isolation of pure fractions of these subsets is critical to provide unbiased expression data.

In this study, we report a microfluidic device that can simultaneously isolate different types of cells using affinity agents. As an example, we show the positive selection of CD4+ T-cells and CD66b+ neutrophils from minute amounts of unprocessed and unfractionated blood. The device design allowed for simultaneous isolation of up to four types of cells. The device architecture and flow parameters allowed for the isolation of very pure subsets (>90%). Total RNA (TRNA) was extracted from the isolated cells and reverse transcribed to monitor mRNA expression changes from the isolated cells. To the best of our knowledge, this is the first report on the simultaneous isolation of multiple leukocyte subsets. The selected subsets were used to expression profile certain genes that possess diagnostic value for stroke. The figures-of-merit for two device geometries were evaluated as well as the applicability of two different polymers, poly(methyl methacrylate), PMMA, and cyclic olefin copolymer, COC, for optimizing antibody load and cell recovery. We also introduce a chemical–based polymer surface activation method that utilized sodium hydroxide and isopropanol, which provided efficient and simple polymer surface activation resulting in high antibody loads.

2.2 Materials and Methods

2.2.1 Buffers and Reagents

PMMA (cover plates and substrates), 6013S-04 COC cover plates and 5013L-10 COC substrates were purchased from Plaskolite (Columbus, OH) and TOPAS Advanced Polymers (Florence, KY). Reagent-grade isopropyl alcohol (IPA), 1-ethyl-3-[3-dimethylaminopropyl] carbodimide hydrochloride (EDC), N-hydroxysuccinimide (NHS), and 2-(4-morpholino)-ethane sulfonic acid (MES), bovine serum albumin (BSA), Triton X-100, and paraformaldehyde (PFA) were obtained from Sigma-Aldrich (St. Louis, MO). Phosphate buffered saline (PBS, pH = 7.4) was purchased from Life Technologies (Grand Island, NY). Sodium dodecyl sulfate (SDS),

Micro-90, sodium hydroxide (NaOH) and histological and laboratory grade IPA were received from Fisher Scientific (Houston, TX) and toluidine blue O (TBO) from Carolina Biological Supply (Burlington, NC). Cy3-labeled oligonucleotides (5′NH_2-C_6-TTT-TTT-TTT-TTC-CGA-CAC-TTA-CGT-TTT-TTT-T-Cy3-3′) were purchased from Integrated DNA Technology (Coralville, IA). Low endotoxin anti-human CD4 antibodies (clone RPA-T4), FITC-conjugated anti-human CD20 antibodies (clone AT80), and PE-conjugated anti-human CD14 antibodies (clone TÜK4) were purchased from AbD Serotec (Raleigh, NC). FITC-conjugated anti-CD66b (clone CLB-B13.9) antibody was obtained from Abcam (Cambridge, MA). Anti-human CD66b antibodies (clone- G10F5) and 4′, 6-diamidino-2-phenylindole (DAPI) were obtained from BD Biosciences (San Jose, CA).

2.2.2 Microfluidic Device Fabrication and Assembly

Microfluidic devices were hot embossed into COC or PMMA substrates via micro-replication from a metal mold master as previously reported.[39] Two architectures (Figure 2.1) were tested in these studies, both possessing four independent cell isolation beds comprised of parallel arrays of curvilinear cell isolation channels with an 8 x 13 mm^2 footprint.[40] Prior to device assembly, inlet and outlet reservoirs (d = 0.85 mm) were drilled into both chip designs followed by cleaning with 10% Micro-90 and IPA and then drying at 60ºC. A 250 µm thick cover plate and the device substrate were activated for 15 min in a home-built UV chamber equipped with a low pressure Hg lamp (22 mW/cm^2 at 254 nm) to generate carboxylic acid scaffolds on the microchannel surfaces.[41] Thermal fusion bonding of the cover plate to the substrate was performed at 132ºC and 100ºC (~25 min) for UV-modified COC and PMMA devices, respectively. PEEK tubing of 175/335 µm id/od (IDEX Health & Science LLC) was

inserted into the reservoirs and glued in place with epoxy. A constant flow programmable syringe pump (Harvard Instruments) was used to introduce fluids into the devices.

The architectures for the 2 devices evaluated herein differed in terms of their addressing of the selection beds (4 per device) employing either a bifurcation network or Z-configuration (Figures 2.1A,C and Figure 2.5). In the Z-configuration device (Figure 2.1C), each cell isolation unit consisted of 64 curvilinear channels that were 9,000 x 25 x 80 µm (l x w x h) with a center-to-center spacing of 200 µm. Two 150 µm wide inlet and outlet channels poised orthogonally to the isolation channels addressed the selection bed. The surface area of a single bed including inlet and outlet channel was 132.3 mm^2 (1.9 mm^2, 1.15 µL per channel).

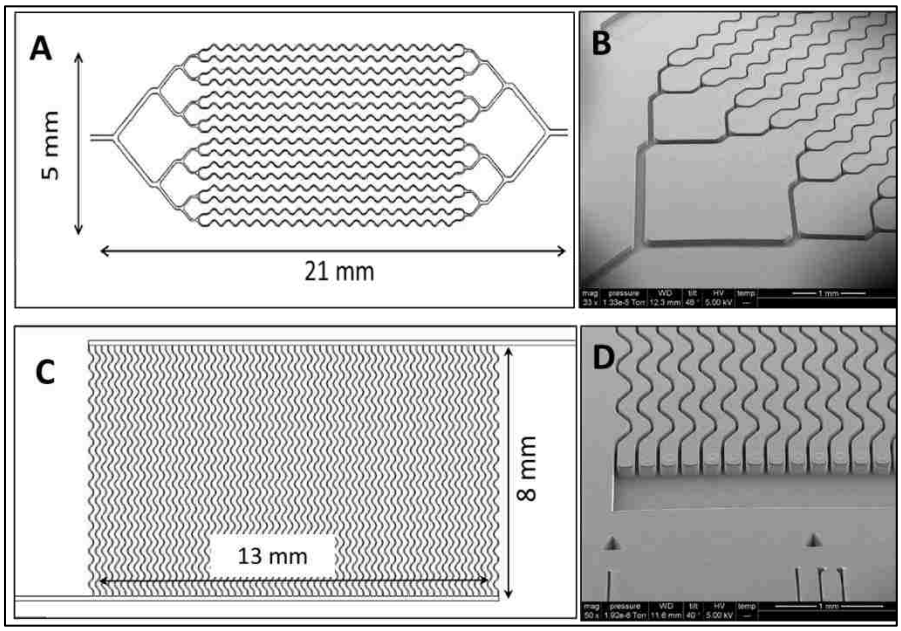

Figure 2.1 An autoCAD drawing of (A) the bifurcated device with the cell isolation bed containing 16 curvilinear channels spaced by 330 µm. (C) Z-configuration isolation bed containing 64 curvilinear channels spaced by 200 µm. All curvilinear channel dimensions were 25 × 80 µm (w × h). (B, D) SEM's of the isolation beds bifurcated and Z devices respectively.

The bifurcated device contained isolation beds with 16 curvilinear channels that were 11,000 x 25 x 80 µm (l x w x h) with a center-to-center spacing of 330 µm between channels (Figure 2.1A). Each isolation bed's surface area was 36.8 mm^2 (2.3 mm^2/channel) with a volume of 352

nL. Addressing each bed required four bifurcations with an additional two bifurcations for the four independent isolation units. All four isolation beds shared a common inlet port with different outlet ports for each cell isolation unit (Figures 2.1B). The total surface area, including the bifurcation network, was 43.4 mm^2.

2.2.3 Antibody (Ab) Immobilization to Activated Polymer Surfaces

Ab immobilization was a two-step process. In the first step, 50 mg/mL EDC and 5 mg/mL NHS in 100 mM MES (pH = 4.8) was introduced into the device and incubated for 15 min at room temperature followed by flushing with PBS. Then, a 15 µL aliquot of 0.5 mg/mL mouse anti-human CD4 or anti-human CD66b monoclonal antibody (mAb) was introduced into the device and incubated overnight at 4ºC. The selection bed was then rinsed with 1 mL PBS (pH = 7.4).

2.2.4 Fluorescence Staining of MOLT-3 Cells and Flow Cytometry Analysis

MOLT-3 cells (human acute lymphoblastic leukemia) were cultured as a suspension in 25 cm^2 culture flasks (Cell Treat Scientific, Shirley, MA) containing RPMI 1640 Medium (Life Technologies, Grand Island, NY) supplemented with 10% fetal bovine serum (FBS) (Life Technologies, Grand Island, NY). FC was performed using a Beckman-Coulter CyAn instrument equipped with a 25 mW, 488 nm Coherent sapphire (blue) laser.

Prior to staining of the MOLT-3 cells for determining CD4 expression, Fc receptors were blocked with 5 µL of 1 mg/mL human IgG-Fc blocker (R&D Systems, Minneapolis, MN) and incubated at 4ºC for 15 min. The following samples were prepared for analysis: (i) Unstained cells serving as an autofluorescence control; (ii) cells stained with 10 µL of 0.1 mg/mL isotype control, IgG1-FITC mAbs (R&D Systems, Minneapolis, MN) and incubated in the dark at 4ºC for 30 min; and (iii) cells stained with 10 µL of 0.1 mg/mL CD4-FITC Abs (BD Biosciences,

Franklin Lakes, NJ) and incubated in the dark at 4ºC for 30 min. Cells were then washed three times: One mL of cold PBS-0.5% BSA was added; the cells were centrifuged for 4 min at 350x g; supernatants were decanted and resuspended in 1 mL PBS. Propidium iodide staining (1 µg/mL) was performed on all the samples (except for the autofluorescence control) just prior to the analysis for the determination of cell viability as detected by red fluorescence. Samples were then analyzed on a CyAn flow cytometer (Beckman-Coulter) equipped with 25 mW 488 nm laser within 2 h after staining. Gain and amplitude settings were set and kept constant throughout the analysis. Ten thousand events were counted for all samples. Data acquisition and analysis was performed using Summit software (Dako, Carpineteria, CA).

2.2.5 Cell Isolation from Whole Blood, Staining and Enumeration

Whole blood samples were obtained from anonymous healthy donors at the UNC Blood Bank in accordance with UNC Institutional Review Board (IRB) procedures. Peripheral blood samples were collected by venipuncture in Vacutainer tubes containing EDTA (7.5% in 0.06 mL; *Tyco* Health Care). Samples were processed within 4 h following collection.

The microfluidic device was connected to the syringe pump with PEEK tubing via a luer lock syringe connector (Hamilton, Reno, NV). A pre-isolation rinse of the chip was performed using PBS/0.5% BSA at 4 mm/s. Fifty µL of whole blood was infused at 3.8 µL/min and 15.3 µL/min for the bifurcation and Z-configuration devices, respectively, yielding nominal linear velocities of 2 mm/s in the isolation beds. A post-isolation rinse was performed at 4 mm/s with 100-200 µL PBS/0.5% BSA to remove blood and unbounded cells. Affinity-bound cells were fixed on-chip with 4% PFA/PBS for 15 min and then rinsed with 50 µL PBS/0.5% BSA. Surface antigens of fixed T-cells and neutrophils were stained with anti-CD3-FITC Abs and anti-CD66b-FITC Abs, respectively, in the dark for 1 h. Then, the chip was rinsed with PBS/0.5% BSA for 10 min (8

µL/min). Cells were permeabilized with 0.1% Triton-X for 5 min and nuclei stained with 1 µg/mL DAPI in PBS for 5 min followed by a rinse with 50 µL PBS/0.5% BSA at 8 µL/min. Finally, cells were identified based on staining results with the total number of isolated cells determined by scanning across the cell selection regions using a fluorescence confocal microscope.

Cell characterization was performed by acquiring images on an Olympus IX71-DSU Spinning Disk Confocal inverted microscope with DAPI, FITC, and Texas Red filter sets, a mercury burner arc lamp and a high sensitivity Hamamatsu EMCCD and high resolution Hamamatsu ORCA-03G CCD cameras. Metamorph software was used for analyzing and processing images. Exposure times for DAPI, FITC and Texas Red were 10, 300, and 500 ms, respectively.

2.2.6 Evaluation and Quantification of Carboxylic acid Surface Densities

Cy3-modified oligonucleotides containing a 5′ pendant amino group served as fluorescent reporters by covalently labeling surface confined carboxylic acids. Carboxylic acid surface densities were also quantified by a colorimetric assay using TBO.

An incubation chamber (BioRad) was glued to the substrate's surface and filled with 0.1% (w/v) toluidine blue O (TBO) in carbonate buffer (50 mM, pH = 10.5). After 15 min, the substrate was submersed in the same buffer for 15 min and air dried. TBO was desorbed using 40% acetic acid (d = 1.0196 g mL^{-1}), collected in a pre-weighed microfuge tube and analyzed with an Ultrospec 4000 UV/Vis spectrophotometer (Pharmacia Biotech) against a 40% acetic acid blank.

2.2.7 Contact Angle Measurements

Changes in surface hydrophobicity were measured via sessile drop water contact angle measurements performed using a VCA 2000 contact angle system (AST Products). Two µL of 18 MΩ·cm deionized water was dispensed onto substrates, images were collected and contact angles were measured using the manufacturer's software. Five measurements were averaged for all reported values.

2.2.8 Fluorescence Imaging

Cy3-labeled oligonucleotides (40 µM) modified with an amino group at their 5′ end were suspended in PBS buffer (100 mM, pH = 7.4) containing EDC (20 mg/mL) and incubated overnight at 4^{o}C within the appropriately activated microfluidic device. The chip was then rinsed with ~2 mL of 0.1% SDS and PBS to remove unreacted molecules. All images were acquired (230 ms acquisition time) with a 200M inverted microscope (Zeiss) that contained an XBO 75 Xe arc lamp, a single band filter set (Omega Optical), and a Cascade 1 K EMCCD camera (Photometrics). Images were analyzed using Image-J software.

2.2.9 Chemical Surface Modification

Assembled devices were filled with a mixture of 5:1 (v/v) 2 M NaOH/100% IPA using input/output tubing sealed to the chip. Once filled, the chips were incubated with the activating solution in a hybridization oven (Boekel Scientific) for 12 h at 65ºC for COC and 30 min at room temperature for PMMA unless otherwise noted. Chips were rinsed with 1 mL nanopure water.

2.2.10 Reverse Transcription (RT) and Polymerase Chain Reaction (PCR)

CD4+ T-cells and neutrophils isolated on-chip were lysed by infusing ~20 µL lysis solution (GenElute Mammalian Total RNA Miniprep Kit, Sigma, St. Louis, MO) through the cell selection bed. The effluent was collected into a microfuge tube and purified using a total RNA

miniprep kit (Sigma) according to the manufacturer's protocol with DNase treatment (On-Column DNase I, Sigma, St. Louis, MO). After purification of TRNA, reverse transcription (RT) was accomplished using a ProtoScript II First Strand cDNA Synthesis Kit (New England BioLabs, Ipswich, MA). Samples were prepared by mixing 10 µL reaction mix, 2 µL poly-T primer, 2 µL enzyme (no enzyme, 2 µL of water for RT) and 6 µL of TRNA. The samples were then incubated at 42˚C for 1 h and heated to 80˚C for 5 min to deactivate the RT enzyme.

2.2.11 Polymerase Chain Reaction (PCR)

PCR was performed with cDNA in a total volume of 20 µL using Taq 2X Master Mix (New England Biolabs, Ipswich, MA). PCR cocktails consisted of 2 µL of primers (final concentration 500 nM), 10 µL Taq 2X Master Mix, 6 µL nuclease free water and 2 µL cDNA. PCR was carried out in a commercial thermal cycler (MJ Research Inc., Waltham, MA) with the following steps: Initial denaturation at 94˚C for 2.5 min followed by 40 cycles of denaturation at 94˚C for 15 s; annealing for 30 s at 63˚C for GAPDH primers and 55˚C for S100 primers; and extension at 72˚C for 30 s. A final extension at 72˚C for 7 min was followed by a cooling step at 4˚C. All primers were obtained from Integrated DNA Technologies, Inc. The sequences (5′-3′) were GAPDH: forward (F) – CTTTTGCGTCGCCAGCCGAG; reverse (R) – TGACCTTGGCCAGGGGTGCT[42]; S100A9 F – CTCGGCTTTGACAGAGTGCAAGAC; R – TCCCCGAGGCCTGGCTTATGG[42]; TCRB F – GTTTTCTTTCAGACTGTGGCTTC; R – CACGGCATACAAGGTGGC; and FPR1 F – TTTGCCTGTAACGCCAC; R – ATGCTCTATGTC TTCATGGG (www.ncbi.nih.gov).

PCR products were electrophoresed at 4.8 V/cm in 1X TBE (Tris–boric acid/EDTA, Bio-Rad Laboratories) on a 4% agarose gel with ethidium bromide (Lonza) staining. Amplicons were

indexed against a DNA sizing ladder 50 – 766 bp (New England Biolabs, Ipswich, MA). Images were collected using a Logic Gel imaging system (Eastman Kodak Company).

2.2.12 Statistical Analysis and Computational Methods

Data were analyzed using a student's two-tailed T-test (ANOVA). Statistical significance was assigned where $p < 0.0500$. Shear stress and flow uniformity through the bifurcated device was evaluated using COMSOL Multiphysics 4.3b.[43] Flow distribution analysis in the Z-configuration device employed a custom numerical algorithm detailed elsewhere.[44]

2.3 Results and Discussion

2.3.1 Polymer Surface Activation for Ab Attachment

Stable attachment of Abs to the surfaces of the selection bed, which were made from a polymer, is critical for efficient recovery and purity of the target cells. Ab density and uniformity throughout the selection channel is dependent on the activation protocol employed in cases where the Ab concentration exceeds the surface functional group number (see Figure 2.6).

We have reported that activating microchannel surfaces via UV/ozone irradiation causes two effects: (i) Optical absorption by the bulk polymer with transmission decreasing with higher dose levels, which can cause functional group surface densities to become increasingly non-uniform as the aspect ratio of the channel is increased; and (ii) fragmentation of the polymer during irradiation reducing functional group surface density, especially during thermal fusion bonding. UV and thermally treated COC devices were less susceptible to these artifacts compared to PMMA.[43]

We sought to avoid these effects by filling assembled devices with an activating chemical solution. Therefore, we investigated the use of a chemical modification protocol following thermal assembly of the device as this could potentially produce more uniform modification

throughout the channel cross-section and avoid thermal effects that would bury the surface functional groups for UV-activated surfaces.[43]

Microchannels were chemically activated via incubation in 5:1 (v:v) 2 M NaOH:IPA. In the case of PMMA, it has been reported that it's ester groups can be hydrolyzed to carboxy groups by incubation with 10M NaOH at 40ºC for 16 h.[45] However, the covalent attachment of Cy3-labeled oligonucleotides containing a pendant amino group serving as a fluorescent reporter of surface-confined carboxylic acids did not indicate the carboxylic acid group formation using this procedure. We hypothesized that the addition of IPA (similar to methanol by Patel *et al.*[46]) would encourage interaction with the hydrophobic polymer (water contact angle of PMMA = 76.4 ±1.4º) and/or solvation of methoxide byproducts.[46, 47] Treatment of PMMA microfluidic channels with 1/1 (v/v) 2M NaOH/IPA for 3 min at 60ºC and 10 min at room temperature resulted in some channel roughening and deformation (Figures 2.2C, D). However, it was found that channel integrity was preserved up to 30 min at 65ºC in 5:1 (v:v) 2M NaOH:IPA (Figure 2.2E). Thus we restricted PMMA modification using the aforementioned conditions to 30 min using 5:1 NaOH:IPA.

Chemical activation of PMMA did not change the water contact angle or carboxylic acid surface density as determined by a TBO assay relative to the pristine surface; this was likely due to poor sensitivity of the TBO assay in comparison to fluorescence assays using Cy3-labeled oligonucleotides containing a pendant amino group that served as a fluorescent reporter of surface-confined carboxylic acids. Chemically activated PMMA microchannels derivatized with Cy3-labeled oligonucleotides showed 232 ±47 cps compared to 503 ±72 cps for UV-activated and thermally treated PMMA microchannels (Figures 2.2A, E).

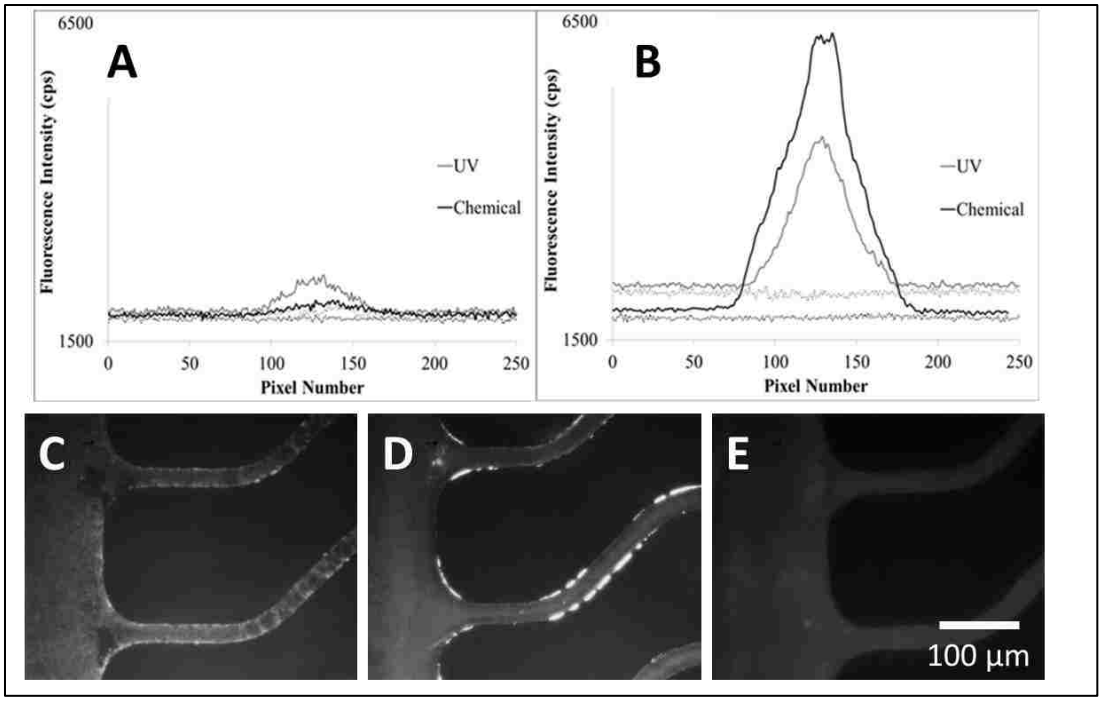

Figure 2.2 Line plots created from 20X fluorescence images for (A) PMMA and (B) COC curvilinear channels modified with 40 µM 3′-Cy3-labeled, 5′-amino modified oligonucleotides that were covalently bound to surface-confined carboxylic acids generated by UV (grey lines) or chemical activation (black lines) of the polymer surface. For controls (dotted lines colored corresponding to their treatments), fluorescently-labeled oligonucleotides were immobilized to identical surfaces without EDC coupling reagents to measure nonspecific adsorption and autofluorescence. UV activation was identical for the two polymers, but chemical activation protocols differed in incubation times, where a 5/1 (v/v) 2 M NaOH/IPA solution was incubated at 65^{o}C for 30 min for PMMA devices and 12 h for COC devices. Fluorescence images of oligonucleotides immobilized to PMMA devices that were chemically treated with (C) 1/1 (v/v) 2 M NaOH/IPA for 3 min at 60^{o}C and (D) 1/1 (v/v) 2 M NaOH/IPA for 10 min at room temperature, and (E) 5/1 (v/v) 2M NaOH/IPA for 5 min at 60^{o}C

COC microchannels were subjected to a similar treatment (5:1 (v:v); 2 M NaOH:IPA) Chemical activation decreased COC's water contact angle from 95.5 ±1.8º (pristine) to 63.3 ±3.2º and increased the carboxyl surface density to 0.6 ±0.2 nmol/cm^2 as determined by the TBO assay, which approached a theoretical monolayer (0.83 nmol/cm^2). Carboxyl formation was also evident by fluorescence analysis, where the surface fluorescence intensity (4369 ±437 cps) for chemical modification was significantly greater than that observed for the UV activated and thermally treated COC microchannels (2357 ±218 cps, see Figure 2.2B). The mechanism for

carboxyl formation for COC using these chemical conditions is currently unknown; literature precedence necessitates a radical-forming catalyst, such as Cu, Fe or other heavy metals to convert alkanes, such as those found in COC, directly to carboxylic acid groups.[48] We suspect that additives incorporated into the COC polymer during manufacturing assist in forming the surface carboxylic acids. Based on covalent labeling of surface-confined carboxylic acid, chemical treatment of COC resulted in the highest production of these functional groups.

2.3.2 Flow Uniformity in Bifurcated and Z-configuration Microfluidic Devices

The uniformity of flow in the two devices, which consisted of four selection units, with each unit containing an array of parallel, curvilinear isolation channels addressed by either a bifurcation or Z-configuration, were studied using fluid dynamic simulations and video microscopy. COMSOL Multiphysics 4.3a was utilized[49] to confirm uniform flow distribution within the devices. The velocity field in Figure 2.3A indicated that flow was uniformly distributed within each bifurcated, cell isolation bed (Figure 2.3B) and also between the four beds. Furthermore, because the Z-configuration device employed the same addressing architecture for the four isolation beds as the bifurcation device, the flow was uniformly distributed between the four Z-configuration cell isolation beds, but the flow was slightly non-uniform within each bed (Figure 2.3B).

The flow distribution simulations were compared to empirical observations acquired by filling the devices with red dye.[44] Time lapse images were extracted from the videos (Figure 2.4). As shown in images depicted in Figure 2.4A-D, the dye front was nearly linear across the four bifurcation beds, indicating uniform flow between and within the bifurcation beds, which agreed with the simulation results (Figures 2.3A and 2.3B). Flow was uniform between the Z-configuration isolation beds, but showed a parabolic profile within each bed (Figure 2.3B). As

shown in the images depicted in Figure 2.4E-G, dye filled more rapidly in the outer channels than the central channels, similar to that depicted in Figure 2.3B. Similar flow profiles were observed for filling devices with blood. These data agreed with previous results using a similar type of device, but consisting of a single cell isolation bed.[44]

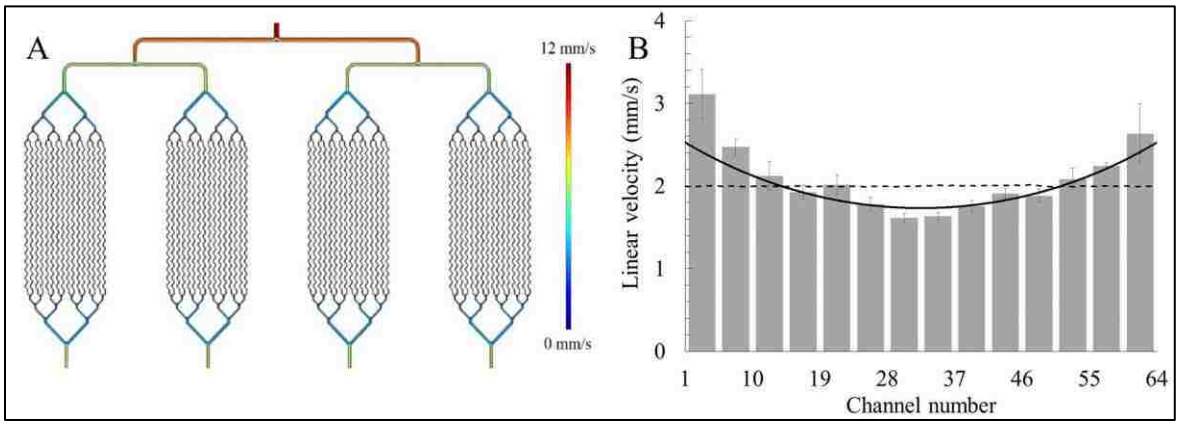

Figure 2.3 (A) COMSOL simulation showing the velocity field of buffer through the bifurcated cell isolation device. (B) Linear velocities normalized to an average of 2 mm/s acquired by (filled bars) 14 groups of the parallel channels in the Z-configuration device based on the results depicted in Figure. 2.4E-H and (solid line) compared to theoretical predictions via numerical simulation (solid black line).Dashed line indicates the distribution of linear flow velocities through all four beds of the simulated in bifurcation device in Figure 2.3A.

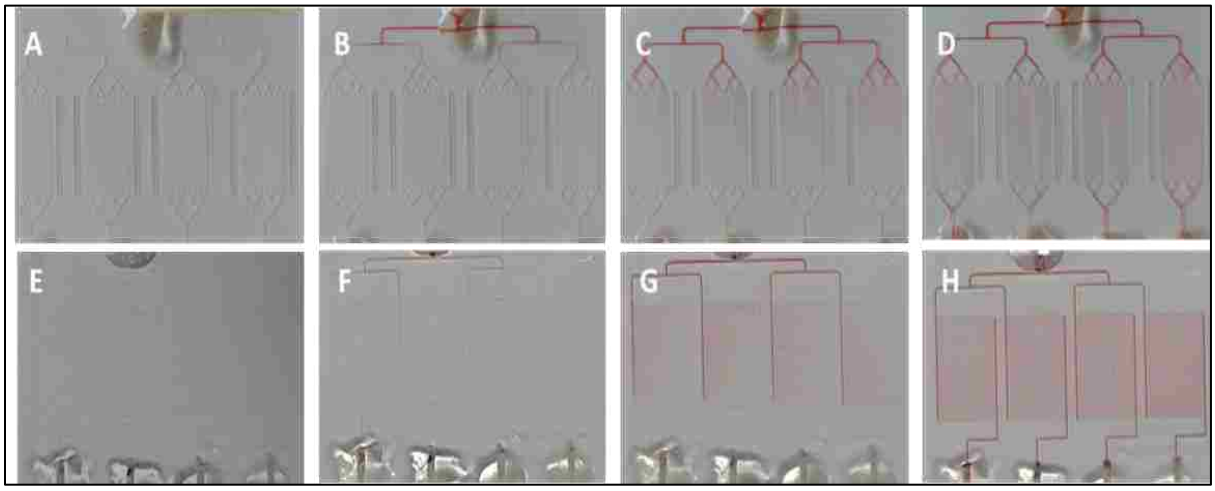

Figure 2.4 Time-lapse images of dye filling the (A-D) bifurcated device and (E-H) Z-configuration device. Images A-D and E-H were taken at 0, 15, 30, and 60 s, respectively.

2.3.3 Microfluidic Architectures and Performance Evaluation

Two microfluidic devices were fabricated both of which contained four separate isolation beds to facilitate the simultaneous positive selection of multiple types of cells. We chose to target T-cells using CD4 and neutrophils were selected using anti-CD66b mAbs. In all cases, the concentration of mAb used to optimize recovery was 0.5 mg/mL (see Figure 2.6). To facilitate simultaneous isolation of T-cells within two beds and neutrophils in the remaining two beds from a blood sample (Figures 2.5A, B), the beds were modified by introducing the EDC/NHS solution through the common inlet followed by mAbs infusion through the individual isolation bed outlets so that beds could be functionalized with different antibodies. This design also enabled the lysis of each subset contained within a bed for downstream analysis, such as mRNA expression, by infusing a lysis solution through the common inlet and lysate collection from the four separate outlets.

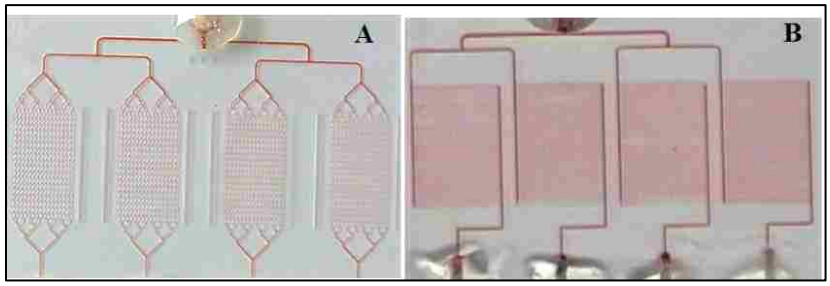

Figure 2.5 Photograph of the four isolation beds filled with red dye in A) bifurcated B) Z-configuration devices

The two microfluidic devices differed in how the parallel channels were addressed. In the first device (Figure 2.5A), a bifurcation network was utilized to address 16 channels, thereby requiring four bifurcations per isolation unit. The second device (Figure 2.5B) employed a Z-configuration, where inlet and outlet channels were poised orthogonal to the cell selection channels (64 per device).[43, 44] Due to the larger number of channels within the Z-configuration,

this device had a higher throughput; 50 µL of blood could be processed in 3 min maintaining a 2 mm/s linear velocity to optimize recovery[40] compared to 13 min for the bifurcated design. Using a previously reported and experimentally validated numerical algorithm,[44] we calculated the flow distribution through the Z-configuration and found that the linear velocity ranged between 1.7 and 2.5 mm/s for each isolation bed in the parallel arrangement (Figure 2.3B). For the bifurcation device (Figures 2.3A and 2.4), the fluid velocity within each isolation bed was uniform. The variability in the flow velocity seen within each isolation bed of the Z-configuration can result in variable cell recoveries.

To evaluate the performance of the two microfluidic designs and surface activation chemistry, T-cells and neutrophils were isolated from blood and their recoveries determined. All cell counts and purities are summarized in Table 2.1. In this discussion, we differentiate the UV and chemical activation modalities by UV- and CH-, respectively. For COC chips and the bifurcated or Z-configuration, these were designated as UV-COC_{bif} and UV-COC_Z, respectively, when UV activated and CH-COC_{bif} and CH-COC_Z when chemically activated.

To ensure Ab concentration was not a limiting factor and cell recovery results reflected the number density of the generated surface-confined carboxylic acids, we quantified cell recovery as a function of the antibody concentration in the COC bifurcated devices. The concentration of anti-CD4 Abs was varied at 0.1, 0.25, 0.5, and 1 mg/mL. Figure 2.6 suggested reduction in recoveries when Ab concentrations were set <0.5 mg/mL and comparable recoveries between 0.5 and 1 mg/mL. Therefore, 0.5 mg/mL was selected to be the optimal concentration for Ab immobilization for all subsequent experiments.

Initial testing of the bifurcated design indicated that with either activation protocol, COC out performed PMMA devices. UV-COC_{bif} isolated 798 ±167 CD4+ T-cells cells compared to 325

±85 cells for UV-PMMA$_{bif}$ from a 50 µL blood sample (Table 2.1). These agree with our previous results, which indicated efficient and uniform activation in COC microchannels providing a higher Ab load and thus, higher recoveries.[43] CH-PMMA$_{bif}$ devices demonstrated extremely poor performance (7 ±3 cells), which reflected the inability to chemically activate PMMA without degrading microstructures (see Figure 2.2). Results for CH-COC$_{bif}$ devices (702 ±386 cells) showed no statistical difference ($p = 0.631$) to UV-COC$_{bif}$ devices (798 ±167) (Figure 2.7). Chemical activation was as efficient as UV activation for the bifurcated COC devices as well.

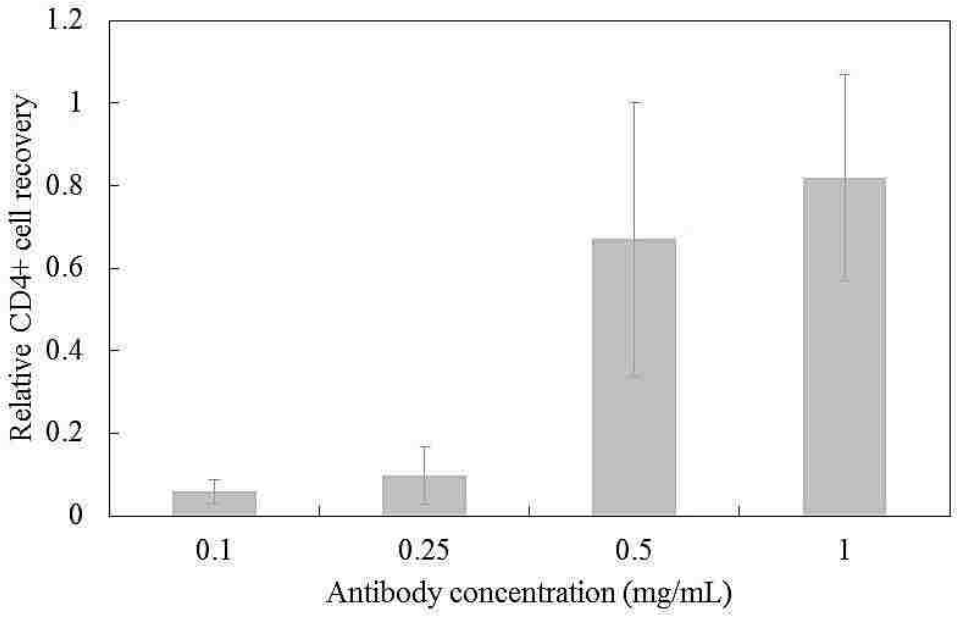

Figure 2.6 T-cell recoveries from healthy donor blood using UV-COC$_{bif}$ devices modified with anti-human CD4 Abs at different concentrations.

Both UV-COC devices produced nearly equal recovered T-cells; 798 ±167 and 596 ±154 using UV-COC$_{bif}$ and UV-COC$_{Z}$ devices, respectively. Considering nearly the same cell recovery and more rapid blood sample processing, the Z-type architecture was determined to be the most efficient from a throughput perspective. Hence, Z-configuration devices were used for simultaneously isolating T-cells and neutrophils.

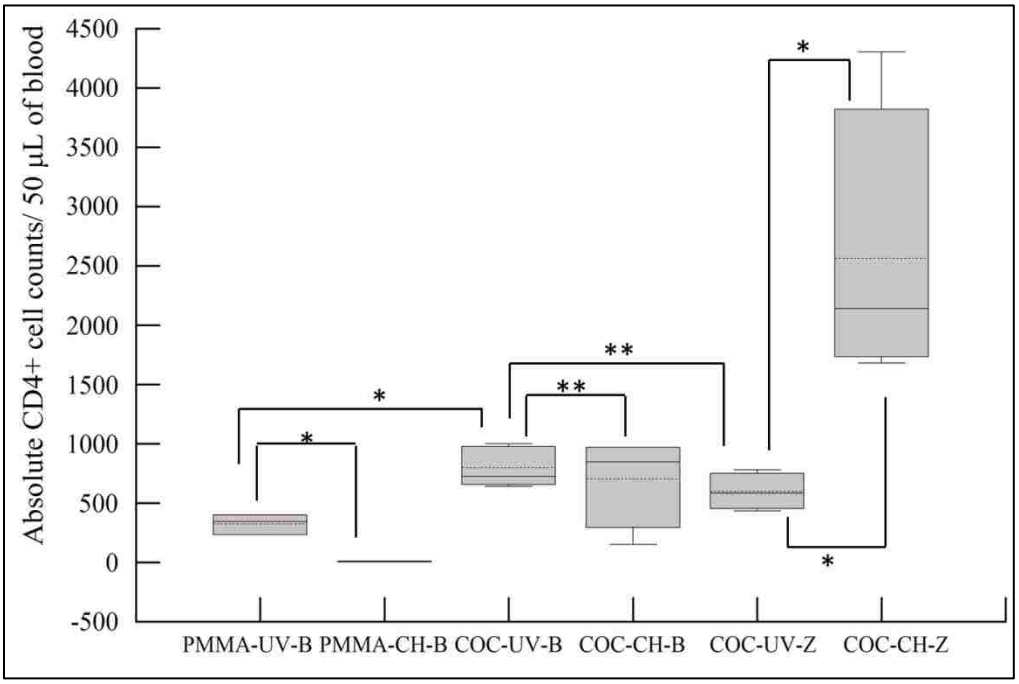

Figure 2.7 Box plot comparing CD4+ T-cell recoveries from 50 µL healthy human blood in UV and chemically modified PMMA and COC devices utilizing either bifurcated or Z-configuration. (*) indicates statistically significant difference (student's two tailed t-test $p < 0.0500$), while (**) implies no statistically different results. Solid lines in the boxes represent median; the dotted line represents mean; the upper and lower edges of the boxes indicate third and first quartiles, respectively; and error bars show maximum and minimum values.

We observed higher cell recovery using CH-COC_Z devices; absolute cell counts increased from 596 ±25 for UV-COC_Z to 2565 ±1194 for the CH-COC_Z devices for T-cell isolation. In the case of neutrophils, 1096 ±537 cells were selected for the UV-COC_Z device compared to 2949 ±901 for the CH-COC_Z device. However, we observed no difference between the activation modalities for bifurcated COC devices, which can be explained by shear stress considerations.[50] In bifurcated devices, ~40% of cells were isolated in the bifurcation regions (Figure 2.8B-E), whereas only 4% were observed in the inlet and outlet addressing channels of the Z-configuration. Inspection of the bifurcation network showed that fluidic shear stress was reduced from 11 dynes/cm^2 in the parallel channels to 6-7 dynes/cm^2 through the bifurcation network,

where ~17.7% of the device's surface area accounted for ~40% of cell isolation. Conversely, shear stress through the Z-configuration inlet and outlet channels ranged between ~1 and 38 dynes/cm^2 along the channel's length and was <11 dynes/cm^2 in ~19% of the length of the inlet and outlet channels.

For the Z-configuration, recovery occurred predominantly in the cell isolation channels, where optical absorption of the activating UV radiation may lead to reduced Ab loads; activating polymer surfaces using chemical modification is not sensitive to device aspect ratio. These effects may be precluded in bifurcated devices due to cell isolation in the low aspect ratio bifurcation regions (Figure 2.8A).

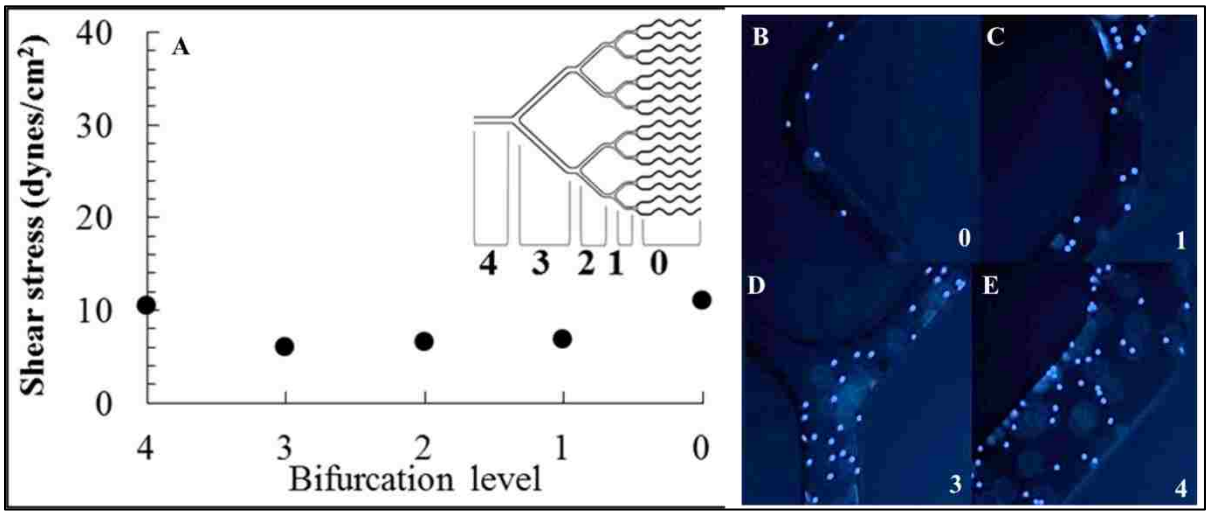

Figure 2.8 (A) Computational simulations showing the shear stresses in the parallel channels of the bifurcated device. (B- E) T-cells isolated from blood from the left in the 3, 2, 1, and 0 bifurcation levels of the bifurcated microchip. All curvilinear channel dimensions are 25 × 80 µm (w × h) and the SEM scale bars are 1 mm for all micrographs.

2.3.4 Determination of CD4 Expression of MOLT-3 Cells by Flow Cytometry

Expression of CD4 antigen on MOLT-3 cells was measured after subtracting isotype control-FITC and CD4-FITC double positive events as shown in the histograms in Figure 2.9.

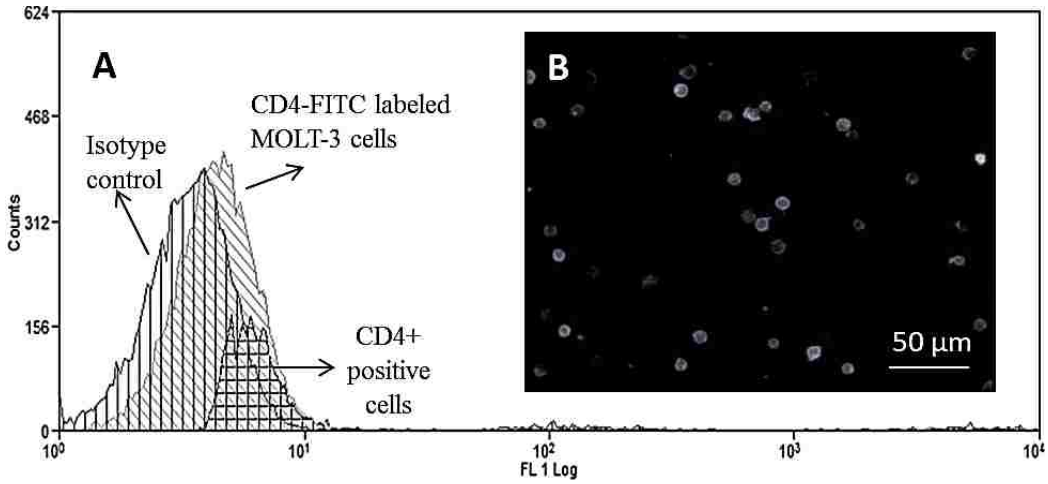

Figure 2.9 (A) Overlay of histograms generated by integration of negative isotype control (vertical lines), CD4- MOLT-3 cells (diagonal lines), and CD4+ MOLT-3 cells (hatched lines). The histogram for the CD4+ MOLT-3 cells was generated by the Overton subtraction method. (B) Visualization of CD4-FITC labelled MOLT-3 cells on a microscope.

The low fluorescence signal observed for CD4+ MOLT-3 cells in flow cytometry (Figure 2.9A) indicated these cells have much lower CD4 expression than T-cells (46,000-202,000 CD4 molecules/cell; mean = 100,000 molecules/cell).[51-53]

2.3.5 Recovery of Different Leukocyte Subsets

Initial recovery tests were performed with MOLT-3 cells (average cell diameter 9.3 ±2.4 µm) using isolation beds modified with anti-CD4. However, we observed very poor recovery of these cells; 0.36 ±0.3% for UV-COC_{bif}, 0.13 ±0.1% for CH-COC_{bif} and 0.52 ±0.1% for CH-COC_Z. After correcting for the CD4-MOLT-3 expression from the flow cytometry analysis (see Figure 2.9), the recoveries were 1.4 ±0.3 %, 0.5 ±0.1% and 2.0 ±0.1%, for the UV-COC_{bif}, CH-COC_{bif} and CH-COC_Z devices, respectively. These efficiencies were lower than that observed for the human T-cells (~10%), but exhibited similar patterns between the activation modality and device design; chemically activated COC_Z devices isolated the highest absolute number of cells.

The two primary factors contributing to the low recovery of MOLT-3 cells were likely the small cell size relative to the channel width and the low CD4 expression levels for these cells.

Because the 9.3 ±2.4 μm diameter MOLT-3 cells were isolated in 25 μm wide channels, we would expect low recovery as there is a low probability of cell/surface-confined Ab interactions. Reduction in channel width to slightly larger than the MOLT-3 cell diameter should improve their recovery.[40] However, the use of much narrower channels may be problematic for blood processing due to the risk of device failure arising from clogging because of the presence of large leukocytes (~15 μm). If the Ag expression level is low, shear forces in the channel may also remove isolated cells from the selection bed due to the small adhesion force and thus, produce lower recovery. These considerations were also true for human T-cell isolation from whole blood; in spite of their smaller size (~7 μm average diameter) compared to MOLT-3 cells, these cells showed higher recovery most likely because of the higher expression of CD4 producing better cell/surface adhesion forces.

We observed higher recoveries for CD4 T-cells (10.3 ±0.5%) compared to CD66b neutrophils (1.5 ±0.1%) in the CH-COC_Z devices, assuming relative abundances of 25,000 and 200,000 cells/50 μL of blood for T-cells and neutrophils, respectively.[54] This difference in recovery may be related to the number of Ab molecules immobilized to the surface. With the size of anti-CD4 and anti-CD66b being 150 kDa IgG_1 and 900 kDa IgM, respectively, they will form monolayers where IgM is ~36x less abundant than a monolayer of IgG, possibly leading to lower neutrophil recovery.[43, 55]

Flow cytometric analysis was performed on T-cells and neutrophils isolated from a buffy coat as described previously. For T-cells, CD4-FITC fluorescence intensity was 5.3 times greater than the IgG isotype control and for neutrophils, CD66b-FITC showed 4.6 times greater intensity compared to its IgM control. However, due to the surface area of neutrophils (~707 μm^2) compared to smaller T-cells (113 μm^2), antigen density (C_∞) of CD4 on T-cells is roughly 7

times denser than CD66b on neutrophils. Consequently, the rate of adhesion (k_{ad}) of T-cells to surface antibodies is ~7 times greater than for neutrophils as stipulated by Chang and Hammer;[55]

$$k_{ad} = k_f C_\infty N_r \quad (1)$$

where (k_f) is the effective antibody-antigen binding rate and (N_r) is the antibody number. Thus, the ~10 times lower recovery observed for neutrophils could be attributed to lower surface density of the IgM anti-CD66b selection antibody and/or reduced surface densities of CD66b on neutrophil cells.

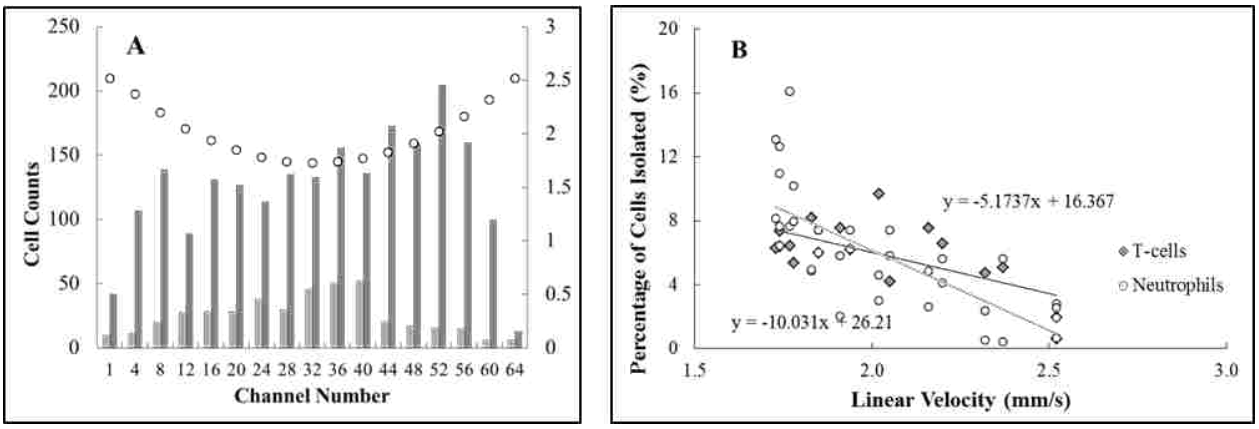

Figure 2.10 (A) Distribution of T-cells and neutrophils in Z-configuration parallel channels, which have varying linear velocities. (B) Scatter plot of the data in (A) showing strong, negative correlation between the percentage of cells isolated in a parallel channel with the linear velocity in that channel.

We also inspected the distribution of isolated cells throughout the parallel channels of the Z-configuration device to relate cell counts to linear velocity (Figure 2.10A). To discern the effects of varying linear velocity on absolute recovery, we normalized the recovered cell counts to the total input cell counts and plotted these results as a function of linear velocity (Figure 2.10B). A strong, negative correlation between linear velocity and cell recovery was observed for both T-cells (Pearson's correlation r = -0.65) and neutrophils (r = -0.72). However, the magnitude of the slope suggests that neutrophils (m = -10.03 cells/mm/s) are more sensitive to linear velocity and

fluidic shear stress than T-cells (m = -5.17 cells/mm/s) due to the effects of lower CD66b antigen surface density as noted by Eq. (1).

2.3.6 Purity of Isolated Leukocytes

When designing systems for mRNA expression analysis of cell subsets isolated from blood, it is critical to isolate pure fractions of the targets. For T-cell isolation via CD4 positive selection, this is challenged by the fact that CD4 is also expressed on the surface of monocytes, macrophages, and dendritic cells at a frequency of 3-8% of the total leukocyte population in blood, albeit, CD4 expression is lower compared to T-cells (46,000-202,000 molecules/cell) and thus, their k_{ad} lower as noted by Eq. (1).[4, 51-53] This means that fluidic shear stress can be used to remove from the selection surface cells with low k_{ad} values.

Purity of isolated CD4+ T-lymphocytes was assessed by immunostaining with CD66b, CD14, and CD20 Abs to identify neutrophils (comprising 40-66% of total leukocyte population), monocytes (4-8%), and B-cells (8-12%), respectively.[3] Purity was defined as the ratio of DAPI+, CD14-, CD66b-, and CD20- cells to the total number of nucleated cells. Fluorescence images (Figures 2.11A-C) showed the absence of cells labeled with CD14/66b/20 Abs. Isolated cells showed intact structures without an obvious change in morphology. It was also observed that T-cells and neutrophils were distributed randomly within the channel (outer and inner curvatures of the curvilinear channels, Figure 2.8A) unlike circulating tumor cells, which we have reported to be predominantly isolated along the inner curvature.[40] To confirm proper identification of T-cells, an anti-CD3 marker was chosen because 87% of T-cells are CD3+ and CD4+ (Figures 2.11D-F).[56] For the UV-COC_{bif} devices, purities were 97 ±1%, and CH-COC_{bif} purities were 92 ±5% (Table 2.1). The lack of contaminating cells most likely resulted from their low CD4

expression and the application of a shear stress between 6 to 11 dynes/cm^2.[51, 52, 57, 58] The purity for the CH-COC_Z for the CD4+ T-cells was found to be 98 ±1%.

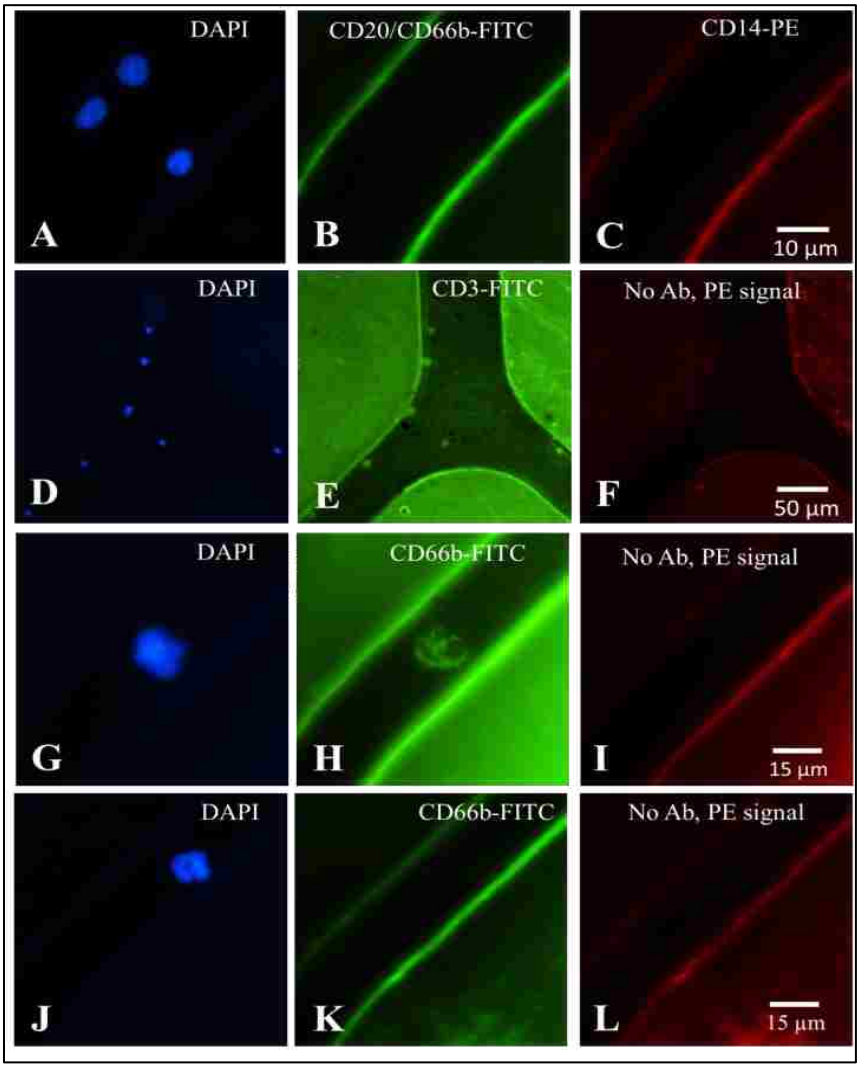

Figure 2.11 (A-F) Fluorescence microscopy images of CD4+ T-cells isolated from whole blood using a bifurcated microfluidic device immobilized with anti-CD4 Ab and stained with (A, D) DAPI (nuclear stain); (B) CD20/CD66b-FITC specific for B-lymphocytes and neutrophils, respectively; (C) CD14-PE specific for monocytes; (E) CD3-FITC specific for T-cells; and (F) no antibody used. Purity of CD4+ T cells was defined as positive for DAPI and negative for PE and FITC stains in (A-C), while specificity was demonstrated by dual staining of cells with CD3-FITC and DAPI (D-F). (G-I) Fluorescence microscopic images of isolated neutrophils: (G) DAPI stained; (H) CD66b-FITC stained; (I) no Ab used; and (J-L) a neutrophil that was (J) DAPI stained with neutrophil morphology, (K) showed lack of CD66b-FITC signal, and (L) no Ab used. Neutrophils were identified only if positive for both DAPI and CD66b

Lastly, we assessed neutrophil purity by counting double positive DAPI and CD66b-FITC cells (Figure 2.11G-I). We observed that some cells were DAPI+ but very faint for CD66b-FITC, but the dimensions and morphology of these cells were consistent with neutrophils (Figure 2.11J-L).[59] These cells were counted as neutrophils and it is plausible that some neutrophils possessed very low CD66b expression and thus, could not be detected thereby artificially lowering purity levels. Neutrophil counts isolated from 50 μL of blood using the UV-COC_{bif} devices averaged 918 ±91 with a purity of 94 ±3 % and CH-COC_Z yielded purities of 97 ±2% (see Table 2.1)

Table 2.1 Enumeration values for isolated T-cells and neutrophils from whole blood using COC and PMMA microfluidic devices with different geometries and activation protocols.

Cell type	Chip Design	Modification -substrate	Cell count (n= 4) Mean ± SD (Median)	Negative control	Purity
T-Cells	Bifurcated	UV-PMMA	325 ±85 (342)	---	---
		UV-COC	798 ±168(723)	19 ±5	97 ±1
		CH-PMMA	7 ±3 (8)	---	---
		CH-COC	703 ±386 (846)	16 ±3	92 ±5
Neutrophils	Bifurcated	UV-COC	918 ±91 (888)	---	94 ±3
Neutrophils	Z-configuration	UV- COC	1096 ±537 (1112)	---	---
		CH-COC	2949 ±901	---	97 ±2
T-cells	Z-configuration	UV-COC	596 ±154 (585)	7 ±1	---
		CH-COC	2565 ±1194 (2139)	30 ±9	98 ±1

2.3.7 Reverse Transcription –Polymerase Chain Reaction (RT-PCR)

The total number of isolated cells in the CH-COC_Z devices ranged from 500 to 2,000 CD4+ T-cells and CD66b+ neutrophils. Considering an average of 10 pg of TRNA per leukocyte, we expected to obtain 5 – 20 ng TRNA (0.25-1 ng of mRNA) per bed, which should provide

sufficient material for cDNA synthesis and gene expression analysis. To make sure that sufficient mRNA was harvested from the T-cells and neutrophils, two beds were used for each cell type. T-cells and neutrophils were isolated from the same blood sample using the CH-COC_Z chip and because of the high purity of isolated fractions, cell lysis was performed directly on chip. Following lysis and TRNA isolation, an RT reaction was performed. cDNA was then used for PCR with expression analysis of 4 genes; *S100A9*, which has been shown to be overexpressed following stroke[38] and plays a prominent role in the regulation of inflammatory processes and immune response,[60-62] *TCRB* and *FPR1* genes, which are specific to T-cells and neutrophils,[63-65] respectively, and *GAPDH*, a housekeeping gene used as a reference. Figure 2.12A shows fluorescence images of the amplicons. Although the expression of *GAPDH* can vary between different types of cells,[66] for these initial results we normalized the amplicon intensities to the intensity of the *GAPDH* product.

As shown in Figure 4B for the T-cell population, we observed significantly lower expression (22x) of *S100A9* than in the neutrophil subset for the same healthy donor.T-cells showed a higher expression of the *TCRB* gene compared to neutrophils as supported from the literature. However, some studies demonstrated neutrophils populations also expressing *TCRB* mRNA as well.[67] *FPR1* gene was 7x higher expressed in neutrophils, similar to that reported in the literature.[68] It is important to emphasize that in the case of mRNA profiling, it is imperative that cell perturbation and handling is reduced to eliminate any phenotypic changes.[69, 70] By using microfluidics, we obtained pure populations of cells and cell lysate within 12 min from the time of blood sample introduction into the microfluidic device. Fast processing allows for securing high quality mRNA (data not shown), lack of centrifugation, and unnecessary storage of blood specimens.

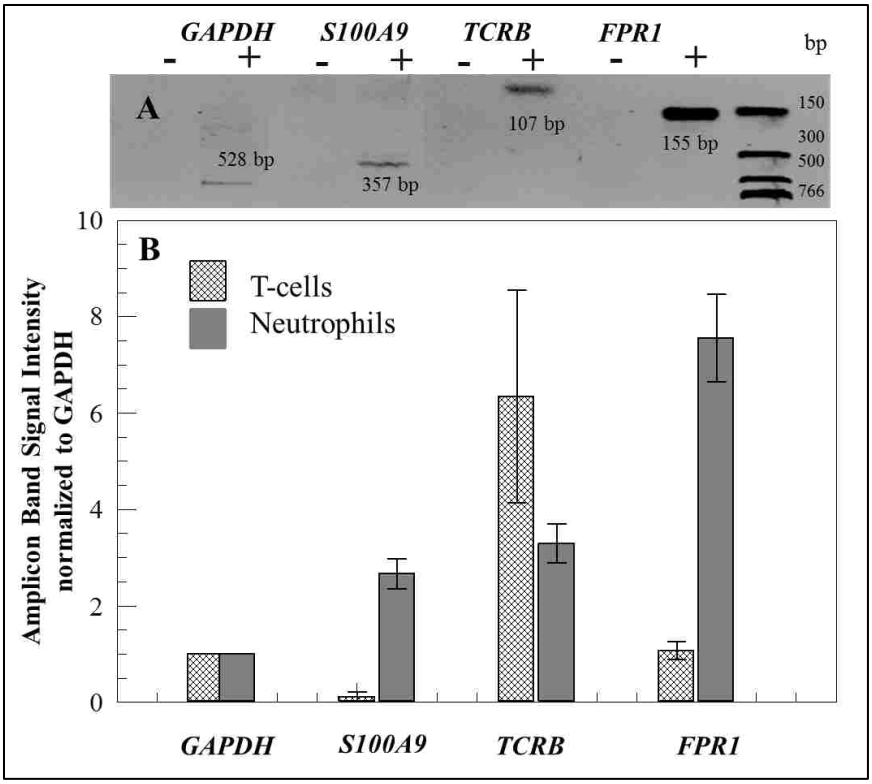

Figure 2.12 (A) Gel electrophoresis inverted image of amplicons generated from cDNA reverse transcribed from TRNA extracted from isolated neutrophils. Negative control (-) and positive (+) amplification reactions for tested genes were performed with products from negative (-) RT (without RT enzyme) and positive (+) RT. Amplicon lengths are shown in the figure. Separation performed at 4.8 V/cm in a TBE buffer. (B) Normalized to GAPDH gene signals (n=3) from the amplicons identified on an agarose gel stained with ethidium bromide for T-cells and neutrophils.

2.4 Conclusions

We have demonstrated an affinity-based microfluidic system capable of isolating highly pure subsets of leukocytes from whole blood. Processing 50 µL of whole blood within 6.6 min provided sufficient genetic material for gene expression profiling. Special emphasis was placed on the fluid dynamics and design architecture of the device for T-cell and neutrophil isolation to obtain high purity leukocytes fractions using a single step. The isolation of two types of cells from whole blood was accomplished with purity >90%.

We assessed the effects of polymeric substrate and surface activation modalities on cell isolation and discovered a chemical activation method for COC, which can be useful for ultra-high aspect ratio microfluidic devices. The demonstrated results are not limited only to CD4+ T-cells and CD66b+ neutrophils but can be expanded to analyze other cell types simply by choosing different affinity agents for the cells of interest. Furthermore, our microfluidic device contains four individually addressable beds, permitting simultaneous isolation of four individual cell sub-populations from the same blood sample with sufficient material to perform mRNA expression analysis on the isolated cells.

2.5 References

1. Feezor, R. J.; Baker, H. V.; Mindrinos, M.; Hayden, D.; Tannahill, C. L.; Brownstein, B. H.; Fay, A.; MacMillan, S.; Laramie, J.; Xiao, W.; Moldawer, L. L.; Cobb, J. P.; Laudanski, K.; Miller-Graziano, C. L.; Maier, R. V.; Schoenfeld, D.; Davis, R. W.; Tompkins, R. G. Whole Blood and Leukocyte Rna Isolation for Gene Expression Analyses. *Physiol Genomics* 2004, 19, 247-54.

2. Gao, Y.; Li, W.; Pappas, D. Recent Advances in Microfluidic Cell Separations. *Analyst (Cambridge, U. K.)* 2013, 138, 4714-4721.

3. Toner, M.; Irimia, D. Blood-on-a-Chip. *Annu. Rev. Biomed. Eng.* 2005, 7, 77-103, 3 plates.

4. Cheng, X.; Irimia, D.; Dixon, M.; Sekine, K.; Demirci, U.; Zamir, L.; Tompkins, R. G.; Rodriguez, W.; Toner, M. A Microfluidic Device for Practical Label-Free Cd4+ T Cell Counting of Hiv-Infected Subjects. *Lab Chip* 2007, 7, 170-178.

5. Cheng, X.; Liu, Y.-s.; Irimia, D.; Demirci, U.; Yang, L.; Zamir, L.; Rodriguez, W. R.; Toner, M.; Bashir, R. Cell Detection and Counting through Cell Lysate Impedance Spectroscopy in Microfluidic Devices. *Lab Chip* 2007, 7, 746-755.

6. Rodriguez, W. R.; Christodoulides, N.; Floriano, P. N.; Graham, S.; Mohanty, S.; Dixon, M.; Hsiang, M.; Peter, T.; Zavahir, S.; Thior, I.; Romanovicz, D.; Bernard, B.; Goodey,

A. P.; Walker, B. D.; McDevitt, J. T. A Microchip Cd4 Counting Method for Hiv Monitoring in Resource-Poor Settings. *PLoS Med.* 2005, 2, 663-672.

7. Kim, S. T.; Kim, D.-J.; Kim, T.-J.; Seo, D.-W.; Kim, T.-H.; Lee, S.-Y.; Kim, K.; Lee, K.-M.; Lee, S.-K. Novel Streptavidin-Functionalized Silicon Nanowire Arrays for Cd4+ T Lymphocyte Separation. *Nano Lett.* 2010, 10, 2877-2883.

8. Kim, D.-J.; Seol, J.-K.; Wu, Y.; Ji, S.; Kim, G.-S.; Hyung, J.-H.; Lee, S.-Y.; Lim, H.; Fan, R.; Lee, S.-K. A Quartz Nanopillar Hemocytometer for High-Yield Separation and Counting of Cd4+ T Lymphocytes. *Nanoscale* 2012, 4, 2500-2507.

9. Thorslund, S.; Larsson, R.; Bergquist, J.; Nikolajeff, F.; Sanchez, J. A Pdms-Based Disposable Microfluidic Sensor for Cd4+ Lymphocyte Counting. *Biomed Microdevices* 2008, 10, 851-7.

10. Warner, E. A.; Kotz, K. T.; Ungaro, R. F.; Abouhamze, A. S.; Lopez, M. C.; Cuenca, A. G.; Kelly-Scumpia, K. M.; Moreno, C.; O'Malley, K. A.; Lanz, J. D.; Baker, H. V.; Martin, L. C.; Toner, M.; Tompkins, R. G.; Efron, P. A.; Moldawer, L. L. Microfluidics-Based Capture of Human Neutrophils for Expression Analysis in Blood and Bronchoalveolar Lavage. *Lab. Invest.* 2011, 91, 1787-1795.

11. Feigin, V. L.; Lawes, C. M. M.; Bennett, D. A.; Barker-Collo, S. L.; Parag, V. Worldwide Stroke Incidence and Early Case Fatality Reported in 56 Population-Based Studies: A Systematic Review. *The Lancet Neurology* 2009, 8, 355-369.

12. Hand, P. J.; Kwan, J.; Lindley, R. I.; Dennis, M. S.; Wardlaw, J. M. Distinguishing between Stroke and Mimic at the Bedside: The Brain Attack Study. *Stroke* 2006, 37, 769-75.

13. Norris, J. W.; Hachinski, V. C. Misdiagnosis of Stroke. *Lancet* 1982, 1, 328-31.

14. Goldstein, L. B.; Simel, D. L. Is This Patient Having a Stroke? *JAMA, J. Am. Med. Assoc.* 2005, 293, 2391-2402.

15. Furlan, A.; Higashida, R.; Wechsler, L.; Gent, M.; Rowley, H.; Kase, C.; Pessin, M.; Ahuja, A.; Callahan, F.; Clark, W. M.; Silver, F.; Rivera, F. Intra-Arterial Prourokinase

for Acute Ischemic Stroke. The Proact Ii Study: A Randomized Controlled Trial. *JAMA, J. Am. Med. Assoc.* 1999, 282, 2003-2011.

16. Hacke, W.; Kaste, M.; Bluhmki, E.; Brozman, M.; Dvalos, A.; Guidetti, D.; Larrue, V.; Lees, K. R.; Medeghri, Z.; Machnig, T.; Schneider, D.; von, K. R.; Wahlgren, N.; Toni, D. Thrombolysis with Alteplase 3 to 4.5 Hours after Acute Ischemic Stroke. *N. Engl. J. Med.* 2008, 359, 1317-1329.

17. Goldstein, L. B. Improving the Clinical Diagnosis of Stroke. *Stroke* 2006, 37, 754-5.

18. Whiteley, W.; Tseng, M.-C.; Sandercock, P. Blood Biomarkers in the Diagnosis of Ischemic Stroke: A Systematic Review. *Stroke* 2008, 39, 2902-9.

19. Hasan, N.; McColgan, P.; Bentley, P.; Edwards, R. J.; Sharma, P. Towards the Identification of Blood Biomarkers for Acute Stroke in Humans: A Comprehensive Systematic Review. *Br. J. Clin. Pharmacol.* 2012, 74, 230-240.

20. Jickling, G. C.; Sharp, F. R. Blood Biomarkers of Ischemic Stroke. *Neurotherapeutics* 2011, 8, 349-360.

21. Saah, A. J.; Hoover, D. R. "Sensitivity" and "Specificity" Reconsidered: The Meaning of These Terms in Analytical and Diagnostic Settings. *Annals of Internal Medicine* 1997, 126, 91-94.

22. Maas, M. B.; Furie, K. L. Molecular Biomarkers in Stroke Diagnosis and Prognosis. *Biomarkers Med.* 2009, 3, 363-383.

23. Yilmaz, G.; Arumugam, T. V.; Stokes, K. Y.; Granger, D. N. Role of T Lymphocytes and Interferon-Gamma in Ischemic Stroke. *Circulation* 2006, 113, 2105-12.

24. Marsh, B. J.; Williams-Karnesky, R. L.; Stenzel-Poore, M. P. Toll-Like Receptor Signaling in Endogenous Neuroprotection and Stroke. *Neuroscience (Amsterdam, Neth.)* 2009, 158, 1007-1020.

25. Tang, S.-C.; Arumugam, T. V.; Xu, X.; Cheng, A.; Mughal, M. R.; Jo, D. G.; Lathia, J. D.; Siler, D. A.; Chigurupati, S.; Ouyang, X.; Magnus, T.; Camandola, S.; Mattson, M. P.

Pivotal Role for Neuronal Toll-Like Receptors in Ischemic Brain Injury and Functional Deficits. *Proc. Natl. Acad. Sci. U. S. A.* 2007, 104, 13798-13803.

26. Gee, J. M.; Kalil, A.; Shea, C.; Becker, K. J. Lymphocytes: Potential Mediators of Postischemic Injury and Neuroprotection. *Stroke* 2007, 38, 783-8.

27. Laudanski, K.; Miller-Graziano, C.; Xiao, W.; Mindrinos, M. N.; Richards, D. R.; De, A.; Moldawer, L. L.; Maier, R. V.; Bankey, P.; Baker, H. V.; Brownstein, B. H.; Cobb, J. P.; Calvano, S. E.; Davis, R. W.; Tompkins, R. G. Cell-Specific Expression and Pathway Analyses Reveal Alterations in Trauma-Related Human T Cell and Monocyte Pathways. *Proc. Natl. Acad. Sci. U. S. A.* 2006, 103, 15564-15569.

28. Baird, A. E. Blood Biologic Markers of Stroke: Improved Management, Reduced Cost? *Curr Atheroscler Rep* 2006, 8, 267-75.

29. Moore, D. F.; Goldin, R.; Violet, W. Using Peripheral Blood Mononuclear Cells to Determine a Gene Expression Profile of Intra-Cerebral Hemorrhage. *Annals of Neurology* 2007, 62, S8.

30. Moore, D. F.; Li, H.; Jeffries, N.; Wright, V.; Cooper, R. A.; Elkahloun, A.; Gelderman, M. P.; Zudaire, E.; Blevins, G.; Yu, H.; Goldin, E.; Baird, A. E. Using Peripheral Blood Mononuclear Cells to Determine a Gene Expression Profile of Acute Ischemic Stroke. *Circulation* 2005, 111, 212-221.

31. Oh, S.-H.; Kim, O.-J.; Shin, D.-A.; Song, J.; Yoo, H.; Kim, Y.-K.; Kim, J.-K. Alteration of Immunologic Responses on Peripheral Blood in the Acute Phase of Ischemic Stroke: Blood Genomic Profiling Study. *Journal of Neuroimmunology* 2012, 249, 60-65.

32. Tang, Y.; Xu, H.; Du, X.; Lit, L.; Walker, W.; Lu, A.; Ran, R.; Gregg, J. P.; Reilly, M.; Pancioli, A.; Khoury, J. C.; Sauerbeck, L. R.; Carrozzella, J. A.; Spilker, J.; Clark, J.; Wagner, K. R.; Jauch, E. C.; Chang, D. J.; Verro, P.; Broderick, J. P.; Sharp, F. R. Gene Expression in Blood Changes Rapidly in Neutrophils and Monocytes after Ischemic Stroke in Humans: A Microarray Study. *J Cereb. Blood Flow Metab.* 2006, 26, 1089-1102.

33. Mateusz G. Adamski, Y. L., Erin Wagner, Hua Yu, Chloe Seales-Bailey, Steven A. Soper, Michael Murphy, Alison E. Baird. *J Biomolecular Screening* 2013, submitted for publication.

34. Du, X.; Tang, Y.; Xu, H.; Lit, L.; Walker, W.; Ashwood, P.; Gregg, J. P.; Sharp, F. R. Genomic Profiles for Human Peripheral Blood T Cells, B Cells, Natural Killer Cells, Monocytes, and Polymorphonuclear Cells: Comparisons to Ischemic Stroke, Migraine, and Tourette Syndrome. *Genomics* 2006, 87, 693-703.

35. Siliciano, R. F.; Lawton, T.; Knall, C.; Karr, R. W.; Berman, P.; Gregory, T.; Reinherz, E. L. Analysis of Host-Virus Interactions in Aids with Anti-Gp120 T Cell Clones: Effect of Hiv Sequence Variation and a Mechanism for Cd4+ Cell Depletion. *Cell (Cambridge, Mass.)* 1988, 54, 561-75.

36. O'Brien, W. A.; Hartigan, P. M.; Daar, E. S.; Simberkoff, M. S.; Hamilton, J. D. Changes in Plasma Hiv Rna Levels and Cd4+ Lymphocyte Counts Predict Both Response to Antiretroviral Therapy and Therapeutic Failure. Va Cooperative Study Group on Aids. *Ann Intern Med* 1997, 126, 939-45.

37. Yarchoan, R.; Tosato, G.; Little, R. F. Therapy Insight: Aids-Related Malignancies-the Influence of Antiviral Therapy on Pathogenesis and Management. *Nat. Clin. Pract. Oncol.* 2005, 2, 406-415.

38. Adamski, M. G.; Li, Y.; Wagner, E.; Yu, H.; Seales-Bailey, C.; Soper, S. A.; Murphy, M.; Baird, A. E. Next-Generation Qpcr for the High-Throughput Measurement of Gene Expression in Multiple Leukocyte Subsets. *J Biomol Screen* 2013, 18, 1008-1017.

39. Hupert, M. L.; Guy, W. J.; Llopis, S. D.; Shadpour, H.; Rani, S.; Nikitopoulos, D. E.; Soper, S. A. Evaluation of Micromilled Metal Mold Masters for the Replication of Microchip Electrophoresis Devices. *Microfluid. Nanofluid.* 2007, 3, 1-11.

40. Adams, A. A.; Okagbare, P. I.; Feng, J.; Hupert, M. L.; Patterson, D.; Gottert, J.; McCarley, R. L.; Nikitopoulos, D.; Murphy, M. C.; Soper, S. A. Highly Efficient Circulating Tumor Cell Isolation from Whole Blood and Label-Free Enumeration Using Polymer-Based Microfluidics with an Integrated Conductivity Sensor. *J. Am. Chem. Soc.* 2008, 130, 8633-8641.

41. Wei, S.; Vaidya, B.; Patel, A. B.; Soper, S. A.; McCarley, R. L. Photochemically Patterned Poly(Methyl Methacrylate) Surfaces Used in the Fabrication of Microanalytical Devices. *J. Phys. Chem. B* 2005, 109, 16988-16996.

42. Adamski, M. G.; Li, Y.; Wagner, E.; Yu, H.; Seales-Bailey, C.; Soper, S. A.; Murphy, M.; Baird, A. E. Next-Generation Qpcr for the High-Throughput Measurement of Gene Expression in Multiple Leukocyte Subsets. *J Biomol Screen* 2013.

43. Jackson, J. M.; Witek, M. A.; Hupert, M. L.; Brady, C.; Pullagurla, S.; Kamande, J.; Aufforth, R. D.; Tignanelli, C. J.; Torphy, R. J.; Yeh, J. J.; Soper, S. A. Uv Activation of Polymeric High Aspect Ratio Microstructures: Ramifications in Antibody Surface Loading for Circulating Tumor Cell Selection. *Lab on a Chip* 2014.

44. Kamande, J. W.; Hupert, M. L.; Witek, M. A.; Wang, H.; Torphy, R. J.; Dharmasiri, U.; Njoroge, S. K.; Jackson, J. M.; Aufforth, R. D.; Snavely, A.; Yeh, J. J.; Soper, S. A. Modular Microsystem for the Isolation, Enumeration, and Phenotyping of Circulating Tumor Cells in Patients with Pancreatic Cancer. *Analytical Chemistry* 2013.

45. Holmberg, K.; Hyden, H. Methods of Immobilization of Proteins to Polymethylmethacrylate. *Prep. Biochem.* 1985, 15, 309-19.

46. Patel, S.; Thakar, R. G.; Wong, J.; McLeod, S. D.; Li, S. Control of Cell Adhesion on Poly(Methyl Methacrylate). *Biomaterials* 2006, 27, 2890-2897.

47. Holmberg, K.; Hyden, H. Methods of Immobilization of Proteins to Polymethylmethacrylate. *Preparative biochemistry* 1985, 15, 309-19.

48. Kirillova, M. V.; Kirillov, A. M.; Kuznetsov, M. L.; Silva, J. A. L.; da Silva, J. J. R. F.; Pombeiro, A. J. L. Alkanes to Carboxylic Acids in Aqueous Medium: Metal-Free and Metal-Promoted Highly Efficient and Mild Conversions. *Chem Commun* 2009, 2353-2355.

49. Soper, S. A.; Battle, K.; Jackson, J. M.; Witek, M. A.; Hupert, M.; Hunsucker, S.; Armistead, P. Solid-Phase Extraction and Purification of Membrane Proteins Using a Uv-Modified Pmma Microfluidic Bioaffinity [Small Micro]Spe Device. *Analyst* 2014.

50. Murthy, S. K.; Sin, A.; Tompkins, R. G.; Toner, M. Effect of Flow and Surface Conditions on Human Lymphocyte Isolation Using Microfluidic Chambers. *Langmuir* 2004, 20, 11649-11655.

51. Beck, M.; Brockhuis, S.; van, d. V. N.; Breukers, C.; Greve, J.; Terstappen, L. W. M. M. On-Chip Sample Preparation by Controlled Release of Antibodies for Simple Cd4 Counting. *Lab Chip* 2012, 12, 167-173.

52. Davis, K. A.; Abrams, B.; Iyer, S. B.; Hoffman, R. A.; Bishop, J. E. Determination of Cd4 Antigen Density on Cells: Role of Antibody Valency, Avidity, Clones, and Conjugation. *Cytometry* 1998, 33, 197-205.

53. Denny, T. N.; Stein, D.; Mui, T.; Scolpino, A.; Holland, B. Quantitative Determination of Surface Antibody Binding Capacities of Immune Subsets Present in Peripheral Blood of Healthy Adult Donors. *Cytometry* 1996, 26, 265-274.

54. Toner, M.; Irimia, D. Blood-on-a-Chip. *Annual Review of Biomedical Engineering* 2005, 7, 77-103.

55. Chang, K.-C.; Hammer, D. A. The Forward Rate of Binding of Surface-Tethered Reactants: Effect of Relative Motion between Two Surfaces. *Biophysical journal* 1999, 76, 1280-1292.

56. Egerton, M.; Scollay, R.; Shortman, K. Kinetics of Mature T-Cell Development in the Thymus. *Proceedings of the National Academy of Sciences* 1990, 87, 2579-2582.

57. Hultin, L. E.; Matud, J. L.; Giorgi, J. V. Quantitation of Cd38 Activation Antigen Expression on Cd8+ T Cells in Hiv-1 Infection Using Cd4 Expression on Cd4+ T Lymphocytes as a Biological Calibrator. *Cytometry* 1998, 33, 123-132.

58. Lee, B.; Sharron, M.; Montaner, L. J.; Weissman, D.; Doms, R. W. Quantification of Cd4, Ccr5, and Cxcr4 Levels on Lymphocyte Subsets, Dendritic Cells, and Differentially Conditioned Monocyte-Derived Macrophages. *Proc. Natl. Acad. Sci. U. S. A.* 1999, 96, 5215-5220.

59. Bainton, D. F.; Ullyot, J. L.; Farquhar, M. G. The Development of Neutrophilic Polymorphonuclear Leukocytes in Human Bone Marrow: Origin and Content of Azurophil and Specific Granules. *The Journal of Experimental Medicine* 1971, 134, 907-934.

60. Srikrishna, G. S100a8 and S100a9: New Insights into Their Roles in Malignancy. *J. Innate Immun.* 2012, 4, 31-40.

61. Brennan, R. M.; Petersen, J.; Neller, M. A.; Miles, J. J.; Burrows, J. M.; Smith, C.; McCluskey, J.; Khanna, R.; Rossjohn, J.; Burrows, S. R. The Impact of a Large and Frequent Deletion in the Human Tcr B Locus on Antiviral Immunity. *J. Immunol.* 2012, 188, 2742-2748.

62. Marrack, P.; Rubtsova, K.; Scott-Browne, J.; Kappler, J. W. T Cell Receptor Specificity for Major Histocompatibility Complex Proteins. *Curr. Opin. Immunol.* 2008, 20, 203-207.

63. Murphy, P. M.; Tiffany, H. L.; McDermott, D.; Ahuja, S. K. Sequence and Organization of the Human N-Formyl Peptide Receptor-Encoding Gene. *Gene* 1993, 133, 285-90.

64. Devosse, T.; Guillabert, A.; D'Haene, N.; Berton, A.; De Nadai, P.; Noel, S.; Brait, M.; Franssen, J.-D.; Sozzani, S.; Salmon, I.; Parmentier, M. Formyl Peptide Receptor-Like 2 Is Expressed and Functional in Plasmacytoid Dendritic Cells, Tissue-Specific Macrophage Subpopulations, and Eosinophils. *J. Immunol.* 2009, 182, 4974-4984.

65. Tunnacliffe, A.; Kefford, R.; Milstein, C.; Forster, A.; Rabbitts, T. H. Sequence and Evolution of the Human T-Cell Antigen Receptor B-Chain Genes. *Proc. Natl. Acad. Sci. U. S. A.* 1985, 82, 5068-72.

66. Reiter, M.; Kirchner, B.; Mueller, H.; Holzhauer, C.; Mann, W.; Pfaffl, M. W. Quantification Noise in Single Cell Experiments. *Nucleic Acids Res.* 2011, 39, e124.

67. Puellmann, K.; Kaminski, W. E.; Vogel, M.; Nebe, C. T.; Schroeder, J.; Wolf, H.; Beham, A. W. A Variable Immunoreceptor in a Subpopulation of Human Neutrophils. *Chir. Forum Exp. Klin. Forsch.* 2007, 247-249.

68. Whitney, A. R.; Diehn, M.; Popper, S. J.; Alizadeh, A. A.; Boldrick, J. C.; Relman, D. A.; Brown, P. O. Individuality and Variation in Gene Expression Patterns in Human Blood. *Proc. Natl. Acad. Sci. U. S. A.* 2003, 100, 1896-1901.

69. Eggleton, P.; Gargan, R.; Fisher, D. Rapid Method for the Isolation of Neutrophils in High Yield without the Use of Dextran or Density Gradient Polymers. *J Immunol Methods* 1989, 121, 105-13.

70. Watson, F.; Robinson, J. J.; Edwards, S. W. Neutrophil Function in Whole Blood and after Purification: Changes in Receptor Expression, Oxidase Activity and Responsiveness to Cytokines. *Biosci. Rep.* 1992, 12, 123-33.

CHAPTER 3. SOLID PHASE EXTRACTION OF RNA FROM ISOLATED T-CELLS AND NEUTROPHILS USING COMBINED MICROFLUIDIC MODULES

3.1 Introduction

Advancements in the field of genomics have allowed better understanding of gene expression changes and provide accurate means of disease diagnosis by potential biomarker measurement.[1] Genomic profiling of peripheral blood samples could be of great value in identifying biomarkers for various complex diseases, including stroke, as evident from the studies which utilized white blood cells to identify discrete patterns of expression associated with the disease states.[2, 3] Therefore, growing interest continues in isolation of pure population of relevant white blood cell subsets and extraction of nucleic acids for applications in clinical diagnostics and forensics. In addition to that, development of small footprint, self-contained, disposable, fast, and inexpensive devices for cell isolation and nucleic acid isolation play a key role in the point-of-care testing specially in resource-poor settings. Greatest areas of potential impact for these miniaturized devices is in molecular diagnostics to facilitate fast diagnostics, low cost, operation by minimally trained personnel, and low contamination risk.

Some of the previously reported cell separation strategies include density gradient methods,[4] magnetic activated cell separation (MACS),[5] micro-fabricated fluorescence activated cell sorting,[6] ultrasonic particle separation,[7] mammalian cells sorted by optical force switching,[8] cell separation by dielectrophoresis chip.[9] However some of the limitations associated with aforementioned techniques are alteration in immunophenotype of leukocytes due to excessive manipulation of sample such as repeating pipetting or centrifugation. Cells are prone to apoptosis as they are very sensitive to the changes in the environment.[10] Although FACS and MACS offer high throughput, however high cost and complexity of these systems limits their implementation

in a clinical setting. Strong polarization charges in non-uniform electric field may cause damage to the cells in dielectrophoresis methods which limits its wide clinical use.

A suitable sample preparation for molecular diagnostics consists of an efficient target recovery, from a biologically relevant sample, preserving the integrity of the nucleic acid (NA) molecules at the same time. Nucleic acid-based assays have been successfully implemented in recent years in many fields exploiting their rapid and accurate analysis (e.g., medical diagnostics, forensics, environmental analysis, and biodefense).[11-14] These assays typically involve cell lysis to release the small amount of NAs (DNA/RNA) present in the sample, purification of these moieties followed by amplification to achieve detectable concentration, and detection using hybridization or electrophoretic methods.[15] The sensitivity of these analyses, among other things depends on the purity and yield of NA obtained that can be transferred into amplification reaction.

Earlier methods of DNA purification, CsCl gradient extraction method,[16] phenol-chloroform phase separation[17] were replaced by solid phase extraction (SPE) methods wherein analytes are retained on a solid support and are subsequently eluted in a concentrated form,[18] thus eliminating the need for the use of toxic chemicals and lengthy centrifuge times. Most of these methods rely on adsorption of DNA with a solid surface, either via hydrogen bonding or via electrostatic interactions.[19] Commercially available NA binding columns require several centrifugation steps and pipetting. Therefore, transition to micro-domain is more amenable to miniaturization than the traditional extraction processes and the use of microfluidic SPE allows for more rapid and straightforward on-chip sample preparation as demonstrated by Tian *et al.*, who established a capillary-based micro-SPE (iSPE).[20] Microchip-based DNA purification was first demonstrated by Christel *et al*. using pillars created in a microchannel using reactive ion etching to increase the

silica surface area available for DNA adsorption but limited by the complexity of the fabrication procedure.[21] Various techniques of microfluidic SPE involved the use of functionalized microparticles, filters, silica gels and beads, and micro- and nano-engineered surfaces.[22]

Microfluidic extraction systems are mostly designed for DNA sample preparation and relatively less research has been reported on the RNA isolation and specifically using microfluidics. This is due to difficulty in isolation and purification of RNA because of significant chemical and biological lability and instability of RNA when compared to DNA. RNases are extremely active enzymes present in human skin, body fluids, lab surfaces, and environment. RNase contamination makes the isolation of RNA from common clinical and forensic samples challenging. Also, RNA derived from complicated matrix like blood may be contaminated with inhibitors of downstream molecular analyses. Therefore, the choice of RNA purification methods is important for successful isolation of high quality of RNA for consistent performance in downstream applications like reverse transcription RT quantitative PCR (RT-qPCR), microarray analyses.

RNA has multiple advantages over DNA in some applications as a biological target material since it is more closely related to cell's machinery. To carry out a gene expression analysis, RNA must be first isolated and purified from biological source of interest. Detection of RNA and mRNA expression can be used for clinical diagnostics, as the increased/decreased levels of expression of specific genes can be indicative of the disease. These methods are based on the inherently variable mRNA expression from different cell types, producing gene-specific patterns which can be verified by the presence of a unique mRNA expression pattern.[23] However, it is known that, within minutes of collection, peripheral blood gene expression profiles change significantly due to transcript degradation, and these purification processes further introduce

changes in expressed transcripts.[24] The correct interpretation of transcript abundance requires stabilization of the transcriptome at the point of sample collection, through storage and transport, in order for gene expression to be detected in a reproducible manner.[25] Traditional assays involve multiple steps involving sample transfer which can cause the degradation of the sample by exposure to outside environment. Microchip based extraction hence offers advantages by providing a contamination free environment because material is isolated in enclosed architectures with minute amount of the sample needed. Examples of microfluidic chips for the SPE of RNA using silica beads as a solid phase, chitosan-coated silica, porous polymer monolith have been demonstrated.[26-29]

To address some of the issues of the aforementioned methods and their applicability for the purification of NAs in clinical settings such as 1) cost of device fabrication and substrate material required for the device; (2) lengthy and labor intensive procedures for SPE bed preparation and; (3) sample recovery, we have demonstrated the use of photoactivated polycarbonate (PPC) devices containing micropillars. SPE active surface on these PC devices is produced by simple UV-photoactivation protocol which generates high density of carboxylic acids on the PC surface that serves as the affinity surface for NA.[30, 31] The advantages of this method include: (1) inexpensive device fabrication through micro-replication into PC; (2) quick and simple bed activation procedure using UV irradiation; (3) scalability of the fabrication process to high volume mass production; (4) versatility – various NAs can be selectively purified by using the proper composition of immobilization buffer and; (5) very high target recoveries with good removal of endogenous proteins. [30-32]

In this study, we present a reliable and fast method using combined microfluidic modules that serve purpose of cell isolation, cell lysis and TRNA isolation. The strategy employed here is

to capture target cells on cell isolation module and following lysis on microchip to isolate RNA using SPE module. RNA extracted using this method was reverse transcribed and resulting cDNA was amplified via PCR. Incorporation of cell isolation, lysis and RNA purification steps into one platform has a potential for development of an on-site setting and reduces the potential for contamination. These integrated modules can be adapted for automation to enable high throughput and can be implemented into microfluidic systems that interface with downstream components.

3.2 Materials and Methods

3.2.1 Surface Characterization Techniques

Surface characterization studies were performed on clean planar polymer substrates. For XPS measurements, C 1s and O 1s photoelectron signals were acquired using an Axis Ultra DLD X-ray photoelectron spectrometer (Kratos Analytical) under ultra-high vacuum conditions (10^{-8} to 10^{-10} Torr) with a monochromatic Al Kα X-ray source, 20 eV pass energy, 370 s acquisition time, 1,600 ms dwell time, and 20° electron take-off angle. Given an inelastic mean free path of 3-4 nm, ~95% of the resultant signal originated 9-12 nm from the surface. ATR-FTIR spectra were scanned from 375-4000 cm^{-1} using an ALPHA FTIR spectrometer and a Platinum ATR module (Bruker Optics).

3.2.2 Chemicals and Reagents

Polyethylene glycol (PEG, Mw 8000), NaCl, ethanol, 2-propanol, were all purchased from Sigma Aldrich. Ethanol was purchased from Fisher Scientific (Houston, TX). The lysis solution, DNase used was from GenElute mammalian genomic RNA Miniprep Kit (Sigma-Aldrich, St. Louis, MO) and used as received. A stock solution of immobilization buffer (IB) was prepared with nuclease-free water to yield an optimal buffer composition of 0.5 M NaCl, 5% PEG, 63%

EtOH. RNA containing samples were suspended in the IB and processed using the SPE microchip as described below. All the primers used in this work were purchased from Integrated DNA Technologies, Coralville, IA.

3.2.3 Design and Fabrication of Microfluidic Modules

The microfluidic device fabrication involved three major steps: (1) Mold insert fabrication using a micro-milling machine (Kern MMP, Kern Micro- and Feinwerktechnik, Murnau-Westried, Germany); (2) hot embossing of the microfluidic structures (HEX02, JenOptik Mikrotechnik, Jena, Germany) on 3 mm thick PMMA/PC substrates (Goodfellow, United Kingdom); and (3) post-processing of the microfluidic device including drilling of sample reservoirs, UV modification of the immobilization beds and cover plate assembly.

The microfluidic devices for cell isolation were hot embossed into cycloolefin copolymer (COC) substrates, via micro replication from a metal mold master as reported earlier.[33] The Z-configuration device, consisted of 64 curvilinear channels (see Figure 3.3A) that were 9,000 x 25 x 80 µm (l x w x h) with a center-to-center spacing of 200 µm. Each isolation bed's surface area was 132.3 mm^2. Addressing each bed required four bifurcations, with an additional two bifurcations for the four individual isolation units. All four capture beds shared a common inlet port, with different outlet ports for each capture bed (Figure 3.3 B).

SPE module for isolation and purification of RNA, was embossed into PC substrate in a single step. This device consisted of six, 24 mm long and 1.4 mm wide channels with microposts. The channel (capture bed) dimensions were 100 µm height, 100 µm diameter, a 50 µm spacing. The extraction bed consisted of series of ~3600 microposts (see Figure 3.2 C, D) which provided a high surface area allowing high mass load of RNA. Each affinity bed had a surface area of 110 mm^2 and volume 260 nL.

3.2.4 Assembly of the Microfluidic Modules

For the device assembly, both COC and PC, inlet and outlet reservoirs were drilled (d=0.85 mm) in both microchip devices, followed by cleaning and then drying at 60ºC. A 250 µm thick coverslips and devices were modified for 15 min in a home built UV chamber equipped with a low pressure Hg lamp (1.5cm from light source, 22 mW/cm^2 measured at 254 nm) to generate carboxylic acid scaffolds on microchannel surfaces.[34] In order to enclose the microfluidic structures, thermal fusion bonding was performed at 132˚C and 144^{o}C (~25 min) for UV-modified COC and PC microdevices, respectively. PEEK tubing, IDEX Health & Science LLC (175/335 µm id/od) was inserted into the drilled reservoirs and glued with epoxy resin to facilitate sealed junction. Constant flow programmable syringe pump (Harvard Instruments) with attached syringe introduced fluids into the device.

3.2.5 Cell Isolation on COC Microfluidic Devices

Following device assembly, Ab immobilization was carried out in two-step process. In the first step, 50 mg/mL EDC and 5 mg/mL NHS in 100 mM MES (pH= 4.8) was introduced into the freshly fabricated device and incubated for 15 min at room temperature to obtain the succinimidyl ester intermediate. EDC/NHS solution was then removed from the device by flushing with PBS, and a 15 µL aliquot of 0.5 mg/mL (unless stated otherwise) mouse anti-human CD4 (T-cell isolation) or mouse anti-human CD66b (neutrophil isolation) was introduced into the device and incubated overnight at 4˚C. The capture bed was then rinsed with 1 mL PBS (pH = 7.4) to remove unreacted molecules.

Whole blood samples were obtained from anonymous healthy donors at UNC Cancer Hospital Blood Bank in accordance with the UNC Institutional Review Board (IRB) procedures. Peripheral blood samples were collected by venipuncture technique in Vacutainer tubes

containing EDTA (K_3) 7.5%, 0.06 mL, (*Tyco* Health Care). Collected samples were processed within 4 h.

The microfluidic device was connected to the syringe pump with PEEK tubing via a luer lock tuberculin syringe connector (Hamilton, Reno, NV). A precapture rinse of the chip was performed using PBS/0.5% BSA at 4 mm/s. 200 µL of whole blood was infused through the common inlet, at 3.8 µL/min which yielded nominal linear velocities of 2 mm/s in the isolation bed. A post capture rinse was performed at 4 mm/s with 100-200 µL PBS/0.5% BSA to remove blood and unbounded cells.

3.2.6 Cell Lysis

T-cells and neutrophils isolated in the bifurcated COC chip. Numbers of isolated cells were enumerated using bright field microscopy. 200 µl of lysis solution was then introduced through the common inlet of the bifurcated device and the lysate is collected into four different microfuge tubes from the outlets. The cell lysate was then suspended in the appropriate IB ready to be introduced to the SPE module.

3.2.7 Operation of Microchip Solid Phase Extraction

The extraction procedure consisted of load, wash, and elution steps. In the load step a cocktail of 50 µL of IB buffer (0.5 M NaCl, 5% PEG, 63 % Ethanol) , 50 µl cell lysate (T-cells/neutrophils) and 170 µl of ethanol (63%), was infused through the SPE bed using a programmable syringe pump at 5 µL/min followed by a 200 µL of wash buffer (85% ethanol) at 5 µL/min. This washing step ensures complete removal of any proteins or possible PCR inhibitors that were adsorbed onto the SPE bed during the load step. Air was drawn through the other end of the SPE bed to remove ethanol and dry the bed. Ethanol removal is critical, because residual amounts of ethanol may serve as a PCR inhibitor. Finally, the RNA was eluted with ~20

µL H_2O pumped through the SPE bed at 5 µL/min and was collected from the SPE bed into PCR tubes. Then, isolation of pure RNA was achieved by a secondary enrichment, through enzymatic removal of genomic DNA (DNase treatment), using DNase 1 digestion set (Sigma Aldrich, St. Louis, MO. The DNase cocktail was prepared by addition of DNase I (10% of the total eluted volume) and buffer (10% of the total eluted buffer). After incubation at room temperature for 15 minutes, the same volume of EDTA stop solution was added and the mixture was incubated at 70˚C for 10 minutes. This solution was then used for subsequent reverse transcription and PCR analysis.

3.2.8 Reverse Transcription

After the purification of total RNA (TRNA), using SPE unit, reverse transcription (RT) of RNA was accomplished using a ProtoScript II First Strand cDNA Synthesis Kit (New England BioLabs, Ipswich, MA). Samples were prepared by mixing 10 µL reaction mix, 2 µL poly-T primer, 2 µL enzyme (no enzyme, 2 µL of water for RT-) and 6 µL of TRNA. The samples were then incubated at 42˚C for 1 h and heated to 80˚C for 5 min to deactivate the RT enzyme.

3.2.9 Polymerase Chain Reactions (PCR)

PCR was performed with synthesized cDNA in a total volume of 20 µL using Taq 2X Master Mix (New England Biolabs, Ipswich, MA). PCR cocktails consisted of 2 µL of primers mix (final concentration 500 nM), 10 µL Taq 2X Master Mix, 6 µL nuclease free water and 2 µL cDNA. PCR was carried out in a commercial thermal cycler (MJ Research Inc., Waltham, MA) with following steps: an initial denaturation at 94˚C for 2.5 min followed by 40 cycles of denaturation at 94˚C for 15 s, annealing for 30 s at 63˚C for GAPDH primers, 55˚C for S100A9 and GUSB primers, 58˚C for TCRB primers, and 54˚C for FPR1 primers, and elongation at 72˚C

for 30 s. A final extension at 72˚C for 7 min was followed by a cooling step at 4˚C. The list of primers used is tabulated below.

Table 3.1 List of primers used for amplification of cDNA.

Gene	Forward primer (5'- 3')	Reverse primer (3'- 5')	Amplicon length (bp)
GAPDH	CTTTTGCGTCGCCAGCCGAG	TGACCTTGGCCAGGGGTGCT	528
S100A9	CTCGGCTTTGACAGAGTGCAAGAC	TCCCCGAGGCCTGGCTTATGG	357
TCRB	GTTTTCTTTCAGACTGTGGCTTC	CACGGCATACAAGGTGGC	107
FPR1	TTTGCCTGTAACGCCAC	ATGCTCTATGTCTTCATGGG	155
GUSB	TCCAGCTTCAATGACATCAG	AGCACCACTCTTGTGCG	122

3.2.10 Gel Electrophoresis

PCR products were electrophoresed at 8.3 V/cm in 1X TBE (Tris–boric acid/EDTA) (Bio-Rad Laboratories) on a 4% agarose gel with ethidium bromide (Lonza). Amplicons were indexed against a DNA sizing ladder 50–766 bp (New England Biolabs, Ipswich, MA). Images were collected using a Logic Gel imaging system (Eastman Kodak Company).

3.2.11 Fluorescence Spectroscopy

Following the SPE protocol described above with known total RNA concentrations of 50, 20, 4, 0.5, 0.3, 0.2 ng, quantification was done with RiboGreen Reagent (excitation 480 nm/ emission 520 nm, Molecular Probes). The emission spectra were acquired using FLUOROLOG-3 spectrofluorometer (Jobin Yvon Inc., Edison, NJ) equipped with a 450 W xenon lamp and a cooled Hamamatsu R928 photomultiplier (Bridgewater, NJ) operated at 900 V in a photon163 counting mode with the resulting emission spectra used for determining the RNA concentration in the samples. A calibration curve was constructed using RiboGreen stained RNAs of concentrations ranging from 1 ng/ µL to 1 µg/µL for RNA standards and correlation coefficient for RNA standards were determined.

3.3 Results and Discussion

3.3.1 Surface Characterization of UV Activated Polycarbonate

To identify the photo-products generated on the UV modified PC surface, we employed both XPS and ATR-FTIR spectroscopies. After UV-activation, a 0.33-fold increase in the O/C ratio was observed due to the appearance of several oxidized carbon species, which were deconvoluted based on previously published functional group binding energies.[35-37]

Pristine PC's C 1s spectrum was deconvoluted into the following peaks: (1) 284.5 eV aromatic C-C and C-H; (2) 285.0 eV aliphatic C-C and C-H; (3) 290.4 eV carbonate C=O; (4) 291.8 π-π^* shake-up satellite; and (5) 286.2 eV aromatic C-O. The ratio of peak areas of C 1s (1):(2):(3):(5) was 8.42:2.85:1.00:1.99, and matches reasonably well with the theoretical ratio of 10:3:1:2.

UV modified PC spectra were deconvoluted by calibrating the C 1s (2) peak to 285.0 eV, fixing the C 1s (3) and C 1s (4) peaks at their pristine positions, adjusting the C 1s (1) peak within ±0.2 eV of its pristine position, and adding C 1s (5), C 1s (6), and C 1s (7) peaks corresponding to phenols, alcohols, or ethers, aldehyde or ketone carbonyls, and ester or carboxylic acid carbonyls, respectively.

ATR-FTIR peak areas indicated the presence of several new oxidized functionalities, such as an increase of 0.5 au·cm^{-1} and 6.3 au·cm^{-1} for the C=O (1650-1850 cm^{-1}) and O-H (3200-3700) regions, respectively. More specifically, using the work of Rivaton, *et al.*, we were able to identify several photo-products shown in Figure 3.1 along with their corresponding carbonyl stretching energies, which are matched to the pristine-subtracted UV-PC.

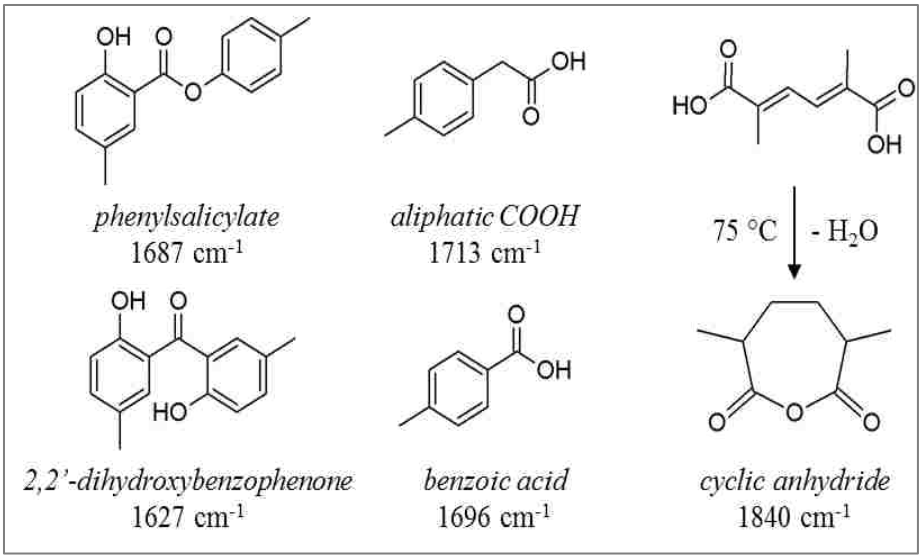

Figure 3.1 Structures and carbonyl stretching frequencies of PC's photo-Fries rearrangement and photo-oxidation products. Reproduced with permission from [39].

Despite being convoluted, we were able to identify several peaks in addition to the pristine carbonate stretch (1767 cm^{-1}) that were generated by UV-activation. The photo-Fries rearrangement products, 2,2'-dihydroxybenzophenone (1627 cm^{-1}) and phenylsalicylate (1687 cm^{-1}), were apparent along with their associated O-H ring substitutions (1617 and 1585 cm^{-1}) and H-bonded carbonate groups (1748 cm^{-1}).[35] The constant level of atomic oxygen and ozone in the UV modification chamber may have also led to photo-oxidation of the gem dimethyl side chains, producing aliphatic carboxylic acids (1713 cm^{-1}) and benzoic acids (1696 cm^{-1}). There was also a very small peak at 1840 cm^{-1}, which could have originated from ring scissions producing aliphatic carboxylic acids that can rearrange to form cyclic anhydrides at the elevated temperatures present in our system. Rivaton, *et al*. observed this rearrangement from 45°C to 75°C , and these conditions occurred within the modification chamber, which was heated to 50°C after a 15 min UV exposure time.[35] However, this peak is small enough that it could be an artifact of background subtraction.

3.3.2 Operation of Serially-connected Micromodules

The combined fluidic system presented here consists of two task-specific modules connected in series to facilitate leukocyte subset isolation, cell lysis and RNA isolation. As demonstrated recently by Wang *et. al.*,[38] the modular design approach offers some appealing advantages compared to monolithic designs, including: (1) flexibility in materials used for designing individual modules to optimize performance of each processing step imposed on that module; (2) the ability to reconfigure the assay format without requiring re-engineering; (3) the ability to use different fabrication schemes optimized for each module; and (4) high production yields of integrated systems, because each module is fabricated and tested separately. Modules fabricated in different thermoplastic materials with desired structures can be custom-designed.

We have demonstrated COC's superb ability to generate COOH functionalities upon exposure to UV light.[39] Probability of COOH functional group generation on COC microchannel surfaces do not decrease with the increase in microchannel's aspect ratio unlike PMMA. Furthermore, COC microdevices were less susceptible to photo-fragmentation upon irradiation. These factors are critical for accessibility and covalent attachment of antibodies to microchannel surfaces via carboxylic acid (COOH) scaffolds leading to efficient attachment of antibody and therefore efficient cell isolation. The cell isolation data shown in chapter 2 clearly indicates that COC devices exhibited superior performance compared to PMMA devices. Chemically modified Z-configuration devices immobilized with anti-CD4 and anti-CD66b yielded 2565 ±1194 T-cells and 2949 ±901 neutrophils respectively (Figure 3.2 A, B).

SPE module was constructed using polycarbonate (PC) due to its unique characteristic to allow the isolation and purification of nucleic acids.[30, 31] Generation of polymer phenyl salicylates, hydroxybenzophenones and a wide range of carbonyl/carboxyl-containing groups

upon UV irradiation (254-300nm) of PC can serve as a capture medium for the isolation, purification and preconcentration of a wide range of molecular weight-sized NA's present in complex biological samples.

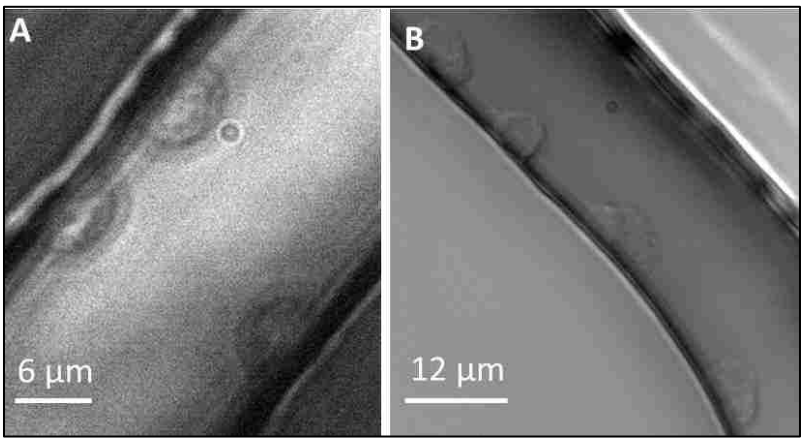

Figure 3.2 Bright field images of (A) T-cells (60X) and (B) neutrophils (40X) captured within the COC microfluidic device immobilized with CD4 and CD66b antibodies respectively.

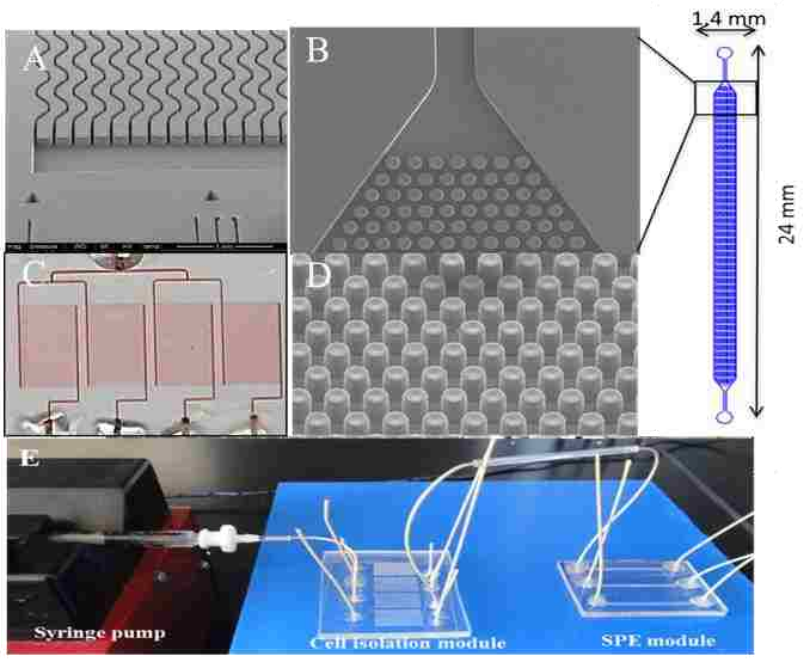

Figure 3.3 (A) SEM image of isolation bed of Z-configuration device with dimensions 25 µm wide and 80 µm deep (B) Photograph of Z-configuration device filled with red dye (C), (D) SEM images of SPE immobilization capture bed, post diameter =100 µm, center-to-center post spacing =50 µm (E) Picture showing the connected micromodules.

Two modules were connected in series using a glass connector (see Figure 3.3 E). T-cells and neutrophils captured on individual cell selection units were lysed by infusing cocktail solution containing 50 µl IB, 50 µl lysis solution, 170 µl EtOH through leukocyte isolation module. The lysate is directed to the SPE module on which RNA is purified and eluted with water for cDNA synthesis and further amplification.

3.3.3 DNase Treatment of the Lysate.

A potential problem with RT-PCR is DNA contamination in RNA sample. DNA removal is therefore critical especially for RT-PCR applications since DNA can serve as a template during the PCR resulting in false positives, background, etc. Therefore, DNase treatment was performed on the RNA isolated from SPE, prior to RT for cDNA synthesis. "Minus RT controls" (without RT enzyme) were performed to identify erroneous signal due to genomic DNA contamination.

To demonstrate the effectiveness of SPE in removing the contaminated DNA, we chose to perform DNase treatment on TRNA that was isolated from MCF-7 cells, a human breast cancer cell line. Following cell lysis and considering 10 pg of TRNA per cell, 2 µl of lysate containing 8,000 cells *i.e*. 80 ng of TRNA was used for SPE. A cocktail mixture of 2 µl of this lysate, 50 µl IB, 48 µl nuclease-free water, 170 µl of ethanol was infused through SPE bed and the TRNA was eluted with 20 µl water. Following elution from SPE bed, DNase treatment for 15 minutes, an RT reaction was performed. cDNA was then PCR amplified using *GAPDH* and *GUSB* primers.

To eliminate amplification of gDNA, PCR primers can be designed to span introns or bridge an exon-exon junction only in cDNA. Primers for *GAPDH* were designed that way, therefore, PCR will not amplify gDNA and thus, any possible DNA contamination could not be identified. *GUSB* primers, however, were not spanning introns and the absence of amplicons clearly

indicates the lack of DNA contamination. PCR products separated on gel for *GUSB* gene (Figure 3.4) indicate that DNase treatment was shown to efficiently degrade contaminating gDNA, since no PCR product was amplified from samples that were DNase-treated but not reverse-transcribed (minus RT controls), whereas the DNase treated and reverse transcribed mRNA show the products of 528 bp and 122 bp for *GAPDH* and *GUSB*, respectively.

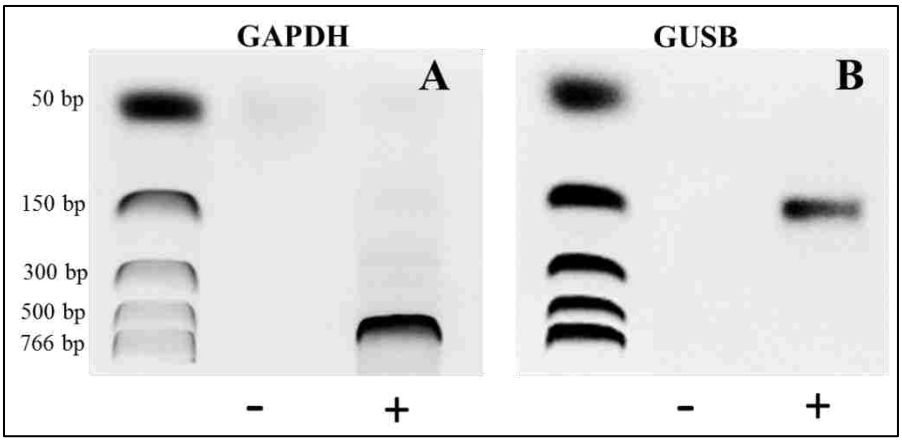

Figure 3.4 Gel electrophoresis images showing DNase treatment after SPE.RNA from MCF-7 cells was DNase treated for 15 min, reverse transcribed and PCR was performed on cDNA with (A) GAPDH primers and (B) GUSB primers The absence of product for the negative RT controls indicates the absence of DNA contamination.

3.3.4 Evaluation of RNA Extraction Efficiency

An efficient cell isolation method will not guarantee successful molecular analysis. In order to perform an analytical assay, preconcentration of target (i.e., DNA or RNA) must be accomplished. Microfluidic chips are especially attractive for cellular-based assays because many of the sample processing steps can be integrated into a single module, minimizing the dilution of intracellular components following cell lysis.

Recovery of TRNA after purification on SPE bed was evaluated by examining the mass of TRNA before and after purification on the microchip. Samples containing TRNA in a mass range of 0.5–180 ng were examined. RNA concentration was determined by staining with

RiboGreen (excitation 500 nm/ emission ~525 nm, Molecular Probes). Calibration curves were constructed using concentrations ranging from 5 pg/ µL to 1000 pg/µL for RNA standards.

After TRNA elution, as judged by fluorescence, the efficiency of recovery for 5 ng TRNA was estimated to be 57% (Figure 3.5 C). Based on the TRNA mass immobilized on chip surface and the available surface area of the capture bed, the surface loading density of TRNA was determined to be 2.6 ng/cm^2. It was observed that the efficiency of recovery decreased as the mass load of TRNA introduced on a SPE bed increased. Efficiency of the recovery was less than 10% for aliquots containing 180 ng of TRNA. This indicates that the amount of TRNA introduced onto bed exceeded the load capacity of the capture bed (i.e. available –COOH sites). The amount of TRNA captured on previously reported 96-well PPC chip was determined to be 582 ± 286 ng/cm^2.[30] This significant difference in the surface load can be explained by use of a different architecture chip. In previous work, SPE bed contained 3,800 20 µm diameter posts with 20 µm spacing and 50 µm depth and surface area of 28.4 mm^2. Such geometry provides advantage for more efficient solid phase extraction because provides higher density of posts and reduced inter-post spacing, providing shorter diffusional distance for RNA to reach surface.

As we could not determine the efficiency of the purification process for samples containing less than 5 ng of TRNA, most likely due to instability of the RNA, we chose to test if TRNA is present in the effluent of these samples by performing RT-PCR. In a separate experiment, a range of different masses of TRNA (0.2-50 ng corresponding to ~10-2,500 cells) was introduced on chip and purified. Immediately after purification, RT was performed with collected TRNA, followed by amplification of *GAPDH* gene. Products were separated and these results are presented in Figure 3.5A.

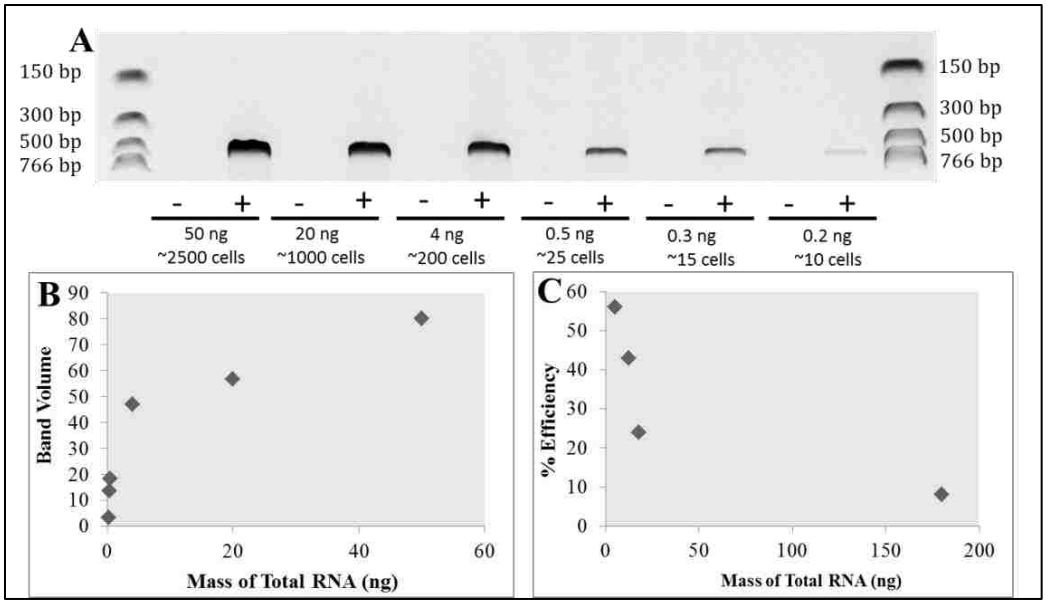

Figure 3.5 SPE was performed on commercial Jurkat T-cell TRNA and isolated RNA was analyzed via RT-PCR with GAPDH PCR primers. (A) Fluorescence image of ethidium-stained 4% agarose gel showing decrease in RNA isolated with a decrease in total RNA input. (B) Band volumes of product bands in part A were quantified using ImageQuant. (C) Efficiency of RNA isolation for different input masses of TRNA evaluated using the RiboGreen assay.

The products were observed for all tested effluents after SPE purification. Even effluent from purification of 0.2 ng of TRNA was successfully amplified, suggesting that purification can be efficient for minute amount of sample. The integrated intensity of the amplicon bands from Figure 3.5A was plotted vs amount of TRNA introduced on SPE bed. The data show linearity for lowest mass loads of TRNA while saturation of the signal on the gel is observed for amplicons generated from 4-50ng TRNA mass load. Even though the SPE process is less efficient for these amounts of TRNA, it can still purify enough material for gene expression analysis in RT-PCR. It is clear, that for a given sample and immobilization buffer, the RNA recovery efficiency will depend on the extraction bed characteristics, including the active surface area and the inter-post distance and post layout.

3.3.5 RT-PCR of RNA Extracted from T-cells and Neutrophils

In previous work we demonstrated that the total number of isolated cells from 50μL blood using the same microfluidic device as reported herein ranged from 500 to 2,000 CD4+ T-cells and CD66b+ neutrophils. We increased blood volume processed to 200 μL to increase the load of isolated cells. If at least 4 times more cells will be isolated, therefore, we expected to obtain between 20 and 80 ng TRNA (1-4 ng of mRNA), which should secure enough material after SPE purification for cDNA synthesis and gene expression analysis. T-cells and neutrophils were isolated from the same blood sample and because of the high purity (94±3%) of isolated fractions, cell lysis was performed directly on chip followed by SPE and RT-PCR analysis in thermocycler. Figure 3.6 presents agarose gel image showing amplicons from amplified *S100A9* and *FPR1* gene. Presence of amplicon products after RT-PCR indicates that high quality TRNA (mRNA) was obtained during processing on integrated cell isolation and SPE unit.

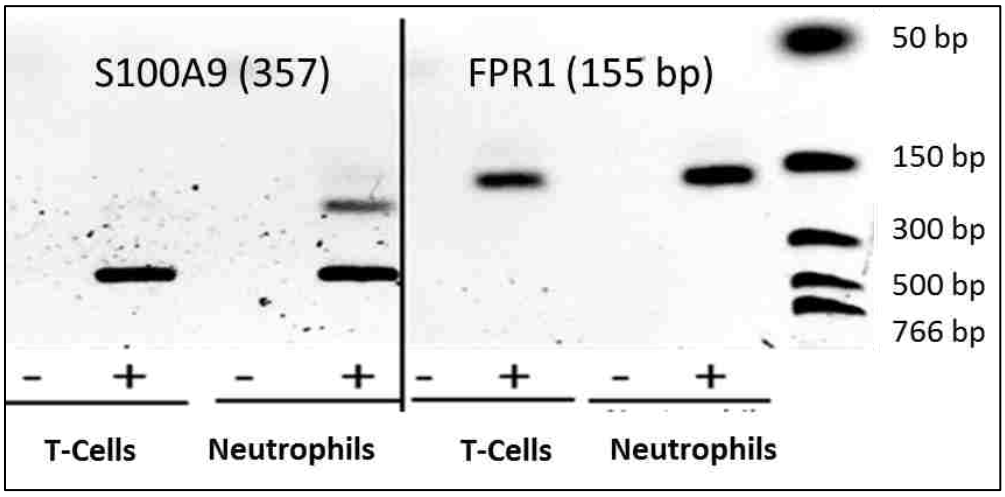

Figure 3.6 Fluorescence images of ethidium-stained 4% agarose gels showing RT-PCR products of TRNA captured from CD4+ T-Cells or neutrophils isolated from 100 μl whole blood. RNA was captured on SPE bed, and reverse transcription was performed. PCR was run with primers targeting *S100A9* and *FPR1* genes. Negative RT controls were performed without RT enzyme.

We have previously demonstrated high quality of TRNA following SPE microchip purification.[30] We assessed integrity of TRNA by monitoring the electrophoretic band pattern for

rRNAs. This method relies on the assumption that rRNA quality and quantity reflect that of the underlying mRNA population.[31] The rRNA species used for this assessment included the 18S and 28S rRNAs for mammalian samples. Ratios of these band intensities of ~2 were indicative of intact TRNA, while for degraded RNA samples, these bands appeared smeared in the electrophoretic bands.

3.4 Conclusions

The use of the PPC-SPE devices along with cell isolation unit is advantageous for RNA purification requiring disposable and one-time use devices for eliminating potential sample contamination and protection of RNA from RNases or other factors that can cause RNA hydrolysis. Chip fabrication method, which use of micro-replication techniques such as hot embossing or injection molding can provide high-volume and low-cost production of these devices which can allow for wide use of these in clinical applications.[33,34]

We demonstrated that RT-PCRs of the SPE purified mRNAs were successful with the amounts of mRNA isolated. The SPE chip showed the ability to provide high quality material from whole cell lysate that could be used for a variety of molecular assays i.e., gene expression analysis, particularly in detection of stroke markers in subpopulations of leukocytes.

The incorporation of SPE protocols into microfluidic formats is very appealing because microfluidics capture occurs in a closed architecture and, therefore, the potential risk of cross-contamination is significantly reduced. By combining NA purification with cell isolation on-chip processing, fully integrated lab-on-a-chip systems can be realized with a concomitant reduction in the time, complexity, and cost of carrying out the analysis.

3.5 References

1. Baird, A. E. Blood Genomics in Human Stroke. *Stroke* 2007, 38, 694-698.

2. Tang, Y.; Lu, A.; Aronow, B. J.; Sharp, F. R. Blood Genomic Responses Differ after Stroke, Seizures, Hypoglycemia, and Hypoxia: Blood Genomic Fingerprints of Disease. *Ann. Neurol.* 2001, 50, 699-707.

3. Tang, Y.; Xu, H.; Du, X.; Lit, L.; Walker, W.; Lu, A.; Ran, R.; Gregg, J. P.; Reilly, M.; Pancioli, A.; Khoury, J. C.; Sauerbeck, L. R.; Carrozzella, J. A.; Spilker, J.; Clark, J.; Wagner, K. R.; Jauch, E. C.; Chang, D. J.; Verro, P.; Broderick, J. P.; Sharp, F. R. Gene Expression in Blood Changes Rapidly in Neutrophils and Monocytes after Ischemic Stroke in Humans: A Microarray Study. *J. Cereb. Blood Flow Metab.* 2006, 26, 1089-1102.

4. English, D.; Andersen, B. R. Single-Step Separation of Red Blood Cells. Granulocytes and Mononuclear Leukocytes on Discontinuous Density Gradients of Ficoll-Hypaque. *J Immunol Methods* 1974, 5, 249-52.

5. Smistrup, K.; Hansen, O.; Bruus, H.; Hansen, M. F. Magnetic Separation in Microfluidic Systems Using Microfabricated Electromagnets-Experiments and Simulations. *J. Magn. Magn. Mater.* 2005, 293, 597-604.

6. Wolff, A.; Perch-Nielsen, I. R.; Larsen, U. D.; Friis, P.; Goranovic, G.; Poulsen, C. R.; Kutter, J. P.; Telleman, P. Integrating Advanced Functionality in a Microfabricated High-Throughput Fluorescent-Activated Cell Sorter. *Lab Chip* 2003, 3, 22-27.

7. Petersson, F.; Nilsson, A.; Holm, C.; Joensson, H.; Laurell, T. Continuous Separation of Lipid Particles from Erythrocytes by Means of Laminar Flow and Acoustic Standing Wave Forces. *Lab Chip* 2005, 5, 20-22.

8. Wang, M. M.; Tu, E.; Raymond, D. E.; Yang, J. M.; Zhang, H.; Hagen, N.; Dees, B.; Mercer, E. M.; Forster, A. H.; Kariv, I.; Marchand, P. J.; Butler, W. F. Microfluidic Sorting of Mammalian Cells by Optical Force Switching. *Nat. Biotechnol.* 2005, 23, 83-87.

9. Huang, Y.; Joo, S.; Duhon, M.; Heller, M.; Wallace, B.; Xu, X. Dielectrophoretic Cell Separation and Gene Expression Profiling on Microelectronic Chip Arrays. *Anal. Chem.* 2002, 74, 3362-3371.

10. Fukuda, S.; Schmid-Schonbein, G. W. Centrifugation Attenuates the Fluid Shear Response of Circulating Leukocytes. *J. Leukocyte Biol.* 2002, 72, 133-139.

11. Ye, N.; Qin, J.; Shi, W.; Liu, X.; Lin, B. Cell-Based High Content Screening Using an Integrated Microfluidic Device. *Lab Chip* 2007, 7, 1696-1704.

12. Liu, P.; Seo, T. S.; Beyor, N.; Shin, K.-J.; Scherer, J. R.; Mathies, R. A. Integrated Portable Polymerase Chain Reaction-Capillary Electrophoresis Microsystem for Rapid Forensic Short Tandem Repeat Typing. *Anal. Chem.* 2007, 79, 1881-1889.

13. Li, H.-F.; Lin, J.-M. Applications of Microfluidic Systems in Environmental Analysis. *Anal Bioanal Chem* 2009, 393, 555-67.

14. Yeung, S. H. I.; Greenspoon, S. A.; McGuckian, A.; Crouse, C. A.; Emrich, C. A.; Ban, J.; Mathies, R. A. Rapid and High-Throughput Forensic Short Tandem Repeat Typing Using a 96-Lane Microfabricated Capillary Array Electrophoresis Microdevice. *J. Forensic Sci.* 2006, 51, 740-747.

15. Hui, W. C.; Yobas, L.; Samper, V. D.; Heng, C.-K.; Liw, S.; Ji, H.; Chen, Y.; Cong, L.; Li, J.; Lim, T. M. Microfluidic Systems for Extracting Nucleic Acids for DNA and Rna Analysis. *Sens. Actuators, A* 2007, 133, 335-339.

16. Carr, S. M.; Griffith, O. M. Rapid Isolation of Animal Mitochondrial DNA in a Small Fixed-Angle Rotor at Ultrahigh Speed. *Biochem. Genet.* 1987, 25, 385-90.

17. Reid, G. Molecular Cloning: A Laboratory Manual, 2nd Edn by J. Sambrook, E. F. Fritsch and T. Maniatis, Cold Spring Harbor Laboratory Press, 1989. $115.00 (3 Vols; 1659 Pages) Isbn 0 87969 309 6. *Trends in biotechnology (Regular ed.)* 1991, 9, 213-214.

18. Svec, F. Less Common Applications of Monoliths: Preconcentration and Solid-Phase Extraction. *J. Chromatogr. B: Anal. Technol. Biomed. Life Sci.* 2006, 841, 52-64.

19. Bloomfield, V. A. DNA Condensation by Multivalent Cations. *Biopolymers* 1998, 44, 269-282.

20. Tian, H.; Huhmer, A. F. R.; Landers, J. P. Evaluation of Silica Resins for Direct and Efficient Extraction of DNA from Complex Biological Matrices in a Miniaturized Format. *Anal. Biochem.* 2000, 283, 175-191.

21. Christel, L. A.; Petersen, K.; McMillan, W.; Northrup, M. A. Rapid, Automated Nucleic Acid Probe Assays Using Silicon Microstructures for Nucleic Acid Concentration. *J Biomech Eng* 1999, 121, 22-7.

22. Kim, J.; Johnson, M.; Hill, P.; Gale, B. K. Microfluidic Sample Preparation: Cell Lysis and Nucleic Acid Purification. *Integr. Biol.* 2009, 1, 574-586.

23. Alberts, B. B., D.; Lewis, J.; Raff, M.; Roberts, K.; Watson, J. D. . *Molecular Biology of the Cell*. Garland Science: New York, 2008.

24. Pahl, A. Gene Expression Profiling Using Rna Extracted from Whole Blood: Technologies and Clinical Applications. *Expert Rev. Mol. Diagn.* 2005, 5, 43-52.

25. Thach, D. C.; Lin, B.; Walter, E.; Kruzelock, R.; Rowley, R. K.; Tibbetts, C.; Stenger, D. A. Assessment of Two Methods for Handling Blood in Collection Tubes with Rna Stabilizing Agent for Surveillance of Gene Expression Profiles with High Density Microarrays. *J. Immunol. Methods* 2003, 283, 269-279.

26. Hagan, K. A.; Bienvenue, J. M.; Moskaluk, C. A.; Landers, J. P. Microchip-Based Solid-Phase Purification of Rna from Biological Samples. *Anal. Chem. (Washington, DC, U. S.)* 2008, 80, 8453-8460.

27. Hagan, K. A.; Meier, W. M.; Ferrance, J. P.; Landers, J. P. Chitosan-Coated Silica as a Solid Phase for Rna Purification in a Microfluidic Device. *Anal. Chem. (Washington, DC, U. S.)* 2009, 81, 5249-5256.

28. Price, C. W.; Leslie, D. C.; Landers, J. P. Nucleic Acid Extraction Techniques and Application to the Microchip. *Lab Chip* 2009, 9, 2484-2494.

29. Satterfield, B. C.; Stern, S.; Caplan, M. R.; Hukari, K. W.; West, J. A. A. Microfluidic Purification and Preconcentration of Mrna by Flow-through Polymeric Monolith. *Anal. Chem. (Washington, DC, U. S.)* 2007, 79, 6230-6235.

30. Witek, M. A.; Hupert, M. L.; Park, D. S. W.; Fears, K.; Murphy, M. C.; Soper, S. A. 96-Well Polycarbonate-Based Microfluidic Titer Plate for High-Throughput Purification of DNA and Rna. *Anal. Chem. (Washington, DC, U. S.)* 2008, 80, 3483-3491.

31. Witek, M. A.; Llopis, S. D.; Wheatley, A.; McCarley, R. L.; Soper, S. A. Purification and Preconcentration of Genomic DNA from Whole Cell Lysates Using Photoactivated Polycarbonate (Ppc) Microfluidic Chips. *Nucleic Acids Res.* 2006, 34, e74/1-e74/9.

32. Hashimoto, M.; Chen, P.-C.; Mitchell, M. W.; Nikitopoulos, D. E.; Soper, S. A.; Murphy, M. C. Rapid Pcr in a Continuous Flow Device. *Lab Chip* 2004, 4, 638-645.

33. Hupert, M. L.; Guy, W. J.; Llopis, S. D.; Shadpour, H.; Rani, S.; Nikitopoulos, D. E.; Soper, S. A. Evaluation of Micromilled Metal Mold Masters for the Replication of Microchip Electrophoresis Devices. *Microfluid. Nanofluid.* 2007, 3, 1-11.

34. Wei, S.; Vaidya, B.; Patel, A. B.; Soper, S. A.; McCarley, R. L. Photochemically Patterned Poly(Methyl Methacrylate) Surfaces Used in the Fabrication of Microanalytical Devices. *J. Phys. Chem. B* 2005, 109, 16988-16996.

35. Rivaton, A. Recent Advances in Bisphenol-a Polycarbonate Photodegradation. *Polym Degrad Stabil* 1995, 49, 163-179.

36. Roy, S.; Yue, C. Y.; Lam, Y. C.; Wang, Z. Y.; Hu, H. Surface Analysis, Hydrophilic Enhancement, Ageing Behavior and Flow in Plasma Modified Cyclic Olefin Copolymer (Coc)-Based Microfluidic Devices. *Sensors and Actuators B: Chemical* 2010, 150, 537-549.

37. Seidel, C.; Kopf, H.; Gotsmann, B.; Vieth, T.; Fuchs, H.; Reihs, K. Ar Plasma Treated and Al Metallised Polycarbonate: A Xps, Mass Spectroscopy and Sfm Study. *Applied Surface Science* 1999, 150, 19-33.

38. Wang, H.; Chen, H.-W.; Hupert, M. L.; Chen, P.-C.; Datta, P.; Pittman, T. L.; Goettert, J.; Murphy, M. C.; Williams, D.; Barany, F.; Soper, S. A. Fully Integrated Thermoplastic Genosensor for the Highly Sensitive Detection and Identification of Multi-Drug-Resistant Tuberculosis. *Angew. Chem., Int. Ed.* 2012, 51, 4349-4353, S4349/1-S4349/10.

39. Jackson, J. M.; Witek, M. A.; Hupert, M. L.; Brady, C.; Pullagurla, S.; Kamande, J.; Aufforth, R. D.; Tignanelli, C. J.; Torphy, R. J.; Yeh, J. J.; Soper, S. A. Uv Activation of Polymeric High Aspect Ratio Microstructures: Ramifications in Antibody Surface Loading for Circulating Tumor Cell Selection. *Lab on a Chip* 2014.

CHAPTER 4. INVESTIGATION OF SURFACE CHARGE AND ELECTROSMOTIC FLOW IN POLYMER NANOSLITS AND NANOCHANNELS

4.1 Introduction

Fluidic channels with one or two of its dimensions in the nanometer scale, nanoslits or nanochannels, respectively, have recently generated great interest because of unique phenomena that occur in nano-confined space such as nanocapillarity,[1] concentration polarization[2, 3] and electrical double layer (EDL) overlap.[4-7] These properties arise when the channel size is comparable to either the length scales of the range of electrostatic interactions in solution or the molecular size of the analytes. Some of the interesting applications that arise from the use of nanochannels and nanoslits include single-molecule interrogations,[8-11] molecular pre-concentration,[12] chemical analyses of mass-limited samples,[13, 14] DNA electrophoresis,[15-17] desalination,[18] nanofluidic diodes,[19] real-time probing of biomolecules,[20-24] ionic transport,[25] and entropic trapping for DNA separations.[26] Nanochannels fabricated in a controlled fashion have enabled the exploration of charge-related effects such as concentration enhancement and depletion and surface-charge-governed transport.[27, 28] Hence, nanofluidic channels have become a fundamental and essential experimental platform for the study of nanoscale-molecular, -fluidic, and -ionic transport properties that offer high throughput with low sample volume requirements.

As described by Chantiwas *et al.*,[29] polymer-based nanoslits/nanochannels have provided an attractive alternative to glass or silicon devices due to their diverse range of physiochemical properties, low material cost and the availability of a plethora of fabrication techniques to design the prerequisite structures. A commonly employed modality for the fabrication of thermoplastic nanofluidic devices is nanoimprint lithography (NIL), a specific sub-type of hot embossing.[30-33] This technique takes advantage of the deformability of the material at elevated temperatures to

produce multi-scale nanostructures in a relatively high production mode over large areas and at low-cost.[34] A distinct benefit of using polymers for the fabrication of nanofluidic devices is the diversity in their surface chemistry, which is determined by the identity of the monomer units comprising the polymer chains. For example, poly(methylmethacrylate), PMMA, possesses functional groups on its backbone that consists of methyl esters while polycarbonate, PC, possesses carbonates. In addition, a diverse range of simple activation techniques can be employed to generate surface functionalities appropriate for the desired application.[35-39]

Common surface modification protocols reported for polymer fluidic devices are ultraviolet (UV) and plasma oxidation.[40-42] These activation techniques have been reported to generate a host of oxygen-containing species, such as different carbonyls (aldehydes, ketones and carboxylic acids) and alcohols on the polymer surface[41, 43] following a sequence of free-radical photo-initiated oxidation reactions. Photochemical activation of polymer substrates possessing nanofluidic structures requires careful control of the dose to minimize activation induced nanoscale roughness that may affect the operational characteristics of the device.[44] Plasma treatment has been the technique of choice for nanofluidic surface activation and low-temperature assembly of the device as it induces minimal surface root-mean-square (RMS) roughness, lacks diffraction limitations and shadowing effects, as reported for UV activation of polymer substrates with microchannels,[38] and allows for low temperature assembly of the nanofluidic device while retaining the surface functionality and minimizing nanostructure deformation.[33] For example, by exposing PMMA to controlled plasma conditions, it is possible to generate surface carboxyl functional groups,[41] which remain accessible for reactions after device thermal assembly.

In a previous work, we reported the generation of positively charged surface moieties in PMMA microchannels following both chemical (*N*-lithiodiaminoethane reaction)[39] and photochemical (UV - [*N*-(3-dimethylaminopropyl)-*N*-ethylcarbodiimide (EDC)] – [ethylenediamine (EDA)]) pathways.[37] To the best of our knowledge, most of the work on nanochannel surface modification has involved functionalization of surface silanol groups,[28] immobilization of biomolecules on the channel walls[25, 45, 46] and ion transport studies performed in glass-based substrates. Glass possesses well-established surface chemistry, hydrophilicity, non-conductivity, rigidity with minimal surface defects, non-deformability at high pressures, excellent optical properties and well-established top-down fabrication techniques.[47, 48] However, with the growing interests in elastomeric,[49-52] thermoplastic[31] and membrane-based[53, 54] nanofluidic devices, it becomes necessary to understand the effects of surface modification on the charge density and surface charge governed ion transport in polymer-based nanofluidic channels, especially when considering such devices for many of the nanofluidic applications discussed previously.[28, 55]

In this work, we report for the first time the surface modification of polymer nanoslits and nanochannels and the investigation of the surface charge density and electroosmotic flow (EOF) in these devices. The nanofluidic devices were fabricated in PMMA substrates using a modified protocol that we previously reported. Carboxyl groups were generated on the walls of PMMA nanoslits and nanochannels under controlled conditions of the plasma exposure time and oxygen gas flow rate.[41, 43] These groups were subsequently aminated by reaction of the surface carboxyl groups with a solution of EDC and EDA. The extent of surface roughness induced by surface activation was assessed in a nanoslit using atomic force microscopy (AFM). Surface conductance plots were generated for the fluidic devices using a range of potassium chloride

(KCl) concentrations. In agreement with our measurements, a modified model of ion transport in nanofluidic devices, based on Schoch *et al.*[55] is presented. It revealed the importance of geometrical parameters of the nanometer-sized channels and a dominating surface charge density inducing a conductance plateau at low ionic strength. In addition, we investigated the effects of solution pH on the surface charge density, reported the electroosmotic flow (EOF) in these devices.

4.2 Materials and Methods

4.2.1 Reagents and Buffers

PMMA sheets and cover plates used for the device fabrication were purchased from Good Fellow (Berwyn, PA). Cycloolefin copolymer backbone (COC 6017) for nanoimprinting was purchased from TOPAS Advanced Polymers (Florence KY). Si <100> wafer was purchased from University wafers (Boston, MA). Isopropanol, 1-ethyl-3-[dimethylaminopropyl] carbodimide hydrochloride (EDC), 2-(4-morpholino)-ethane sulfonic acid (MES), Ethylenediamine (EDA), tripropylene glycol diacrylate (TPGA), trimethylolpropane triacrylate (TMPA), Irgacure 651 (photo-initiator), 50% potassium hydroxide (KOH) and potassium chloride (KCl) were purchased from Sigma-Aldrich (St. Louis, MO). Anti-adhesion monolayer of (Tridecafluoro – 1,1,2,2 – Tetrahydrooctyl) Tricholorosilane (T-Silane) was purchased from Gelest, Inc. Tris buffer (pH 8.0) was obtained from Fisher Scientific (Houston, TX). Phosphate-buffered saline (PBS, pH = 7.4) was purchased from Life Technologies (Carlsbad, CA). All required dilutions were performed using 18 MΩ/cm milliQ water (Millipore technologies) and all measurements were performed at 25°C unless specified otherwise.

4.2.2 Fabrication of Nanofluidic Devices

Previously, we have reported the development of nanoslits and nanochannels in polymer substrates following a single step fabrication scheme that is based on nanoimprint lithography (NIL).[31, 32] Briefly, the device fabrication involves four key steps. First, the silicon master was developed by initially patterning two V-shaped access microfluidic channels, 55 µm wide, 12 µm deep 1.5 cm long in Si <100> wafer using standard photolithography followed by anisotropic etching with 50% KOH solution. Next, nanofluidic channels were patterned across the microchannels by FIB milling using a Helios NanoLab 600 DualBeam instrument (FEI Company). The spot size (beam current) and sputtering rate were carefully controlled to ensure that the desired channel dimensions were designed.

Following this, an anti-adhesion monolayer of T-Silane was coated on the Si master from gas phase in a desiccator under vacuum for 2 h to facilitate the demolding process. The structures on the Si master were then carefully transferred into a UV-curable resin polymeric blend, containing 68 wt% TPGA as the base, 28 wt% TMPA as the crosslinking agent and 4 wt% Irgacure 651 as photo-initiator) coated onto a cyloolefin copolymer (COC) backbone, *via* UV-NIL to produce polymer stamps with protrusive structures. To achieve this, the Si master (mold) was initially coated with the UV resin by dispensing with a pipette, followed by gentle pressing of the COC backbone on the resin-coated master to ensure complete filling of the resin into mold cavities. This was followed by exposure to a 365nm UV light (10 J/m^2) through the COC backbone for 5 min in a CL-100 Ultraviolet Crosslinker. After curing, the UV-curable resin was gently demolded from the Si mold to get the negative copy on UV-curable resin.

Next, the patterned UV-curable resin was used as the stamp to hot emboss into a 3 mm-thick PMMA sheet (Lucite CP) with access holes for reservoirs, drilled prior to embossing. The

imprinting was performed at a pressure of 1910 kN/m^2 for 120 s with the top and bottom plates maintained at a temperature of 125°C using the Hex03 hot-embosser (JenOptik). Pressure was applied after 30 s preheating of the stamp and the substrate at the desired molding temperature, and was maintained during the imprinting process until the system was cooled down to 45°C. Upon cooling, PMMA copy was easily demolded from the UV-resin stamp. A 175µm thick PMMA sheet (Goodfellow Corporation) was used as the cover plate. Both the patterned PMMA sheet and cover plate were pre-activated with oxygen plasma at 50W for 35 s and 5.5 sccm gas flow rate. Thermal assembly was performed immediately at 80°C for 400 s under a 370 kN/m^2 pressure. This approach not only helped with achieving a low temperature device assembly with the desirable bond strength but also contributed to the effective functionalization of the nanochannel surface with carboxyl (hydrophilic) functional groups necessary for amine modification.

4.2.3 Surface Modification

The reaction was initially tested on pre-cut pieces of PMMA (1 cm x 1 cm) without micro or nanostructures. Clean PMMA substrates were exposed to 50 W (5.5 sccm) oxygen plasma for 35 s to generate the carboxyl functional scaffolds necessary for amination reaction (Scheme 4.1a). The plasma modified samples were then soaked in a solution containing 300 mg EDA and 250 mg EDC in 5 ml of 0.1 M MES buffer (pH 4.8) for 20 min at room temperature. The amide linkage between the surface carboxyl group and a terminal –NH_2 group from EDA was achieved through EDC linker chemistry. EDA attachment onto the surface is possible under the buffer conditions described (pH 5 to 9) as the molecule does not contain functional groups susceptible to hydrolysis (Scheme 4.1b).[56] After incubation, samples were thoroughly rinsed with deionized water and air dried. These amine modified samples along with the pristine and plasma activated

substrates were then subjected to XPS analysis to determine the surface chemical composition and AFM analysis to probe changes in surface morphology (roughness) induced by plasma etching or chemical swelling/dissolution. The same protocol was adopted for the amination of the assembled PMMA devices containing nanoslits and nanochannels. In this case, the plasma assembled devices were immediately filled with EDC-EDA and allowed to incubate for 20 min in a closed chamber. All devices were rinsed with deionized water prior to experiments.

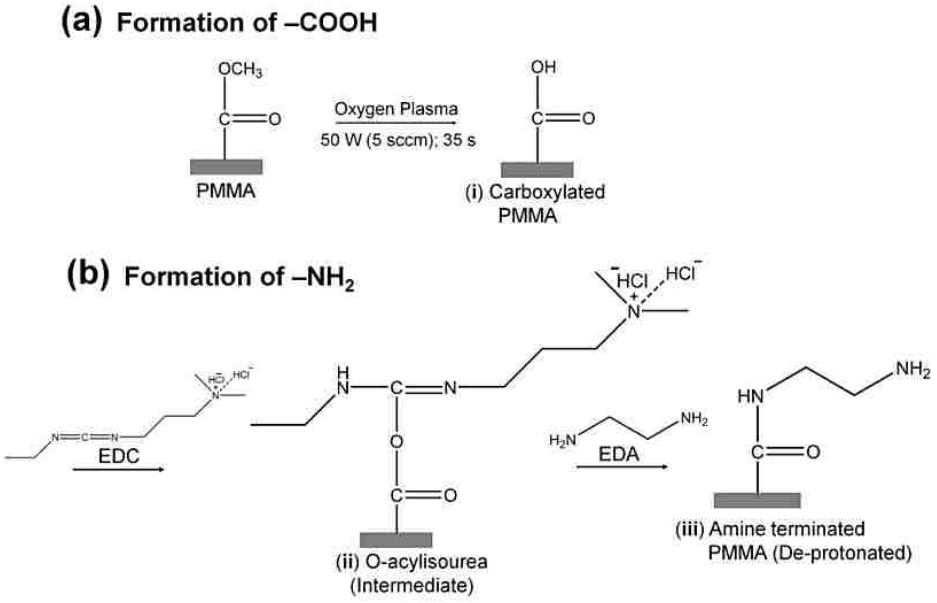

Scheme 4.1 Protocol for the surface modification of PMMA with (a) carboxyl groups by plasma activation, and (b) amine groups by chemical reaction with ethylenediamine through EDC coupling chemistry to the plasma activated PMMA.

4.2.4 Water Contact Angle and Surface Energy

The wettability of the unmodified and surface treated PMMA were assessed by water contact-angle measurements using a VCA Optima instrument (AST Products). 3 mm thick PMMA sheet was cut to 15 mm x 18 mm dimensions and the surface was modified as described above. A volume of 2.0 μL nanopure water (18.2MΩ.cm at 25^{o}C) was dispensed on to the substrate and the photograph of each droplet was captured immediately for analysis using the

software provided by the manufacturer. The measurements were repeated at least five times at separate positions on the substrate, and the values reported as the mean ± one standard deviation.

4.2.5 Atomic Force Microscopy (AFM)

The topographies of unmodified, O_2-PMMA and NH_2-modified flat PMMA surface and the bottom of PMMA nanoslits were investigated using the Asylum Research MFP-3D Atomic Force Microscope (tip radius ~2nm) in repulsive tapping mode at a rate of 1.0 Hz. The Tap300A1-G cantilever tips (Ted Pella) had a frequency of 300 kHz and force constant of 40 N/m. For the flat surfaces, the scans were taken over a 3.5 µm x 3.5 µm scan size, presented in 3D and RMS surface roughness computed using manufacturer's software. In the nanoslit, a scan size of 4 µm x 500 nm was taken and the RMS roughness computed for the entire area.

4.2.6 Spectroscopies

For XPS measurements, C 1s, O 1s and N 1s photoelectron signals were acquired using an Axis Ultra DLD X-ray photoelectron spectrometer (Kratos Analytical) under ultra-high vacuum conditions (10^{-8} to 10^{-10} Torr) with a monochromatic Al Kα X-ray source, 20 eV pass energy, 370 s acquisition time, 1,600 ms dwell time, and 20° electron take-off angle. Given an inelastic mean free path of 3-4 nm, ~95% of the resultant signal originated 9-12 nm from the surface.[57-59] To examine the molecular nature of the treated and untreated surfaces, IR studies were employed using pre-cut Silicon wafers coated with 200 nm Au layer (Au wafer). Commercial PMMA sheet was dissolved in dichloromethane and serially diluted to yield a solution with final concentration of 0.5 mg of PMMA/mL of dichloromethane. This was spin coated on the Au wafer at 2500 rpm for 60 s to yield a 5 nm thick polymer layer. The coated Au-wafers were allowed to dry in an oven after which they are ready for surface modification and analysis. This approach helped to minimize interference from bulk material in the IR spectra. IR spectra were collected at a

resolution of 2 cm^{-1} scans on a 670-IR spectrophotometer (Varian, US) using a monolayer/grazing-angle specular reflectance accessory. For SEM, COC stamp and PMMA substrate were pre-coated with a 2-3 nm layer of Au/Pd and were imaged under high vacuum with an FEI Quanta 200 field emission gun at a 10 kV accelerating voltage and an Everhart-Thornley detector.

4.2.7 Surface Charge Measurement

Following each step of surface modification of the nanofluidic vias, electrical conductance of the nanochannels was investigated using different dilutions of KCl from 1M to 10^{-6}M in Tris buffers, pH 7.8 for all devices. The DC electrical conductance of the nanochannels was monitored through Ag/AgCl electrodes immersed in the access reservoirs at the ends of microchannels using a low noise Axopatch 200B amplifier with real-time control and analysis using pClamp10 software. The conductance values were determined by fitting the slope of the ionic current as a function of the applied voltage, which was stepped from -1V to 1V with 100mV step size and 5 s delay time for each data point. We found that the delay time was sufficient for the device to reach a steady state current. The measurement was performed in triplicate with the mean conductance plotted against the electrolyte concentration in log-log plot and the surface charge was determined from these graphs. This experiment was repeated at pH range between 3 and 12 to investigate the pH effects on the surface charge. The solution pH was adjusted using hydrochloric acid or potassium chloride. No pressure difference across the nanochannel was induced during the measurements.

To equilibrate the system, the fluidic device was first flushed with a binary mixture of methanol/ultrapure water (50% v/v) by capillary force assisted with vacuum from the outlet port to ensure complete filling and the elimination of air-bubbles. Next, deionized water (18

MΩcm) was used to rinse the previous solution from the fluidic network followed by the addition of the chosen electrolyte solution until the resistance of the fluidic channels reached a stable minimum. Each rinsing cycle took 5 to 10 min until the flow was stopped and the measurements were made. To avoid errors from solution interference, each measurement was performed using a new device.

4.2.8 Electroosmotic Flow (EOF) Measurement

The EOF was measured using the Axopatch 200B amplifier. Two devices, one possessing a single PMMA nanoslit (138 μm long, 50 nm high, and 1 μm wide) and the other a single nanochannel (138 μm long, 120 nm high and 120 nm wide), connecting two opposite V-shaped access microchannels, were fabricated as described previously. Fluidic channels were activated and the EOF was assessed using the current monitoring method. EOF values were measured using 0.1 and 0.05 M KCl solution in 10mM Tris buffer at pH 7.8. First, the entire device was primed with 50% v/v water/methanol then drained and flushed with deionized water for 5-10 min. Next, the device was filled with 0.1 M solution and allowed to equilibrate for 3 min under a 1V DC bias. Following equilibration, as evident by a constant current trace, one access reservoir was emptied and 0.05 M KCl was introduced. Ag/AgCl electrodes were placed in the reservoirs across the channels under a 200 mV DC bias. Signals were acquired using pClamp10 software and Digidata 1440A digitizer set at 10 kHz sampling frequency.

4.3 Results and Discussion

4.3.1 Device Fabrication

The Silicon (Si) master, which consisted of micron-scale access channels (fabricated using photolithography) and an array of connecting nanoslits or nanochannels (fabricated using Focused Ion Beam (FIB) milling), was used to fabricate the protrusive polymer stamp, which

was made from a UV-curable resin. Thermal imprinting was used to transfer the nanofluidic structures into PMMA from the UV-curable resin stamp and the device was sealed with a PMMA cover plate using low-temperature plasma assisted bonding to build the enclosed mixed-scale polymer device. UV-NIL conditions were carefully controlled to ensure that patterns from the Si master were transferred with high fidelity and minimum deformations into the resin stamp. Figure 4.1 shows scanning electron microscope (SEM) images of the original Si master, cured UV-resin stamp and thermally imprinted PMMA substrate with an array of four nanoslits (Figure 4.1a – 4.1c) and seven nanochannels (Figure 4.1d – 4.1f).

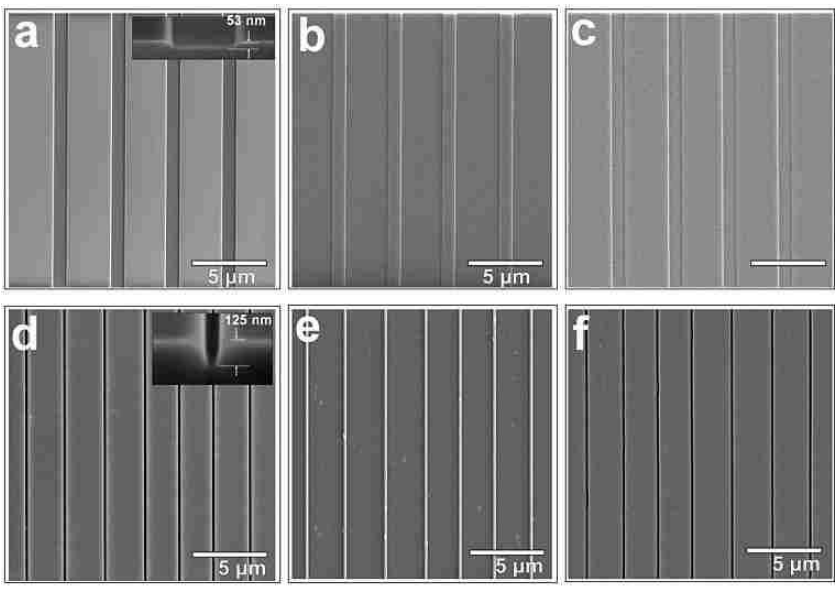

Figure 4.1 Scanning electron micrographs (SEM) of the Si master, resin stamp and PMMA substrate for the nanoslits (a, b, c) and nanochannel (d, e, f), respectively. – Inset shows the off–axis (52°) cross section SEM images of the Si masters. The dimensions ($l \times w \times h$) were 21 µm x 1µm x 50 nm for each of the 4 nanoslits and 46 µm × 120 nm × 120 nm for each of the 7 nanochannels. (Note that the roughness on the SEM image of the stamp and substrate are artifacts from coating with 3 nm AuPd for imaging).

The original channel fabricated by FIB milling into the Si master was purposely designed with dimensions (width × depth) of 980 nm × 53 nm and 110 nm × 125 nm for the nanoslit and nanochannel, respectively, to account for slight deformation of the UV resin stamp during the high pressure and temperature thermal imprinting.[32] The final PMMA devices had the

dimensions of 1 µm × 50 nm and 120 nm × 120 nm, with the same polarity as the structures in the Si master. Although we have previously reported the nanochannels in PMMA with the width & depth <80 nm but for proof-of-concept, we deliberately chose these channel dimensions. The UV resin stamp possessed a thermal expansion coefficient similar to PMMA (6×10^{-5}/°C) and was chosen due to its capability to fabricate micro- and nano-scale patterns via UV-NIL and reduce thermal stress following thermal-NIL production of the nanofluidic device.[60,61] A single UV resin stamp was used for thermal imprinting for up to 10 times without any noticeable damage to the structures.

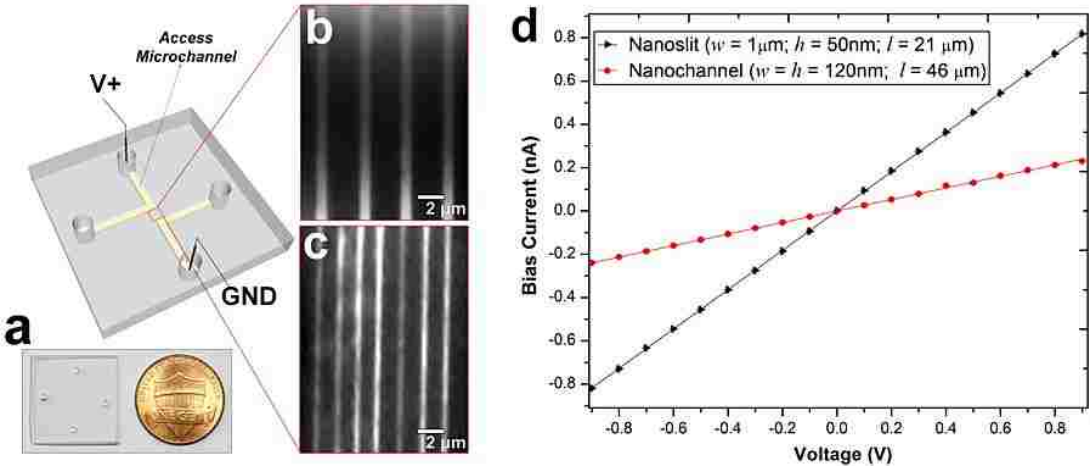

Figure 4.2 (a) Photograph of the thermally assembled nanofluidic devices fabricated in PMMA. The fluorescence images for the sealed nanoslit (b) and nanochannel (c) devices seeded with 5 mM FITC in 0.5X TBE buffer. The images shows channel continuity and the absence of leakages. (d) IV plot generated between -0.9V to 0.9V for the nanofluidic devices filled with 1 mM KCl solution revealing an electrical resistance of 266.4 MΩ and 908.5 MΩ for the nanoslits and nanochannels, respectively. The measured currents have similar absolute values for the respective voltages of opposing polarities; hence, the channels are symmetric (absence of rectification)

The PMMA substrates were sealed using plasma assisted low temperature thermal fusion bonding (Figure 4.2a). The formation of leak-free fluidic devices or discontinuities due to channel collapse during assembly was evaluated by introducing 5 mM fluorescein isothiocyanate (FITC) solution in 0.5X TBE buffer into the fluidic network and allowing the channels to be

filled by capillarity. As shown in Figure 4.2b and 4.2c, the fluidic channels did not show any leakage between the substrate and the cover plate. Current-voltage plots acquired after filling with 1 mM KCl as shown in Figure 4.2d revealed that the measured currents for voltages of opposite polarity had similar absolute values and showed good linearity (non-rectification). The absence of voltage gating and rectification indicated homogeneity in surface charge along the walls of the PMMA nanoslits and nanochannels when using symmetrical electrolyte conditions. Using low thermal bonding temperatures (~80^{o}C) also minimized the amount of surface reorganization of the polar functional groups following plasma treatment. (Figure 4.3).

4.3.2 Surface Characterization

4.3.2.1 Effects of Annealing Temperature on the Wettability of Plasma-activated PMMA

Previous reports have shown that thermal annealing for nanofluidic device assembly affects the surface wettability/solid surface tension of polymer surfaces.[38] Here, we investigated the effects of temperature on the wettability of PMMA activated under oxygen plasma (50 W, 5.5 sccm gas flow rate for 35 s) by measuring the water contact angle between 75˚C and 100˚C, the typical temperature range reported for thermal assembly of PMMA nanofluidic devices. As represented by Chai *et al.*[41] the interpretation of contact angles in terms of the solid surface tension relies on the validity of Young's equation, which interrelates the Young's contact angle, θ_Y, with the interfacial tension of the liquid-vapor , γ_{lv}, solid-vapor, γ_{sv}, and solid-liquid, γ_{sl}, interface;

$$\gamma_{lv} \cos\theta_Y = \gamma_{sv} - \gamma_{sl} \qquad (1)$$

Typically, θ_Y is expected to be a good approximation of the measured contact angle for a surface with RMS roughness $\leq$ 5 nm.[62] The solid surface tension (surface energy) γ_{sv} can be calculated from the water contact angle using;[62]

$$\gamma_{sl} = \gamma_{lv} + \gamma_{sv} - 2\sqrt{\gamma_{lv}\gamma_{sv}}(1 - \beta(\gamma_{lv} - \gamma_{sv})^2) \qquad (2)$$

where β is 1.057×10^{-4} $(m^2/mJ)^2$ and γ_{lv} is the surface tension of water (72.70 mJ/m^2).

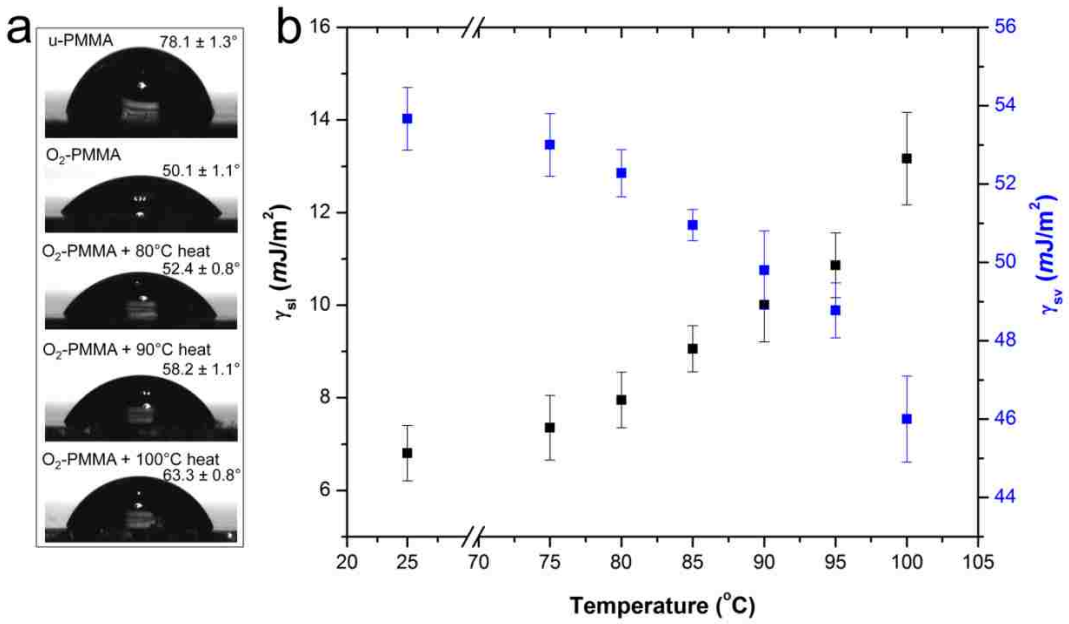

Figure 4.3 Variation of surface energy with annealing temperature for plasma activated PMMA substrate. As shown, there was no significant change in the surface energy at temperatures below 80ºC. At temperatures above 85ºC, the wettability significantly reduced as indicated by an increase in the water contact angle. Each reported value represents the average of five values measured at different positions on the substrate and the vertical bars represent the error of one standard deviation.

As shown in Figure 4.3a, there was a gradual increase in the water contact angle as the temperature of the plasma-activated PMMA was increased. Heating the plasma activated substrate at temperatures ≤ 80˚C did not result in a significant change in the solid surface tension/wettability. However, at temperatures ≥ 85˚C, there was a significant increase in surface tension at the solid-liquid interface. As described by Jackson *et al.*,[38] this increase arises because the functional groups generated after plasma activation (≤ 10 nm from the surface) undergo thermally induced rearrangement and are buried into the bulk substrate when heated. To avoid this, we performed thermal fusion bonding of the nanofluidic device at 80˚C for 400 s. The

wettability was retained at this condition and allowed the devices to be fill easily with aqueous solvents by capillary action and low pressure suction.

The surface wettability and solid surface tensions for the unmodified, plasma and amine-modified PMMA samples were then assessed using water contact angle measurements (see equations 1& 2). Unmodified PMMA showed a contact angle of 78.0 ±1.5°, which corresponds to a solid-vapor surface tension (surface energy) of ~36.8 mJ/m^2. After plasma treatment, the contact angle decreased to 50.1 ±1.1° implying an increase in surface energy to ~54.6 mJ/m^2. Amine modification led to an increase in the water contact angle to 62.92 ±2.0° with an associated surface energy of 45.8 mJ/m^2. The observed trends are consistent with literature values.[39]

4.3.2.2 XPS Analysis

X-ray photoelectron spectra (XPS) was used to analyze the surfaces of the unmodified, plasma activated and amine-terminated PMMA sheets for the chemical composition. The O/C and N/C ratio was used to assess the extent of surface modification of different tested schemes (Figure 4.4c). For convenience, we designate unmodified, plasma activated and amine terminated PMMA as u-PMMA, O_2-PMMA and NH_2-PMMA, respectively. The modification scheme employed will determine the type of functional moieties generated. XPS was used to monitor the O/C and N/C ratio on plasma-activated and amine-modified PMMA surfaces. In all XPS spectra acquired here, a Shirley background was subtracted by averaging at least 10 end points associated with the background. As shown in Figure 4.4c, plasma activation of PMMA led to an increase in the O/C ratio confirming the addition of oxygen containing functional groups.[41] For amination of the plasma activated polymer, several schemes involving EDC or EDC-NHS coupling chemistries were tested with concentrations between 0.1 and 1 M EDA; in all cases,

there was a decrease in the O/C ratio (Figure 4.4c). However, the amount of nitrogen containing groups differed with different conditions. As depicted in Figure 4.4d, the highest N/C ratio (and lowest O/C ratio) was observed for animation involving the reaction of O_2-PMMA with a solution of 1 M EDA in EDC.

To identify the surface groups generated after treatment of PMMA, the C1s spectra for all treated surfaces was deconvoluted based on previously published work.[63] Pristine PMMA C1s spectrum showed the presence of four Gaussian components: (1) 284.6 eV aliphatic C-C and C-H; (2) 285.2 eV quaternary C-C α to the pristine ester; (3) 286.4 eV methoxy C-O ester; and (4) 288.7 eV carbonyl C=O ester (Figure 4.4e). The theoretical peak area ratio of the C1s components (1) - (4) of 2:1:1:1 was found to be 1.90:1.18:1.20:1.00 in our data. The slight deviation may have been attributed to additives and plasticizers introduced into the substrate by the manufacturer.[64] Furthermore, in addition to the peaks listed above for u-PMMA, the deconvoluted C1s peak of O_2-PMMA showed the presence of a peak at a binding energy of 289.7 eV (Figure 4.4f). This peak corresponds to the OC=O for a carboxylic acid group. After amination, the deconvoluted C1s peak showed the absence of the carboxylic acid peak and the presence of two peaks; 285.8 eV, C-N bond of an amine, and 287.9 eV for a O=C-N bond associated with an amide (Figure 4.4g).

The combined survey spectra are shown in Figure 4.4a. The trace for u-PMMA showed the presence of only two peaks at 284.8 eV and 532.0 eV, indicative of C1s and O1s core levels, respectively. After exposure to 50 W (5.5 sccm) oxygen plasma for 35 s, there were observable changes in the individual intensities of the C1s and O1s peaks when compared to the untreated samples (red trace in Figure 4.4a). There was an increase in the O/C atomic ratio from 0.331 ±0.006 for u-PMMA to 0.403 ±0.003 for O_2-PMMA, indicating the incorporation of oxygen

containing polar functional groups onto the surface. The survey spectrum taken from the amine-terminated PMMA (blue trace) shows the presence of a new peak centered at 399.69 eV in addition to the C1s and O1s peaks. This peak is characteristic of surfaces possessing nitrogen-containing functionalities (N1s core level) and is in agreement with literature values.[39,65]

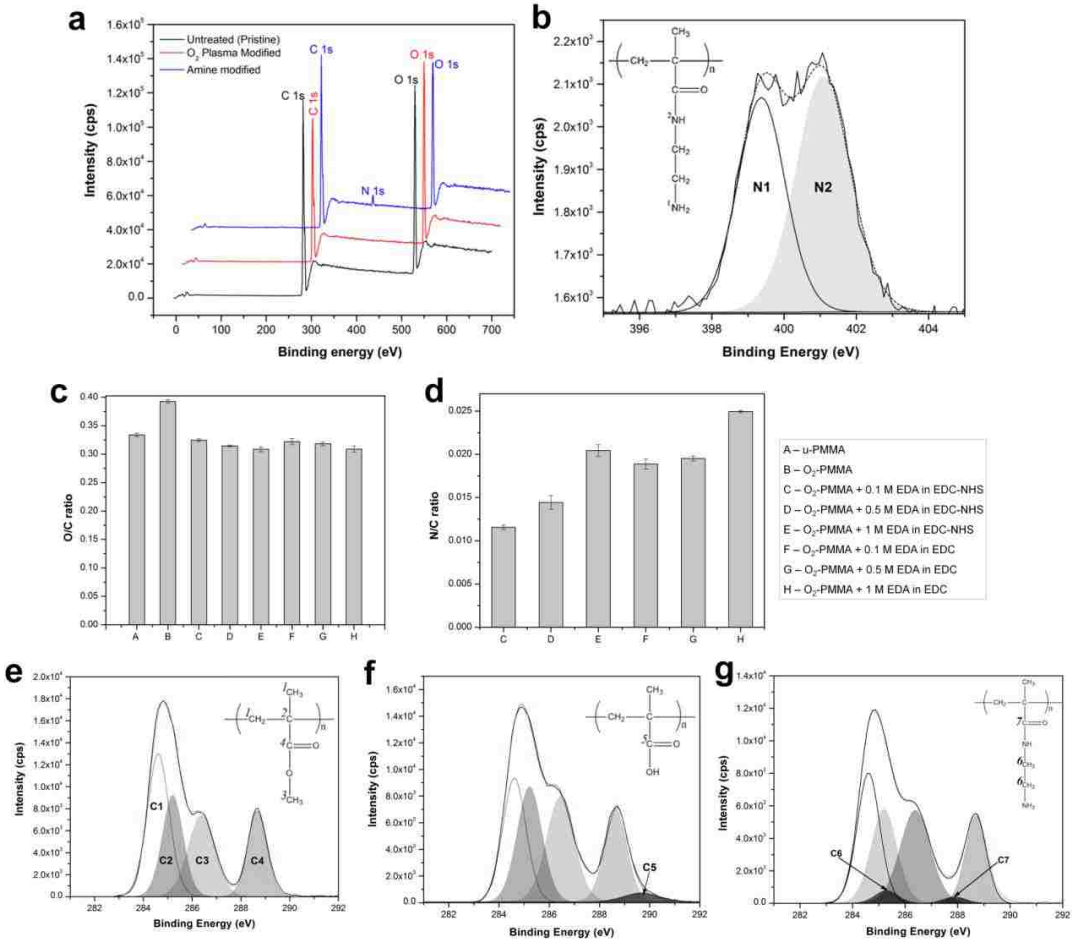

Figure 4.4 (a) Full XPS survey spectrum of unmodified (black trace), plasma activated (red trace) and amine modified (blue trace) PMMA (b) N 1s deconvoluted spectrum showing two forms of nitrogen atoms (insert shows the chemical structure of aminated PMMA surface with the forms of nitrogen labeled N1 and N2 .Bar graphs showing the (c) O/C ratio and (d) N/C ratio for different surface modification schemes C-H tested for both unmodified-PMMA and O_2-PMMA (plasma treated PMMA), obtained from XPS data. Deconvoluted C1s spectra for (e) unmodified, (f) O_2-PMMA and (g) NH_2-PMMA obtained by reacting the plasma activated PMMA with 1 M ethylenediamine in the presence of EDC. PMMA peaks are labeled and assigned to the polymer's monomer. Spectra for the plasma activated PMMA contained an additional peak for COOH functionalities and the amine modified surface showed the presence of two peaks corresponding to the C-N amine and amide carbon atoms.

Further analysis of the XPS data revealed that the atomic ratio of the peak area of the O1s peak to the C1s peak was 0.309 ±0.006 with the ratio of the O1s to C1s peak areas ~10.9% less for NH_2-PMMA compared to u-PMMA. This result demonstrated that not only was nitrogen successfully incorporated onto the surface of the PMMA but the amount of oxygen present on the surface was less than what was present for the u-PMMA or O_2-PMMA. The N/C ratio was 0.025 ±0.001. The N1s peak obtained was deconvoluted as shown in Figure 4.4b. This peak consisted of two individual peaks, one centered at 399.1 eV and the other at 400.9 eV. The peak at the lower binding energy corresponded to the N1s core level of an amine (N1), while the higher energy peak was assigned to an amide (N2).[39] The deconvoluted C1s peaks for u-PMMA, O_2-PMMA and NH_2- PMMA are presented in Figure 4.4e-g and described in detail.

The observations in the XPS data were in agreement with the infrared spectra shown in Figure 4.6, which indicated the presence of fewer ester groups for the amine-terminated PMMA. Collectively, these results indicated successful oxidation and amination reactions of the PMMA surface, an outcome that is important for applications requiring surface modification of the nanofluidic devices.

4.3.2.3 AFM Imaging

Typically, surface modification reactions induce not only chemical changes but also some topographical changes. These changes are in the form of nanometer or sub-nanometer random surface roughness on solid walls with roughness amplitude a_r. Results obtained from previously reported molecular dynamic simulations showed that the roughness may dramatically affect the wettability of surfaces and EOF in nanofluidic channels depending on the magnitude of a_r.[66] For the case where $\lambda_D/a_r << 1$, where λ_D is the Debye length, the EOF can be significantly different compared to $\lambda_D/a_r \sim 1$; the presence of a rough surface that is comparable to the double layer

thickness can alter the electrical double layer near the surface and significantly reduce the EOF[67] and streaming potential.[68] For a homogeneously charged rough channel (such as considered here), the EOF is expected to decrease when the roughness is larger than 5% of the channel width.[69] However, this effect becomes insignificant for surfaces with $\lambda_D/a_r > 1$.[70,66] Also, the water contact angle (wettability) is expected to be larger for very rough surfaces than a smooth surface with identical chemical properties.[71,62]

First, we investigated the surface topography of PMMA substrates to monitor any changes in surface roughness induced by surface treatment. Figure 4.5 a-c shows representative AFM scans for unmodified, plasma and amine-modified PMMA nanoslit devices following assembly of the cover plate to the substrates. The measured RMS roughness for u-PMMA nanoslit devices was 1.16 nm, which originated from the Si master due to ion sputtering. The RMS roughness values increased to 1.42 nm for O_2-PMMA and 1.63 nm for NH_2-PMMA nanoslit devices.

The roughness of PMMA nanoslits was measured by AFM only because the bottom surface could be easily profiled without interference due to tip-wall interactions. Figure 4.5d shows a representative AFM image of a nanoslit. AFM scans of 4 μm × 500 nm were acquired for the bottom surfaces of the unmodified, plasma and amine modified nanoslits. For the u-PMMA nanoslit shown in Figure 4.5e, the measured RMS surface roughness was 0.80 nm. This value was approximately equal to the measured roughness obtained from the bottom surface of the FIB milled nanoslit in the original Si master (data not shown). After surface modification, there was an increase in RMS surface roughness to 1.15 nm and 1.23 nm for the plasma and amine-modified PMMA, respectively. This increase in surface roughness of O_2-PMMA is due to etching by the oxygen plasma. However, the increase in surface roughness for the aminated surface can be attributed to slight swelling and/or dissolution of the PMMA by the EDC/EDA

solution and the additional C-C bonds introduced onto the surface from EDA. (see Figure 4.5 a-c). Nevertheless, because the experiments were performed at solution ionic strengths producing a debye length which is smaller than ten times the channel dimension but larger than the wall roughness (λ_D > 2.0 nm,)[17,72] we expect the contributions of surface roughness to wettability and EOF in our PMMA nanoslit and nanochannel devices to be insignificant relative to contributions from changes in surface chemistry and/or charge.

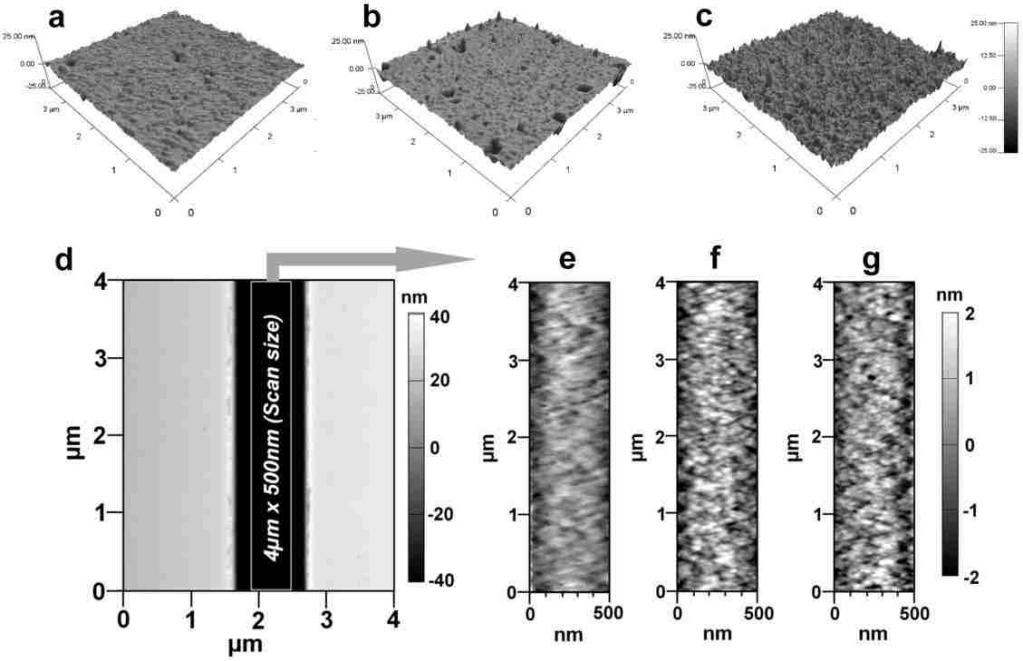

Figure 4.5 AFM images acquired for (a) u-PMMA (b) O_2-PMMA and (c) NH_2-PMMA. All images were scanned over a surface area of 3 μm x 3 μm (d) AFM characterization of the device with 1 μm x 50 nm nanoslit. AFM surface scans of (e) unmodified (f) plasma activated and (g) amine-terminated nanoslit in PMMA substrate. This was performed in the nanoslit (4 μm x 500nm scan size) since the bottom surface could be easily profiled without the interference of tip-wall interactions. The measured root-mean-square (RMS) surface roughness was 0.80 nm, 0.95 nm and 1.03 nm, respectively

4.3.2.4 Fourier Transform Infra-red (FTIR) Spectroscopy

FTIR was employed to characterize the functional groups on pristine, plasma and amine modified PMMA. The typical IR spectrum of pristine PMMA with characteristic peaks between 4000 and 650 cm^{-1} are shown in Figure 4.6a. The most prominent band was ν(C=O), at 1733 cm^{-1}

assigned to stretching of esters. The absorption bands at 1270, 1241 cm^{-1} and 1195, 1153 cm^{-1} could be assigned to *v*(C–O) and *v*(COC) stretching of an ester, respectively. This spectrum correlated well with the absorbance spectrum of PMMA documented in the literature.[39] After plasma treatment, bands appeared at 3430 cm^{-1} and at 1700 cm^{-1} assigned to the *v*(O-H) and *v*(C=O) of a carboxylic acid (Figure 4.6b). Amination with EDA led to peaks at 3396 cm^{-1} and 1675 cm^{-1} corresponding to the *v*(N-H) stretch of a primary amine and *v*(C=O) of an amide (Figure 4.6c). These support the XPS results and confirm successful surface modification of the PMMA devices.

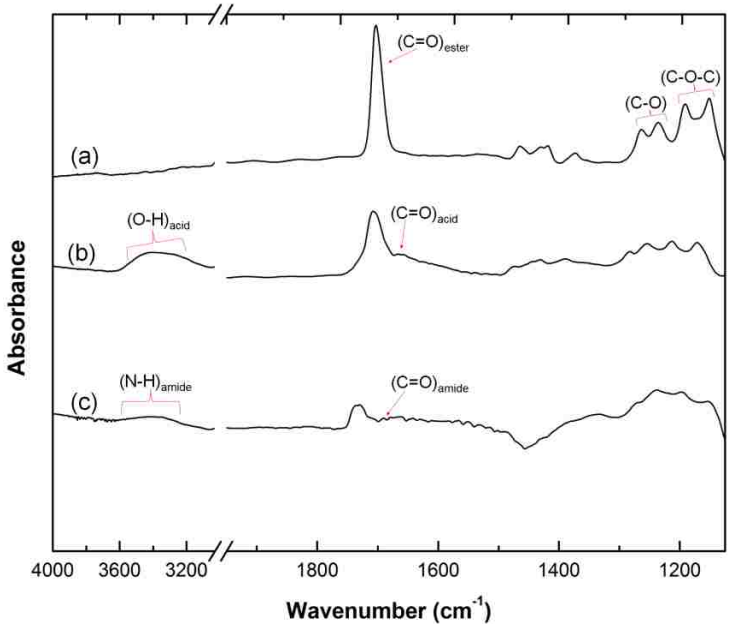

Figure 4.6 ATR-FTIR Spectra for (a) Untreated (b) Plasma activated (c) Amine modified PMMA substrates

4.3.3 Surface Charge and pH Effects

Considering that a solid in contact with a liquid electrolyte will bear a surface charge, which may be due to dissociation of surface groups or specific (nonelectric) adsorption of ions in solution, one would expect that the contributions of the surface charge to fluid transport dynamics and molecular interactions becomes significant in devices possessing high surface-to-

volume ratios. Depending on the solution pH and the surface chemistry, the solid can have either a positive or negative surface charge density, σ_s, described as $\sigma_s = \sum_i q_i / A$; where $q_i = z_i e$ and is the net charge of ion i, z_i is the valency of ion i, e is the electron charge, and A is the surface area. This can be used to compute the number of charged sites per unit area Γ in nm^{-1}.

Due to the fixed surface charge, an oppositely charged region called the electric double layer (EDL), which consists of a layer of immobile surface charge and a layer of mobile counterions, develops in the liquid to maintain the electroneutrality of the solid/liquid interface.[73] In nanofluidic channels, the EDL can represent a significant fraction of the total channel volume. For a channel filled with a symmetrical 1:1 electrolyte like KCl with ionic concentration c, the EDL thickness or Debye length, λ_D, is represented as $(\epsilon_0 \epsilon_r RT/2F^2 c)^{1/2}$, where F is the Faraday constant ($C \cdot m^{-1}$), R is the molar gas constant ($J \cdot mol^{-1} K^{-1}$), ϵ_0 is the permittivity of vacuum ($F \cdot m^{-1}$), ϵ_r is the dielectric constant of the medium, and T is the Kelvin temperature. Depending on the ionic concentration, λ_D can vary from less than 1 nm at high ionic strength to a few tens of nanometers at low ionic strength.[27]

Electrical conductance measurements across nanofluidic channels filled with ionic salt solutions have been an approach used to deduce the magnitude of the surface charge density. Here, we present a modified electrokinetic model based on the report from Stein *et al.*[28] for deducing σ_s. When an external electric field is applied across a nanochannel filled with an ionic salt solution, the measured electrical conductance (neglecting electroosmotic effects) is a sum of the bulk conductance (G_B) and the secondary surface conductance (G_S);

$$G_T = G_B + G_S \tag{3}$$

At high salt concentrations, the surface charges in the nanochannel are shielded by the mobile ions and have negligible influence on the ion concentration in the nanochannel. In this

case, the ionic transport is dominated by the ions in the bulk solution and $G_T \approx G_B$. The value of G_B depends on the nanochannel dimensions and electrolyte concentration according to the following expression;[55,72,45]

$$G_B = 10^3 \left(\mu_{K^+} + \mu_{Cl^-}\right) c\, N_A\, e \cdot \frac{n\, w\, h}{L} \qquad (4)$$

where w, L and h are the nanochannel width, length and height, respectively, N_A is the Avogadro constant, c is the electrolyte concentration in mol/L, n is the number of nanochannels and μ_{K+} and μ_{Cl^-} are the ion mobilities of K^+ and Cl^- ions, respectively ($\mu_{K+} = 7.619 \times 10^{-8}$ m^2/V s and $\mu_{Cl^-} = 7.912 \times 10^{-8}$ m^2/V s). At low salt concentrations, the nanochannels are filled with counterions. For electroneutrality inside the nanochannel, excess counterions in the EDL compensate for the net surface charge, which governs the excess counterion concentration c_e (mol/L) inside the channel.[74] G_B becomes negligible and σ_s governs the total ion conductance in the nanochannel ($G_T \approx G_S$). Considering that a nanochannel possesses four surfaces in contact with the electrolyte solution and by the principle of charge conservation, c_e is given by;

$$c_e\ [\text{mol/L}] = 10^{-3}\ \frac{2\,\sigma_s\,(w + h)}{e\, N_A \cdot w\, h} \qquad (5)$$

For 1D nanochannels (*i.e.*, nanoslits), such as reported by Stein *et al.*,[28] Schoch *et al.*,[55] Karnik *et al.*,[46] and Martins *et al.*,[45] $h << w$; hence $(w + h) \approx w$. However, for 2D nanochannels with $h \leq w$, the channel width also contributes to c_e and G_S. Therefore,

$$G_S = 2\, \mu_{opp} \sigma_s\, n \frac{(w + h)}{L} \qquad (6)$$

Substituting equations (2) and (4) into equation (1) yields the expression;

$$G_T = 10^3 \left(\mu_{K^+} + \mu_{Cl^-}\right) c\, N_A\, e \cdot \frac{n\, w\, h}{L} + 2\, \mu_{opp} \sigma_s\, n \frac{(w + h)}{L} \qquad (7)$$

When $G_B \approx G_S$, a transition ion concentration, c_t is observed on the log-log plot of G_T versus the ion concentration.[55]

We investigated the effects of surface modification of polymer nanofluidic devices by experimentally measuring the surface charge density of modified PMMA nanoslits and nanochannels by monitoring ionic conductance plots performed on nanofluidic devices. Figure 4.7a and 4.7b show the conductance traces for an array of surface modified nanoslits (22 μm × 1 μm × 50 nm) and nanochannels (45 μm × 120 nm × 120 nm) measured over the range of concentrations between 10^{-5} M and 1 M KCl in Tris buffer (pH 7.8). In both nanofluidic devices, the conductance results obtained before and after surface modification differed essentially in the low ionic concentration regime. This effect is characterized by a shift of the plateau conductance suggesting a change in the surface charge dependent on the nature of the modification. When the modified surfaces were in contact with a KCl solution at pH 7.8, ~99.9 % of the surface –COOH groups (pK_a = 4.66) would be deprotonated and ~99.0% of the $–NH_2$ groups (pK_a = 10.42) would be protonated.[75] At extreme pH values and very low buffer concentrations, the total counterions in solution necessary to maintain electroneutrality are H^+ and K^+ for the O_2-PMMA and Cl^- and OH^- for the NH_2-PMMA devices. However, at pH 7.8 and KCl concentration $\geq 10^{-5}$ M, $[K^+] >> [H^+]$ and $[Cl^-] >> [OH^-]$ ($[H^+] \approx 1.6 \times 10^{-8}$ M and $[OH^-] \approx 6.31 \times 10^{-7}$ M); hence, G_S is computed from equation (4) using μ_{K+} and μ_{Cl-} as μ_{opp} for the $–COO^-$ and $–NH_3^+$ surfaces, respectively. Nevertheless, due to the different size of the K^+ (0.27 nm) and Cl^- (0.36 nm) and the discreteness of the water molecules, we expect differences in surface conductance between the positively and the negatively charged channel.[76]

At a KCl concentration greater than 10^{-2} M (geometry governed region), the measured ionic conductance in both the nanoslits and nanochannels fit linearly with the theoretical bulk conductance (Fig. 4.7) and was reproducible from one device to another. This confirmed that there was no significant change in the dimensions of the fluidic channels during thermal

imprinting, device assembly and surface chemical modification with EDC/EDA. However, at low electrolyte concentrations (surface charge-governed regime), the nanochannel conductance deviated from linearity and plateaued for both the plasma and amine treated PMMA nanoslits and nanochannels with the measured surface conductance lower for the $-NH_3^+$ terminated devices compared to the $-COO^-$ terminated devices.

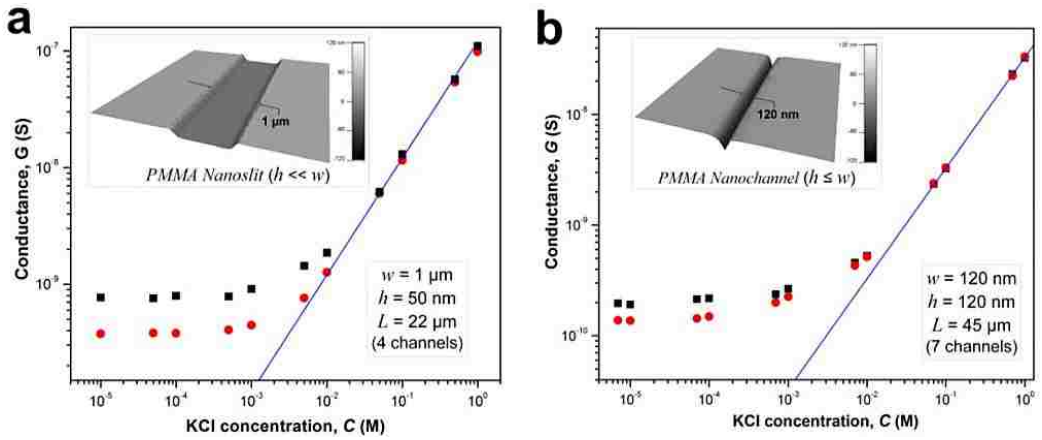

Figure 4.7 Conductance plots obtained from surface modified devices consisting an array of (a) four nanoslits (each 1 μm wide, 50 nm deep and 22 μm long), and (b) seven nanochannels (each 120 nm wide, 120 nm deep and 45 μm long) (square and circle markers represent the data obtained for the plasma and amine modified surfaces, respectively. The solid blue line represents the trace of the theoretical bulk conductance calculated with equation (2)). Each data point represents the average of five measurements with a scatter in the data within 5-8% of the mean value. From the graph, the effective surface charge density as calculated from the transition concentration, c_t, was 38.2 *m*C/m^2 for plasma treated nanoslit, 28.4 *m*C/m^2 for amine treated nanoslit, 40.5 *m*C/m^2 for plasma treated nanochannel and 22.9 *m*C/m^2 for the amine treated nanochannel.

For the nanoslit devices, the average surface conductance at this region was 7.5×10^{-10} S for the O_2-PMMA device. After amination, the conductance dropped to 3.8×10^{-10} S, ~50.7 % of its original value (Fig. 4.7a). The transition concentration, c_t, used to compute σ_s was approximately 6.60 *m*M and 3.52 *m*M for the plasma and amine modified surfaces, respectively. For plasma treated PMMA nanoslits, we obtained $|\sigma_s|$ of ~ 38.2 *m*C/m^2, which was less than 60 *m*C/m^2 reported by Stein *et al.*[28] and 214 *m*C/m^2 reported by Schoch *et al.*[55] for glass-based nanoslits measured at pH 8. For the amine modified nanoslit, $|\sigma_s|$ was 28.4 *m*C/m^2. In the nanochannels,

the conductance in the low ionic strength region for the amine-modified device dropped to ~67.6% of its plasma modified counterpart. The surface charge densities were 40.5 *m*C/m^2 and 22.9 *m*C/m^2 for the plasma and amine devices, respectively.

We also monitored the effect of pH on the surface charge density of nanoslits and nanochannels. As depicted in Figure 4.8 for both the plasma modified nanoslits and nanochannels the surface charge gradually increased as the pH of the electrolyte solution increased because at low pH (high H^+ concentration), the surface carboxy groups are converted to the protonated form. This leads to a corresponding measurable decrease in the surface conductance as less counterions are attracted into the fluidic channel. On the other hand, at high pH, the –COOH groups become deprotonated and are converted to the negatively charged –COO^- thereby increasing σ_s.

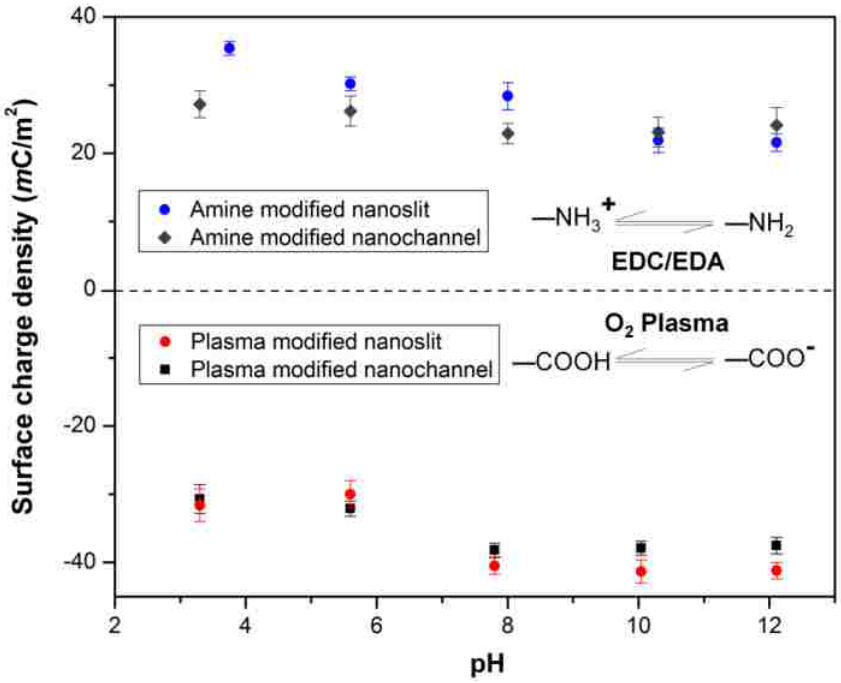

Figure 4.8 Plot showing the effect of pH on the surface charge density σ_s, in plasma and amine modified nanoslits and nanochannels

For the amine modified surfaces, an opposite trend was observed. The measured surface conductance was higher at low pH values and lower at high pH. This is due to the conversion of the reactive $-NH_2$ groups to the positively charged $-NH_3^+$ groups. At pH $\geq$ 8, the surfaces of the O_2-PMMA devices were fully deprotonated and the $|\sigma_s|$ for the nanochannel was found to be greater than the nanoslits. The values were 38.3 *m*C/m^2 ($\Gamma \approx 4.2$ nm^{-2}) and 40.5 *m*C/m^2 ($\Gamma \approx 4.0$ nm^{-2}) for the fully deprotonated PMMA nanoslit and nanochannel, respectively. These values were found to remain relatively constant at pH > 10. In the nanochannel, the width was comparable to the height and the implication is that the surface charge density contribution from the vertical walls, which is typically neglected in the nanoslits, also contributed to ion transport within the channel.[77] Surplus counterions would be attracted into the nanochannel and more coions will be excluded. Despite the contribution of vertical surfaces on the aminated surfaces, at pH $\leq$ 8, $|\sigma|$ was greater in the nanoslits than the nanochannels. This is likely due to incomplete conversion of the carboxyl functional groups into the amine groups in the nanochannels for the reaction conditions reported, a consequence of EDA depletion in the nanochannel with higher surface-to-volume ratio when compared to the nanoslit.

4.3.4 Electrical Model of a Nanofluidic Device

Figure 4.9a shows the experimental setup of a nanofluidic device setup for conductance measurements and the equivalent circuit (Figure 4.9b). The device contained two oppositely placed V-shaped access microchannels (with equal dimensions) and two reservoirs placed at both ends of the microchannel for introducing fluids into the nanochannels. We represented the total voltage applied across reservoirs 1 and 3 as $\boldsymbol{V}$ and the voltage drops across the micro- and nanochannel as $\boldsymbol{V_m}$ and $\boldsymbol{V_n}$, respectively. In this study, it was important that the microchannel dimensions were carefully controlled in such a way that most of the voltage drop across the

device occurred within the nanochannel. The measured electrical resistance, R, across reservoirs 1 and 3 for a given electrolyte was expressed as a combination of the resistance of the microchannels, R_m, and that of the nanochannel, R_n:

$$R = \frac{R_n}{n} + 2R_m \tag{8}$$

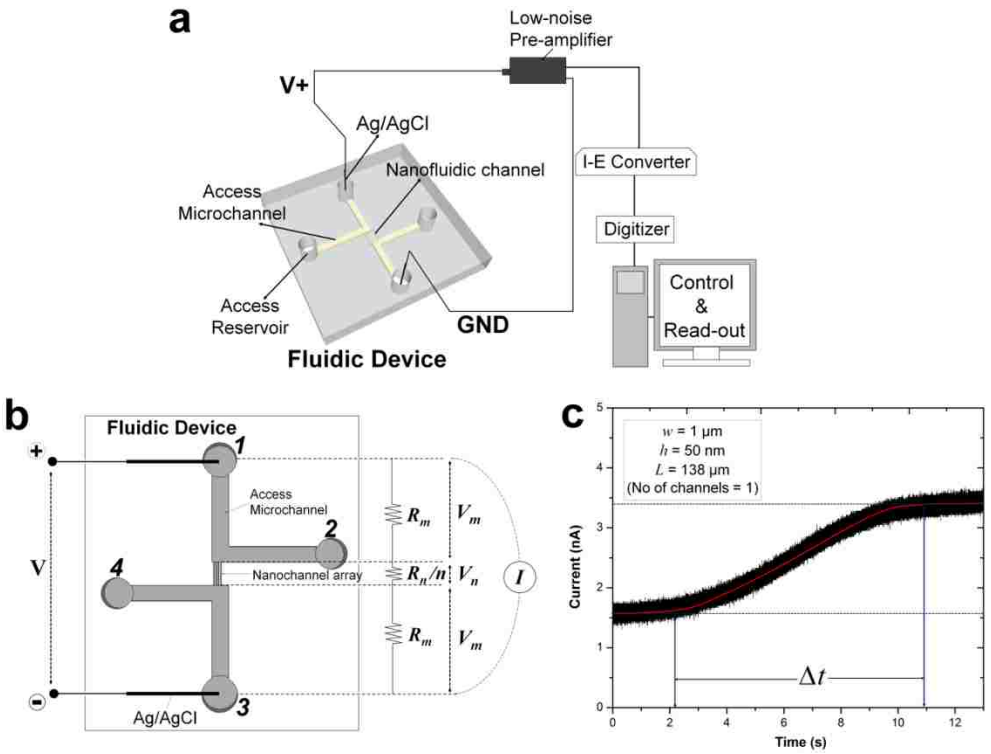

Figure 4.9 (a) Schematic showing the experimental setup for measuring the conductance of the nanochannels. It shows the nanofluidic device interfaced to an axopatch 200B amplifier connected to a Digidata 1440A and computer for readout. (b) Diagram showing the voltage drop and resistances across micro- and nanochannels. (c) Current versus time trace showing the current generated across the nanoslit arising from the replacement of a low ionic strength buffer (0.05 M KCl in 10 mM Tris buffer phosphate buffer) with a higher ionic strength buffer (0.1 M KCl in 10 mM Tris buffer) for the O_2-PMMA nanoslit. The buffer replacement within the nanochannel arises from the electroosmotic flow.

To assess the percent voltage drop across each nanofluidic array, the mixed-scale devices were filled with 0.5 M KCl and the values of R_m and R measured using the Axopatch 200B current amplifier. From these values, R_n/n was calculated for the nanoslits (n = 4) and nanochannels (n = 7) using equation (8) and the voltage drop calculated from;

$$\%V = \left[\left(\frac{R_n}{n}\right)/R\right] \times 100 \quad (9)$$

The data is summarized in Table 4.1

Table 4.1. Measured and calculated electrical resistances across the microchannel R_m, nanoslit/nanochannel R_n and percent voltage drop.

Device	**Dimensions of Nanofluidic device ($l \times w \times h$)**	**R_m (kΩ)**	**R (MΩ)**	**$\frac{R_n}{n}$ (MΩ)**	**Voltage drop (%V)**
Nanoslit	22 μm × 1 μm × 50 nm	501.7 ± 10.2	19.9 ± 1.2	18.9 ± 1.1	95.2 ± 1.1
Nanochannel	45 μm × 50 nm × 50 nm	997.2 ± 12.5	60.9 ± 1.8	58.9 ± 1.6	96.7 ± 1.2

4.3.5 Electroosmotic Flow (EOF) Measurements

The electroosmotic flow is a surface driven fluidic transport that is generated when an external electric field E, applied in the direction tangential to the wall of a channel filled with an electrolyte solution, induces a fluid drag by motion of ions in the EDL. Because of its scalability and ease-of-control, electroosmotic transport has been widely used in many nanofluidic systems. The EOF can be described in terms of a mobility, $\boldsymbol{\mu}_{eof} = \boldsymbol{\upsilon}_{eof}/E$, where $\boldsymbol{\upsilon}_{eof}$ is the steady-state bulk EOF velocity. It is possible to derive an expression for $\boldsymbol{\mu}_{eof}$ from the solvent viscosity η, and the zeta potential ζ using the Helmholtz-Smoluchowski relation:[78]

$$\boldsymbol{\mu}_{eof} = \frac{\epsilon_0 \epsilon_r \zeta}{\eta} \quad (10)$$

The Zeta potential depends on σ_s and λ_D for different electrolyte solutions as noted by the nonlinear Poisson-Boltz-Mann equation:[41, 79]

$$\zeta = \frac{2\ k_B T}{e}\ ln\left[\frac{2\ e\ \sigma_s\ \lambda_D}{\epsilon_r\ \epsilon_0\ k_B T} + \sqrt{1+\left[\frac{\left(e\ \lambda_D / \epsilon_r\ \epsilon_0\ k_B T\right)^2}{4}\right]}\ \right] \quad (11)$$

With ϵ_0 and ϵ_r constants, conditions that cause a change in the σ_s, ζ, λ_D, or η will alter the magnitude of the EOF.

Typically, $\boldsymbol{\mu}_{eof}$ is measured using the well-established current monitoring method.[80] In this work, 0.1 M and 0.05 M KCl solutions were used for the measurement to allow for the generation of a large amount of readable current and measurements at regions with the EDL (see Figure 4.9c for a typical current trace). For this investigation, we fabricated PMMA devices possessing a single nanofluidic channel, 138 µm long, interfaced across two access microchannels as shown in Figure 4.1c and 4.1f. This single channel geometry eliminated errors in migration time that may arise due to preferential filling across an array of nanochannels during electrolyte replacement. A negative EOF value indicated that the solution flow was from cathode to anode and consistent with a positively charged fluidic channel wall. Positive values indicated a negatively charged wall and a reverse EOF.

Previously, we have shown that exposing PMMA to controlled plasma conditions can generate carboxylate groups with a surface coverage of $2.7 \pm 0.5 \times 10^{-9}$ mol/cm^2.[43] We also reported the EOF (pH 7.4) for carboxylated and NH_2-terminated PMMA microfluidic devices to be $4.43 \pm 0.58 \times 10^{-4}$ cm^2/ Vs and $-1.34 \pm 0.21 \times 10^{-4}$ cm^2/Vs, respectively.[37] As shown in Table 4.2, we obtained an EOF mobility of $0.93 \pm 0.03 \times 10^{-4}$ cm^2/Vs and $-0.82 \pm 0.01 \times 10^{-4}$ cm^2/Vs for plasma activated and NH_2-terminated PMMA nanoslits, respectively. For the plasma and NH_2-terminated PMMA nanochannels, the EOF was found to be $1.02 \pm 0.02 \times 10^{-4}$ cm^2/Vs and $-0.75 \pm 0.02 \times 10^{-4}$ cm^2/Vs, respectively. The trend and magnitude of the EOF mobilites observed in the PMMA nanofluidic devices scales with the measured surface charge density in the nanochannel and was consistent with the molecular dynamic simulation results reported by Qiao *et al.*[81] The values reported above for the O_2-PMMA nanochannels were similar to that reported by Menard *et al.*[17] for fused silica nanochannels (≤ 100 nm) measured using 2X TBE, with 2%

polyvinylpyrrolidone (PVP) (0.79 ±0.01 × 10^{-4} cm^2/Vs) and ~35.8 ±4.4% lower when compared to the value obtained in fused silica measured with only 2X TBE (1.58 ±0.01 × 10^{-4} cm^2/Vs).

Table 4.2 Measured and expected EOF mobility values as well as surface charge and zeta potentials for the plasma activated and amine terminated devices investigated at pH 7.8.

Device	Terminating groups	σ_s (mC/m^2)	ζ (mV)	μ_{eof} (cm^2/Vs) × 10^{-4}	
				Expected*	Measured
Nanoslit	O_2-PMMA	- 38.3	- 57.1	4.53	0.93 ± 0.025
	NH_2-PMMA	28.4	45.8	- 3.63	- 0.82 ± 0.012
Nanochannel	O_2-PMMA	- 40.5	- 59.8	4.74	1.02 ± 0.017
	NH_2-PMMA	22.9	38.3	- 3.04	- 0.75 ± 0.021

*Calculated from equation (7) using the values for σ_s and ζ

A possible reason for the low EOF observed in the PMMA nanofluidic device is the low ζ potential of the surface (at the reported experimental conditions). This conclusion is supported by the results from the continuum theory, based on the Poisson–Boltzmann equation for the ion distribution and Navier–Stokes equations for the fluid transport,[78] and the atomistic simulations.[81] Both models show that the EOF in a nanofluidic channel varies almost linearly with the ζ, with the latter model true for surface charge densities $\leq$ 80 mC/m^2.[81] As previously described, the zeta potential depends on the chemistry of the solid–fluid interface and is related to the surface charge density by parameters such as the ionic strength, density of chargeable sites on the surface, their pK_a values and the solution pH, which modulates the rate of dissociation of the surface groups (see Figure 4.8). However, the difference in the EOF values observed for the negatively charged O_2-PMMA devices when compared to the positively charged NH_2-PMMA devices is due to the difference in the distribution of counterions in both devices due to the

different size of the K^+ and Cl^- ions.[76] Therefore, at a fixed pH and electrolyte concentration, as the surface σ_s reduces, ζ is lowered resulting in a corresponding lowering effect on the EOF.

Although the trend of the measured EOF mobilities in the PMMA nanofluidic devices presented in Table 4.2 followed the results of the surface charge density, they remained less than the expected values, which were similar to that observed in the microchannels. The expected values were calculated using $\lambda_D \approx 1.5$ nm and assuming that the μ_{eof} is independent of the size or shape of the channels but rather on the charge distribution around several tens of nanometers from the surface of the channels. However, recent reports have shown that downsizing the size of fluidic channels from the micro- to nano- dimensions can result in reduction of the net flow (EOF) within a channel due to the apparent increase in the viscosity of a fluid confined in the charged nanochannel resulting from the induced counterflow of the streaming potential to the electroosmotic flow.[82-85] This phenomenon, termed electroviscosity, can cause the ratio apparent viscosity to the true viscosity to be as high as 1.3 depending on the material of the channel wall, with spatial size and shape of the channel, the ionic concentration, zeta potential, temperature, dielectric constant and other properties of the liquid.[84] In the derivation of equation (6), the electroviscous effect was not considered. However, due to relatively higher ζ in glass based devices, large streaming potentials are generated resulting in greater electroviscosity in than polymer devices. This can explain why the EOF measured in glass nanoslits at pH 8.5 (~1.3×10^{-3} cm^2/Vs) was lower than that of fused silica and glass capillaries (5×10^{-4} cm^2/Vs and 1.5×10^{-3} cm^2/Vs, respectively)[86] or glass microchannels (4.82×10^{-4} cm^2/Vs).[87] It also described the reason for low EOF observed in a glass microchannel device populated with nanopillars spaced by ~700 nm (1×10^{-5} cm^2/Vs).[88] In PMMA nanoslits and nanochannels, the zeta potential was lower for the conditions reported. The implication is that small streaming currents will be

generated and the contributions of electroviscosity to the EOF will be minimal; hence, the measured EOF will be due majorly due to low surface charge densities.

In summary, our results reveal that in polymer nanofluidic devices (nanoslit or nanochannels), the surface modification scheme adopted, pH and ionic strength of the electrolyte play crucial roles in determining the magnitude of the surface charge density and the extent of electroviscosity effects on the EOF. Parameters that take predominance will depend upon the spatial size of the fluidic device. The effects of Joule heating on the solution viscosity in these channels were considered negligible because very small electric currents were generated due to the high nanochannel resistance compared to microchannels (see Table 4.1).

4.4 Conclusions

In this work, we reported the successful modification of thermoplastic nanoslits and nanochannels for the first time to the best of our knowledge. Carboxyl moieties were generated by plasma activation and amino groups were introduced by reaction with EDC and covalent coupling of EDA molecules. The presence of the surface functional groups was confirmed by wettability/surface energy studies and XPS/FTIR analysis. Changes in surface topography induced from surface modification were assessed using AFM. The effect of pH on the surface charge density σ_s in the nanofluidic devices was reported and the EOF in the plasma activated and amine-terminated devices was measured. The magnitude of σ_s and ζ for the polymer nanofluidic devices were carefully controlled by the choice of substrate, plasma dose and pH of the electrolyte solution.

For the conditions reported in this work, the plasma treated polymer nanoslits and nanochannels were observed to possess $|\sigma_s|$ of 38.2 mC/m^2 and 40.5mC/m^2, respectively, at pH 7.8. These values were lower than that reported for the glass-based counterpart (60 mC/m^2)

thereby making polymer nanochannels a great prospect in applications involving molecular separations. Also, low surface charge densities in fluidic devices help to minimize artifacts of ion exclusion from concentration polarization. The ability to generate positively charged $-NH_3^+$ moieties in a simple modification scheme with $|\sigma_s|$ of 28.4 *m*C/m^2 in the nanoslits and 22.9 *m*C/m^2 in the nanochannel offer a unique venue for performing nanochannel chromatography. The substrate material can potentially serve as the stationary phase without the need for appending different monolayer assemblies to the support and the solute/wall interactions of biomolecules traversing through the nanochannels can be investigated.

The reduced EOF observed in the PMMA devices compared to polymer microchannels and glass nanochannels was likely due to lower surface charge density (and zeta potential) for polymer devices and electroviscosity effects due to confinement. Generally, low EOF is desirable in applications involving DNA analysis for regulation of gene expression, mapping and sequencing since it enables the introduction of these biomolecules into the fluidic channels without the need of EOF suppressors. Polymer nanofluidic devices can be tuned to possess the desired surface functionality and charge density by carefully controlling the modification protocol that is employed. We are currently investigating the electrokinetic properties of other viable thermoplastic substrates for the fabrication of nanochannels.

4.5 References

1. van, H. J. W.; Brunets, N.; Tas, N. R. Capillarity at the Nanoscale. *Chem. Soc. Rev.* 2010, 39, 1096-1114.

2. Anand, R. K.; Sheridan, E.; Knust, K. N.; Crooks, R. M. Bipolar Electrode Focusing: Faradaic Ion Concentration Polarization. *Analytical Chemistry* 2011, 83, 2351-2358.

3. Mani, A.; Zangle, T. A.; Santiago, J. G. On the Propagation of Concentration Polarization from Microchannel−Nanochannel Interfaces Part I: Analytical Model and Characteristic Analysis. *Langmuir* 2009, 25, 3898-3908.

4. Wang, Y.-C.; Stevens, A. L.; Han, J. Million-Fold Preconcentration of Proteins and Peptides by Nanofluidic Filter. *Analytical Chemistry* 2005, 77, 4293-4299.

5. Kim, S. J.; Wang, Y.-C.; Lee, J. H.; Jang, H.; Han, J. Concentration Polarization and Nonlinear Electrokinetic Flow near a Nanofluidic Channel. *Physical Review Letters* 2007, 99, 044501.

6. Kim, S. J.; Li, L. D.; Han, J. Amplified Electrokinetic Response by Concentration Polarization near Nanofluidic Channel. *Langmuir* 2009, 25, 7759-7765.

7. Pu, Q.; Yun, J.; Temkin, H.; Liu, S. Ion-Enrichment and Ion-Depletion Effect of Nanochannel Structures. *Nano Letters* 2004, 4, 1099-1103.

8. Craighead, H. Future Lab-on-a-Chip Technologies for Interrogating Individual Molecules. *Nature (London, U. K.)* 2006, 442, 387-393.

9. Craighead, H. G. Nanostructure Science and Technology: Impact and Prospects for Biology. *J. Vac. Sci. Technol., A* 2003, 21, S216-S221.

10. Saleh, O. A.; Sohn, L. L. An Artificial Nanopore for Molecular Sensing. *Nano Lett.* 2003, 3, 37-38.

11. Menard, L. D.; Mair, C. E.; Woodson, M. E.; Alarie, J. P.; Ramsey, J. M. A Device for Performing Lateral Conductance Measurements on Individual Double-Stranded DNA Molecules. *ACS Nano* 2012, 6, 9087-9094.

12. Zangle, T. A.; Mani, A.; Santiago, J. G. Theory and Experiments of Concentration Polarization and Ion Focusing at Microchannel and Nanochannel Interfaces. *Chemical Society Reviews* 2010, 39, 1014-1035.

13. Piruska, A.; Gong, M.; Sweedler, J. V.; Bohn, P. W. Nanofluidics in Chemical Analysis. *Chemical Society Reviews* 2010, 39, 1060-1072.

14. Tsukahara, T.; Mawatari, K.; Kitamori, T. Integrated Extended-Nano Chemical Systems on a Chip. *Chemical Society Reviews* 2010, 39, 1000-1013.

15. Keyser, U. F.; van Dorp, S.; Lemay, S. G. Tether Forces in DNA Electrophoresis. *Chemical Society Reviews* 2010, 39, 939-947.

16. Pennathur, S.; Baldessari, F.; Santiago, J. G.; Kattah, M. G.; Steinman, J. B.; Utz, P. J. Free-Solution Oligonucleotide Separation in Nanoscale Channels. *Analytical Chemistry* 2007, 79, 8316-8322.

17. Menard, L. D.; Ramsey, J. M. Electrokinetically-Driven Transport of DNA through Focused Ion Beam Milled Nanofluidic Channels. *Analytical Chemistry* 2013, 85, 1146-1153.

18. Kim, S. J.; Ko, S. H.; Kang, K. H.; Han, J. Direct Seawater Desalination by Ion Concentration Polarization (Vol 5, Pg 297, 2010). *Nat. Nanotechnol.* 2013, 8, 609-609.

19. Cheng, L.-J.; Guo, L. J. Nanofluidic Diodes. *Chemical Society Reviews* 2010, 39, 923-938.

20. Persson, F.; Tegenfeldt, J. O. DNA in Nanochannels-Directly Visualizing Genomic Information. *Chem. Soc. Rev.* 2010, 39, 985-999.

21. Levy, S. L.; Craighead, H. G. DNA Manipulation, Sorting, and Mapping in Nanofluidic Systems. *Chem. Soc. Rev.* 2010, 39, 1133-1152.

22. Liang, X.; Chou, S. Y. Nanogap Detector inside Nanofluidic Channel for Fast Real-Time Label-Free DNA Analysis. *Nano Letters* 2008, 8, 1472-1476.

23. Reccius, C. H.; Mannion, J. T.; Cross, J. D.; Craighead, H. G. Compression and Free Expansion of Single DNA Molecules in Nanochannels. *Physical Review Letters* 2005, 95, 268101.

24. Levy, S. L.; Mannion, J. T.; Cheng, J.; Reccius, C. H.; Craighead, H. G. Entropic Unfolding of DNA Molecules in Nanofluidic Channels. *Nano Letters* 2008, 8, 3839-3844.

25. Daiguji, H. Ion Transport in Nanofluidic Channels. *Chemical Society Reviews* 2010, 39, 901-911.

26. Han, J.; Craighead, H. G. Separation of Long DNA Molecules in a Microfabricated Entropic Trap Array. *Science* 2000, 288, 1026-1029.

27. Plecis, A.; Schoch, R. B.; Renaud, P. Ionic Transport Phenomena in Nanofluidics: Experimental and Theoretical Study of the Exclusion-Enrichment Effect on a Chip. *Nano Letters* 2005, 5, 1147-1155.

28. Stein, D.; Kruithof, M.; Dekker, C. Surface-Charge-Governed Ion Transport in Nanofluidic Channels. *Physical Review Letters* 2004, 93, 035901.

29. Chantiwas, R.; Park, S.; Soper, S. A.; Kim, B. C.; Takayama, S.; Sunkara, V.; Hwang, H.; Cho, Y.-K. Flexible Fabrication and Applications of Polymer Nanochannels and Nanoslits. *Chemical Society Reviews* 2011, 40, 3677-3702.

30. Chou, S. Y.; Krauss, P. R.; Renstrom, P. J. Imprint of Sub-25 Nm Vias and Trenches in Polymers. *Applied Physics Letters* 1995, 67, 3114-3116.

31. Chantiwas, R.; Hupert, M. L.; Pullagurla, S. R.; Balamurugan, S.; Tamarit-Lopez, J.; Park, S.; Datta, P.; Goettert, J.; Cho, Y.-K.; Soper, S. A. Simple Replication Methods for Producing Nanoslits in Thermoplastics and the Transport Dynamics of Double-Stranded DNA through These Slits. *Lab on a Chip* 2010, 10, 3255-3264.

32. Wu, J.; Chantiwas, R.; Amirsadeghi, A.; Soper, S. A.; Park, S. Complete Plastic Nanofluidic Devices for DNA Analysis Via Direct Imprinting with Polymer Stamps. *Lab on a Chip* 2011, 11, 2984-2989.

33. Abgrall, P.; Low, L.-N.; Nguyen, N.-T. Fabrication of Planar Nanofluidic Channels in a Thermoplastic by Hot-Embossing and Thermal Bonding. *Lab on a Chip* 2007, 7, 520-522.

34. Rotting, O.; Ropke, W.; Becker, H.; Gartner, C. Polymer Microfabrication Technologies. *Microsyst. Technol.* 2002, 8, 32-36.

35. Soper, S. A.; Henry, A. C.; Vaidya, B.; Galloway, M.; Wabuyele, M.; McCarley, R. L. Surface Modification of Polymer-Based Microfluidic Devices. *Analytica Chimica Acta* 2002, 470, 87-99.

36. Hawthorne, S. B.; Yang, Y.; Grabanski, C. B.; Miller, D. J.; Lee, M. L. Response to Comments on Adsorption Versus Absorption of Polychlorinated Biphenyls onto Solid-Phase Microextraction Coatings. *Anal. Chem.* 2000, 72, 642-643.

37. Llopis, S. L.; Osiri, J.; Soper, S. A. Surface Modification of Poly(Methyl Methacrylate) Microfluidic Devices for High-Resolution Separations of Single-Stranded DNA. *Electrophoresis* 2007, 28, 984-993.

38. Jackson, J. M.; Witek, M. A.; Hupert, M. L.; Brady, C.; Pullagurla, S.; Kamande, J.; Aufforth, R. D.; Tignanelli, C. J.; Torphy, R. J.; Yeh, J. J.; Soper, S. A. Uv Activation of Polymeric High Aspect Ratio Microstructures: Ramifications in Antibody Surface Loading for Circulating Tumor Cell Selection. *Lab on a Chip* 2014, 14, 106-117.

39. Henry, A. C.; Tutt, T. J.; Galloway, M.; Davidson, Y. Y.; McWhorter, C. S.; Soper, S. A.; McCarley, R. L. Surface Modification of Poly(Methyl Methacrylate) Used in the Fabrication of Microanalytical Devices. *Analytical Chemistry* 2000, 72, 5331-5337.

40. Chan, C. M.; Ko, T. M.; Hiraoka, H. Polymer Surface Modification by Plasmas and Photons. *Surface Science Reports* 1996, 24, 1-54.

41. Chai, J.; Lu, F.; Li, B.; Kwok, D. Y. Wettability Interpretation of Oxygen Plasma Modified Poly(Methyl Methacrylate). *Langmuir* 2004, 20, 10919-10927.

42. Wei, S.; Vaidya, B.; Patel, A. B.; Soper, S. A.; McCarley, R. L. Photochemically Patterned Poly(Methyl Methacrylate) Surfaces Used in the Fabrication of Microanalytical Devices. *J. Phys. Chem. B* 2005, 109, 16988-16996.

43. Xu, F.; Datta, P.; Wang, H.; Gurung, S.; Hashimoto, M.; Wei, S.; Goettert, J.; McCarley, R. L.; Soper, S. A. Polymer Microfluidic Chips with Integrated Waveguides for Reading Microarrays. *Analytical Chemistry* 2007, 79, 9007-9013.

44. Yang, Z.; Min, Z. D. Cardiac Markers and Their Point-of-Care Testing for Diagnosis of Acute Myocardial Infarction. *Clin Biochem* 2006, 39, 771-80.

45. Martins, D. C.; Chu, V.; Conde, J. P. The Effect of the Surface Functionalization and the Electrolyte Concentration on the Electrical Conductance of Silica Nanochannels. *Biomicrofluidics* 2013, 7, -.

46. Karnik, R.; Castelino, K.; Fan, R.; Yang, P.; Majumdar, A. Effects of Biological Reactions and Modifications on Conductance of Nanofluidic Channels. *Nano Letters* 2005, 5, 1638-1642.

47. Tas, N. R.; Berenschot, J. W.; Mela, P.; Jansen, H. V.; Elwenspoek, M.; van den Berg, A. 2d-Confined Nanochannels Fabricated by Conventional Micromachining. *Nano Letters* 2002, 2, 1031-1032.

48. Menard, L. D.; Ramsey, J. M. Fabrication of Sub-5 Nm Nanochannels in Insulating Substrates Using Focused Ion Beam Milling. *Nano Letters* 2011, 11, 512-517.

49. Huh, D.; Mills, K. L.; Zhu, X. Y.; Burns, M. A.; Thouless, M. D.; Takayama, S. Tuneable Elastomeric Nanochannels for Nanofluidic Manipulation. *Nat. Mater.* 2007, 6, 424-428.

50. Chung, S.; Lee, J. H.; Moon, M.-W.; Han, J.; Kamm, R. D. Non-Lithographic Wrinkle Nanochannels for Protein Preconcentration. *Adv. Mater. (Weinheim, Ger.)* 2008, 20, 3011-3016.

51. Park, K. D.; Lee, S. W.; Takama, N.; Fujii, T.; Kim, B. J. Arbitrary-Shaped Nanochannels Fabricated by Polymeric Deformation to Achieve Single DNA Stretching. *Microelectron. Eng.* 2009, 86, 1385-1388.

52. Park, S.-m.; Huh, Y. S.; Graighead, H. G.; Erickson, D. A Method for Nanofluidic Device Prototyping Using Elastomeric Collapse. *Proc. Natl. Acad. Sci. U. S. A.* 2009, 106, 15549-15554, S15549/1-S15549/6.

53. Shao, P. E.; van Kan, A.; Wang, L. P.; Ansari, K.; Bettiol, A. A.; Watt, F. Fabrication of Enclosed Nanochannels in Poly(Methylmethacrylate) Using Proton Beam Writing and Thermal Bonding. *Applied Physics Letters* 2006, 88, -.

54. Kwak, R.; Kim, S. J.; Han, J. Continuous-Flow Biomolecule and Cell Concentrator by Ion Concentration Polarization. *Anal. Chem. (Washington, DC, U. S.)* 2011, 83, 7348-7355.

55. Schoch, R. B.; Renaud, P. Ion Transport through Nanoslits Dominated by the Effective Surface Charge. *Applied Physics Letters* 2005, 86, 25311 1-3.

56. Larson, R. A. *Reaction Mechanisms in Environmental Organic Chemistry*. Lewis Publishers: Boca Raton, [Fla.], 1994.

57. Seah, M. P.; Dench, W. A. Quantitative Electron Spectroscopy of Surfaces: A Standard Data Base for Electron Inelastic Mean Free Paths in Solids. *Surface and Interface Analysis* 1979, 1, 2-11.

58. Mitchell, D. F.; Clark, K. B.; Bardwell, J. A.; Lennard, W. N.; Massoumi, G. R.; Mitchell, I. V. Film Thickness Measurements of Sio2 by Xps. *Surface and Interface Analysis* 1994, 21, 44-50.

59. Powell, C. J.; Jablonski, A.; Tanuma, S.; Penn, D. R. Effects of Elastic and Inelastic Electron Scattering on Quantitative Surface Analyses by Aes and Xps. *Journal of Electron Spectroscopy and Related Phenomena* 1994, 68, 605-616.

60. Chan-Park, M. B.; Yan, Y.; Neo, W. K.; Zhou, W.; Zhang, J.; Yue, C. Y. Fabrication of High Aspect Ratio Poly(Ethylene Glycol)-Containing Microstructures by Uv Embossing. *Langmuir* 2003, 19, 4371-4380.

61. Becker, H.; Gärtner, C. Polymer Microfabrication Technologies for Microfluidic Systems. *Anal Bioanal Chem* 2008, 390, 89-111.

62. Kwok, D. Y.; Neumann, A. W. Contact Angle Measurement and Contact Angle Interpretation. *Advances in Colloid and Interface Science* 1999, 81, 167-249.

63. Seidel, C.; Kopf, H.; Gotsmann, B.; Vieth, T.; Fuchs, H.; Reihs, K. Ar Plasma Treated and Al-Metalized Polycarbonate: A Xps, Mass Spectroscopy and Sfm Study. *Appl. Surf. Sci.* 1999, 150, 19-33.

64. Ben, A. S.; Baud, G.; Jacquet, M.; Nanse, G.; Fioux, P.; Nardin, M. Xps Characterization of Plasma-Treated and Alumina-Coated Pmma. *Appl. Surf. Sci.* 2000, 153, 172-183.

65. Gröning, P.; Collaud, M.; Dietler, G.; Schlapbach, L. Plasma Modification of Polymethylmethacrylate and Polyethyleneterephthalate Surfaces. *Journal of Applied Physics* 1994, 76, 887-892.

66. Messinger, R. J.; Squires, T. M. Suppression of Electro-Osmotic Flow by Surface Roughness. *Physical Review Letters* 2010, 105.

67. Ziarani, A. S.; Mohamad, A. A. Effect of Wall Roughness on the Slip of Fluid in a Microchannel. *Nanoscale and microscale thermophysical engineering* 2008, 12, 154-169.

68. Park, H. M.; Lee, H. D. Effects of Wall Roughness and Velocity Slip on Streaming Potential of Microchannels. *International Journal of Heat and Mass Transfer* 2012, 55, 3295-3306.

69. Wang, M.; Wang, J.; Chen, S. Roughness and Cavitations Effects on Electro-Osmotic Flows in Rough Microchannels Using the Lattice Poisson–Boltzmann Methods. *Journal of Computational Physics* 2007, 226, 836-851.

70. Kim, D.; Darve, E. Molecular Dynamics Simulation of Electro-Osmotic Flows in Rough Wall Nanochannels. *Physical Review E* 2006, 73, 051203.

71. Wenzel, R. N. Surface Roughness and Contact Angle. *The Journal of Physical and Colloid Chemistry* 1949, 53, 1466-1467.

72. Schoch, R. B.; Han, J.; Renaud, P. Transport Phenomena in Nanofluidics. *Reviews of Modern Physics* 2008, 80, 839-883.

73. Sonnefeld, J.; Göbel, A.; Vogelsberger, W. Surface Charge Density on Spherical Silica Particles in Aqueous Alkali Chloride Solutions. *Colloid Polym Sci* 1995, 273, 926-931.

74. Daiguji, H.; Yang, P.; Majumdar, A. Ion Transport in Nanofluidic Channels. *Nano Letters* 2003, 4, 137-142.

75. Meisenberg, G. *Principles of Medical Biochemistry*. Mosby Elsevier: Philadelphia, 2006.

76. Qiao, R.; Aluru, N. R. Atomistic Simulation of Kcl Transport in Charged Silicon Nanochannels: Interfacial Effects. *Colloids and Surfaces A: Physicochemical and Engineering Aspects* 2005, 267, 103-109.

77. Bhattacharyya, S.; Zheng, Z.; Conlisk, A. Electro-Osmotic Flow in Two-Dimensional Charged Micro-and Nanochannels. *Journal of Fluid Mechanics* 2005, 540, 247-268.

78. Slater, G.; Tessier, F.; Kopecka, K. The Electroosmotic Flow (Eof). In *Microengineering in Biotechnology*, Hughes, M. P.; Hoettges, K. F., Eds. Humana Press: 2010; Vol. 583, pp 121-134.

79. Kirby, B. J.; Hasselbrink, E. F., Jr. Zeta Potential of Microfluidic Substrates: 2. Data for Polymers. *Electrophoresis* 2004, 25, 203-213.

80. Huang, X.; Gordon, M. J.; Zare, R. N. Current-Monitoring Method for Measuring the Electroosmotic Flow Rate in Capillary Zone Electrophoresis. *Anal. Chem.* 1988, 60, 1837-8.

81. Qiao, R.; Aluru, N. R. Scaling of Electrokinetic Transport in Nanometer Channels. *Langmuir* 2005, 21, 8972-8977.

82. Tas, N. R.; Haneveld, J.; Jansen, H. V.; Elwenspoek, M.; van den Berg, A. Capillary Filling Speed of Water in Nanochannels. *Applied Physics Letters* 2004, 85, 3274-3276.

83. Kaji, N.; Ogawa, R.; Oki, A.; Horiike, Y.; Tokeshi, M.; Baba, Y. Study of Water Properties in Nanospace. *Anal Bioanal Chem* 2006, 386, 759-764.

84. Wang, M.; Chang, C.-C.; Yang, R.-J. Electroviscous Effects in Nanofluidic Channels. *The Journal of Chemical Physics* 2010, 132, -.

85. Neogi, P.; Ruckenstein, E. Viscoelectric Effects in Reverse Osmosis. *Journal of Colloid and Interface Science* 1981, 79, 159-169.

86. Hug, T.; Rooij, N. d.; Staufer, U. Fabrication and Electroosmotic Flow Measurements in Micro- and Nanofluidic Channels. *Microfluid. Nanofluid.* 2006, 2, 117-124.

87. Milanova, D.; Chambers, R. D.; Bahga, S. S.; Santiago, J. G. Effect of Pvp on the Electroosmotic Mobility of Wet-Etched Glass Microchannels. *ELECTROPHORESIS* 2012, 33, 3259-3262.

88. Yasui, T.; Kaji, N.; Mohamadi, M. R.; Okamoto, Y.; Tokeshi, M.; Horiike, Y.; Baba, Y. Electroosmotic Flow in Microchannels with Nanostructures. *ACS Nano* 2011, 5, 7775-7780.

CHAPTER 5 FUTURE WORK: INTEGRATION OF TASK SPECIFIC MODULES TO DEVELOP A MODULAR FLUIDIC BIOPROCESSOR FOR POINT-OF-CARE DIAGNOSIS OF STROKE

5.1 Introduction

Emerging innovations of point-of-care (POC) diagnostic test devices is due to their ability to provide rapid results on an ever expanding range of medical tests.[1] The need for extremely simple (in terms of use without need for trained personnel) devices in POC applications has fueled an interest in the construction of field deployable instruments using microfluidics.[2] As mentioned earlier in chapter 1, various biomarkers have been reviewed and their role in clinical utility has been signified. The need for a POC device arises from the longer times required for clinical distinction of subtypes of stroke with existing neuroimaging methods and shorter time window available for treatment and patient management. POC devices also reduce the turn-around-time (TAT) for the identification of stroke subtype in a prehospital setting as a confirmation test for diagnosis.

Attractive features offered by microfluidics like low consumption of reagents and samples, miniaturization, and fast turnaround time for analysis to perform various laboratory functions and assessments make them a perfect fit for point-of-care diagnostic devices. These devices are fully enclosed due to which a there is a reduction in contaminant carryover, sample dilution and losses. In addition, microfluidics is a versatile technology which offer features such as feasibility of integrating electronics, reconfigurability, the possibility of automation and high throughput, miniaturization of complex fluid handling and integrated detection. Various proof- of-concept studies have shown the advantages of lab-on-a-chip (LOC) systems over laboratory testing.[3-6] Transformation of microfluidic systems into point-of-care diagnostic systems from a laboratory into clinical setting requires automation and also efficient strategies for combining several

individually tested modules including pumping, valving, mixing and sample preparation obviating the need for moving or spinning components. The ultimate goal is to achieve resolution & sensitivity similar to benchtop instruments.

5.2 Proposed Molecular Processing Strategy

We focus on developing a portable, automated instrument which would serve as a near patient technology for the diagnosis of ischemic and/or hemorrhagic stroke using mRNA expression profiling directly from whole blood within a processing time <20 min to accommodate effective therapeutic treatment of this disease. This will be achieved by developing a fluidic bio-processor fabricated in polymers via micro-replication technology and integrating task specific modules on a fluidic motherboard. The material selected for each module will depend selected for each module based upon the application needed to produce optimal performance. All the relevant steps required for the molecular assay are depicted in Figure 5.1.

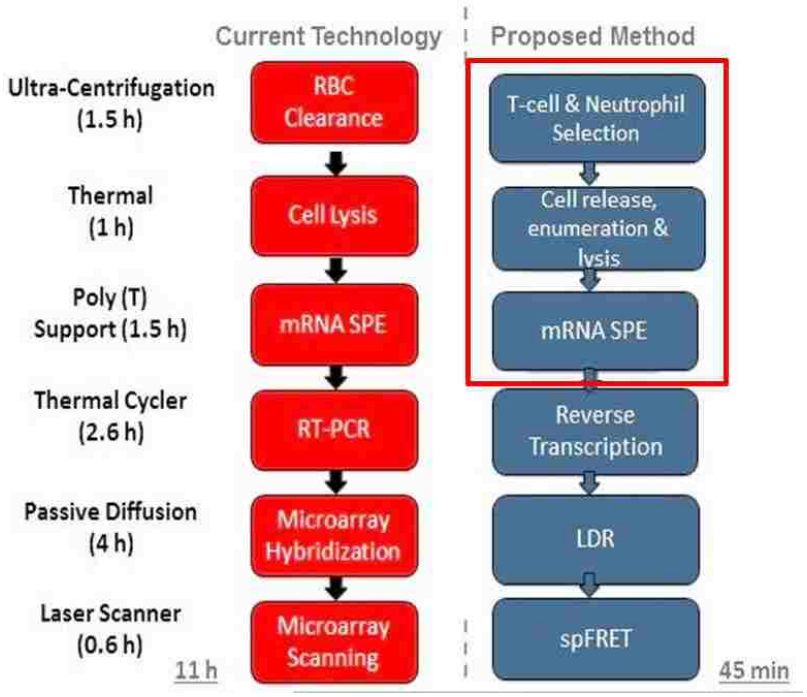

Figure 5.1 Processing pipelines using a conventional bench-top strategy for processing mRNAs specifically for obtaining expression data and the processing pipeline that will be employed in POC system for the rapid reporting of mRNA signatures associated with stroke.

This includes i) cell isolation (*i.e.*, positive selection of T-cells and neutrophils), ii) cell lysis of isolated cells, extraction/purification of the target material (mRNA), iii) thermal enzymatic reactions including reverse transcription (RT) to build cDNAs iv) Ligase detection reaction (LDR) to generate molecular beacons unique to each mRNA biomarker using primers that carry reporter sequences for the target and readout of successful ligation events using single pair Fluorescence Resonance Energy Transfer (spFRET).The use of spFRET obviates the need for a PCR step, which not only reduces processing time, but also produces exquisite analytical sensitivity. The most important and notable feature of the molecular processing strategy delineated in Figure 5.1, is the TAT. When compared to a conventional approach for mRNA expression profiling, TAT is projected to be ~45 min for the proposed strategy compared to the conventional approach, which may require nearly 11 h to secure similar information. Next sections will provide a description of each processing step and the fluidic device for its implementation. Detailed description of each of these modules will be given in the next sections.

5.3 Fluidic Bioprocessor for mRNA Expression Profiling

A fully integrated polymer-based fluidic bio-processor for mRNA expression profiling will consist of individual or a group of processing steps poised on a single module and systems built from modules connected to a fluidic motherboard. All these modules will be combined in plug and play like setup.The primary advantages of this design approach include; (1) the ability to match the material properties to the processing step(s) situated on the chip; (2) allow individual testing of the modules to optimize performance; (3) simplify the fabrication process for producing integrated systems; and (4) provide flexibility in assembling modules to accommodate different assay strategies. Wang et al. demonstrated this approach for POC detection of

Mycobacterium Tuberculosis (Mtb).[7] This system could determine the multi-drug resistance of Mtb resulting from strains that fail to respond to first-line drugs, such as rifampin.

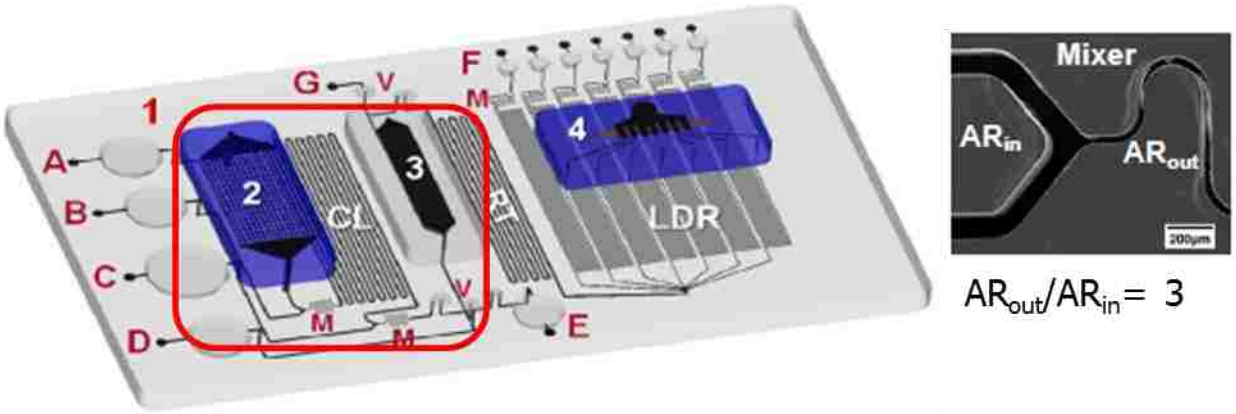

Figure 5.2 Fluidic bio-processor for the analysis of mRNAs in PBMCs. The fluidic bio-processor has 3 modules that are used for positive cell selection (T-cells and neutrophils), (2) SPE isolation/purification of RNA (3) and spFRET readout (4). All these modules will be "plugged" into a fluidic motherboard. Also shown are locations of on-chip valves (V) pumps (A-F) and high-aspect ratio mixers (M). A – sample input; B – lysing buffer; C – SPE buffer; D – ethanol; E – RT cocktail; F – LDR cocktail; G – connection to off-chip vacuum pump. Box in red shows the modules which have been described in previous chapters.

The proposed fluidic bio-processor shown schematically in Figure 5.2 consists of different modules. In chapters 2 & 3, we have focused our efforts to isolate T-cells and neutrophils. For this application, cell sorting module was fabricated in COC due to its high optical transparency and uniform modification of high aspect-ratio channels.[8] We were able successfully isolate the cells of interest and isolate TRNA from the lysate of these cells both by commercially available silica columns and also by using UV activated PC SPE module. The RNA SPE module and fluidic motherboard are made from PC due to its relatively high glass transition temperature to allow it to withstand the temperatures required for the thermal reactions and also its unique characteristic to allow the SPE of nucleic acids For the initial studies, TRNA was reverse transcribed to cDNA and amplified via bench top PCR.[9-11] Gene expression studies were shown for a housekeeping gene (GAPDH), a gene overexpressed in ischemic stroke event (S100A9), T-

cell specific gene (TCRB) and neutrophil specific gene (FPR1). However, gene expression of mRNA's specific for ischemic and hemorrhagic stroke are yet to be studied. In order to reduce the final TAT, gene expression analysis can also be performed by carrying out reverse transcription (RT) in a continuous flow mode on a microfluidic chip. An mRNA will be copied to cDNA in continuous flow reverse transcription (CFRT) using an oligo dT primer. CFRT's will be used for the RT and LDRs with the devices optimized for processing speed and product yield. Reaction time (RT phase) and the number of thermal cycles (LDR phase) required for obtaining viable quantitative information from the mRNA transcripts required for the stroke diagnosis will be investigated.

5.4 Fabrication of Microfluidic Modules

Polymer microchips can be replicated from metal masters using either hot embossing or injection molding with the principle advantages of this fabrication protocol being; (1) the ability to produce large quantities of microchips at low-cost; (2) once the master is made, a wide selection of materials can be used for the final parts without requiring additional lithographic processing; (3) mixed-scale, multi-level and double-sided molding can be used to fabricate the prerequisite microchips. The metal masters can be made using a variety of techniques, including UV-*LiGA*, X-ray *LiGA* or high precision micromilling, with the choice predicated on the required structures and the stage of development of the microchip; we have developed the infrastructure to generate masters using all of these techniques.[10, 12-14] As the fluidic bio-processor is to be used for diagnostic applications requiring one-time use operation, it is critical to simplify the manufacturing of this fluidic processor to reduce chip cost.

As seen from Figure 5.2 the fluidic bioprocessor will consist of 3 modules with 1 made in PMMA and another in the appropriate waveguiding material (blue, see Figure 5.2) and the third

made from PC (light gray). The fluidic motherboard in which the modules will be inserted using the appropriate interconnect technology will be made from PC. The modules and motherboard will be replicated from metal masters fabricated by lithographic or non-lithographic techniques with the selected technique based on the required dimensional features of each. These masters will be then used to replicate parts in the appropriate polymeric substrate using hot-embossing.[12, 14, 15] The spFRET readout module must be made of a polymeric material that has favorable optical properties and also, supports waveguiding.

For structures possessing lateral dimensions below 20 μm and aspect ratios exceeding 5:1, UV-LiGA must be used to make the mold master. For the hemispherical lenses, we will use X-ray LiGA to fabricate the mold master. Whichever fabrication technique we use, the master is used to replicate the appropriate parts via hot embossing (Jenoptik HEX02). Through-holes required as the interconnects between modules can be made using excimer laser drilling, which can machine holes ~50 μm in diameter through a substrate as thick as 2 mm.[10] The exact channel lengths and cross-sectional dimensions will be determined from experimental results. As can be seen in Figure 5.2, several mixers in the fluidic motherboard are required. Because flow in microchannels is laminar (Re << 100), the rate of mixing between two miscible fluids is determined by molecular diffusion. To facilitate mixing between sample and reagents and to keep the bio-processor operation simple, we will employ a Y-shaped, high-aspect ratio (AR, where AR = channel height / channel width) passive micromixer configuration (see Figure 5.2). In this type of mixer, input streams are fed into a narrow but deep channel, which effectively increases the contact area between the two streams and reduces diffusional distances. The increased channel depth also keeps the pressure drop low when feeding liquids into this narrow channel.

5.5 LDR/spFRET for mRNA Quantitation

The molecular assay's foundation is based on the ability to identify unique sequences from mRNAs (actually cDNA) using an LDR coupled to spFRET.[16] In this project, we do not will expression profile single cells, but detect single mRNA molecules through their respective cDNA surrogates subjected to a LDR (superior sequence specificity for single base variations[17])

to form molecular beacons undergoing spFRET that are digitally counted to provide exquisite analytical sensitivity. The major advantages of this single molecule detection in molecular analyses include; (1) the ability to alleviate the need for amplifying the target material via PCR, which produces potential difficulties in obtaining quantitative information; (2) reduces the number of processing steps and; (3) significantly reduces processing time and assay cost.

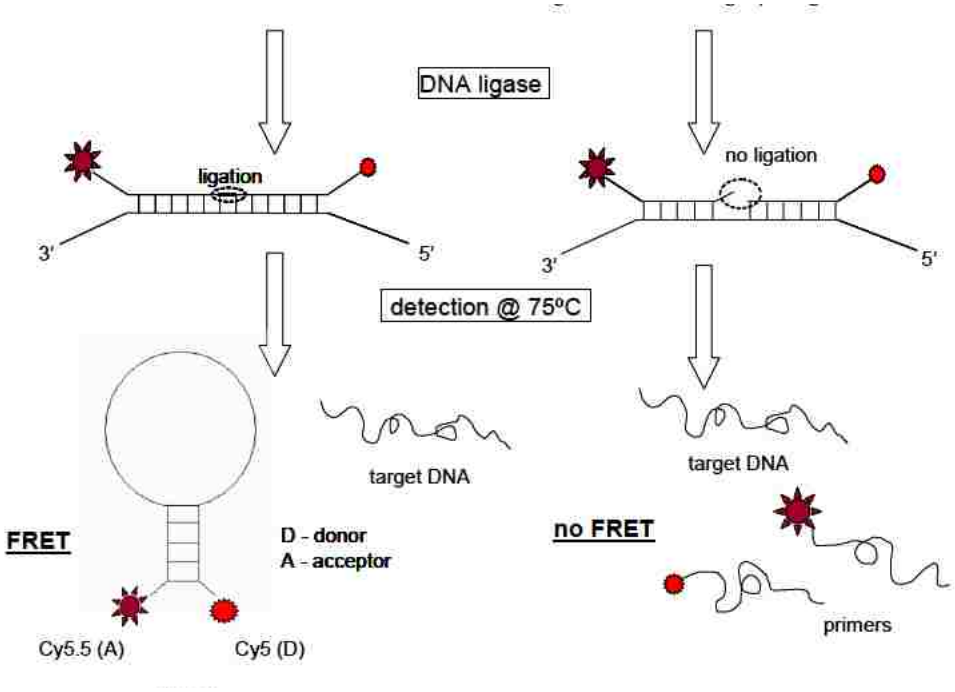

Figure 5.3 Illustration of LDR-spFRET assay[18]

LDR involves the use of two primers that recognize a reporter sequence of the target, which in this case is a cDNA, and ligates the two primers only if there is complete complementarity between the primers and the cDNA. If this condition is met, the primers are successfully ligated,

forming a molecular beacon bringing the donor/acceptor dyes into close proximity to allow for spFRET to occur (see Figure 5.3). If the primers are not perfectly matched to the reporter sequence of the cDNA, no ligation occurs and consequently, no spFRET results. LDR-spFRET provided the necessary specificity and sensitivity to detect single point mutations in as little as ~600 copies of human genomic DNA without PCR at a level of 1 mutant per 1,000 wild- type sequences in less than 5 min.[16]

5.6 Inter and Intra Modular Assembly

In this phase of the project, the individual fluidic modules required for each processing step of the molecular assay will be integrated to form a fluidic bio-processor consisting of task-specific modules assembled to a fluidic motherboard using the appropriate interconnect technologies. Super hydrophobic seals will be used to prevent "leakage" of fluid at the interconnects. Various interconnect geometries and architectures will be evaluated as well. To align the modules during assembly, V-grooves and pins (kinematic constraints) will be used. Effective thermal isolation between modules will also be investigated and optimized.

While the proposed system is targeted for field diagnosis of stroke using mRNA biomarkers, the system can be envisioned for other applications as well that require quantitative expression analysis of mRNA. In the case of stroke diagnoses, the fluidic bio-processor can be configured to detect other biomarkers necessary for the diagnoses, such as serum proteins, without hardware reconfiguration.

5.7 References

1. Menendez-Botet, C.; Celia, J. M.-B. Principles & Practices of Point-of-Care Testing. *Clinical chemistry (Baltimore, Md.)* 2003, 49, 1424.

2. Whitesides, G. M. The origins and the future of microfluidics. *Nature (London, U. K.)* 2006, 442, 368-373.

3. Hong, J. W.; Quake, S. R. Integrated nanoliter systems. *Nat. Biotechnol.* 2003, 21, 1179-1183.

4. Janasek, D.; Franzke, J.; Manz, A. Scaling and the design of miniaturized chemical-analysis systems. *Nature (London, U. K.)* 2006, 442, 374-380.

5. Lion, N.; Reymond, F.; Girault, H. H.; Rossier, J. S. Why the move to microfluidics for protein analysis? *Curr. Opin. Biotechnol.* 2003, 15, 31-37.

6. Manz, A.; Eijkel, J. C. T. Miniaturization and chip technology. What can we expect? *Pure Appl. Chem.* 2001, 73, 1555-1561.

7. Wang, H.; Chen, H.-W.; Hupert, M. L.; Chen, P.-C.; Datta, P.; Pittman, T. L.; Goettert, J.; Murphy, M. C.; Williams, D.; Barany, F.; Soper, S. A. Fully integrated thermoplastic genosensor for the highly sensitive detection and identification of multi-drug-resistant tuberculosis. *Angew. Chem., Int. Ed.* 2012, 51, 4349-4353, S4349/1-S4349/10.

8. Jackson, J. M.; Witek, M. A.; Hupert, M. L.; Brady, C.; Pullagurla, S.; Kamande, J.; Aufforth, R. D.; Tignanelli, C. J.; Torphy, R. J.; Yeh, J. J.; Soper, S. A. UV activation of polymeric high aspect ratio microstructures: ramifications in antibody surface loading for circulating tumor cell selection. *Lab on a Chip* 2014.

9. Hashimoto, M.; Chen, P.-C.; Mitchell, M. W.; Nikitopoulos, D. E.; Soper, S. A.; Murphy, M. C. Rapid PCR in a continuous flow device. *Lab Chip* 2004, 4, 638-645.

10. Witek, M. A.; Hupert, M. L.; Park, D. S. W.; Fears, K.; Murphy, M. C.; Soper, S. A. 96-Well Polycarbonate-Based Microfluidic Titer Plate for High-Throughput Purification of DNA and RNA. *Anal. Chem. (Washington, DC, U. S.)* 2008, 80, 3483-3491.

11. Witek, M. A.; Llopis, S. D.; Wheatley, A.; McCarley, R. L.; Soper, S. A. Purification and preconcentration of genomic DNA from whole cell lysates using photoactivated polycarbonate (PPC) microfluidic chips. *Nucleic Acids Res.* 2006, 34, e74/1-e74/9.

12. Ford, S. M.; Kar, B.; McWhorter, S.; Davies, J.; Soper, S. A.; Klopf, M.; Calderon, G.; Saile, V. Microcapillary electrophoresis devices fabricated using polymeric substrates and x-ray lithography. *J. Microcolumn Sep.* 1998, 10, 413-422.

13. Hupert, M. L.; Guy, W. J.; Llopis, S. D.; Shadpour, H.; Rani, S.; Nikitopoulos, D. E.; Soper, S. A. Evaluation of micromilled metal mold masters for the replication of microchip electrophoresis devices. *Microfluid. Nanofluid.* 2007, 3, 1-11.

14. Ford, S. M.; Davies, J.; Kar, B.; Qi, S. D.; McWhorter, S.; Soper, S. A.; Malek, C. K. Micromachining in plastics using X-ray lithography for the fabrication of microelectrophoresis devices. *J Biomech Eng* 1999, 121, 13-21.

15. Soper, S. A.; Ford, S. M.; Qi, S.; McCarley, R. L.; Kelly, K.; Murphy, M. C. Polymeric microelectromechanical systems. *Anal. Chem.* 2000, 72, 643A-651A.

16. Wabuyele, M. B.; Farquar, H.; Stryjewski, W.; Hammer, R. P.; Soper, S. A.; Cheng, Y.-W.; Barany, F. Approaching Real-Time Molecular Diagnostics: Single-Pair Fluorescence Resonance Energy Transfer (spFRET) Detection for the Analysis of Low Abundant Point Mutations in K-ras Oncogenes. *J. Am. Chem. Soc.* 2003, 125, 6937-6945.

17. Pingle, M. R.; Granger, K.; Feinberg, P.; Shatsky, R.; Sterling, B.; Rundell, M.; Spitzer, E.; Larone, D.; Golightly, L.; Barany, F. Multiplexed identification of blood-borne bacterial pathogens by use of a novel 16S rRNA gene PCR-ligase detection reaction-capillary electrophoresis assay. *J. Clin. Microbiol.* 2007, 45, 1927-1935

18. Peng, Z.; Soper, S. A.; Pingle, M. R.; Barany, F.; Davis, L. M. Ligase Detection Reaction Generation of Reverse Molecular Beacons for Near Real-Time Analysis of Bacterial Pathogens Using Single-Pair Fluorescence Resonance Energy Transfer and a Cyclic Olefin Copolymer Microfluidic Chip. *Anal. Chem. (Washington, DC, U. S.)* 2010, 82, 9727-9735.

APPENDIX:PERMISSIONS

ELSEVIER LICENSE
TERMS AND CONDITIONS

Apr 09, 2014

This is a License Agreement between SWATHI REDDY PULLAGURLA ("You") and Elsevier ("Elsevier") provided by Copyright Clearance Center ("CCC"). The license consists of your order details, the terms and conditions provided by Elsevier, and the payment terms and conditions.

All payments must be made in full to CCC. For payment instructions, please see information listed at the bottom of this form.

Supplier	Elsevier Limited The Boulevard,Langford Lane Kidlington,Oxford,OX5 1GB,UK
Registered Company Number	1982084
Customer name	SWATHI REDDY PULLAGURLA
Customer address	924 NORTH HERITAGE CIRCLE CHAPEL HILL, NC 27516
License number	3364900638940
License date	Apr 09, 2014
Licensed content publisher	Elsevier
Licensed content publication	Trends in Neurosciences
Licensed content title	Pathobiology of ischaemic stroke: an integrated view
Licensed content author	Ulrich Dirnagl,Costantino Iadecola,Michael A. Moskowitz
Licensed content date	1 September 1999
Licensed content volume number	22
Licensed content issue number	9
Number of pages	7
Start Page	391
End Page	397
Type of Use	reuse in a thesis/dissertation
Portion	figures/tables/illustrations
Number of figures/tables/illustrations	1
Format	both print and electronic
Are you the author of this Elsevier article?	No
Will you be translating?	No
Title of your thesis/dissertation	Polymer micro- and nanofluidic systems for in vitro diagnostics: Analyzing single cells and molecules
Expected completion date	May 2014
Estimated size (number of pages)	200

Elsevier VAT number	GB 494 6272 12
Permissions price	0.00 USD
VAT/Local Sales Tax	0.00 USD / 0.00 GBP
Total	**0.00 USD**

Terms and Conditions

INTRODUCTION

1. The publisher for this copyrighted material is Elsevier. Byclicking "accept" in connection with completing this licensingtransaction, you agree that the following terms and conditions apply to thistransaction (along with the Billing and Payment terms and conditionsestablished by Copyright Clearance Center, Inc. ("CCC"), at the timethat you opened your Rightslink account and that are available at any time at http://myaccount.copyright.com).

GENERAL TERMS

2. Elsevier hereby grants you permission to reproduce the aforementionedmaterial subject to the terms and conditions indicated.
3. Acknowledgement: If any part of the material to be used (for example,figures) has appeared in our publication with credit or acknowledgement toanother source, permission must also be sought from that source. If suchpermission is not obtained then that material may not be included in yourpublication/copies. Suitable acknowledgement to the source must be made, eitheras a footnote or in a reference list at the end of your publication, asfollows:
"Reprinted from Publication title, Vol /edition number, Author(s), Title ofarticle / title of chapter, Pages No., Copyright (Year), with permission from Elsevier [OR APPLICABLE SOCIETY COPYRIGHT OWNER]." Also Lancet special credit -"Reprinted from The Lancet, Vol. number, Author(s), Title of article, PagesNo., Copyright (Year), with permission from Elsevier."
4. Reproduction of this material is confined to the purpose and/or media forwhich permission is hereby given.
5. Altering/Modifying Material: Not Permitted. However figures andillustrations may be altered/adapted minimally to serve your work. Any otherabbreviations, additions, deletions and/or any other alterations shall be madeonly with prior written authorization of Elsevier Ltd. (Please contact Elsevierat permissions@elsevier.com)
6. If the permission fee for the requested use of our material is waived inthis instance, please be advised that your future requests for Elseviermaterials may attract a fee.
7. Reservation of Rights: Publisher reserves all rights not specificallygranted in the combination of (i) the license details provided by you andaccepted in the course of this licensing transaction, (ii) these terms andconditions and (iii) CCC's Billing and Payment terms and conditions.
8. License Contingent Upon Payment: While you may exercise the rightslicensed immediately upon issuance of the license at the end of the licensingprocess for the transaction, provided that you have disclosed complete andaccurate details of your proposed use, no license is finally effective unlessand until full payment is received from you (either by publisher or by CCC) asprovided in CCC's Billing and Payment terms and conditions. If fullpayment is not received on a timely basis, then any license preliminarilygranted shall be deemed automatically revoked and shall be void as if nevergranted. Further, in the event that you breach any of these terms andconditions or any of CCC's Billing and Payment terms and conditions, thelicense is automatically revoked and shall be void as if never granted. Use of materials as described in a revoked license, as well as any use of thematerials beyond the scope of an unrevoked license, may constitute copyrightinfringement and publisher reserves the right to take any and all action toprotect its copyright in the materials.
9. Warranties: Publisher makes no representations or warranties with respectto the licensed material.
10. Indemnity: You hereby indemnify and agree to hold harmless publisher andCCC, and their respective officers, directors, employees and agents, from andagainst any and all claims arising out of your use of the licensed materialother than as specifically authorized pursuant to this license.
11. No Transfer of License: This license is personal to you and maynot besublicensed, assigned, or transferred by you to any other person withoutpublisher's written permission.
12. No Amendment Except in Writing: This license may not be amended exceptin a writing signed by both parties (or, in the case of publisher, by CCC onpublisher's behalf).
13. Objection to Contrary Terms: Publisher hereby objects to any termscontained in any purchase order, acknowledgment, check endorsement or otherwriting prepared by you, which terms are inconsistent with these terms andconditions or CCC's Billing and Payment terms and conditions. These termsand conditions, together with CCC's Billing and Payment terms and conditions(which are incorporated herein), comprise the entire agreement between you andpublisher (and CCC) concerning this licensing transaction. In the eventof any conflict between your obligations established by these terms andconditions and those established by CCC's Billing and Payment terms andconditions, these terms and conditions shall control.
14. Revocation: Elsevier or Copyright Clearance Center may deny thepermissions described in this License at their sole

discretion, for any reason or no reason, with a full refund payable to you. Notice of such denial will be made using the contact information provided by you. Failure to receive such notice will not alter or invalidate the denial. In no event will Elsevier or Copyright Clearance Center be responsible or liable for any costs, expenses or damage incurred by you as a result of a denial of your permission request, other than a refund of the amount(s) paid by you to Elsevier and/or Copyright Clearance Center for denied permissions.

LIMITED LICENSE

The following terms and conditions apply only to specific license types:

15. **Translation**: This permission is granted for non-exclusive world **English** rights only unless your license was granted for translation rights. If you licensed translation rights you may only translate this content into the languages you requested. A professional translator must perform all translations and reproduce the content word for word preserving the integrity of the article. If this license is to re-use 1 or 2 figures then permission is granted for non-exclusive world rights in all languages.

16. **Posting licensed content on any Website**: The following terms and conditions apply as follows: Licensing material from an Elsevier journal: All content posted to the web site must maintain the copyright information line on the bottom of each image; A hyper-text must be included to the Homepage of the journal from which you are licensing at http://www.sciencedirect.com/science/journal/xxxxx or the Elsevier homepage for books at http://www.elsevier.com; Central Storage: This license does not include permission for a scanned version of the material to be stored in a central repository such as that provided by Heron/XanEdu.

Licensing material from an Elsevier book: A hyper-text link must be included to the Elsevier homepage at http://www.elsevier.com . All content posted to the web site must maintain the copyright information line on the bottom of each image.

Posting licensed content on Electronic reserve: In addition to the above the following clauses are applicable: The web site must be password-protected and made available only to bona fide students registered on a relevant course. This permission is granted for 1 year only. You may obtain a new license for future website posting.

For journal authors: the following clauses are applicable in addition to the above: Permission granted is limited to the author accepted manuscript version* of your paper.

***Accepted Author Manuscript (AAM) Definition:** An accepted author manuscript (AAM) is the author's version of the manuscript of an article that has been accepted for publication and which may include any author-incorporated changes suggested through the processes of submission processing, peer review, and editor-author communications. AAMs do not include other publisher value-added contributions such as copy-editing, formatting, technical enhancements and (if relevant) pagination.

You are not allowed to download and post the published journal article (whether PDF or HTML, proof or final version), nor may you scan the printed edition to create an electronic version. A hyper-text must be included to the Homepage of the journal from which you are licensing at http://www.sciencedirect.com/science/journal/xxxxx. As part of our normal production process, you will receive an e-mail notice when your article appears on Elsevier's online service ScienceDirect (www.sciencedirect.com). That e-mail will include the article's Digital Object Identifier (DOI). This number provides the electronic link to the published article and should be included in the posting of your personal version. We ask that you wait until you receive this e-mail and have the DOI to do any posting.

Posting to a repository: Authors may post their AAM immediately to their employer's institutional repository for internal use only and may make their manuscript publically available after the journal-specific embargo period has ended.

Please also refer to Elsevier's Article Posting Policy for further information.

18. **For book authors** the following clauses are applicable in addition to the above: Authors are permitted to place a brief summary of their work online only.. You are not allowed to download and post the published electronic version of your chapter, nor may you scan the printed edition to create an electronic version. Posting to a repository: Authors are permitted to post a summary of their chapter only in their institution's repository.

20. **Thesis/Dissertation**: If your license is for use in a thesis/dissertation your thesis may be submitted to your institution in either print or electronic form. Should your thesis be published commercially, please reapply for permission. These requirements include permission for the Library and Archives of Canada to supply single copies, on demand, of the complete thesis and include permission for UMI to supply single copies, on demand, of the complete thesis. Should your thesis be published commercially, please reapply for permission.

Elsevier Open Access Terms and Conditions

Elsevier publishes Open Access articles in both its Open Access journals and via its Open Access articles option in subscription journals.

Authors publishing in an Open Access journal or who choose to make their article Open Access in an Elsevier subscription journal select one of the following Creative Commons user licenses, which define how a reader may

reusetheir work: Creative Commons Attribution License (CC BY), Creative CommonsAttribution – Non Commercial - ShareAlike (CC BY NCSA) and Creative Commons Attribution – Non Commercial – No Derivatives (CC BYNC ND)

Terms & Conditions applicable toall Elsevier Open Access articles:

Any reuse of the article must not represent the author as endorsing theadaptation of the article nor should the article be modified in such a way asto damage the author's honour or reputation.

The author(s) must be appropriately credited.

If any part of the material to be used (for example, figures) has appearedin our publication with credit or acknowledgement to another source it is theresponsibility of the user to ensure their reuse complies with the terms andconditions determined by the rights holder.

Additional Terms & Conditionsapplicable to each Creative Commons user license:

CC BY: You may distribute andcopy the article, create extracts, abstracts, and other revised versions,adaptations or derivative works of or from an article (such as a translation),to include in a collective work (such as an anthology), to text or data minethe article, including for commercial purposes without permission from Elsevier

CC BY NC SA: For non-commercialpurposes you may distribute and copy the article, create extracts, abstractsand other revised versions, adaptations or derivative works of or from anarticle (such as a translation), to include in a collective work (such as ananthology), to text and data mine the article and license new adaptations or creationsunder identical terms without permission from Elsevier

CC BY NC ND: For non-commercialpurposes you may distribute and copy the article and include it in a collectivework (such as an anthology), provided you do not alter or modify the article,without permission from Elsevier

Any commercial reuse of Open Access articles published with a CC BY NC SA or CC BY NC NDlicense requires permission from Elsevier and will be subject to a fee.

Commercial reuse includes:

- Promotional purposes (advertising or marketing)
- Commercial exploitation (e.g. a product forsale or loan)
- Systematic distribution (for a fee or free ofcharge)

Please refer to Elsevier'sOpen Access Policy for further information.

21. **Other Conditions**:

v1.7

If you would like to pay for this license now, please remit this license along with your payment made payable to "COPYRIGHT CLEARANCE CENTER" otherwise you will be invoiced within 48 hours of the license date. Payment should be in the form of a check or money order referencing your account number and this invoice number RLNK501274268. Once you receive your invoice for this order, you may pay your invoice by credit card. Please follow instructions provided at that time.

Make Payment To:
Copyright Clearance Center
Dept 001
P.O. Box 843006
Boston, MA 02284-3006

For suggestions or comments regarding this order, contact RightsLink Customer Support:
customercare@copyright.com **or +1-877-622-5543 (toll free in the US) or +1-978-646-2777.**

Gratis licenses (referencing $0 in the Total field) are free. Please retain this printable license for your reference. No payment is required.

ELSEVIER LICENSE
TERMS AND CONDITIONS

Apr 09, 2014

This is a License Agreement between SWATHI REDDY PULLAGURLA ("You") and Elsevier ("Elsevier") provided by Copyright Clearance Center ("CCC"). The license consists of your order details, the terms and conditions provided by Elsevier, and the payment terms and conditions.

All payments must be made in full to CCC. For payment instructions, please see information listed at the bottom of this form.

Supplier	Elsevier Limited The Boulevard,Langford Lane Kidlington,Oxford,OX5 1GB,UK
Registered Company Number	1982084
Customer name	SWATHI REDDY PULLAGURLA
Customer address	924 NORTH HERITAGE CIRCLE CHAPEL HILL, NC 27516
License number	3364900948048
License date	Apr 09, 2014
Licensed content publisher	Elsevier
Licensed content publication	Drug Discovery Today
Licensed content title	Therapeutic strategies for the treatment of stroke
Licensed content author	A. Richard Green,Ashfaq Shuaib
Licensed content date	August 2006
Licensed content volume number	11
Licensed content issue number	15–16
Number of pages	13
Start Page	681
End Page	693
Type of Use	reuse in a thesis/dissertation
Intended publisher of new work	other
Portion	figures/tables/illustrations
Number of figures/tables/illustrations	1
Format	both print and electronic
Are you the author of this Elsevier article?	No
Will you be translating?	No
Title of your thesis/dissertation	Polymer micro- and nanofluidic systems for in vitro diagnostics: Analyzing single cells and molecules
Expected completion date	May 2014

Estimated size (number of pages)	200
Elsevier VAT number	GB 494 6272 12
Permissions price	0.00 USD
VAT/Local Sales Tax	0.00 USD / 0.00 GBP
Total	**0.00 USD**
Terms and Conditions	

INTRODUCTION

1. The publisher for this copyrighted material is Elsevier. Byclicking "accept" in connection with completing this licensingtransaction, you agree that the following terms and conditions apply to thistransaction (along with the Billing and Payment terms and conditionsestablished by Copyright Clearance Center, Inc. ("CCC"), at the timethat you opened your Rightslink account and that are available at any time at http://myaccount.copyright.com).

GENERAL TERMS

2. Elsevier hereby grants you permission to reproduce the aforementionedmaterial subject to the terms and conditions indicated.
3. Acknowledgement: If any part of the material to be used (for example,figures) has appeared in our publication with credit or acknowledgement toanother source, permission must also be sought from that source. If suchpermission is not obtained then that material may not be included in yourpublication/copies. Suitable acknowledgement to the source must be made, eitheras a footnote or in a reference list at the end of your publication, asfollows:
"Reprinted from Publication title, Vol /edition number, Author(s), Title ofarticle / title of chapter, Pages No., Copyright (Year), with permission fromElsevier [OR APPLICABLE SOCIETY COPYRIGHT OWNER]." Also Lancet special credit -"Reprinted from The Lancet, Vol. number, Author(s), Title of article, PagesNo., Copyright (Year), with permission from Elsevier."
4. Reproduction of this material is confined to the purpose and/or media forwhich permission is hereby given.
5. Altering/Modifying Material: Not Permitted. However figures andillustrations may be altered/adapted minimally to serve your work. Any otherabbreviations, additions, deletions and/or any other alterations shall be madeonly with prior written authorization of Elsevier Ltd. (Please contact Elsevierat permissions@elsevier.com)
6. If the permission fee for the requested use of our material is waived inthis instance, please be advised that your future requests for Elseviermaterials may attract a fee.
7. Reservation of Rights: Publisher reserves all rights not specificallygranted in the combination of (i) the license details provided by you andaccepted in the course of this licensing transaction, (ii) these terms andconditions and (iii) CCC's Billing and Payment terms and conditions.
8. License Contingent Upon Payment: While you may exercise the rightslicensed immediately upon issuance of the license at the end of the licensingprocess for the transaction, provided that you have disclosed complete andaccurate details of your proposed use, no license is finally effective unlessand until full payment is received from you (either by publisher or by CCC) asprovided in CCC's Billing and Payment terms and conditions. If fullpayment is not received on a timely basis, then any license preliminarilygranted shall be deemed automatically revoked and shall be void as if nevergranted. Further, in the event that you breach any of these terms andconditions or any of CCC's Billing and Payment terms and conditions, thelicense is automatically revoked and shall be void as if never granted. Use of materials as described in a revoked license, as well as any use of thematerials beyond the scope of an unrevoked license, may constitute copyrightinfringement and publisher reserves the right to take any and all action toprotect its copyright in the materials.
9. Warranties: Publisher makes no representations or warranties with respectto the licensed material.
10. Indemnity: You hereby indemnify and agree to hold harmless publisher andCCC, and their respective officers, directors, employees and agents, from andagainst any and all claims arising out of your use of the licensed materialother than as specifically authorized pursuant to this license.
11. No Transfer of License: This license is personal to you and maynot besublicensed, assigned, or transferred by you to any other person withoutpublisher's written permission.
12. No Amendment Except in Writing: This license may not be amended exceptin a writing signed by both parties (or, in the case of publisher, by CCC onpublisher's behalf).
13. Objection to Contrary Terms: Publisher hereby objects to any termscontained in any purchase order, acknowledgment, check endorsement or otherwriting prepared by you, which terms are inconsistent with these terms andconditions or CCC's Billing and Payment terms and conditions. These termsand conditions, together with CCC's Billing and Payment terms and conditions(which are incorporated herein), comprise the entire agreement between you andpublisher (and CCC) concerning this licensing transaction. In the eventof any conflict between your obligations established by these terms andconditions and those established by CCC's Billing and Payment terms andconditions,

these terms and conditions shall control.

14. Revocation: Elsevier or Copyright Clearance Center may deny thepermissions described in this License at their sole discretion, for any reasonor no reason, with a full refund payable to you. Notice of such denialwill be made using the contact information provided by you. Failure toreceive such notice will not alter or invalidate the denial. In no eventwill Elsevier or Copyright Clearance Center be responsible or liable for anycosts, expenses or damage incurred by you as a result of a denial of yourpermission request, other than a refund of the amount(s) paid by you toElsevier and/or Copyright Clearance Center for denied permissions.

LIMITED LICENSE

The following terms and conditions apply only to specific license types:

15. **Translation**: This permission is granted fornon-exclusive world **English** rights only unless yourlicense was granted for translation rights. If you licensed translation rights you may only translate this content into the languages you requested. Aprofessional translator must perform all translations and reproduce the contentword for word preserving the integrity of the article. If this license is tore-use 1 or 2 figures then permission is granted for non-exclusive world rightsin all languages.

16. **Posting licensed content on any Website**: The followingterms and conditions apply as follows: Licensing material from an Elsevierjournal: All content posted to the web site must maintain the copyright informationline on the bottom of each image; A hyper-text must be included to the Homepageof the journal from which you are licensing at http://www.sciencedirect.com/science/journal/xxxxx orthe Elsevier homepage for books at http://www.elsevier.com; CentralStorage: This license does not include permission for a scanned version of thematerial to be stored in a central repository such as that provided byHeron/XanEdu.

Licensing material from an Elsevier book: A hyper-text link must be includedto the Elsevier homepage at http://www.elsevier.com . Allcontent posted to the web site must maintain the copyright information line onthe bottom of each image.

Posting licensed content on Electronic reserve: In addition to the above the following clausesare applicable: The web site must be password-protected and made available onlyto bona fide students registered on a relevant course. This permission isgranted for 1 year only. You may obtain a new license for future websiteposting.

For journal authors: the following clauses are applicable inaddition to the above: Permission granted is limited to the author acceptedmanuscript version* of your paper.

***Accepted Author Manuscript (AAM) Definition:** An accepted authormanuscript (AAM) is the author's version of the manuscript of an article thathas been accepted for publication and which may include any author-incorporatedchanges suggested through the processes of submission processing, peer review,and editor-author communications. AAMs do not include other publishervalue-added contributions such as copy-editing, formatting, technicalenhancements and (if relevant) pagination.

You are not allowed to download and post the published journal article (whetherPDF or HTML, proof or final version), nor may you scan the printed edition tocreate an electronic version. A hyper-text must be included to the Homepage ofthe journal from which you are licensing at http://www.sciencedirect.com/science/journal/xxxxx. As part of our normal production process, you will receive an e-mail noticewhen your article appears on Elsevier's online service ScienceDirect(www.sciencedirect.com). That e-mail will include the article's Digital ObjectIdentifier (DOI). This number provides the electronic link to the publishedarticle and should be included in the posting of your personal version. We askthat you wait until you receive this e-mail and have the DOI to do any posting.

Posting to a repository: Authorsmay post their AAM immediately to their employer's institutional repository forinternal use only and may make their manuscript publically available after thejournal-specific embargo period has ended.

Please also refer to Elsevier'sArticle Posting Policy for further information.

18. **For book authors** the following clauses are applicable in addition tothe above: Authors are permitted to place a briefsummary of their work online only.. You are notallowed to download and post the published electronic version of your chapter,nor may you scan the printed edition to create an electronic version. Posting to a repository: Authors arepermitted to post a summary of their chapter only in their institution'srepository.

20. **Thesis/Dissertation**: If your license is for use in athesis/dissertation your thesis may be submitted to your institution in eitherprint or electronic form. Should your thesis be published commercially, pleasereapply for permission. These requirements include permission for the Libraryand Archives of Canada to supply single copies, on demand, of the completethesis and include permission for UMI to supply single copies, on demand, ofthe complete thesis. Should your thesis be published commercially, pleasereapply for permission.

Elsevier Open Access Terms andConditions

Elsevier publishes Open Access articles in both its Open Access journals andvia its Open Access articles option in subscription journals.

Authors publishing in an Open Access journal or who choose to make theirarticle Open Access in an Elsevier subscription journal select one of thefollowing Creative Commons user licenses, which define how a reader may reusetheir work: Creative Commons Attribution License (CC BY), Creative CommonsAttribution – Non Commercial - ShareAlike (CC BY NCSA) and Creative Commons Attribution – Non Commercial – No Derivatives (CC BYNC ND)

Terms & Conditions applicable toall Elsevier Open Access articles:

Any reuse of the article must not represent the author as endorsing theadaptation of the article nor should the article be modified in such a way asto damage the author's honour or reputation.

The author(s) must be appropriately credited.

If any part of the material to be used (for example, figures) has appearedin our publication with credit or acknowledgement to another source it is theresponsibility of the user to ensure their reuse complies with the terms andconditions determined by the rights holder.

Additional Terms & Conditionsapplicable to each Creative Commons user license:

CC BY: You may distribute andcopy the article, create extracts, abstracts, and other revised versions,adaptations or derivative works of or from an article (such as a translation),to include in a collective work (such as an anthology), to text or data minethe article, including for commercial purposes without permission from Elsevier

CC BY NC SA: For non-commercialpurposes you may distribute and copy the article, create extracts, abstractsand other revised versions, adaptations or derivative works of or from anarticle (such as a translation), to include in a collective work (such as ananthology), to text and data mine the article and license new adaptations or creationsunder identical terms without permission from Elsevier

CC BY NC ND: For non-commercialpurposes you may distribute and copy the article and include it in a collectivework (such as an anthology), provided you do not alter or modify the article,without permission from Elsevier

Any commercial reuse of Open Access articles published with a CC BY NC SA or CC BY NC NDlicense requires permission from Elsevier and will be subject to a fee.

Commercial reuse includes:

- Promotional purposes (advertising or marketing)
- Commercial exploitation (e.g. a product forsale or loan)
- Systematic distribution (for a fee or free ofcharge)

Please refer to Elsevier'sOpen Access Policy for further information.

21. **Other Conditions**:

v1.7

If you would like to pay for this license now, please remit this license along with your payment made payable to "COPYRIGHT CLEARANCE CENTER" otherwise you will be invoiced within 48 hours of the license date. Payment should be in the form of a check or money order referencing your account number and this invoice number RLNK501274274. Once you receive your invoice for this order, you may pay your invoice by credit card. Please follow instructions provided at that time.

Make Payment To:
Copyright Clearance Center
Dept 001
P.O. Box 843006
Boston, MA 02284-3006

For suggestions or comments regarding this order, contact RightsLink Customer Support:
customercare@copyright.com **or +1-877-622-5543 (toll free in the US) or +1-978-646-2777.**

Gratis licenses (referencing $0 in the Total field) are free. Please retain this printable license for your reference. No payment is required.

NATURE PUBLISHING GROUP LICENSE TERMS AND CONDITIONS

Apr 09, 2014

This is a License Agreement between SWATHI REDDY PULLAGURLA ("You") and Nature Publishing Group ("Nature Publishing Group") provided by Copyright Clearance Center ("CCC"). The license consists of your order details, the terms and conditions provided by Nature Publishing Group, and the payment terms and conditions.

All payments must be made in full to CCC. For payment instructions, please see information listed at the bottom of this form.

License Number	3364901198131
License date	Apr 09, 2014
Licensed content publisher	Nature Publishing Group
Licensed content publication	Nature Reviews Neuroscience
Licensed content title	Astrocyte|[ndash]|endothelial interactions at the blood|[ndash]|brain barrier
Licensed content author	N. Joan Abbott,Lars RönnbäckandElisabeth Hansson
Licensed content date	Jan 1, 2006
Volume number	7
Issue number	1
Type of Use	reuse in a dissertation / thesis
Requestor type	academic/educational
Format	print and electronic
Portion	figures/tables/illustrations
Number of figures/tables/illustrations	1
High-res required	no
Figures	Figure 2 | Cellular constituents of the blood–brain barrier.
Author of this NPG article	no
Your reference number	None
Title of your thesis / dissertation	Polymer micro- and nanofluidic systems for in vitro diagnostics: Analyzing single cells and molecules
Expected completion date	May 2014
Estimated size (number of pages)	200
Total	**0.00 USD**
Terms and Conditions	

Terms and Conditions for Permissions

Nature Publishing Group hereby grants you a non-exclusive license to reproduce this material for this purpose, and for no other use,subject to the conditions below:

1. NPG warrants that it has, to the best of its knowledge, the rights to license reuse of this material. However, you should ensure that the material you are requesting is original to Nature Publishing Group and does not carry the copyright of another entity (as credited in the published version). If the credit line on any part of the material you have requested indicates that it was reprinted or adapted by NPG with permission from another source, then you should also seek permission from that source to reuse the material.

2. Permission granted free of charge for material in print is also usually granted for any electronic version of that work, provided that the material is incidental to the work as a whole and that the electronic version is essentially equivalent to, or substitutes for, the print version.Where print permission has been granted for a fee, separate permission must be obtained for any additional, electronic re-use (unless, as in the case of a full paper, this has already been accounted for during your initial request in the calculation of a print run).NB: In all cases, web-based use of full-text articles must be authorized separately through the 'Use on a Web Site' option when requesting permission.

3. Permission granted for a first edition does not apply to second and subsequent editions and for editions in other languages (except for signatories to the STM Permissions Guidelines, or where the first edition permission was granted for free).

4. Nature Publishing Group's permission must be acknowledged next to the figure, table or abstract in print. In electronic form, this acknowledgement must be visible at the same time as the figure/table/abstract, and must be hyperlinked to the journal's homepage.

5. The credit line should read:
   Reprinted by permission from Macmillan Publishers Ltd: [JOURNAL NAME] (reference citation), copyright (year of publication)
   For AOP papers, the credit line should read:
   Reprinted by permission from Macmillan Publishers Ltd: [JOURNAL NAME], advance online publication, day month year (doi: 10.1038/sj.[JOURNAL ACRONYM].XXXXX)

   Note: For republication from the *British Journal of Cancer*, the following credit lines apply.
   Reprinted by permission from Macmillan Publishers Ltd on behalf of Cancer Research UK: [JOURNAL NAME] (reference citation), copyright (year of publication)For AOP papers, the credit line should read:
   Reprinted by permission from Macmillan Publishers Ltd on behalf of Cancer Research UK: [JOURNAL NAME], advance online publication, day month year (doi: 10.1038/sj.[JOURNAL ACRONYM].XXXXX)

6. Adaptations of single figures do not require NPG approval. However, the adaptation should be credited as follows:

   Adapted by permission from Macmillan Publishers Ltd: [JOURNAL NAME] (reference citation), copyright (year of publication)

   Note: For adaptation from the *British Journal of Cancer*, the following credit line applies.
   Adapted by permission from Macmillan Publishers Ltd on behalf of Cancer Research UK: [JOURNAL NAME] (reference citation), copyright (year of publication)

7. Translations of 401 words up to a whole article require NPG approval. Please visit http://www.macmillanmedicalcommunications.com for more information.Translations of up to a 400 words do not require NPG approval. The translation should be credited as follows:

   Translated by permission from Macmillan Publishers Ltd: [JOURNAL NAME] (reference citation), copyright (year of publication).

   Note: For translation from the *British Journal of Cancer*, the following credit line applies.
   Translated by permission from Macmillan Publishers Ltd on behalf of Cancer Research UK: [JOURNAL NAME] (reference citation), copyright (year of publication)

We are certain that all parties will benefit from this agreement and wish you the best in the use of this material. Thank you.
Special Terms:
v1.1

If you would like to pay for this license now, please remit this license along with your payment made payable to "COPYRIGHT CLEARANCE CENTER" otherwise you will be invoiced within 48 hours of the license date. Payment should be in the form of a check or money order referencing your account number and this invoice number RLNK501274288. Once you receive your invoice for this order, you may pay your invoice by credit card. Please follow instructions provided at that time.

Make Payment To:
Copyright Clearance Center
Dept 001
P.O. Box 843006
Boston, MA 02284-3006

For suggestions or comments regarding this order, contact RightsLink Customer Support:
customercare@copyright.com or +1-877-622-5543 (toll free in the US) or +1-978-646-2777.

Gratis licenses (referencing $0 in the Total field) are free. Please retain this printable license for your reference. No payment is required.

ELSEVIER LICENSE
TERMS AND CONDITIONS

Apr 09, 2014

This is a License Agreement between SWATHI REDDY PULLAGURLA ("You") and Elsevier ("Elsevier") provided by Copyright Clearance Center ("CCC"). The license consists of your order details, the terms and conditions provided by Elsevier, and the payment terms and conditions.

All payments must be made in full to CCC. For payment instructions, please see information listed at the bottom of this form.

Supplier	Elsevier Limited The Boulevard,Langford Lane Kidlington,Oxford,OX5 1GB,UK
Registered Company Number	1982084
Customer name	SWATHI REDDY PULLAGURLA
Customer address	924 NORTH HERITAGE CIRCLE CHAPEL HILL, NC 27516
License number	3364910459104
License date	Apr 09, 2014
Licensed content publisher	Elsevier
Licensed content publication	Biosensors and Bioelectronics
Licensed content title	Elongated oligonucleotide-linked immunosorbent assay for sensitive detection of a biomarker in a microwell plate-based platform
Licensed content author	Ki-Cheol Han,Eun Gyeong Yang,Dae-Ro Ahn
Licensed content date	15 December 2013
Licensed content volume number	50
Licensed content issue number	None
Number of pages	4
Start Page	421
End Page	424
Type of Use	reuse in a thesis/dissertation
Intended publisher of new work	other
Portion	figures/tables/illustrations
Number of figures/tables/illustrations	1
Format	both print and electronic
Are you the author of this Elsevier article?	No
Will you be translating?	No
Title of your thesis/dissertation	Polymer micro- and nanofluidic systems for in vitro diagnostics: Analyzing single cells and molecules

Expected completion date	May 2014
Estimated size (number of pages)	200
Elsevier VAT number	GB 494 6272 12
Permissions price	0.00 USD
VAT/Local Sales Tax	0.00 USD / 0.00 GBP
Total	**0.00 USD**

Terms and Conditions

INTRODUCTION

1. The publisher for this copyrighted material is Elsevier. Byclicking "accept" in connection with completing this licensingtransaction, you agree that the following terms and conditions apply to thistransaction (along with the Billing and Payment terms and conditionsestablished by Copyright Clearance Center, Inc. ("CCC"), at the timethat you opened your Rightslink account and that are available at any time at http://myaccount.copyright.com).

GENERAL TERMS

2. Elsevier hereby grants you permission to reproduce the aforementionedmaterial subject to the terms and conditions indicated.
3. Acknowledgement: If any part of the material to be used (for example,figures) has appeared in our publication with credit or acknowledgement toanother source, permission must also be sought from that source. If suchpermission is not obtained then that material may not be included in yourpublication/copies. Suitable acknowledgement to the source must be made, eitheras a footnote or in a reference list at the end of your publication, asfollows:
"Reprinted from Publication title, Vol /edition number, Author(s), Title ofarticle / title of chapter, Pages No., Copyright (Year), with permission from Elsevier [OR APPLICABLE SOCIETY COPYRIGHT OWNER]." Also Lancet special credit -"Reprinted from The Lancet, Vol. number, Author(s), Title of article, PagesNo., Copyright (Year), with permission from Elsevier."
4. Reproduction of this material is confined to the purpose and/or media forwhich permission is hereby given.
5. Altering/Modifying Material: Not Permitted. However figures andillustrations may be altered/adapted minimally to serve your work. Any otherabbreviations, additions, deletions and/or any other alterations shall be madeonly with prior written authorization of Elsevier Ltd. (Please contact Elsevierat permissions@elsevier.com)
6. If the permission fee for the requested use of our material is waived inthis instance, please be advised that your future requests for Elseviermaterials may attract a fee.
7. Reservation of Rights: Publisher reserves all rights not specificallygranted in the combination of (i) the license details provided by you andaccepted in the course of this licensing transaction, (ii) these terms andconditions and (iii) CCC's Billing and Payment terms and conditions.
8. License Contingent Upon Payment: While you may exercise the rightslicensed immediately upon issuance of the license at the end of the licensingprocess for the transaction, provided that you have disclosed complete andaccurate details of your proposed use, no license is finally effective unlessand until full payment is received from you (either by publisher or by CCC) asprovided in CCC's Billing and Payment terms and conditions. If fullpayment is not received on a timely basis, then any license preliminarilygranted shall be deemed automatically revoked and shall be void as if nevergranted. Further, in the event that you breach any of these terms andconditions or any of CCC's Billing and Payment terms and conditions, thelicense is automatically revoked and shall be void as if never granted. Use of materials as described in a revoked license, as well as any use of thematerials beyond the scope of an unrevoked license, may constitute copyrightinfringement and publisher reserves the right to take any and all action toprotect its copyright in the materials.
9. Warranties: Publisher makes no representations or warranties with respectto the licensed material.
10. Indemnity: You hereby indemnify and agree to hold harmless publisher andCCC, and their respective officers, directors, employees and agents, from andagainst any and all claims arising out of your use of the licensed materialother than as specifically authorized pursuant to this license.
11. No Transfer of License: This license is personal to you and maynot besublicensed, assigned, or transferred by you to any other person withoutpublisher's written permission.
12. No Amendment Except in Writing: This license may not be amended exceptin a writing signed by both parties (or, in the case of publisher, by CCC onpublisher's behalf).
13. Objection to Contrary Terms: Publisher hereby objects to any termscontained in any purchase order, acknowledgment, check endorsement or otherwriting prepared by you, which terms are inconsistent with these terms andconditions or CCC's Billing and Payment terms and conditions. These termsand conditions, together with CCC's Billing and Payment terms and conditions(which are incorporated herein), comprise the entire agreement between you

UV activation of polymeric high aspect ratio microstructures: ramifications in antibody surface loading for circulating tumor cell selection

J. M. Jackson, M. A. Witek, M. L. Hupert, C. Brady, S. Pullagurla, J. Kamande, R. D. Aufforth, C. J. Tignanelli, R. J. Torphy, J. J. Yeh and S. A. Soper, *Lab Chip*, 2014, 14, 106
DOI: 10.1039/C3LC50618E

Alila Medical Media info@alilamedicalimages.com via photodeck.com
to me

Dear swathi reddy pullagurla,

This is the receipt for your payment.

The following order has been paid for:

Description	Qty	USD
Image brain_stroke - Standard License : XXS - 300x300 pixels (Model release: No) (Property release: No)	1	6.00
	TOTAL (US $)	6.00

Thank you!

Alila Medical Media

Dear Alila Medical Media Customer,
The following is a legal agreement between you or the employer or other entity on whose behalf you are entering into this agreement and Alila Medical Media. Please read these Terms of Service (TOS) carefully before downloading any images/videos. By downloading any image/video, you agree to be bound by the terms of these TOS.

All Images/Videos on Alila Medical Media website and all made-to-order (custom made) Images/Videos are protected by United States and international copyright laws and treaties. Alila Medical Media owns all rights, including the copyrights in and to the Images/Videos. Alila Medical Media reserves all rights in and to the Images/Videos not expressly granted to you by the terms of selected license.

STUDENT/TEACHER LICENSE: This license is reserved for students and teachers using images for school projects and classroom lectures ONLY. No web usage is allowed under this license. By purchasing the selected images you hereby agree and acknowledge that you are not acquiring any right, title or interest in or to the images or any associated copyrights, other than the right to possess, hold and use the images for personal, non-commercial purposes. Furthermore, you agree that you will not scan, copy, duplicate, distribute or otherwise reproduce the images. This is a SINGLE SEAT license, it authorizes one natural person to license, download, and use images.

STANDARD LICENSE: You are granted a non-exclusive, non-transferable, non-sublicensable right to use the licensed images/videos in any and all media for the following purposes:

1. Advertising and promotional materials, for print runs of up to one hundred thousand (100,000) copies in the aggregate;
2. Broadcast and theatrical exhibitions, for an intended audience of up to one hundred thousand (100,000) viewers in the aggregate;
3. Print publications and physical products, for print runs of up to one hundred thousand (100,000) copies in the aggregate;
4. Electronic publications, for up to one hundred thousand (100,000) end users licenses or for an intended audience of up to one hundred thousand (100,000) viewers in the aggregate;
5. On website, provided that no image is displayed at a resolution greater than 800 x 800 pixels; and
6. Any other uses approved by Alila Medical Media in writing.

Standard License is a SINGLE SEAT license, it authorizes one natural person to license, download, and use images/videos. You may use images/videos on behalf of your company/organization but you are the only one who can handle the images/videos. If you work in a team within a company, please use our Extended License.
If you are a web designer using images for your clients, you would need to obtain a new license for each of your client.

EXTENDED LICENSE: Same as Standard License above except that there is no limit to the number of print run copies, end user licenses or intended audience viewers.
Extended License is also MULTIPLE SEATS allowing many users within ONE organization/company/institution to share the same images/videos while working on common projects and for common projects of the organization/company/institution ONLY.
Extended License may also be used for legal proceedings (personal injury, medical malpractice

lawsuits), limited to ONE case per license and provided that you will take ALL responsibility regarding the use of the images/videos. Alila Medical Media will NOT be liable for any losses, damages, disputes of any nature resulting from the use and accuracy of contents of the images/videos.

RESTRICTIONS FOR ALL LICENSES:

1. Images/videos may not be resold, sublicensed, assigned, transferred or otherwise made available to third parties except as incorporated into Works for Distribution. Images/videos may not be distributed to third parties as a standalone file or in a way that unreasonably permits the recipient to extract the images/videos for use separate and apart from the Work for Distribution. You will make reasonable best efforts to safeguard against unauthorized third-party access to licensed images/videos.
2. You may not distribute the images/videos in any library or reusable template, electronic or otherwise, including but not limited to website templates, intended to allow reproduction by third parties on electronic or printed products. You may not distribute the licensed images/videos in a manner meant to enable third parties to create derivative works incorporating the images/videos.
3. You may not make “print on demand” sale of the images (you may not post them for sale on "print on demand" sites such as Zazzle or Cafepress or similar; you are welcome, however, to order products from these sites with our images for your own use).
4. You may not post the videos on Youtube or similar video sharing websites as standalone files or in a derivative product where the video(s) constitute more than 50% of the product. You may, however, upload them as unlisted/unsearchable videos accessible ONLY to yourself and for the SOLE purpose of embedding the videos to your website.
5. You may not upload the images/videos to social media websites such as Facebook and the like.
6. You may not superficially modify the images/videos and sell/distribute them to others for consumption, reproduction or re-sale. For example, you may not resell/distribute video content as a screensaver or images as desktop background, wallpapers.
7. You may not incorporate the images/videos into a logo, trademark or service mark.
8. You may not use the images/videos in a manner that violates the law of any applicable jurisdiction.
9. You may not use the images/videos in a pornographic or defamatory manner, whether directly or in context or juxtaposition with other materials.

NOTE ABOUT CUSTOM WORK: All custom made images/videos are subject to the same licensing terms as all other images/videos on our website. Alila Medical Media is the sole copyright holder of all custom works.

CREDIT ATTRIBUTIONS AND COPYRIGHT NOTICES:
We require that all images/videos in use are properly credited to © Alila Medical Media.

DISCLAIMER : Medical information illustrated on images/videos on this website is for educational purposes only and is NOT intended to be medical advice in any cases. Alila Medical Media will NOT be liable for any losses, damages, disputes of any nature resulting from the use and accuracy of contents of the images/videos.

Image license description

April 12, 2014

Licensed to
swathi reddy pullagurla
Louisiana State University
chapel hill, NC 27516
United States
spulla1@tigers.lsu.edu

IMAGE ID	DESCRIPTION
brain_stroke	Image brain_stroke - Standard License : XXS - 300x300 pixels (Model release: No) (Property release: No)

VITA

Swathi Reddy Pullagurla was born to Mr. Vittal Reddy Pullagurla and Mrs. Dhana Lakshmi Pullagurla in Andhra Pradesh, India. She attended Naagarjuna High School from 1993-2001. After schooling, she attended Kakatiya Academy from 2001-2003. Thereafter, she received her Bachelor of Science in Chemistry and Mathematics and Physics (May 2006) from Nizam College, Osmania University. She then enrolled in Nizam College, Osmania University and completed her Master of Science in Physical Chemistry in May 2008. It was while pursuing the Master of Science Degree under the guidance of Dr. Uma Vuruputuri that Swathi received an assistantship to pursue doctoral studies at Louisiana State University (Fall 2008). In the Spring of 2009, she joined Prof. Steven A. Soper research research group at Louisiana State University. In the graduate school, she received Charles E. Coates memorial travel award to attend PITTCON Conference 2013 in Philadelphia, PA and 2014 in Chicago, IL. Swathi is currently a candidate for the Doctor of Philosophy in bioanalytical chemistry, which is expected to be awarded during May 2014 Commencement at LSU, Baton Rouge.